Free Infragravity Waves and their Effect on Coastal Dune Safety

Christodoulos Solomou

Free Infragravity Waves and their Effect on Coastal Dune Safety

by

Christodoulos Solomou

to obtain the degree of
Master of Science in Hydraulic Engineering
at the Delft University of Technology,
to be defended publicly on August 25th, 2022.

Student number:	4816021	
Thesis committee:	Prof. Dr. ir. A.J.H.M. Reniers,	TU Delft, supervisor
	Dr. M.F.S. Tissier,	TU Delft
	Dr. ir. M.A. de Schipper,	TU Delft
	Dr. J. Rutten,	TU Delft
	Dr. ir. D. Rijnsdorp	TU Delft
	Ir. P. van Wiechen,	TU Delft

Preface

The present document marks the final part of my journey as a Master of Science student at TU Delft. Through my journey I had the opportunity to dive into Coastal Engineering, as a result allowing me to have a better understanding of the ocean hydrodynamics and be a part of a project that involves using nature and being able to assess it for coastal safety that can be potentially used as a basis for a future assessment of coastal safety. More importantly being able to be among the brightest people in my field and provide me guidance for my project.

Through my time spent towards completing this project, I had the opportunity to dive deeper into programming, and computational modelling while developing my research skills that all will surely be useful to me for my future. I had the opportunity to grow as an individual and have a better understanding of my field. For this opportunity I would like to thank my supervisor, Ad for giving me the opportunity to be able to be a part of this project, while being able to supervise and advise me on a weekly basis. As a result, allowing me to learn at my own pace while being patient with me throughout the completion of this project.

In addition, I would like to express my thanks to my committee; Marion for being able to provide advice to me for my project direction and modelling advice at times I require it, Jantien, and Paul for providing a very deep insight on the modelling aspect of the thesis, Dirk for his insight on computational modelling and ocean waves, and lastly Matthieu for his advice on formatting and presentation advice next to his coastal knowledge for my project. I could not have asked for a better committee for my journey, as it was a very positive experience for me, by having feedback from different perspectives and expertise, therefore depth to the project.

Lastly I would also like to thank my family for being patient and there for me when I needed them. My friends, and my brothers for listening to me non-stop about this project, while also providing a space that I was able to relax while being there for me when I needed a break regardless if they were on the same or a different country as me.

Christodoulos Solomou
Delft, August 18th, 2022

Abstract

The coastal safety of the dunes are of high importance for low laying countries (Chen et al., 2017). This is especially true for the Netherlands as it is used officially as a safety measure against flooding from extreme weather since 1984 (Rijkswaterstaat, 1989). As of current 1D modelling of the waves is an acceptable method for the Dutch coast to assess the safety of the dunes (Den Heijer, 2013). For assessing the dune coastal safety the 98^{th} percentile of the runup $R_{2\%}$ (Stockdon et al., 2006) is used for defining the wave response during a storm on the dunes. The current dune coastal safety studies consider bound waves (infragravity and sea-swell waves) propagating from offshore to nearshore. However, due to the Dutch coast being located at a very large semi-enclosed basin additional free infragravity waves can be present during a storm next to the bound waves that are reflected from other coasts (Daouk, 2020) as leaky waves (Herbers et al., 1995), and potentially increasing the $R_{2\%}$ magnitude. Here we show that the $R_{2\%}$ with the additional free infragravity waves in the wave domain can have a significant response on the dune coastal safety. The additional free infragravity waves can have tens of centimetres of $R_{2\%}$ magnitude increase that is dependent on the slope of the domain. For the additional free infragravity waves a higher $R_{2\%}$ is observed for steeper slopes, while a larger $R_{2\%}$ growth is observed at the milder slopes when the free infragravity waves are initially introduced to the slope. The dune coastal safety assessments conducted thus far do not consider the effects from leaky waves from other coasts, therefore underestimating the safety provided from the dunes against flooding. With the research conducted by considering additional free infragravity waves with the traditionally bound waves originating in a storm, a better insight can be provided for dune coastal safety. As a result, companies and governmental bodies such as Rijkswaterstaat in the Netherlands that assess the coastal safety of the dunes can benefit by having a more complete representation of the coastal hydrodynamics that can as a result prevent flooding or provide dune nourishment after the episodic event (Sallenger, 2000).

Contents

1

Introduction

1.1. Coastal Safety of Dunes

Coastal defences are becoming more important for low laying countries where the global sea level (GMSL) has been rising at a faster than expected rate (Chen et al., 2017). Coastal dunes are one such features that protects coasts against flooding and has been used as a primary defence mechanism since 1984 in the Netherlands (Rijkswaterstaat, 1989). However, the dunes require sediment nourishment when there are severe storms large enough that dunes cannot replenish naturally over time (Sallenger, 2000). Therefore, the need to understand how the dunes are affected during extreme storms is necessary for understanding dune coastal safety and therefore erosion of the lowlands infrastructure situated inland behind the dunes. Figure 1.1 shows a sketch of the dune wave attack of long and short waves, that create dune erosion and accretion zones.

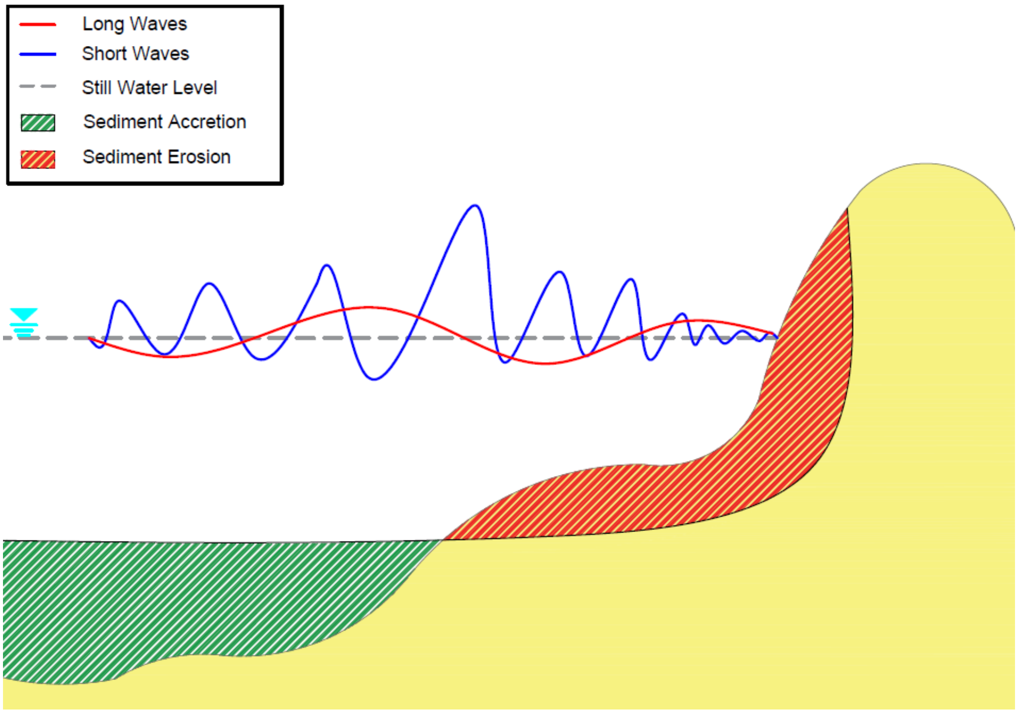

Figure 1.1: Dune erosion and sediment deposition sketch under severe wave attack

1.2. Infragravity Waves

Infragravity waves are a product from the generation of wind waves with a frequency range of 0.004Hz -0.04Hz. The infragravity waves as a whole, contribute to the runup, and dune erosion which affect the dune coastal safety.

There are two types of infragravity waves identified that are approaching the coast, the bound and free infragravity waves (Longuet-Higgins and Stewart, 1962). Bound infragravity waves travel as a group with sea-swell waves and are released as free once the group velocity starts to reduce due to a forcing mechanism such as a breaker zone (Symonds et al., 1982) or high friction environment such as coral reefs (Gawehn et al.,2016) to name a few. Therefore, allowing for free infragravity waves to be present at the surf zone and are the ones affecting the dune coastal safety.

Free infragravity waves become important for coastal safety as they reflect at the shoreline and then as a result propagate in the offshore direction (Ruessink, 1998; Roelvink and Reniers, 2011) that differs in magnitude for each bed slope (Janssen et al., 2003). The freely propagating waves at the coast can be trapped in the surf zone (edge waves) if they are approaching the coast with an oblique angle causing additional free infragravity waves to be present bouncing off at the edge of the surf zone and the swash zone (Herbers et al., 1995) saturating the free infragravity waves present in the surf zone. However, when the waves approach the the surf zone with an incident wave angle that is acute, the free infragravity waves leave the surf zone and propagate offshore, also known as leaky waves (Herbers et al., 1995). The edge waves can then potentially enhance the infragravity wave magnitude in the surf zone, while the leaky waves can propagate offshore to different coastline that can enhance the wave field during a storm (Daouk 2020).

1.3. Problem Statement

The dunes are important for the coastal defence that is utilised against flooding in the Netherlands (Rijkswaterstaat, 1989). Dunes during extreme storms experience severe conditions that can cause erosion thus requiring manual dune maintenance (Sallenger, 2000). Dune erosion and wave hydrodynamics during storms are very sensitive to morphological boundary conditions such as the beach slope, which need to be better understood as it has significant effects under different wave conditions (van Rijn, 2009)
The reliability assessment of the coastal safety needs to be considered and therefore critically assessed. As of current in the Dutch coast, a 1D model is being used to assess the dune erosion (Den Heijer, 2013). A 1D model is still to be fully utilised to assess the effect of the free infragravity wave, which can be present next to the bounded waves during a storm.

There is a necessity for assessing the effect of the additional free infragravity waves that can come from other coasts and affect larger basins such as the North sea, therefore, the Dutch coast. This effect can be better highlighted during more severe wave phenomena, such as during storm conditions. The effect of these incident additional free infragravity waves were recently researched in a 1D model by Daouk, (2020) which has a significant impact on the coastal safety, and is therefore concerning. The effects that the additional free infragravity waves have on coastal safety are not yet clear that originate from leaky waves of other coasts. The added free infragravity waves can therefore potentially affect the dune coastal safety with higher runup and erosion rates, which can have unexpected effects on coastal process. However, what is known is that the free infragravity waves are sensitive to the bottom slope which does need further research to be conducted to fully grasp the extent of the effect different slope angles can have to the coastal safety (Daouk, 2020). The slope of the beach changes how much the infragravity waves contribute toward runup and hence dune erosion (De Bakker et al., 016a; de Bakker et al.,2014) due to the natural sensitivity of this parameter. As a result the slope parameter should be considered when considering the wave runup.

1.4. Hypothesis and research questions

The free infragravity waves located at the offshore boundary can be a very important parameter for coastal safety. The variable slope is seen to be a sensitive parameter for free infragravity waves, thus defining a lot of different characteristics on the surf zone and as a result the coastal safety. The milder slopes have more infragravity wave contribution to the runup effect associated with them (Guza and Feddersen, 2012) and hence it is hypothesised that the added infragravity wave at the offshore boundary will therefore enhance this effect. Higher wave runup, means higher threat to the dune coastal safety and, as a result erosion. Therefore, confirming that the current way of defining the dune safety during storm conditions can be underestimating the potential scale of storms.

The addition of the free infragravity waves at the offshore wave boundary will cause an increase in the infragravity and low frequency band allowing for more pronounced processes such as (artificial) resonance to be of higher concern to look out for.

The focus of this thesis revolves around the coastal safety of the dunes when considering free infragravity waves in a 1D model environment under a severe storm event. Therefore the following research questions are proposed:

1. What is the effect of the computational randomness of the VLF wave hydrodynamics during a storm event?
2. What is the contribution of resonance to the VLF and Infragravity response?
3. Can resonance be removed?
4. What is the role of the infragravity and VLF waves response on the runup for different slopes?
5. What is the effect of the wave run up with different additional free infragravity waves?

1.5. Report Outline

In this chapter the overview of the relevance of this research is considered. In Chapter 2 theoretical background and literature review is considered. In Chapter 3 the methodology which includes the approach, and boundary conditions for the 1D model domain is considered with the relevant literature and equations that are used for formulating the results. In Chapter 4 a statistical and resonance analysis is conducted to find the effect of the computational randomness in the set model domain under storm conditions, for the different slopes, this is where the research question (RQ.) 1, 2, and 3 is addressed. In Chapter 5 three different slopes are considered steep (1:35), mild (1:70), and very mild (1:140) slopes and are used to analyse the bound linear and non-linear wave propagation in the wave domain leading to RQ. 4 being addressed. Chapter 6 investigates the addition of the free infragravity wave at the offshore wave boundary and is then assessed with the different slopes for the dune safety, hence RQ. 5 is addressed. Chapter 7 showcases all the conclusions of the report with all the research questions set out to answered are summarised. Lastly, Chapter 8 shows the recommendations suggested for future research to be conducted.

2

Theoretical Background

In this chapter the background information that is identified for dune coastal safety is conducted through a literature review. These include already conducted research that is relevant for addressing the research questions set out to answer.

2.1. Introduction

In order to understand the coastal safety provided by the dunes, it is vital to identify the hydrodynamic processes that affect dune erosion. This report will focus on better understanding wave effects on the coastal safety of the dunes. In this chapter a literature review is conduced to identify the relevant hydrodynamic processes which include, the hydrodynamics of the waves, standing wave patterns and resonance, wave runup, and coastal morphology.

2.2. Waves

There are numerous waves that are identified when approaching the coast that then interact and affect the coastal dunes. A better classification for the different wave types was first introduced by Munk (1950) who sorted the waves by their respectable wave period in Figure 2.1. The sea-swell waves (gravity waves), infragravity waves and very low frequency waves (a part of the long period waves), as described in Figure 2.1, are further discussed in this report.

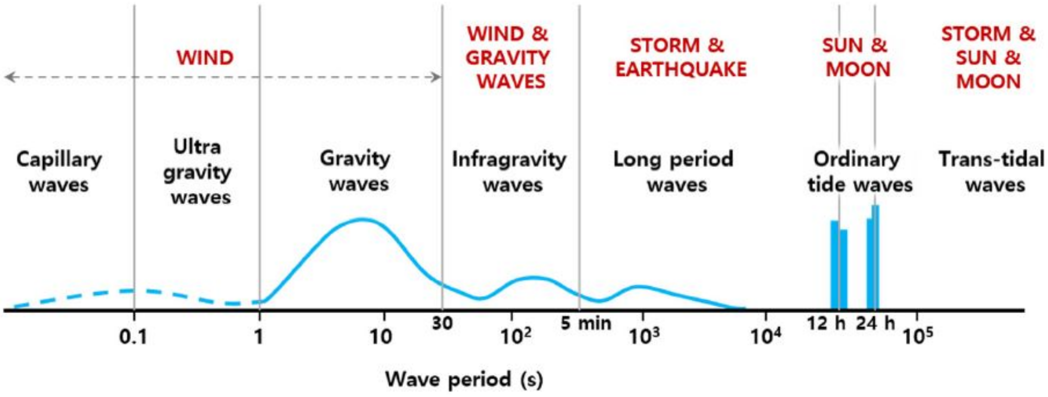

Figure 2.1: Ocean wave classification according to the wave period ((Oh et al., 2020), after Munk (1950))

2.2.1. Sea-Swell Waves

Sea-swell waves are gravity waves (0.04Hz-0.4Hz) that are wind generated as defined in Figure 2.1. Swell waves are generated from a distant storm and can travel long distances resulting in lower frequencies than the sea-wind waves that are generated locally at the storm with a higher frequency. Both are wind driven, and generated during a storm. The sea-swell waves are well documented and researched during storms for dune and coastal safety (de Vries et al., 2008). As sea-swell waves propagate to the coast, they tend to mostly dissipate when they reach the coastline (Janssen et al., 2003).

2.2.2. Infragravity Waves

Of particular interest for coastal safety and the primary focus of this report are the infragravity waves (0.004Hz-0.04Hz). The infragravity waves are caused by the generation of wind waves which causes a surf beat to occur that release the infragravity waves (Longuet-Higgins and Stewart, 1962; Bertin et al., 2018). The infragravity waves are generated thorough three major mechanisms (1) released from bound waves, (2) breakpoint mechanism, (3) bore merging. that are looked into detail at section 2.3. The infragravity waves however contribute to the wave height and wave runup that can both affect in return the dune coastal safety. In contrast to the sea swell waves the infragravity waves can reflect from the coastline (Janssen et al., 2003) and as a result can interact with the incident waves forming a standing wave pattern.

2.2.3. Very Low Frequency (VLF) Waves

Very low frequency, VLF waves (≤ 0.004Hz) similar to infragravity waves are generated by variations in the wave group, and released in the surf zone. VLF waves are more notably researched at regions where additional friction exists, such as regions that have coral reefs (Péquignet et al., 2014; Gawehn et al., 2016). VLF waves are seen in a coral reef environment and exhibit large amplitudes and bore like shapes in the coastline, these are major factors that can contribute to coastal flooding (Gawehn et al., 2016). There can be a significant wave height contribution observed from VLF wave band in reef environments which can be as important as infragravity waves (Péquignet et al., 2009; Cheriton et al., 2016). VLF waves therefore are considered to be at a frequency easily excitable that can lead to resonance most notable in coral reef environments.

2.3. Infragravity Wave Generation

The infragravity waves are generated through the bound waves first discovered through the surf beat (Longuet-Higgins and Stewart, 1962), through the the breakpoint mechanism (Symonds et al., 1982), and through bore merging (Sénéchal et al., 2001).

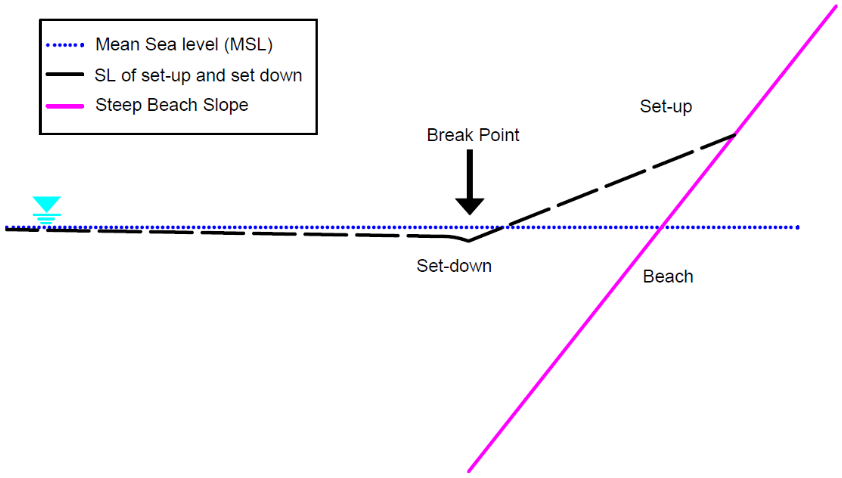

Figure 2.2: Set-up and set-down of the water level for an arbitrary steep beach slope.

2.3.1. Release of bound waves

The infragravity waves are caused by the generation of wind waves (Longuet-Higgins and Stewart, 1962; Bertin et al., 2018). The infragravity waves generation were first sighted in the surf zone unexpectedly by Munk, (1949). Munk (1949) conducted an experiment for swell and short waves propagating to the surf zone where he noticed that the waves had a particular wave oscillation at the infragravity range, and therefore first described the waves as a surf beat. Tucker (1950) conducted an experiment to replicate the same wave phenomena as Munk (1949). Further analysis was conducted by Longuet-Higgins and Stewart (1962) while revisiting both Munk (1949) and Tucker (1950) results, where he concluded that the waves which are described as the surf beat have different oscillation due to the wave groups partially feeling the bottom. As a result, the waves reflect, causing the bound wave group to unbound and release to form a free infragravity wave next to the short wave envelope they were originally in, resulting in two waves propagating at two different velocities (Longuet-Higgins and Stewart, 1962). This phenomena causes a water level depression (set down) at the start of the surf zone because the infragravity waves release from their wave groups and propagate freely. In contrast a wave set up is present at the waterline when the waves dissipate (Longuet-Higgins and Stewart, 1962; Symonds et al., 1982) see Figure 2.2.

2.3.2. Breakpoint Mechanism

The generation of the surf beat and subsequently infragravity waves are obtained by the time varying break point (Baldock et al. 2000) that is induced due to the magnitude of the amplitude of the waves also known as breakpoint mechanism. The breakpoint mechanism was first introduced by Symonds et al. (1982) which defined an energy transfer to low frequency waves in the breaker zone. Larger sea-swell amplitude waves exhibit a breakpoint further offshore and lower amplitude waves further shoreward, as a result creating a breaker zone illustrated at Symonds et al. (1982) Figure 2.3. The breaker zone is treated as a combination of breakpoints (most commonly referred to as breakpoint mechanism) that act as an infragravity wave-maker causing the waves to propagate seaward as outgoing waves, and shoreward as incident waves (Moura and Baldock 2017). Therefore, the waves breaking further offshore due to larger amplitudes cause a higher runup at the coastline whilst the waves breaking more shoreward cause lower runup Figure 2.3.

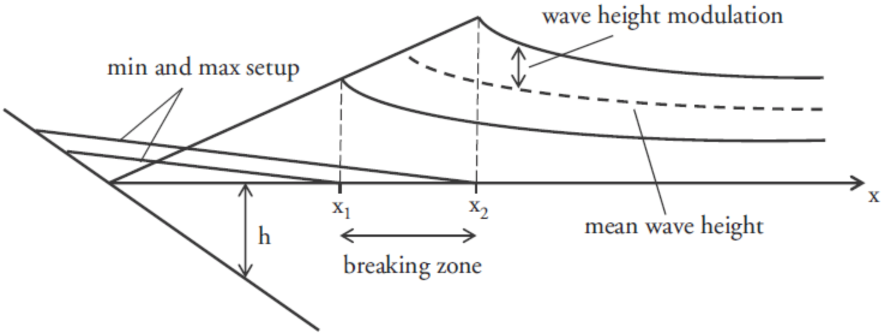

Figure 2.3: The breaker zone constructed through multiple different break point locations causing the sea-swell waves break at different locations creating a varied wave height modulation and as a result different wave-setup (from Sénéchal et al. 2001).

2.3.3. Bore Merging

The waves start to break in the breaker zone, and when moving into the inner surf zone, the waves transform into bores which act like hydraulic jumps. The bores can travel at different celerity in which then can merge with other existing bores Tissier et al. 2015, and therefore amplify the bore effect (Bertin et al. 2018). This increases the wave period in the inner surf zone to twice as much as that as the offshore wave period (Sénéchal et al., 2001). As a result, this bore merging contributes to energy transfer from sea-swell wave frequencies to infragravity frequencies (Bertin et al. 2018; Rieneke, 2021). Bore merging occurs in the inner surf zone, where the infragravity wave height are already dominating the wave field (Tissier et al. 2017). Therefore bore merging is more pronounced for a larger inner surf zones, milder slopes since there is a larger distance for the bores to merge, while also where the infragravity waves are more dominant.

2.4. Standing Waves and Resonance

The wave group oscillates from offshore to the nearshore and eventually (partially or) fully reflects at the coast. When there is a (sloping beach or) vertical wall, it creates a (partially) standing wave pattern for the velocity and surface elevation alike due to the incoming and reflected (Infragravity waves) interaction (Sheremet et al., 2002). The standing wave formation for the amplitude is illustrated at Figure 2.4, the wave modulates horizontally from a minimum, node, to a maximum, antinode. For the surface elevation, as indicated in Figure 2.4, there is an antinode at the wall, whereas for a velocity for the same location at the wall, it would be a node (not shown here) (Holthuijsen, 2010). Standing wave patterns are widely observed for reflected, low frequency waves (Pomeroy et al., 012b; Gawehn et al., 2016; Buckley et al., 2018).

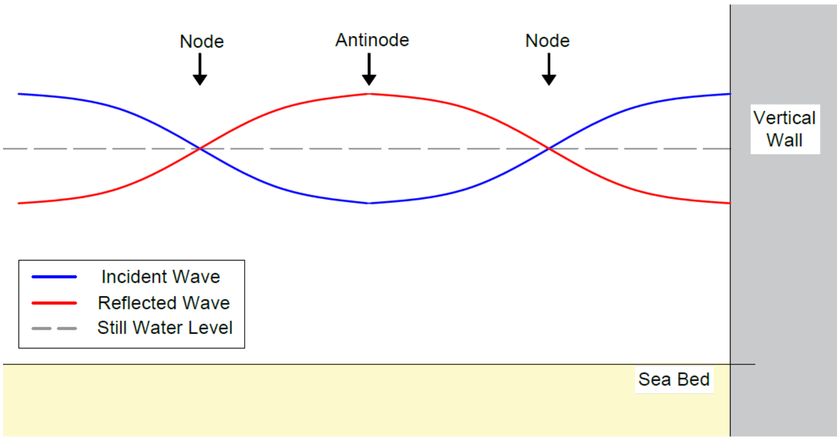

Figure 2.4: Standing wave pattern of the surface elevation on a fully reflective wall.

Resonance is a natural phenomena that the waves undergo for a set body of water, basin or coast. It occurs when the waves are in a set system (e.g. basin) that allows for the (forcing) incoming waves to interact with the reflected waves at their natural frequency. When the forcing and the natural frequency of the reflected waves are in phase resonance, amplification occurs (Buckley et al., 2018). An increase in the magnitude of the wave height observed by the incoming or reflected wave in the domain, can cause significant effects due to the very high amplitude generated. Near resonance can also have a considerable effect on the wave height since it is still affected by the natural frequency. Resonance on the coastal region is seen to be applicable for a situation where there is a set cross shore distance. As a result, when the wave start to break and reflect due to sandbars through Bragg reflection (Liu and Cho, 1993), edge waves (Herbers et al., 1995) and at the coral reefs where the waves start to heavily dissipate due to the high bottom friction (Péquignet et al., 2009; Gawehn et al., 2016; Buckley et al., 2018).

2.5. Wave Runup

The runup is an important parameter to identify how high the waves interact with the dune profile, which can lead to dune erosion. Runup is defined as the maximum water elevation at the shoreline (Holman, 1986), which consists of two different processes, (1) setup, water level elevation on the shoreline, and (2) swash, time varying fluctuations about the mean water level (Stockdon et al., 2006).

Empirically extreme runup is defined by Holman, (1986) as the runup elevation that exceeds by 2% the runup peaks that was parameterised by Stockdon et al. (2006). This definition for runup is widely used (Stockdon et al., 2006; Rutten et al., 2021). These in turn serve as a definition for the runup and then used to be defined at a storm impact regime (Sallenger, 2000). Waves breaking on the shoreline results in a maximum and a minimum runup, R_{HIGH} and R_{LOW} respectively, which are compared to the dune crest D_{HIGH} and to the dune toe, D_{LOW}. Four different storm impact regimes can be identified according to Sallenger, (2000): (1) swash ($R_{HIGH}<D_{LOW}$), (2) collision ($D_{HIGH}>R_{HIGH}>D_{LOW}$), (3) overwash ($R_{HIGH}>D_{HIGH}\&R_{LOW}<D_{LOW}$), and (4) inundation ($R_{LOW}>D_{HIGH}$) regime.

Swash regime, as seen in Figure 2.5, is the only regime that the dune can make a full recovery of the sediment lost after the storm in a set amount of time, whereas in the other three regimes (collision, overwash, inundation) the sediment eroded does not get fully replenished at the dune through the passage of time.
As a result, runup is an important parameter to evaluate coastal safety, and is most commonly split into two components (1) the infragravity, and (2) sea-swell contribution (Guza and Feddersen, 2012). Both the incident infragravity wave direction and incident frequency spread, affect strongly the runup observed at the shoreline (Guza and Feddersen, 2012) and hence the dunes.

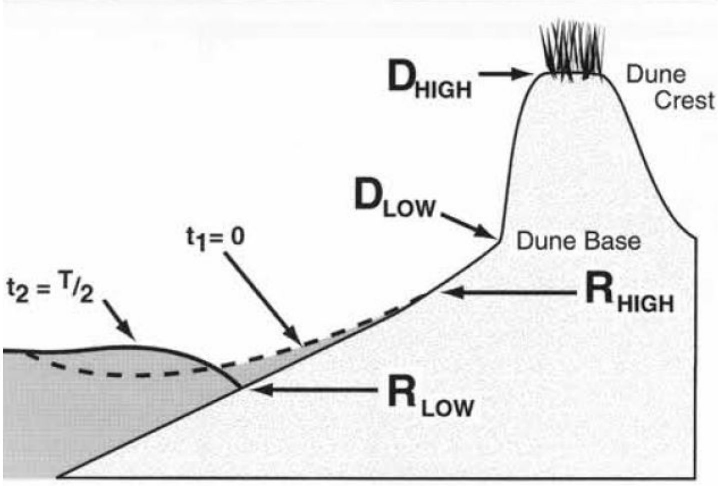

Figure 2.5: Swash regime defined for when (R_{HIGH}<D_{LOW}) (from Sallenger 2000).

2.6. Hydrodynamic processes

Hydrodynamic boundary conditions originating from infragravity waves can also negatively contribute to the coastal safety as they affect the dune morphodynamics. Janssen et al. (2003) considered both low-frequency and high-frequency waves and concluded that although both reflect at the shoreline, the infragravity (or low frequency) waves have a pronounced reflection at the coastline. The reason behind the pronounced reflection of the infragravity waves is due to the waves themselves not fully dissipating on the coastline, whereas higher frequency waves tend to dissipate significantly as they travel towards the shoreline and as a result can only partially reflect at the waterline.

2.6.1. Infragravity Wave Dissipation

Dissipation of infragravity waves is mostly observed close to the shore, at shallower water (Ruessink, 1998; Sheremet et al., 2002 Henderson et al., 2006; de Bakker et al., 2014), as a result, contributing to the wave hydrodynamic effects and processes. The main dissipation mechanisms that are more widely identified are due to bottom friction and non-linear wave transfer. Bottom friction is considered to be of importance in infragravity waves (Henderson and Bowen, 2002), however its effect as a primary constituent of the dissipation of the infragravity wave is considered to be minimal (Henderson et al., 2006; Van Dongeren et al., 2007; de Bakker et al., 2014). Bottom friction can be seen as a more significant mechanism when the sea bed is rougher, such as in coral reef environments (Pomeroy et al., 012a). Infragravity wave dissipation through non-linear energy transfer from infragravity back to sea-swell wave energy is considered more widely acceptable for coastal areas (Henderson et al., 2006; Thomson et al., 2006), and found to be a more dominant dissipation mechanism than the bottom friction (Henderson et al., 2006; de Bakker et al., 2014).

2.6.2. Rollers

As the sea-swell waves start to propagate from offshore to nearshore, the waves start to break which cause wave dissipation and hence the wave energy dissipates. When the waves start to break, a surface roller is created called a bore which is the volume of water carried shore-wards as illustrated in Figure 2.6 (Svendsen, 984b). The wave energy, as a result of this, does not dissipate immediately when breaking and in turn causes the wave energy to be spread along the domain. This in turn means the wave energy is at different locations where waves start to break by having store energy and mostly found in the surf zone due to more frequent and probable wave breaking (Svendsen 984a). The surface roller can have significantly increased radiation stressS_{xx} and energy flux when compared without a roller (Svendsen, 984b).

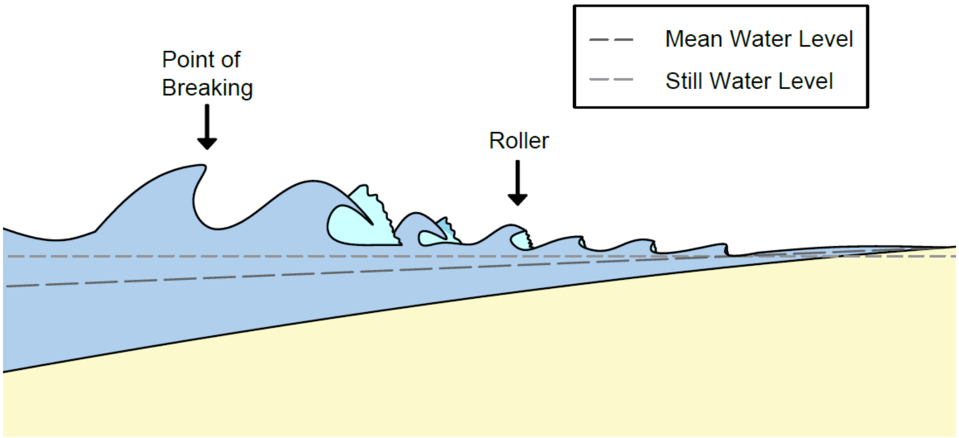

Figure 2.6: Sketch of the roller formation at the surfzone.

2.6.3. Edge and Leaky waves

There are two types of infragravity waves that are approaching the coast, the bound and free infragravity waves (Longuet-Higgins and Stewart, 1962), as mentioned above. Free infragravity waves become important for coastal safety as they reflect at the shoreline and then as a result propagate in the offshore direction (Ruessink, 1998; Roelvink and Reniers, 2011). Free infragravity waves are identified as one of the main contributors to the dune erosion.

The reflected (free) infragravity waves at the coastline can cause the waves to travel in an oblique angle and hence causing them to be trapped in the coastline, most commonly referred to as edge waves (Herbers et al., 1995). Otherwise if the reflected wave angle is acute they can propagate offshore as leaky waves. Both edge and leaky waves originate from swell wave interactions as seen in Figure 2.7 (Herbers et al., 1995). The leaky waves that were once reflected from a certain coastline can then propagate to other coastlines (Daouk, 2020). This allows for free infragravity waves to travel from offshore to nearshore, and hence further endangering coastal safety. Coastlines in semi-enclosed basins (like the North Sea) are especially vulnerable to such effects that can potentially enhance the dune erosion.

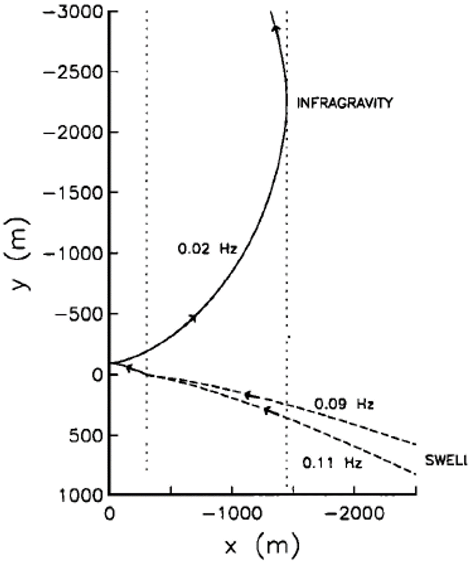

Figure 2.7: Infragravity wave generated by non-linear interaction of two swell waves. The reflected free infragravity wave is seen to be trapped (Herbers et al. 1995).

2.6.4. Longshore Current

Another relevant mechanism to keep in mind is the sediment transport caused by the longshore current. Wave parameters in the offshore boundary, such as the wave period, wave height and incident wave angle, are very influential in coastal erosion especially when the waves start breaking in the surf zone. One such parameter contributing to this is the longshore current that is produced by wave breaking at the breaker zone thus transforming the abrupt change in the radiation stress that is being dissipated in the surf zone to a current in the alongshore direction (Thornton and Guza, 1986).

For a large incident wave angle, an increase of radiation stress in the alongshore direction (S_{yx}) is observed which increases the longshore current intensity (Thornton and Guza, 1986). The longshore current is produced in the (wave) breaker zone which can become relatively large under severe storm conditions as it increases the sediment transport capacity in the surf zone (van Rijn, 2009; Rijnsdorp et al., 2015).

2.7. Coastal Morphology

De Bakker et al., (016b) and van Rijn, (2009) demonstrated that on steep sloping beaches the erosion is larger but the contribution of the infragravity waves is significantly lower since the sea-swell waves are not dissipated as much when they travel onshore. Contrary to that, the infragravity wave effect on sediment transport is significantly larger for gentler slopes as the dissipation of the sea-swell waves is larger (De Bakker et al., 016a; De Bakker et al., 016b). Since the free infragravity wave effects vary in intensity, then the bed slope is crucial for the erosion rates and effect in the dune coastal safety (Daouk, 2020).

2.7.1. Curved Coastline

The coastal morphology can have an important effect on coastal safety. A curved coastline can affect the wave hydrodynamics and the way the waves interact with the shore. Den Heijer, (2013) considered a curved coastline, and observed that a convex coastline has significantly more erosion compared to straight coastlines. The curved coastlines have two different profiles, concave and convex as shown in Figure 2.8. The waves travelling to a convex/concave coastline will experience convergence/divergence. This will eventually result in different morphodynamics in the coast and in turn, can affect the dune erosion considerably.

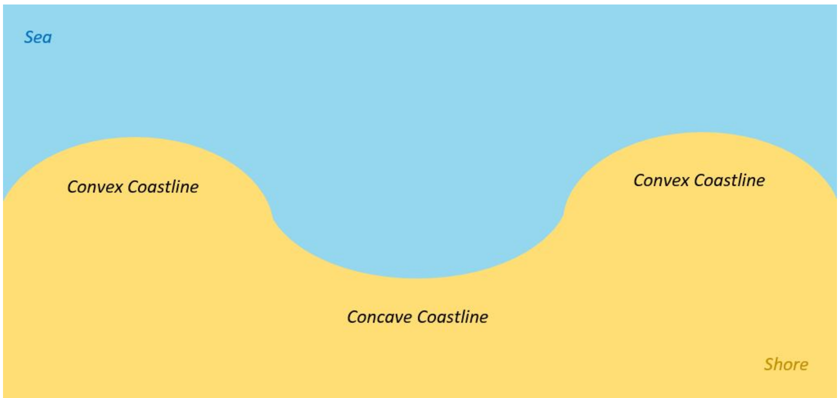

Figure 2.8: Curve coastline depicting both convex and concave profiles.

2.7.2. Avalanching - Dune Process

In addition to the coastline shape, other morphological effects are dune processes. One such dune process is avalanching, which causes large amounts of erosion and therefore affect the coastal safety (van Rijn, 2009). Avalanche process is an effect that usually occurs when a critical bed slope is exceeded hence slumping and therefore a chunk of the dune profile is being eroded and transported to the foreshore. For XBeach which is the focus of this report, this process is based on a wet and dry critical angle on which this slumping effect occurs (Roelvink et al., 2009).

3

Methodology

In this chapter the model set up and boundary conditions are defined. Details on the simulation runs and parameters to be analysed in this report, are also defined. The different methods used to produce our model with their relevant computational and theoretical background are presented in this chapter.

3.1. Model Description

In the Netherlands dune erosion is being assessed using 1D empirical models, 1D modelling is a useful tool that can be used in numerous coastal regions as described by van Santen et al., (2012). The focus of the thesis is on 1D modelling of storms and their effects on the coastal safety of the dunes, its importance is highlighted with the green regions at Figure 3.1. The orange transect at Figure 3.1 is the transect in Noordwijk that is of interest better defined and analysed later on in this report. The focus of the report is on low frequency waves ($\leq 0.04 Hz$) present during storms. This includes bound waves with as to be investigated in this report with the addition of free infragravity waves present at the offshore wave boundary. The definition of the offshore wave boundary, and as a result he modelling setup is therefore crucial for the wave hydrodynamics which in return affect the dune coastal safety.

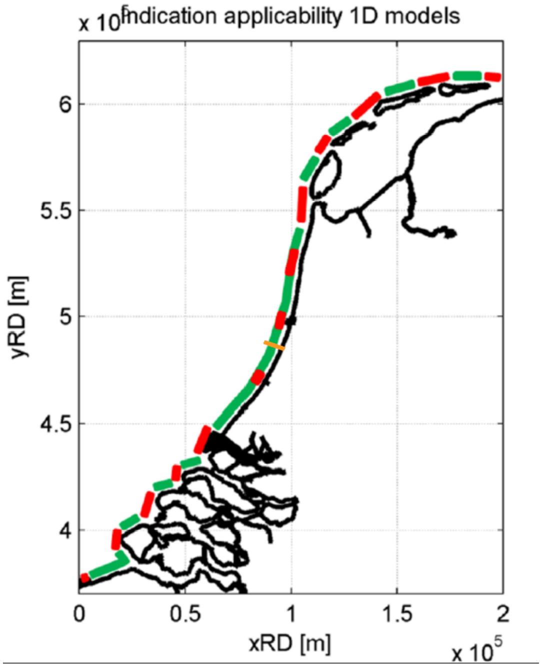

Figure 3.1: Identifying locations where 1D dune-erosion models are applicable (green), and locations where they are not applicable (red) for safety assessments. The Jarkus Transect approximate location used for this report is indicated (orange), located at Noordwijk. This metric is based on the complexity of the bathymetry and the presence or absence of coastal structures after van Santen et al. (2012)

For this report a 1D model is used to asses the dune coastal safety, XBeach (a process based model) in Surf beat mode as it define the low frequency waves set out to assess. XBeach is a useful tool that can effectively model the dune erosion, and therefore dune coastal safety of the dunes. This process based model allows for free infragravity wave effects in the nearshore to be modelled, and is developed for morpho-hydrodynamics in a length scale of kilometres and a duration of storms. Additionally, XBeach identifies the effect of different storm impact regimes, most commonly used for dune erosion, overwash, and inundation (Roelvink and Reniers, 2011). Surf beat mode can be used in XBeach which simulates the infragravity waves while also resolving the short wave effects so that it reduces the computational time of the simulation. The surf beat mode has similar results to non-hydrostatic models when considering the wave transformation and setup effects at the coastline (de Beer et al., 2021). Therefore for this report the XBeach model run using the surf beat mode simulates the infragravity and low frequency waves effects on dunes.

3.2. Model Setup

The goal of this report is to define the dune runup under storm conditions when free infragravity waves are present in the offshore wave boundary. It seeks to understand how the free infragravity waves affect the coastal dune safety, defining and analysing the bed slope effect, potential resonance and free infragravity waves. To achieve this, the model domain needs to be defined, which this section will serve for. First the 1D model will be defined through identifying and setting the boundary conditions which consist of (1) the storm conditions at the offshore wave boundary (wave maker) through a random phase model, (2) morphological conditions (bed slope and dune shape), and (3) the computational model restrains in XBeach (run time and bed friction to name a few). Once the model boundary conditions are defined the boundary conditions are then fed and run through XBeach using surf beat mode, since the focus of the model is on identifying the effect of the low frequency waves, and in more specific free infragravity waves. The XBeach output hydrodynamics are then compared with different hydrodynamic methods to simulate the waves from offshore to nearshore using MATLAB for a better insight on the hydrodynamics. As a result, allowing to answer the research questions set out to answer with for the different bed slopes, the resonance effect and the effect of the addition of the free infragravity waves added at the offshore wave boundary.

3.2.1. Morphology Setup

The 1D domain is modelled using a Jarkus transect with ID 8007200 located at Noordwijk located at Figure 3.1 marked with the orange area. Therefore the model domain for this report includes a realistic dune with a dune foot at the Dutch coast. For a more realistic dune morphology the dune at 1.98 m above mean sea level (MSL) is used, where the sea bed leading to the dune is replaced with a predefined beach slopes as shown at Figure 3.2.

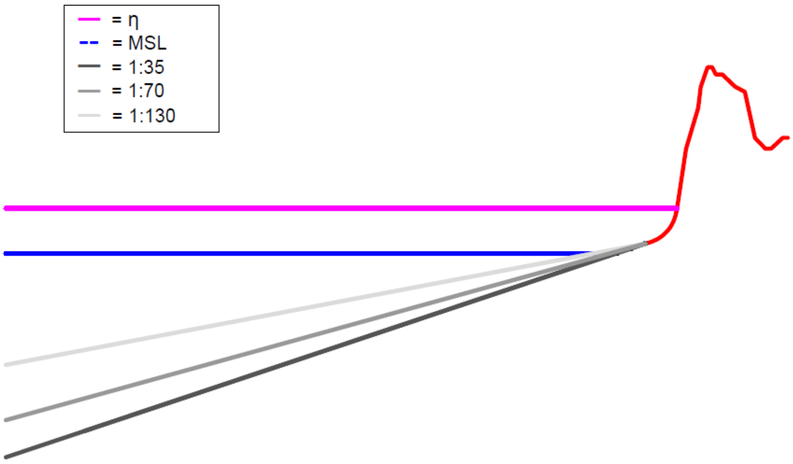

Figure 3.2: Bed slope sketch of 1D model at Noordwijk with a Jarkus transect ID of 8007200 marked in red, where the magenta line represent the mean surface elevation, blue line represent the Mean sea level, black line the steep slope (1:35) grey line the mild slope (1:70), and the light grey line the very mild slope (1:130).

At Figure 3.2 the red line defines the Jarkus transect that is left unchanged signifying the realistic dune, with three different linear bed slope to be considered in this report, a steep slope (1:35) coloured red, a mild slope (1:70) coloured grey, and a very mild slope (1:130) coloured light grey. This defines the morphology of our domain where these slopes are extended to a depth (y) of 20 m forming different cross shore distances (x) at 5 m increments, where x = 0 m is at the highest height at the dune. These three different transects from Figure 3.2 are later used for the morphology for the 1D surf beat mode XBeach model.

3.2.2. Storm Conditions Setup

The storm conditions are created using a random phase model produced previously by Daouk (2020). The random phase model used follows Herbers et al. (1995) method for the bound (or free) long wave variance density spectrum as summarised at equation 3.10 (or equation (3.11)) which is discussed in more detail in section 3.3.1 of this chapter. The random phase model also includes the desired hydrodynamic boundary conditions for the storm generation to be fed in XBeach, summarised in Table 3.1. The desired hydrodynamic boundary conditions include the directional spreading of the waves σ_θ, significant wave height H_{s0}, peak period T_{p0}, water density ρ, and incident wave angle θ. A JONSWAP wave spectrum is used for simulating the storm conditions with peak enhancement factor $\gamma = 3.3$. As a result, the model uses random phase generation of the bound waves at different randomly generated numbers at a random order for the storm conditions using a predefined seed number. The storm duration is set to run for 2 hours with frequency resolution of 0.000139 Hz and a cut off frequency f_c of 0.04 Hz to distinguish the low frequency waves from the incident waves.

Parameter	**Notation**	**Value**
Water depth	h	20 m
Directional spread	σ_θ	30°
Significant wave height	H_{s0}	9 m
Peak period	T_{p0}	12 s
Water density	ρ	1020 kg/m^3
Incident Wave angle	θ	0°

Table 3.1: The set parameters used for the random phase model, in generating the model's storm conditions.

The model is run with different waves that are induced at the offshore wave boundary. The model includes bound waves during a storm, with free infragravity waves of different intensities to be added at the offshore wave boundary. The free infragravity waves induced are scaled as a multiple of the low frequency wave band present in the bound waves during the storm. The IG_{free} defines the free infragravity waves that have bound waves with the addition of free infragravity waves of different intensities (marked by a number) that correspond to the magnitude of infragravity waves in the bound waves during the storm simulation. There are three different free infragravity wave intensities IG_{free} that are defined for this report that include the bound waves (1) $IG_{free} = 0$ for a situation of only bound waves (no free infragravity waves added to the domain), (2) $IG_{free} = 1$ bound waves with free infragravity waves of the same magnitude present in the bound waves during a storm, and (3) $IG_{free} = 2$ bound waves with the addition of free infragravity waves of twice the magnitude present in the bound waves during a storm, all three are summarised in Table 3.2.
Lastly, for the situation with only the free infragravity waves IG_{only} waves have the same description of IG_{free} conditions, however without any bound waves present for the storm conditions. The two free infragravity waves only cases include (1) $IG_{only} = 1$ for only free infragravity waves of the same magnitude present in the bound waves during a storm, and (2) $IG_{only} = 2$ of free infragravity waves of twice the magnitude present in the bound waves during a storm, which are both summarised at Table 3.2. The storm conditions created by the IG_{free} or IG_{only} intensities are then run through this random phase model for the set simulation time of 2 hours. The wave conditions are then obtained and "fed" as an input variable into the XBeach software to recreate the storm conditions at the offshore wave boundary.

Notation	Description
$IG_{free} = 0$	Bound wave only, no additional free infragravity wave present
$IG_{free} = 1$	Bound Infragravity waves with additional free infragravity waves that have a magnitude equal to the bounded infragravity waves present
$IG_{free} = 2$	Bound Infragravity waves with additional free infragravity waves that have a magnitude double the bounded infragravity waves present
$IG_{only} = 1$	Free infragravity waves that have a magnitude equal to the bounded infragravity waves present
$IG_{only} = 2$	Free infragravity waves that have a magnitude double the bounded infragravity waves present

Table 3.2: The 5 different free infragravity intensities imposed on the offshore wave boundary

3.2.3. XBeach Setup

Once the morphology and storm conditions are defined, XBeach is then used at a surf beat mode to simulate the results. However, XBeach allows for additional boundary and numerical conditions to be further defined for the model domain which include the physical properties of the bed and waves. For the physical parameter of the waves, Wettelijk Toets Instrumentarium (WTI) parameters are used in XBeach, indicated in Table 3.3 as defined by Van Geer et al. (2015). The WTI parameters are optimised for the Dutch coast and are also better in line with experimental results than the default XBeach conditions when it comes to dune erosion (Do et al., 2018). In addition to the WTI parameters at Table 3.3, a surge level z_s0, of 5 meters is used and a simulation time of 2 hour is then used (therefore having the same duration as the storm conditions setup as defined at section 3.2.2).

WTI Parameter	XBeach Notation	Description
Bed Friction Factor (f_w)	fw+	0.000
Bed Friction Coefficient (c_f)	bedfriccoef	0.001
Wave Height to Water Depth	gamma+	2.364
Breaker Parameter	gamma	0.541
Breaker Slope Coefficient	beta	0.138
Critical Avalanching Under Water	wetslp	0.26
Wave Dissipation Coefficient	alpha	1.262
Calibration Factor, Time Averaged Flow due to Wave Skewness	facSk	0.375
Calibration Factor, Time Averaged Flow due to Wave Asymmetry	facAs	0.123

Table 3.3: The three different free infragravity intensities imposed on the offshore wave boundary

Once the XBeach boundary conditions are set, XBeach is then run and as a result multiple output variables are produced. The output variables used are the wave energy (E_w), roller energy (E_w), cross-shore velocity u, surface elevation η, water level z, water depth h, and cross-shore distance x, all which are summarised in Table 3.4. The output variables obtained from XBeach, are then post processed with the use of different methods to define incoming and outgoing waves since the waves obtained from the XBeach describes the overall linear and non-liner wave contribution.

The output variables from XBeach as defined, are then used to obtain a variance density spectrum for the surface elevation (Holthuijsen, 2010) with the use of jspect method. That is then converted to significant wave height which is essentially XBeach defined (H_{XB}). The wave height obtained will differ for each run, due to the seed number and slope alike. As a result, in this report 3 different slopes and 10 different predefined seed numbers are used, amounting to 30 unique model runs. The seed number for each slope creates an inherit randomness in the model due to the storm conditions which need to be addressed. As a result the XBeach significant wave heights (H_{XB}) are then analysed through a statistical analysis to express the deviation that they exhibit from one another which is analysed at chapter 4 of this report. The unique

Parameter Notation	Parameter
E_w	Wave Energy
E_r	Roller Energy
u	Cross-Shore (Eulerian) Velocity
x	Cross-Shore Distance
η	Surface Elevation
h	Water Depth
z	Water Level

Table 3.4: Output XBeach variables that are to be used in the wave models

combination of set seed number and slope is then assessed for potential resonance effect if they are suspected of such, with the use of surface elevation and velocity variance density spectra.

The phase between the surface elevation and velocity can be obtained through the cospectra variable velocity and pressure as described by Sheremet et al. (2002), looked into more detail in section 3.3 of this report and implemented in Chapter 4. The variance density spectrum is conducted for the whole cross shore distance of our domain next to the phase of the velocity, and surface elevation/ similarly as what Buckley et al., (2018) did to define the natural frequency nodes as seen in section 3.3.4.

To obtain sufficient information from the wave field, the incoming and outgoing wave are then formulated as linear wave propagation through the use of Guza et al., (1984) method which uses surface elevation and (hydrostatic pressure), and compared with a more complicated method of Sheremet et al., (2002) which uses autospetra and cospectra to obtain the energy flux. Both methods define an incoming and outgoing wave which allows to simulate, analyse, and compare these two methods with one another to assess the reliability of each method. Once the reliability of the wave method is confirmed, non-linear wave contributions are added, the radiation stress through the use of Battjes et al., (2004) method.

Another non-linear contribution is the roller energy which is considered to define the wave energy dissipation in the surf zone as through the use of Svendsen (984a) method which can be added on the radiation stress component. Battjes et al., (2004) method is usedto address the infragravity non-linear wave contribution through the use of the radiation stress. The non-linear wave contribution of Battjes et al., (2004) methods are then compared with the linear wave contribution of Sheremet et al., (2002) method. All these methods are all described in more detailed in the following section, section 3.3.

3.3. Theoretical Background

The background information, equations and definitions of each method used in 1D modelling is presented in this section where it serves as a reference for all the different equations used in this report. This section is therefore split into (1) random phase model, (2) linear wave contribution, (3) non-linear wave contributions, (4) wave spectral density and resonance, and (5) runup.

3.3.1. Random-phase model

The random phase model is used in this report to simulate the bound and free low frequency waves for the extreme storms. The random phase model follows Herbers et al. (1995), and subsequently Daouk (2020) methodology.

The random phase model uses a JONSWAP (JOint North Sea Wave Project) surface elevation spectra $E_S(f)$ from Hasselmann et al. (1973) as shown in equation (3.1), where f_p is the peak frequency, γ is the peak enhancement, α is the energy scale, and σ_k is the peak-width parameter.

$$E_S(f) = \alpha g^2 (2\pi)^{-4} f^{-5} \exp\left[-\frac{5}{4}\left(\frac{f}{f_{peak}}\right)^{-4}\right] \gamma^{\exp\left[-\frac{1}{2}\left(\frac{f/f_{\text{peak}}-1}{\sigma_k}\right)^2\right]} \tag{3.1}$$

The JONSWAP spectrum is then therefore scaled to be used to define the scaled wave spectra $E_D(f)$ of the storm at equation (3.2), where H_{m0} is the offshore wave height, h is the defined water depth (20 m) and k is the wave number obtained from linear dispersion.

$$E_(f) = \frac{(E_S(f) / \int^f E_S(f))\, H_{m0}^{2/16}}{\cosh^2 kh} \tag{3.2}$$

For identifying the random phase model, first the wave domain needs to be defined by using variance density spectra of both the bound and free infragravity waves. Herbers et al. (1995) described the bound long wave variance density spectrum through the interaction of two short waves bounded E_{bound} as shown in equation (3.3).

$$E_{\text{bound}}(f) = \int_{0.04}^{f_{\max}} \int_0^{2\pi} \int_0^{2\pi} C^2 \left(f - f', f', \Delta\theta\right) \mathrm{E}\left(\mathrm{f} - \mathrm{f}', \theta_1\right) E\left(f', \theta_2\right) d\theta_1 d\theta_2 df \tag{3.3}$$

Through equation (3.3) $E\left(f,\theta\right)$ is the frequency-directional variance density spectrum of the sea-swell waves, f and f' is the frequency of two different short waves, θ is the wave direction, and C is the bound wave interaction coefficient.

The bound interaction coefficient C is defined at equation (3.4), where σ_i is the radial frequency of the sea swell and infragravity waves.

$$\begin{aligned} C\left(s_1 f_1, s_2 f_2, \Delta\theta\right) = {} & \frac{g k_1 k_2 \cos(\Delta\theta)}{2\sigma_1\sigma_2} + \frac{g\left(\sigma_1 + \sigma_2\right)\cosh\left(k_1 h\right)\cosh\left(k_2 h\right)}{\left[g k_3 \tanh\left(k_3 h\right) - \left(\sigma_1 + \sigma_2\right)^2\right]\sigma_1\sigma_2\cosh\left(k_3 h\right)} \\ & \cdot \left(\left(\sigma_1 + \sigma_2\right)\left[\frac{\left(\sigma_1\sigma_2\right)^2}{g^2} - k_1 k_2 \cos(\Delta\theta)\right] - \frac{1}{2}\left[\frac{\sigma_1 k_2^2}{\cosh^2\left(k_2 h\right)} + \frac{\sigma_2 k_1^2}{\cosh^2\left(k_1 h\right)}\right]\right) \end{aligned} \tag{3.4}$$

The radial frequencies are defined at equation 3.5, where $sigma$ is the frequencies of the sea-swell wave, k_1, and k_2 are the wave number from the linear dispersion relation equation (3.6), while k_3 is the product wave number at equation (3.7).

$$\sigma_i = 2\pi \cdot s_i \cdot f_i \tag{3.5}$$

$$\omega^2 = g k \tanh(kh) \tag{3.6}$$

$$k_3 = \sqrt{k_1^2 + k_2^2 + k_1 k_2 \cos(\Delta\theta)} \tag{3.7}$$

The bound long wave variance density spectrum is allowed to oscillate with a phase that is obtained from the difference of two short waves components shifted by 180 degrees.
The free long wave variance density spectra E_{free} (or E_{only})is used to define the freely propagating waves in the wave domain, with the use of IG_{free} at equation (3.8) (or IG_{only} at equation (3.9)).

$$E_{\text{free}}(f) = IG_{free} \cdot E_{\text{bound}}(f) \tag{3.8}$$

$$E_{\text{only}}(f) = IG_{only} \cdot E_{\text{bound}}(f) \tag{3.9}$$

Once the bound, and free long wave variance density spectrum are obtained the amplitude is obtained through linear wave theory for E_{bound} at equation (3.10), E_{free} at equation (3.11), and E_{only} at equation (3.12).

$$a_{bound}(f) = \sqrt{2 \cdot E_{bound}(f) \cdot df} \tag{3.10}$$

$$a_{free,0}(f) = \sqrt{2 \cdot E_{free}(f) \cdot df} \tag{3.11}$$

$$a_{only}(f) = \sqrt{2 \cdot E_{only}(f) \cdot df} \tag{3.12}$$

The surface elevation is obtained by assigning random phases to the previously obtained amplitudes $a_{bound}(f)$, $a_{free}(f)$, and $a_{only}(f)$ at equation (3.13), equation (3.14), and equation (3.15) respectively. The phase, ψ at equation (3.16) is the phase difference between randomly generated phases ψ_i of the two sea-swell waves in the domain at equation (3.17) where N_{RNG} is the random number generated for the individual short waves. As a result, the phase ψ_i provided provides the randomness, and therefore forcing of the random phase model that can made consistent by using a seed number.

$$\eta_{bound} = a_{bound} \cdot \cos(2\pi t + \psi) \tag{3.13}$$

$$\eta_{free} = a_{free} \cdot \cos(2\pi t + \psi) \tag{3.14}$$

$$\eta_{only} = a_{only} \cdot \cos(2\pi t + \psi) \tag{3.15}$$

$$\psi = -\psi_{i1} + \psi_{i2} \quad , \quad where \tag{3.16}$$

$$\psi_i = 2\pi \cdot N_{RNG} \tag{3.17}$$

As a result, when there are both bound and free infragravity waves the amplitude of the waves present in the domain are added with one another to form the random phase model generated surface elevation at equation (3.18). The random phase model at equation (3.18) however has a combination of two different random phases in the wave domain.

$$\eta_{total} = \eta_{bound} + \eta_{free} \tag{3.18}$$

3.3.2. Linear-wave contribution

Guza et al. (1984) describe the incoming and outgoing wave using collocated wave gauges and velocity $u$meters, therefore identifying the wave direction through the surface elevationη time series. With this method the incoming surface elevation of the infragravity waves η^+_{IG} and outgoing surface elevation of the infragravity waves η^-_{IG} is simulated as seen in equation (3.19), where u_{IG} is the infragravity cross shore velocity, h is the water depth, and is the gravitational acceleration. To obtain only the infragravity variables, applying a low pass filter for and u at the infragravity frequency (0.04 Hz) is used.

$$\eta^{\pm}_{IG} = \frac{1}{2}\left(\eta_{IG} \pm \sqrt{\frac{h}{g}}u_{IG}\right) \tag{3.19}$$

Originally Guza et al. (1984) formulated equation is(3.19), however, the equation is only valid for shallow water, as it only identifies free infragravity waves, and therefore no bound infragravity waves are considered. As a result, the above equation is only used for the reflected, outgoing waves in this report, as the outgoing waves are assumed to be freely propagating.

To account for the incoming infragravity waves, equation (3.19) is modified to account for bound waves propagating from deep water to shallow water. This is achieved by utilising the group velocity c_{gp} variable through the dispersion equation. Equation (3.19) is then expressed as a function of the group velocity and shallow water celerity, allowing for the depth to define where the bound and free infragravity waves are present, therefore formulating equation (3.20) for the incoming (bound) free infragravity waves. The gravitational acceleration g, is set to $9.81 m/s^2$.

$$\eta^{+}_{IG} = \frac{\eta_{IG}\sqrt{gh} + h \cdot u_{IG}}{c_{gp} + \sqrt{gh}} \tag{3.20}$$

The above equations, equation(3.19) and equation (3.20) define the linear waves propagation, surface elevation as the infragravity waves propagate from offshore to nearshore for free and bound waves. The surface elevation can be then transformed to (spectral) significant wave height $H_{m0,IG}$ through equation (3.21) where it is considered as 4 times the standard deviation of the surface elevation σ_η.

$$H^{\pm}_{m0,IG} = 4\sigma_{\eta^{\pm}} \tag{3.21}$$

Sheremet et al. (2002) defined the incoming and outgoing infragravity waves using energy flux for collocated pressure and cross shore velocity signals. This method therefore, does not require surface elevation unlike Guza et al. (1984) method, and instead uses pressure (or water depth) p next to the cross shore velocity u. Sheremet et al. (2002) uses the pressure and velocity components through cospectra and autospectra C_f at different frequency ranges to define the incoming linear energy flux (F_L^+) and outgoing linear energy flux (F_L^-) of the free infragravity waves in equation (3.22). The first and second term of the right hand side of equation (3.22) are the autospectra (power spectral density) for the pressure and velocity variables respectively, while the third term is the cospectra (cross spectral density) between the pressure and velocity variables.

$$F_L^{\pm}(f) = \frac{1}{4}\sqrt{gh}\left(C_f(p,p) + \frac{h}{g}C_f(u,u) \pm 2\sqrt{\frac{h}{g}}C_f(p,u)\right) \tag{3.22}$$

Sheremet et al. (2002) similar to Guza et al. (1984) defined the waves for free infragravity waves in shallow water. Therefore, for the bound waves, the incoming linear energy flux F_L^+ needs to be better defined. Similar to equation (3.20), the dispersion relationship is used to define the group velocity, hence allowing for the linear energy flux to be a function of the shallow water celerity and group velocity.

$$F_L^+(f) = \frac{1}{2}c_{gp}\left(\frac{\sqrt{gh}C_f(p,p) + \sqrt{\frac{h^3}{g}}C_f(u,u) + 2hC_f(p,u)}{\sqrt{gh} + c_{gp}}\right) \tag{3.23}$$

This allows for the linear energy flux to be used for both free and bounded infragravity waves. The energy flux is then converted to significant wave height $H_{m0,IG}$ through the use of equation (3.24) and equation (3.25) for free and bounded infragravity waves respectively. Therefore Sheremet et al. (2002) method is used following equations to a form that is comparable to that of Guza et al. (1984) equation (3.21).

$$H_{m0,IG}^{\pm} = 4\frac{F_L^{\pm}}{\sqrt{gh}} \tag{3.24}$$

$$H_{m0,IG}^{+} = 4\frac{F_L^{+}}{c_{gp}} \tag{3.25}$$

When there are only free low frequency waves and there is no dissipation, the low frequency waves outgoing significant wave height H_{m0} propagate only with a dependency on the water depth h as defined by Green's law, indicated in equation (3.26) (Battjes et al., 2004). Green's law is a linear wave theory that describes the evolution of the outgoing wave with dependency on the water depth for a linear slope when there is no wave dissipation.

$$H_{\mathrm{m0}} \sim h^{-0.25} \tag{3.26}$$

Guza et al. (1984) and Sheremet et al. (2002) methods define the linear effect from the waves, without introducing any non-linear effects that can occur as the waves propagate to the shore, such as the radiation stress, non-linear transfer of energy from infragravity wave energy to sea-swell and the roller energy flux. For the effect of the above variables the non-linear contributions need to be identified.

For a description of the breaker zone, the definition of the sea-swell wave height is required H_{ss}. However, XBeach model is run in XBeach and cannot resolve the sea swell waves individually. However the sea-swell wave response can be obtained through the wave energy E_w that is present in the model. Through linear wave method, the wave energy can be transformed to significant sea-swell wave height $H_s s$ from equation (3.27), where ρ is the density at sea (1020 kg/m^3), and g is the gravitational acceleration (g = 9.81 m/s^2) .

$$H_{ss} = \sqrt{\frac{8E_w}{\rho g}} \tag{3.27}$$

3.3.3. Non Linear wave contributions

In the previous subsection, section 3.3.2 only the linear effects relating to the waves were considered. There are more effects that can affect the waves as they propagate from offshore to the coast. The non-linear wave contributions from the radiation stress, roller energy flux contribution, sea-swell and infragravity wave interaction can have different effects on the wave characteristics which are considered in this section. However, infragravity waves have numerous documented sources that can affect the wave propagation, which include bottom friction, non-linear infragravity to sea-swell wave interactions, and radiation stress combination between the waves (Henderson et al., 2006) The roller momentum flux is another component for the non-linear wave contribution that accounts for the bore of the waves as described by Svendsen (984a). There are numerous inputs on the importance of each to define the wave field. Bottom friction namely is a controversial non-linear effect and after extensively researched for low frequnecy waves (Battjes et al., 2004, Van Dongeren et al., 2007) it is safe to assume that it does not contribute much to the current model setup used in this report, as its effect is highest in a tens of centimetres of water, therefore, shallow water (Van Dongeren et al., 2007). In this case due to the surge of 5 m its effect can be assumed to be not as significant. Therefore only the radiation stress, and roller energy flux are considered in this report as non-linear wave contributions for a better insight of the wave propagation and low frequency contribution on the dune coastal safety.

Henderson et al. (2006) assessed the nonlinear energy transfer with sea-swell waves concluding that it has a significant effect on the generation and loss of energy of the infragravity waves. An energy balanced was defined based on Henderson and Bowen (2002) who describe a depth integrated conservative energy balance for statistically steady alongshore-uniform shallow water infragravity wave at equation (3.28), where $F(f)$ is the energy flux and $W(f)$ is the non-linear transfer of energy.

$$\frac{\partial F(f)}{\partial x} = W(f) \tag{3.28}$$

The non-linear transfer of energy $W(f)$ is described in equation (3.29) by Henderson et al. (2006) through different cospectra. The first term in the right hand side of equation (3.29) is the linear contribution of energy propagation as described by Sheremet et al. (2002) of collocated pressure and cross shore velocity, the second is the non-linear contribution of the sea-swell mass flux M which defines the depth integrated Stokes' drift q_{drift}, and the third term is the component of the sea-swell radiation stress S_{xx}. This equation defines three different components at infragravity wave frequency as indicated with the tilde sign.

$$F(f) = ghC_f(\tilde{\eta}, \tilde{u}) + gC_f(\tilde{\eta}, M) + C_f(S_{xx}, \tilde{u}) \tag{3.29}$$

Battjes et al. (2004) also defines the contribution of the radiation stress by considering an energy balance in the steady state without any dissipation contributions present in equation (3.30).

$$\frac{\mathrm{d}F(f)}{\mathrm{d}x} = F_x \equiv -\left\langle U \frac{\mathrm{d}S_{xx}}{\mathrm{d}x} \right\rangle \cong \frac{1}{2}\kappa \hat{U}\hat{S}\sin(\Delta\psi) \tag{3.30}$$

Equation (3.30) describes a similar contribution of the radiation stress of equation (3.29), the validity of equation (3.30) is only possible for shoaling zone (Battjes et al., 2004). Battjes et al. (2004) describes the total radiation stress contribution that is present in the wave field where F_x is the rate of work done per unit area (mass flux). This is also further defined by having the amplitude of the infragravity cross-shore velocity $\tilde{U}$ and radiation stress $\tilde{S}$ with a wave number $\kappa = 2\pi f / c_{gp}$ and cross shore variation of additional phase lag $\Delta\psi$ $(\Delta\psi = \psi - \pi)$.

The rate of work done per unit area F_x is then converted to wave height H_{m0} through equation (3.31) and equation (3.32) for free and bounded wave description respectively.

$$H^{\pm}_{m0,IG} = 4\frac{F^{\pm}_L}{\sqrt{g^3 h}} \tag{3.31}$$

$$H^{+}_{m0,IG} = 4\frac{F^{+}_L}{c_{gp} g} \tag{3.32}$$

The last variable that can contribute to the energy flux and description of the wave field, is the roller energy E_r. The roller energy E_r can be defined through equation(3.33) where ρ is the density of the water ($\rho ==$

$1020 kg/m^3$), c is the phase speed, A is the area of the roller and L is the wavelength (Svendsen 984a). The roller area A is better defined in Figure 3.3.

$$E_r = \frac{\rho A c^2}{2L} \tag{3.33}$$

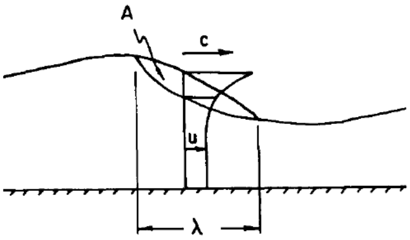

Figure 3.3: Roller produced at the surf zone after Svendsen (984a)

The radiation stress $S_{xx,w}$ equation (3.35), and the roller momentum flux $S_{xx,r}$ equation (3.36), are related to compute the setup of the mean water level through equation (3.34) (Svendsen 984a). Equation (3.34) is used to define the roller contribution next to the wave contribution on the wave elevation and setup. The contribution of the roller momentum flux is always added when there is a contribution from the radiation stress, therefore at Battjes et al. (2004.

$$\frac{\mathrm{d}S_{xx,\mathrm{w}}}{\mathrm{d}x} + \frac{\mathrm{d}S_{xx,\mathrm{r}}}{\mathrm{d}x} + \rho g h \frac{\mathrm{d}\bar{\eta}}{\mathrm{d}x} = 0 \quad , \quad where \tag{3.34}$$

$$S_{xx,w} = \left(\frac{c_{\mathrm{g}}}{c} \left(1 + \cos^2\theta\right) - \frac{1}{2} \right) E_{\mathrm{w}} \tag{3.35}$$

$$S_{xx,r} = 2E_r \cos^2(\theta) \tag{3.36}$$

3.3.4. Variance Spectral Density and Resonance

Variance density spectrum $E\{\frac{1}{2}a^2\}$ is a useful tool to assess the frequency bands that are present at a set location for a certain variable, most commonly used for the surface elevation. For the surface elevation variance spectral density the sea surface is considered as a stochastic process of an observation at a set location, shown in equation (3.37), where Δf is the frequency interval and variance density spectrum is $E\{\frac{1}{2}a^2\}$ which in this case refers to the amplitude a spectrum (Holthuijsen, 2010).

$$E(f) = \lim_{\Delta f \to 0} \frac{1}{\Delta f} E\left\{\frac{1}{2}a^2\right\} \tag{3.37}$$

The summation of numerous random harmonics, a Fourier series is one way to reproduce a spectral density (Holthuijsen, 2010). For a Fourier transform, the estimation of the amplitude must be written in a Fourier series where that allows for the amplitude and the phase of the model to be defined for the two Fourier amplitudes A, and B obtained from the Fourier integrals as indicated in equation (3.38), and equation (3.39) respectively. For a more in depth explanation refer to Holthuijsen (2010).

$$A_i = \frac{2}{D} \int_D \eta(t) \cos\left(2\pi f_i t\right) \mathrm{d}t \quad \text{for } f_i = i/D \tag{3.38}$$

$$B_i = \frac{2}{D} \int_D \eta(t) \sin\left(2\pi f_i t\right) \mathrm{d}t \quad \text{for } f_i = i/D \tag{3.39}$$

For numerical computations, the spectral variance density equation (3.37), involves, removing the limit $\lim_{\Delta f \to 0}$ to create an estimation of the spectrum as that would remove the dependence of infinite duration D ($D = \frac{1}{\Delta f}$).

Another method to assess the spectral variance density, with the similar ideology to Fourier transforms, is to use jspect (used in this report) made original by J. MacMahan (from Naval Postgraduate School, Monterey, CA). Jspect provides the (cross-)spectral estimates with their corresponding frequencies for the data set (e.g. surface elevation) that detrends (linearly for this report) with a Hanning window function, which acts similarly to crosgk.m script as defined in Winde (2012).

To assess the significant wave height H_{m0} from the variance density spectrum of the raw data for set location, equation (3.40) can be used (Holthuijsen, 2010). This is defined for the surface elevation variance density spectrum $E\{\frac{1}{2}a^2\}$ where f is the frequency and m_0 is the zeroth-order moment.

$$H_{\mathbf{m0}} \approx 4\sqrt{\int E(f)df} = 4\sqrt{m_0} \tag{3.40}$$

Buckley et al. (2018) defined the variance spectral density in a cross shore distance and frequency plot with a colour map to define the spectral density for each location as seen in Figure 3.4. In addition to the surface elevation variance density spectrum, the colour map was also simulated for the phase difference which both plots identified the location of the nodes of the eigen modes (or natural frequencies) for the standing wave pattern that occur, marked as a red curve in Figure 3.4. This graph schematics is used in Chapter 4 of this report.

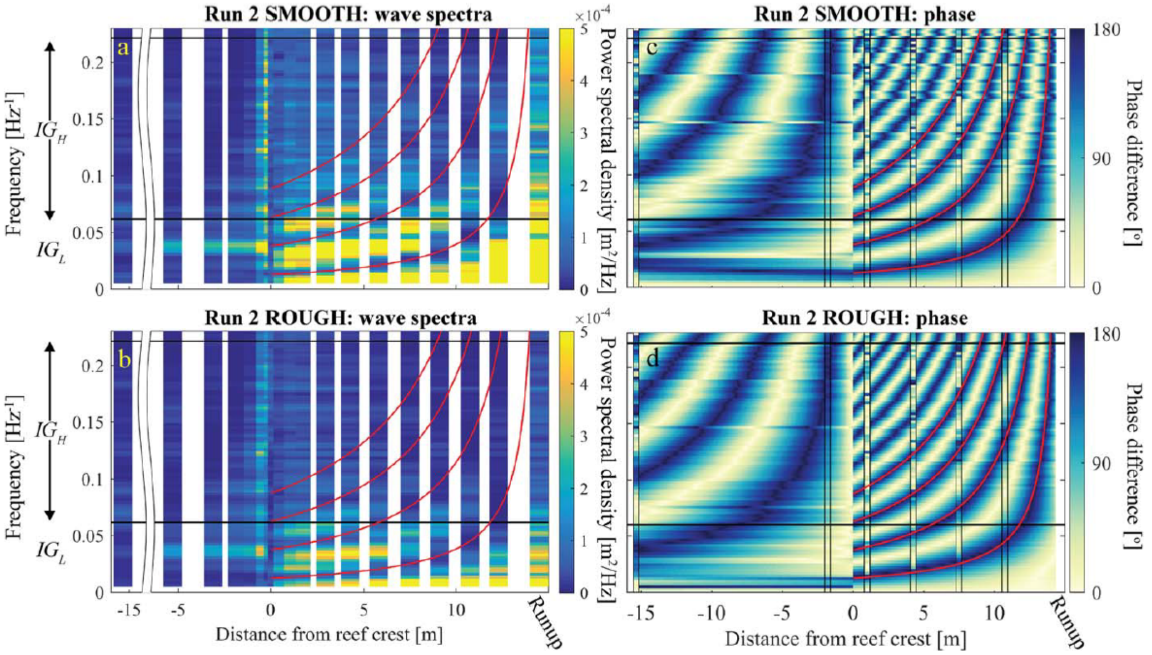

Figure 3.4: The high (IG_H) and low (IG_L) infragravity portions of the wave spectra at each wave gauge and the swash spectra at the shoreline for Run 2 (a) smooth and (b) rough coral reef bed. The red curves show the calculated standing wave nodes through equation (3.41). Natural frequencies occur when the phase difference is 180 degrees out of phase, and the first four natural frequencies occur where the x-axis is at 0 m from the reef crest, after Buckley et al., (2018).

Resonance is affected by the domain that is set; for this report the domain is considered to be a semi-enclosed basin. For a semi-enclosed basin the natural frequency or the eigen modes f_{eigen} can be defined using equation (3.41) which identify the locations of the nodes as defined by Buckley et al. (2018). At equation (3.41), $x_{\text{shoreline}}$ is the point of reflection at the shoreline, n is the number of modes, h_0 is the still water depth, and $\bar{\eta}$ is the wave setup.

$$f_{\text{eigen}} = \frac{1}{4}(2n-1)\left(\int_{x}^{x_{\text{shoreline}}} \frac{1}{\sqrt{g\left(h_0+\bar{\eta}\right)}}dx\right)^{-1} \tag{3.41}$$

3.3.5. Runup

The runup is used for the coastal safety of the dunes. Identifying the runup allows to be used for our research questions of the effect of the slopes and additional free infragravity waves to be assessed. The 2 % exceedance of the runup $R_{2\%}$ is used as defined by Stockdon et al. (2006). $R_{2\%}$ is defined as (1) maximum setup $<\eta>$ that is time averaged at the coastline, and (2) swash S which is the time varying fluctuations above the mean water line.

The swash S needs to be defined, and a depth of 5 cm is chosen for that. The surface elevation that is obtained for a depth lower than 5 cm $r_{h=0.05m}$ is first obtained. The $r_{h=0.05m}$ is then detrended with respect to time and a used through jspect method to obtain the variance density spectra of the swash $E_{Swash}(f)$. The swash S can then be obtained for the whole domain at equation (3.42), where S_{HF} is def ind for high frequencies ($f_{LF} > 0.04Hz$) at equation (3.43), and S_{LF} for low frequencies ($f_{LF} \leq 0.04Hz$) at equation (3.44).

$$S = \sqrt{S_{HF}+S_{LF}} \quad , \quad where \tag{3.42}$$

$$S_{HF} = \int^{f_{HF}} (E_{Swash}(f))\,df \tag{3.43}$$

$$S_{LF} = \int^{f_{LF}} (E_{Swash}(f))\,df \tag{3.44}$$

As a result, the empirical runup with 2% exceedance, $R_{2\%}$ can then be obtained as defined by Stockdon et al. (2006) at equation (3.45), where 1.1 is by definition the slope of regression and the "slightly non-Gaussian nature of the slope" (Stockdon et al., 2006).

$$R_{2\%} = 1.1\cdot(<\eta>+\frac{S}{2}) \tag{3.45}$$

Stockdon et al. (2006) $R_{2\%}$ empirical runup method is then compared to the cumulative distribution function $F_{data}(x)$, of the individual runup maxima R obtained for our specific case. The 98^{th} percentile is chosen $R_{2\%}$ where different empirical distribution functions are fitted $F_{emp.}(x)$ and compared with. The use of kolmogorov smirnov test ks equation (3.47), and the sum of square differences SSD equation (3.46) for the best fit curve to our specific case $F_{data}(x)$.

$$SSD = \sum((F_{data}(x) - F_{emp.}(x))^2) \tag{3.46}$$

$$ks = \max_{x}\left(\left|\widehat{F}_{data}(x) - \widehat{F}_{emp.}(x)\right|\right), \tag{3.47}$$

From the variance density spectra of $r_{h=0.05m}$ previously obtained E_{Swash}, the mean significant time period T_{m01}. T_{m01} can be obtain that represents the mean low frequency waves present that contribute to the $R_{2\%}$ as defined in equation (3.48).

$$T_{m01} = \frac{1}{\int(f_{LF}\cdot E_{Swash,LF})df} \tag{3.48}$$

The equations presented in this chapter, are then used in the upcoming chapters. Since the focus of this report is the free infragravity waves, the wave parameters addressed will be all in infragravity wave domain (with frequency range of 0.004 to 0.04 Hz) therefore, the parameter notations will be referring to the infragravity wave frequency by default if not otherwise specified. The models produced will be run for 10 different seed numbers (seed number 1 to 10) in MATLAB, and with 3 slopes, steep (1:35), mild (1:70) and very mild (1:130) slope.

4

Model Randomness Effect

In this chapter the effect of the randomness of the random phase model that generates the storm condition is assessed by considering the effect of the predefined numerous seed numbers (number 1 to 10) at each slope (steep (1:35), mild (1:70), and very mild (1:130) slope). The boundary conditions and storm conditions obtained from the random phase model equation (3.13) are run in XBeach for seed number 1 to 10. The H_{m0} is obtained through the variance density spectra, where then a statistical analysis is used to see the variation of seed number randomness exhibiting on the model for each slope. Resonance analysis is then conducted to identify if the seed numbers do exhibit resonance properties, or if its a standing wave pattern that is observed. As a result the seed number and slope exhibiting the highest potential resonance is chosen to confirm the resonance through a sensitivity analysis. The sensitivity analysis is then used to pave the direction of the models and conditions (seed number, hydrodynamic, and morphological) that are more realistic and therefore to be used for the basis for the dune coastal safety for the rest of the report.

4.1. Introduction

The storm conditions simulated have an inherit randomness due to the random phase model equation (3.13) which are specified through a predefined seed number for the bound and free infragravity in the pre-analysis. The effect of this randomness needs to be assessed before identifying and assessing the effect of the free and bound infragravity waves on the dunes. To identify the effect of the randomness, 10 seed numbers (1 to 10) are used for the 3 different slopes, steep (1:35), mild (1:70), very mild (1:130) slope, allowing for 30 total runs in total through XBeach. Each seed number at each slope is then simulated and post analysed after XBeach is run. The outputted surface elevation of XBeach is for a surface elevation variance density spectra (through jspect) to obtain the significant wave height denoted as H_{XB} (see equation (3.40)). To identify the effect of the VLF and IG waves, the VLF waves are both included and excluded for each slope to assess the effect of the VLF waves in the model domain, therefore, amounting for a total of 60 different realisations (10 different seed numbers at 3 different slopes for both the inclusion, and exclusion of VLF wave frequency). The inclusion and exclusion of VLF waves is conducted after XBeach is run.

4.2. Statistical Analysis

The surface elevation obtained from XBeach is converted into significant wave height H_{XB} from the variance density spectrum for each seed number at each of the three different slopes. The variance density spectrum has a cutoff frequency of 0.04 Hz which allows for both infragravity (IG) waves and very low frequency (VLF) waves to be present in the simulations. To isolate the effect of the VLF waves and assess their effect on the wave domain, both IG and VLF waves are included, and in addition the VLF is filtered to allow only the infragravity wave band to be present (0.004Hz - 0.04Hz). Therefore, this allows two different frequency restrictions for each slope and seed number, (1) the inclusion of VLF waves, and (2) exclusion of VLF waves (where only the IG waves are present). The randomness of each seed number is then assessed for the different slopes and frequency band conditions. The steep slope (1:35) and mild slope (1:70) are seen in Figure 4.1 and very mild slope (1:130) at Figure 4.2. Both figures, Figure 4.1 and Figure 4.2 includes both the inclusion of VLF waves in part (a), (c), and exclusion of VLF waves in part (b), (d) in each figure.

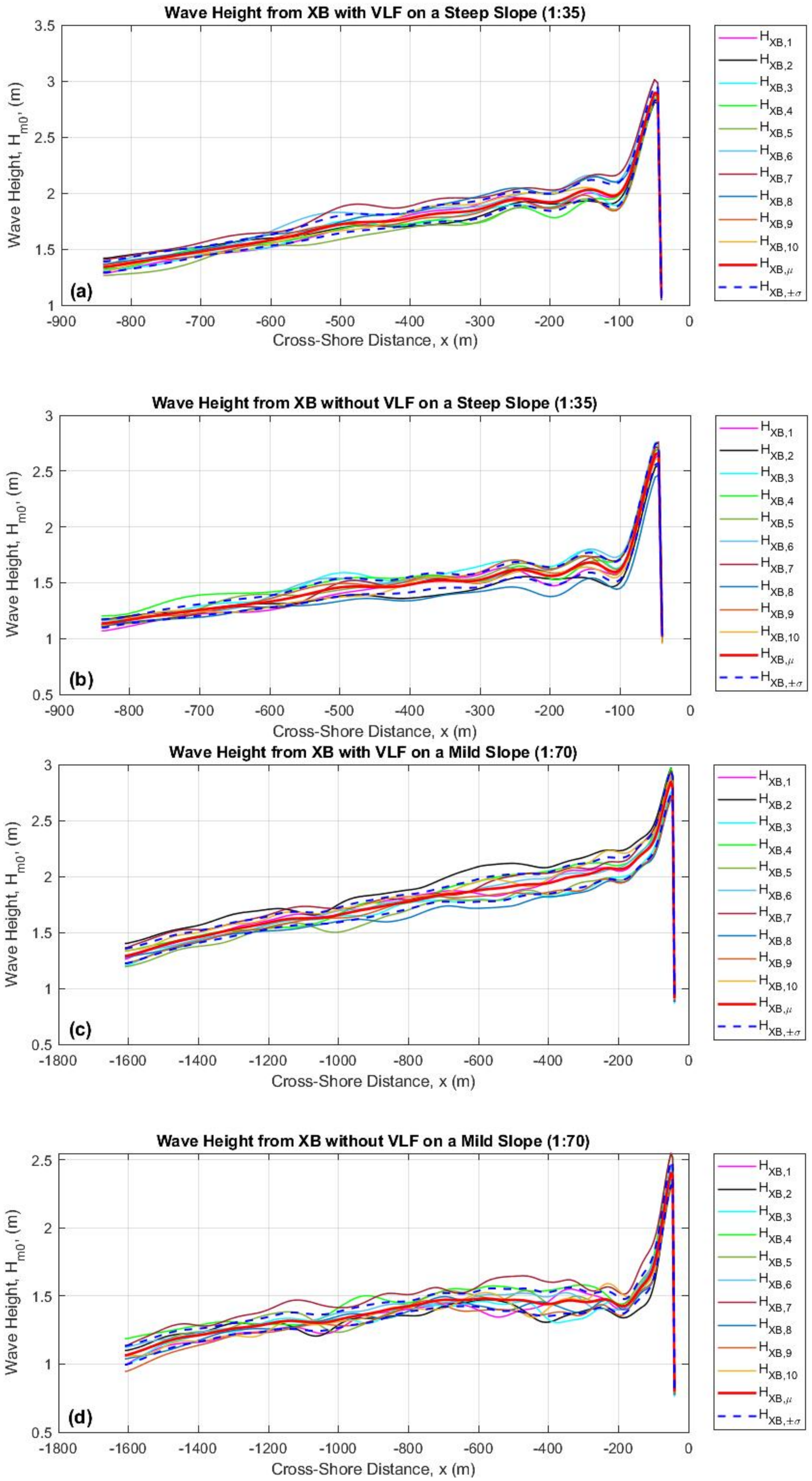

Figure 4.1: Plot of significant wave height H_{XB} and cross shore distance x for a steep slope (1:35) (a), (b), and mild slope (1:70) (c), (d), obtained for seed number 1 to 10 marked with a subscript. The LF wave band including VLF waves is seen at (a) and (c) whereas only IG waves is seen at (b) and (d) plots. Red line is the mean, and the dashed blue line is the standard deviation of all the seed numbers.

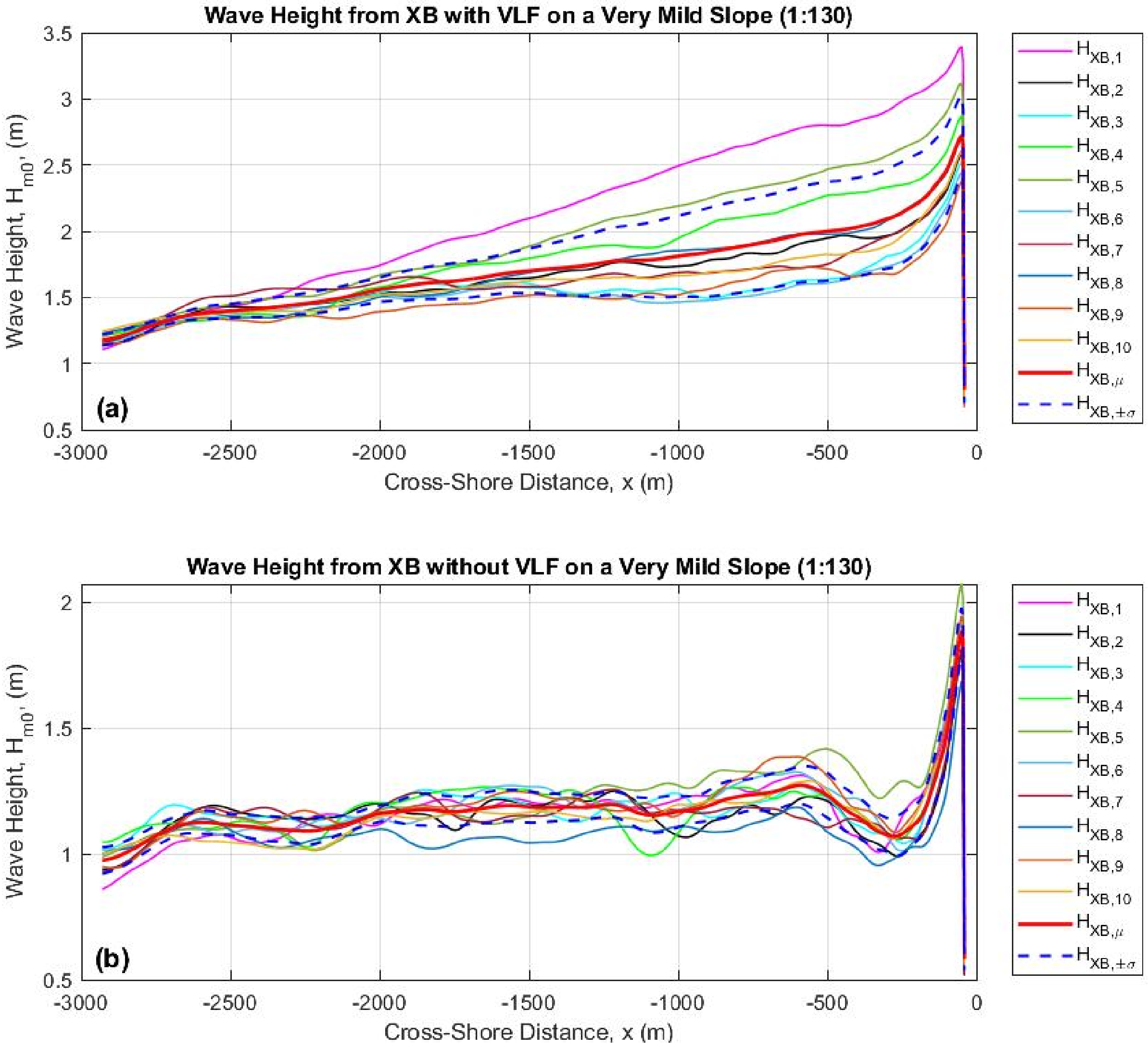

Figure 4.2: Plot of significant wave height H_{XB} and cross shore distance for a very mild slope (1:130), obtained for seed number 1 to 10 marked at different colours, with the inclusion of VLF waves (a) and, only IG waves are present (b). Red line is the mean, and the dashed blue line is the standard deviation of all the seed numbers.

The sample size N, (for each slope) is 10, representing the 10 seed numbers, the mean μ, and the standard deviation σ of the sample size is plotted with a red bold line and blue dash line respectively, whilst the subscript numbers define the (bound wave) seed number. The mean, and standard deviation indicate how much each seed number can deviate between each slope for the situation of the inclusion or exclusion of the VLF wave band for each of the slope. It should be noted that the waves propagate from offshore shown as more negative x values (-850 m, -1600 m, -2850 m) toward more positive x values which is closer to the coast (x = -40m is where the coastline is located).

For the steep slope, when we include the VLF waves (with the IG waves) at Figure 4.1(a) we observe that some waves are deviating from the standard deviation of the sample size wave field (blue dashed line). More importantly for seed number 7 (maroon line - $H_{XB,7}$), indicating the effect of the randomness of the different seed number in our model.
When we compare the inclusion and exclusion of the VLF waves for the steep slope the mean wave height $Hm_{0,\mu}$ (red bold line) at Figure 4.1(b), is lower for the exclusion of VLF waves (only IG waves) with the highest difference of 0.24 m located at x = - 50 m, while the deviation with and without the inclusion of VLF waves is at most 0.01 m.

Similarly, for the mild slope when the VLF waves are included Figure 4.1(c), although seed number 2 (black line - $H_{\mathrm{XB},2}$) is seen to deviate the most, the deviation has a very similar magnitude as the steep slope. At Figure 4.1(d) it can be seen that the waves are modulating considerably, and a lot of the waves are deviating at a standing wave pattern as it propagate from offshore to the nearshore. When we include the VLF waves at the mild slope Figure e4.1(c) a more pronounce VLF standing wave pattern is observed, indicative of the VLF waves having a more significant effect for milder slope than the steep slope.

In Figure 4.2(a) at the very mild slope, there is a very large deviation for the seed number 1 (orange line - $H_{\mathrm{XB},1}$) and seed number 6 (dark green line -$H_{\mathrm{XB},6}$). It can be concluded that the deviations observed and modulations can be potentially linked to the standing wave pattern of the VLF wave and the IG wave. As a result, the VLF wave is more pronounced as a quarter of a standing wave pattern is oscillating for the very mild, and similarly for the mild slope. However, when the VLF waves are considered for the very mild slope, a larger wave height can be observed when the VLF are included which its effect can deviate considerably between the different seed numbers.

The maximum mean wave height $Hm_{0,\mu,max}$ (red bold line) for each slope with and without the VLF waves (at x = -50), and the maximum standard deviation σ_{max} for the seed numbers are all summarised in Table 4.1.

	Steep Slope (1:35)		**Mild Slope (1:70)**		**Very Mild Slope (1:130)**	
	LF	***VLF***	***LF***	***VLF***	***LF***	***VLF***
$H_{m0,\mu,max}$	2.89	2.65	2.85	2.40	2.72	1.88
σ_{max}	0.10	0.09	0.11	0.10	0.38	0.11

Table 4.1: The maximum significant mean wave height $H_{m0,\mu,max}$ (at cross shore distance x = -50 m), and the overall maximum standard deviation σ_{max} for: (1) steep slope (1:35), (2) mild slope (1:70), and (3) very mild slope (1:135) are summarised. The σ_{max} and $H_{m0,\mu,max}$ are shown for both with and without the VLF waves.

From the different slopes considered the wave heights obtained for the steep slope seem to have the highest mean wave heights for when when compared to the very mild slope with a difference of 0.17 m, and 0.78 m for when the VLF are included, and excluded from the simulations respectively. More notably, the VLF wave band can affect the wave height considerably for milder slopes when compared to the situation of only IG waves present, with a difference of 0.24 m and 0.84 m for steep and very mild slope respectively. Therefore, the VLF have a larger wave height contribution on milder slopes.

The VLF wave effect can then be compared on the cross shore distance through an amplification factor α, as a ratio of the Low frequency waves (LF, LF = IG + VLF), and only IG waves ($\alpha_{LF/IG} = H_{\mathrm{XB},\mu,\mathrm{LF}} \div H_{\mathrm{XB},\mu,\mathrm{IG}}$), which is illustrated in Figure 4.3(a).

The VLF response for the very mild slope is as a result larger when compared to other slopes as it had potentially more time to develop and mature Figure 4.3(a). The cross shore distance of the steep slope is considerably less, hence having less time for the VLF response to develop, and therefore the VLF waves contributed ultimately less wave height. For very mild slope, the amplification factor $\alpha = 1.98$. This indicates that the VLF waves are approximately twice the significant wave height contribution of the IG waves present for the very mild slope. The high amplification factor and the abnormal deviation for the mean significant wave height for the very mild slope can indicate that there is a potential resonance effect present, where it needs to be further assessed. Therefore, a spectral density analysis is constructed in the following section, and the natural frequency of one seed number is analysed in detail to identify if the large value of the VLF contribution is linked to resonance. To conduct the spectral analysis, seed number 1 is chosen for the very mild slope due to the larger amplification factor exhibited Figure 4.2(a) and the highest deviating seed number in this slope Figure 4.3(a).

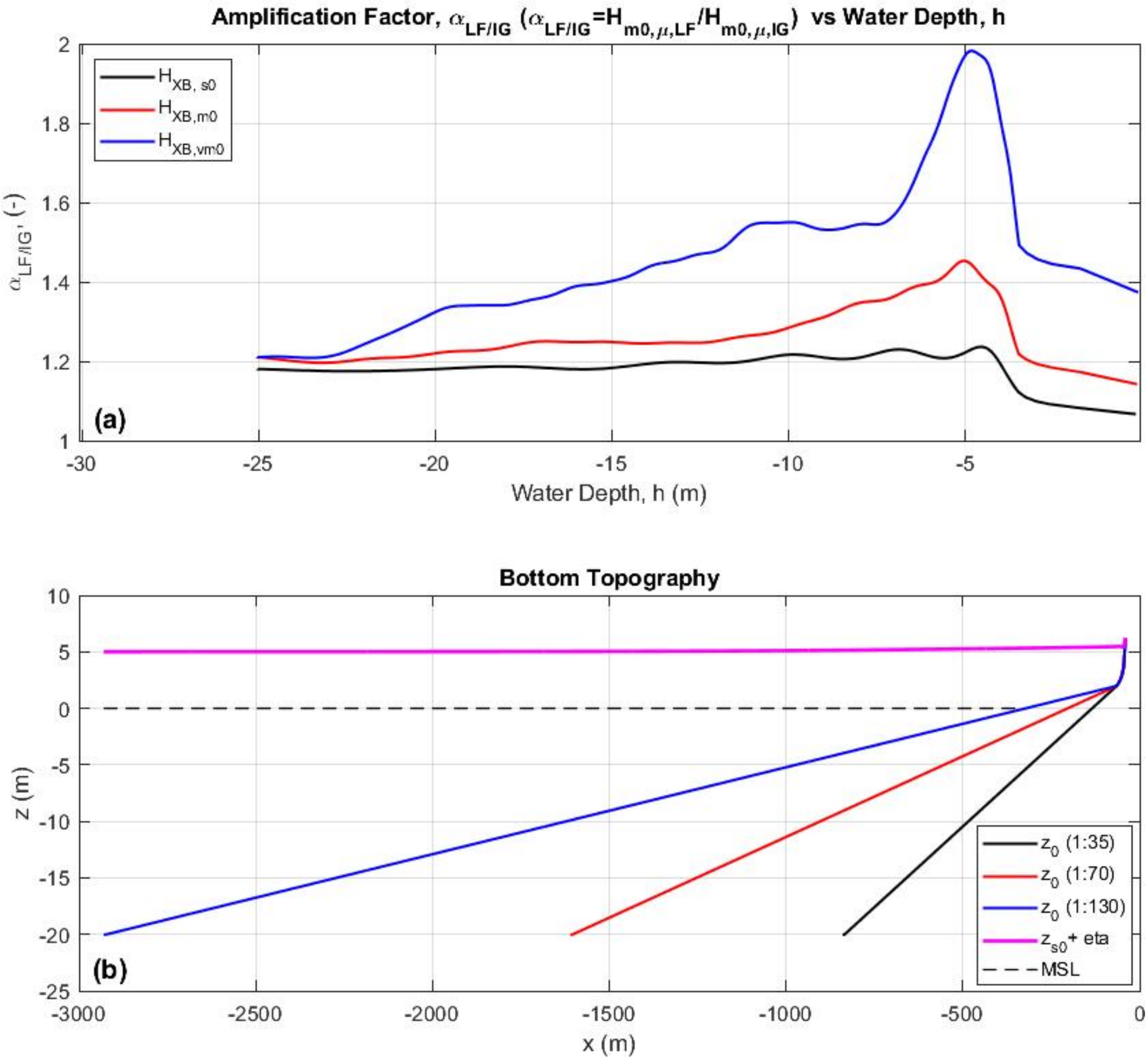

Figure 4.3: (a) Plot of the effect of the VLF wave band in a cross shore distance through the use of an amplification ratio $\alpha_{LF/IG}$ which is a ratio of the means significant wave height with inclusion of all Low Frequencies LF, and only infragravity IG waves ($\alpha_{LF/IG}$ = $H_{\mathrm{XB},\mu,\mathrm{LF}}$ ÷ $H_{\mathrm{XB},\mu,\mathrm{IG}}$). (b) The bottom topography is illustrated for the steep slope (1:35), mild slope (1:70), and very mild slope (1:130) for the set cross shore distance, where MSL is the mean sea level, h_0 is the water depth, η is the surface elevation, and z_{s0} is the surge level.

.

4.3. Spectral Density Analysis

The VLF contribution to the wave height is concluded to be high, however there is a considerable difference between the different seed numbers especially for the very mild slope (1:130) as previously seen in Figure 4.2(a). The effect of resonance is therefore considered to be probable. To assess if what is observed is indeed resonance, the origin of the sensitivity between the seed numbers and VLF response needs to be further analysed. Therefore, one seed number is then used for the spectral analysis, seed number 1 due to its large response for the very mild slope, which is most susceptible to more eigen modes at VLF. The very mild slope (1:130) is used due to the large α response (α = 1.98) and more eigen modes present in the VLF domain at Figure 4.3 seed number 1 is used as it has the largest σ in Figure 4.2. The natural (or eigen) frequency is first obtained through equation (3.41) in Chapter 3 of this report, where the surface variance spectral density is then conducted for the whole cross-shore domain. The spectral peaks of the surface elevation variance density spectrum is compared with the natural frequencies for the very mild slope as seen in Table 4.2. A surface elevation and velocity variance density spectra, and the phase between the two are all three conducted for the whole cross shore domain (rather than at a set observation frequency) with different frequency wave bands. at the closest eigen mode, $f_{eigen,1}$.

As mentioned, seed number 1 is used at a very mild slope (1:130) for the following simulations. The natural frequency (or eigen mode) for the very mild slope is obtained through equation (3.41), where the first 5 eigen modes are used as summarised in Table 4.2. The surface variance density spectrum $E(f)$, and the wave energy variance density spectrum $E(f)$ are then illustrated in Figure 4.4 for offshore (marked with blue line at x = -2925 m), and at nearshore (marked with a red line at x = -1100 m) with the relevant eigen modes. The nearshore location spectral density effects is seen to have a more considerable effect, due the reflected waves in addition to the forced waves present at the offshore wave boundary. The first eigen mode intercept the peak of the surface elevation $E(f)$ which have a magnitude of $272 m^2/Hz$ as indicated in Figure 4.4 at the cross shore distance of x = -1100 m. The energy variance density spectrum at Figure 4.4(b) shows the wave envelope of the wave groups which has more energy at the offshore location (blue line) than the nearshore where the low frequency waves are freely propagating. The very defined peak in the surface elevation $E(f)$ in Figure 4.4(a) intercepts the first eigen mode $f_{\text{eigen, 1}}$ which can be indicative of resonance. However, it is not yet conclusive if it is indeed resonance as it is only an observation point, thus multiple different cross shore locations are required to be used for a better description of the domain.

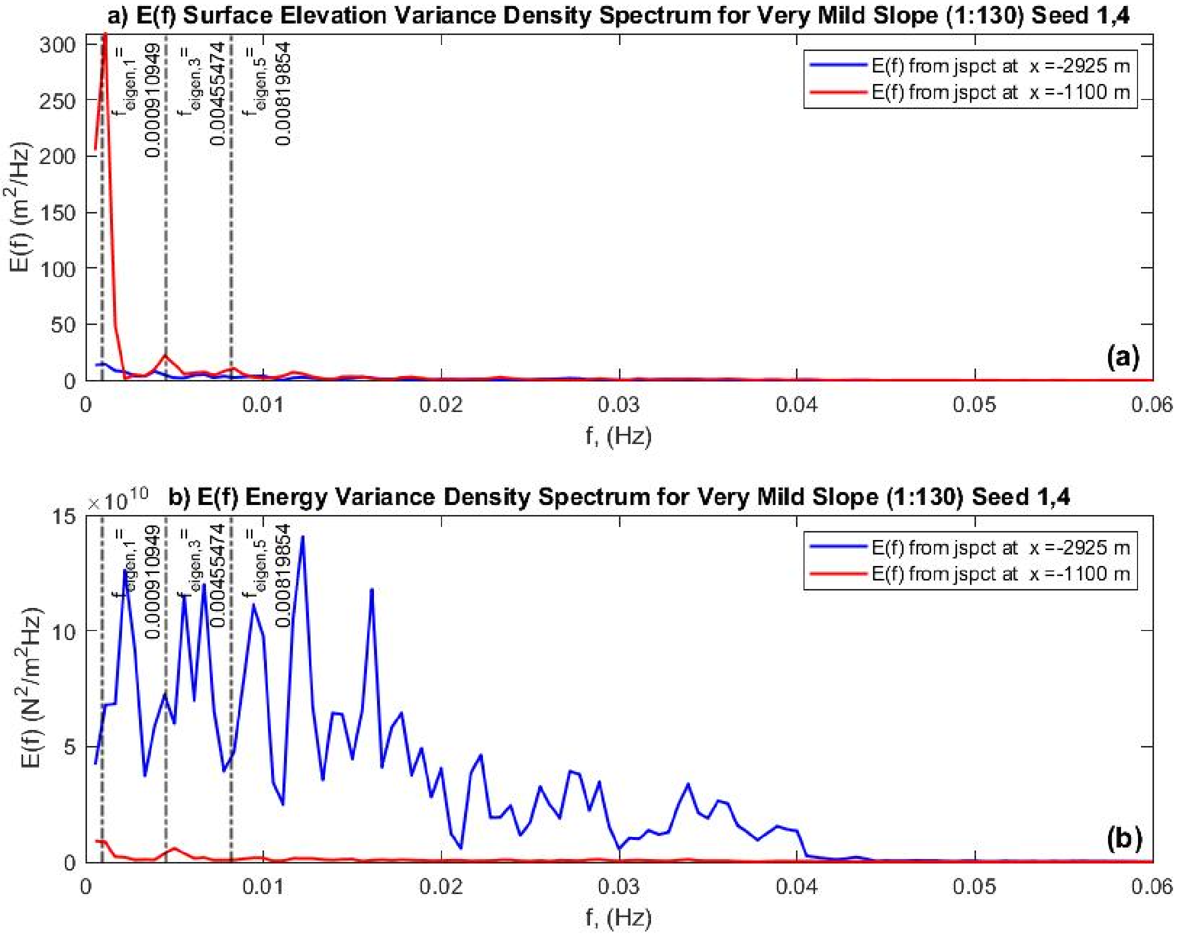

Figure 4.4: (a) Surface elevation variance density spectrum, and (b) Wave energy variance density spectrum (wave envelope) using jspct for a location at the offshore (x = -2925 m) and at the nearshore (x= -1100m). The eigen modes that interact with the wave are indicated on each graph

The surface elevation variance density spectrum Figure 4.4(a) is therefore expanded to show its effect throughout the cross shore distance for the low frequency wave domain Figure 4.6(a). Similarly, the velocity variance density spectrum is also conducted throughout the cross shore distance at Figure 4.5. Patterns are formed in both the velocity and surface elevation variance density spectra resembling the standing wave pattern, where there are high and low $E(f)$ magnitudes throughout our model domain indicating the antinodes and nodes respectively of the $E(f)$ variable. The patterns in the surface, and velocity wave spectra graphs indicates the locations of maxima and minima (antinodes and nodes respectively) with respect to the variance density variable, and indicates the standing wave pattern for different frequencies through the wave propagation.

	Steep Slope (1:35)	**Mild Slope (1:70)**	**Very Mild Slope (1:130)**
Eigen Mode	***Frequency (Hz)***	***Frequency (Hz)***	***Frequency (Hz)***
1	0.0032	0.0017	0.0009
2	0.0096	0.0050	0.0027
3	0.0160	0.0083	0.0045
4	0.0224	0.0116	0.0064
5	0.0288	0.0149	0.0082

Table 4.2: The first 6 eigen modes frequency for steep (1:35), mild (1:70), and very mild slope (1:130) configuration

Lastly, the phase can then be constructed through the use of the cospectra component $C_f(p,u)$ of Sheremet et al. (2002) as described in equation (3.22). The phase is obtained since the cospectra variable has a real and imaginary part present for the two variables used, (1) the pressure (or surface elevation related), and (2) cross-shore velocity contribution. As a result, the phase between the velocity and surface elevation (or pressure) is obtained and can be seen in Figure 4.6(b). The phase is therefore the contribution between the surface elevation, and cross shore velocity $E(f)$ which are illustrated in Figure 4.6(a), and Figure 4.5 respectively.

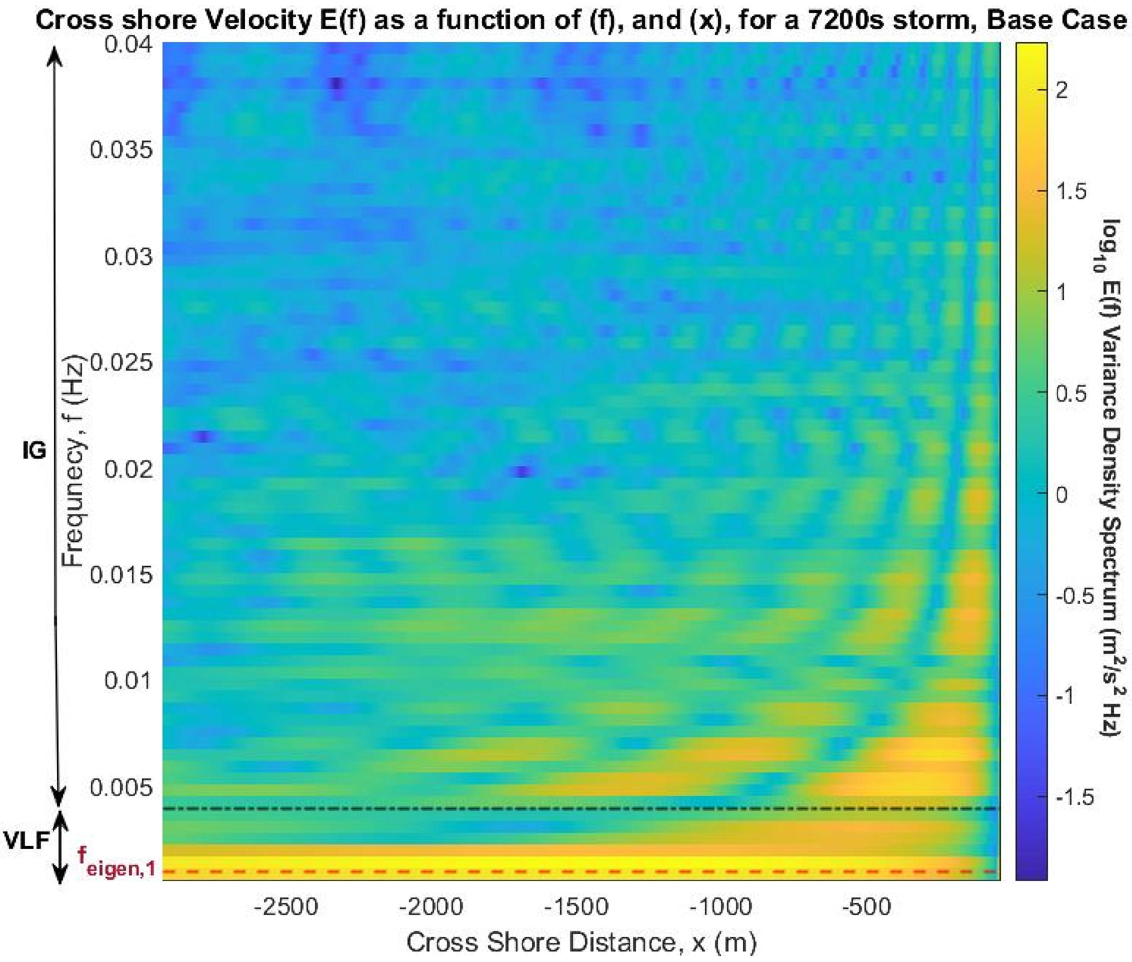

Figure 4.5: Velocity variance density spectrum at different frequency, and cross shore distance for the very mild slope (1:130). The eigen nodes for the velocity are located at the blue areas (negative $E(f)$) when they are between the yellow areas (positive $E(f)$). The black dashed line indicated the frequency wave boundary between the IG and VLF waves at f = 0.004 Hz, and the red dashed line is the first eigen mode $f_{eigen,1}$ at f = 0.0009 Hz.

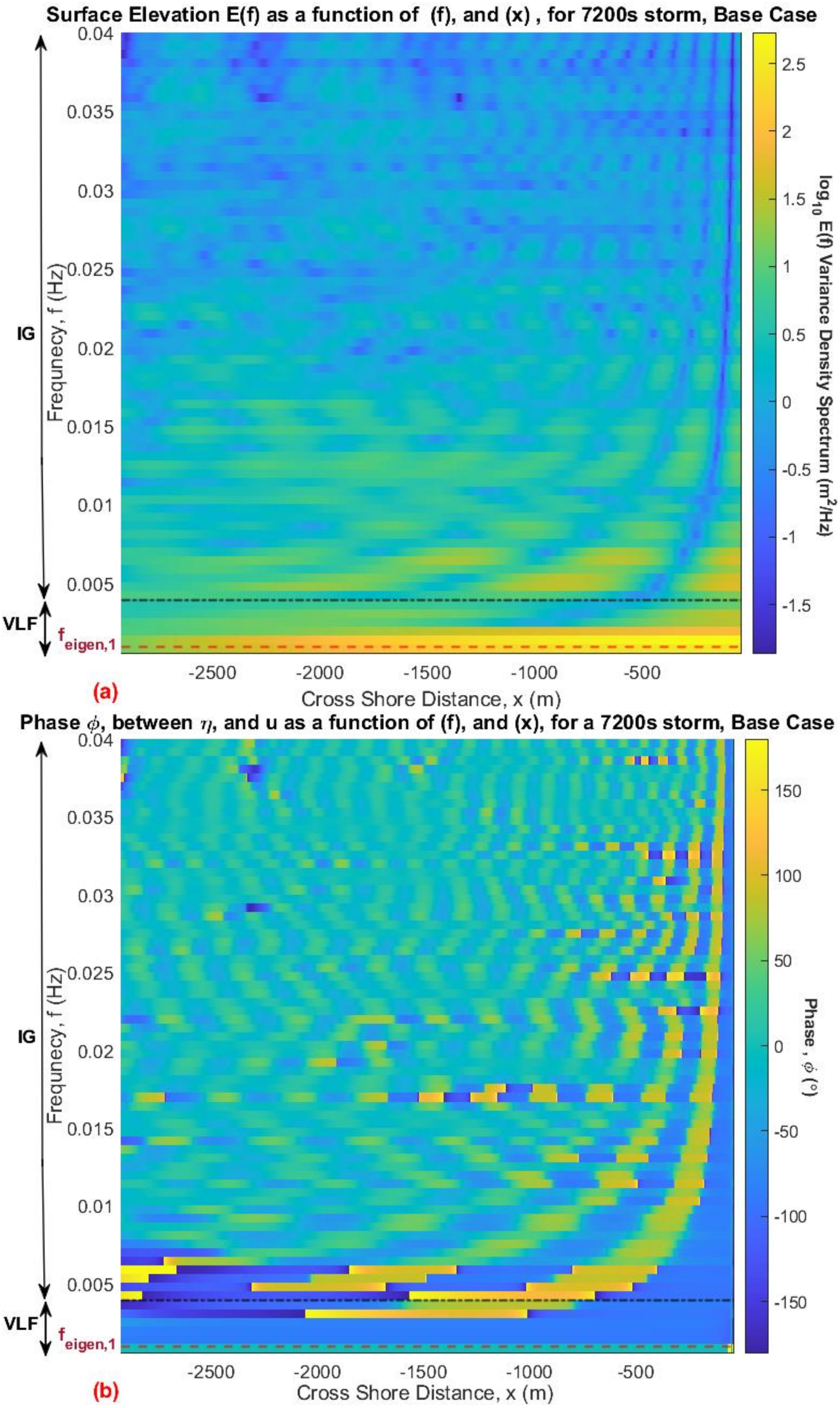

Figure 4.6: (a)Surface elevation variance density spectrum at different frequency, and cross shore distance for the very mild slope (1:130). The eigen nodes are located at the blue areas (negative logarithmic $E(f)$) when they are between the yellow areas (positive logarithmic $E(f)$). (b) Phase between the surface elevation and velocity at different frequencies. The black dashed line indicated the frequency wave boundary between the IG and VLF waves at f = 0.004 Hz, and the red dashed line is the first eigen mode $f_{eigen,1}$ at f = 0.0009 Hz.

A standing wave pattern emerges from the velocity and surface elevation $E(f)$ plots (Figure 4.5 and Figure 4.6(a) respectively), formed by the nodes (the negative logarithmic $E(f)$ locations marked in blue), for the same frequency band. There are, as expected more harmonics present in the higher IG frequencies and the harmonics reduce as you move towards the VLF band. The VLF and IG waves are separated by a black dashed line at 0.004 Hz, and the first eigen mode $f_{eigen,1}$ is indicated with a red dashed line at 0.0009 Hz for both Figure 4.5, and Figure 4.6. For the VLF waves, at a set set VLF, it can be seen only one node and antinode present for both Figure 4.5 and Figure 4.6(a). The phase in Figure 4.6(b) shows the same effect, where the standing wave pattern is also reflected, with more harmonics at higher frequencies and a lot lower especially in the VLF. Similarly to the statistical analysis for this seed number and slope Figure 4.2, the VLF waves have a considerable effect in the wave domain. In addition to the wave height previously seen in the statistical analysis and the surface elevation $E(f)$, the velocity $E(f)$ magnitude is also considerably high for the VLF wave bands which further solidified the potential of resonance. The potential of resonance is present throughout the domain for VLF closer to the first eigen mode. In order to identify by what degree do we have resonance, a sensitivity analysis is required by varying the boundary conditions for a wave force frequency (or observation frequency) closest to the first eigen mode.

4.4. Sensitivity Analysis

A sensitivity analysis is necessary to identify by how much the resonance can affect our results, the potential changes are identified for different changes in the boundary conditions which include the cross shore distance, storm duration and cross shore distance in line with equation (3.41). As a result, a resonance sensitivity analysis is conducted for a forcing (or observation) frequency of f = 0.0011 Hz, which is the closest to the first eigen mode that is seen to have the highest response. For this analysis initially the cross shore distance is extended for a (1) horizontal bed, (2) the storm duration, and (3) the depth are all increased. All these variables are then compared to the initial (or base) case that is seen so far. To identify the effect of resonance in our results, the closest frequency to the first eigen frequency ($f_{eigen,1}$ = 0.0009 Hz) need to be used. Finally a sensitivity analysis that allows to exclude the resonance effect through a frequency cut off is conducted. Through the frequency cut off, the effect the most optimal frequencies that will allow consistency between the slopes without any resonance affecting our computational models.

4.4.1. Resonance Analysis

For the very mild slope the first eigen mode $f_{eigen,1}$ = 0.0009 Hz) is seen to have the majority of the wave energy and therefore can be more susceptible to resonance. To confirm the potential effect of resonance, an observation frequency is chosen that is closest to the first eigen mode of 0.0011 Hz that will act as a forcing frequency for the different boundary conditions. At the observation frequency f = 0.0011 Hz the surface elevation, velocity, and the phase $E(f)$ are all plotted. For the base case, the set up used in the spectral and statistical analysis, the surface elevation, velocity $E(f)$, and phase are all illustrated at Figure 4.7[(a)-(c)] respectively. As expected,$E(f)$ at Figure 4.7(a) an antinode (x = -40 m), can be seen at the coastline for the surface elevation, and a node at the offshore location (x = -2930 m). The opposite effect is observed with the cross shore velocity having a a node at the coastline location and an antinode at the offshore location at Figure 4.7(b) which both are in line for a semi-enclosed basin.

The VLF wave effect is highlighted at this observation frequency as it has a quarter of a standing wave pattern, which is in line with the amplification factor VLF presence. The maximum surface elevation $E(f)$ at Figure 4.7(a) can be seen to have a magnitude of 538 m^2/Hz, which is substantial, indicative of resonance especially considering the standing wave pattern. Furthermore, at Figure 4.7(c) the phase confirms that there are no significant phase changes throughout the domain (with the exception at the coastline) which further highlights the VLF waves affecting the domain with a very pronounced quarter standing wave pattern.

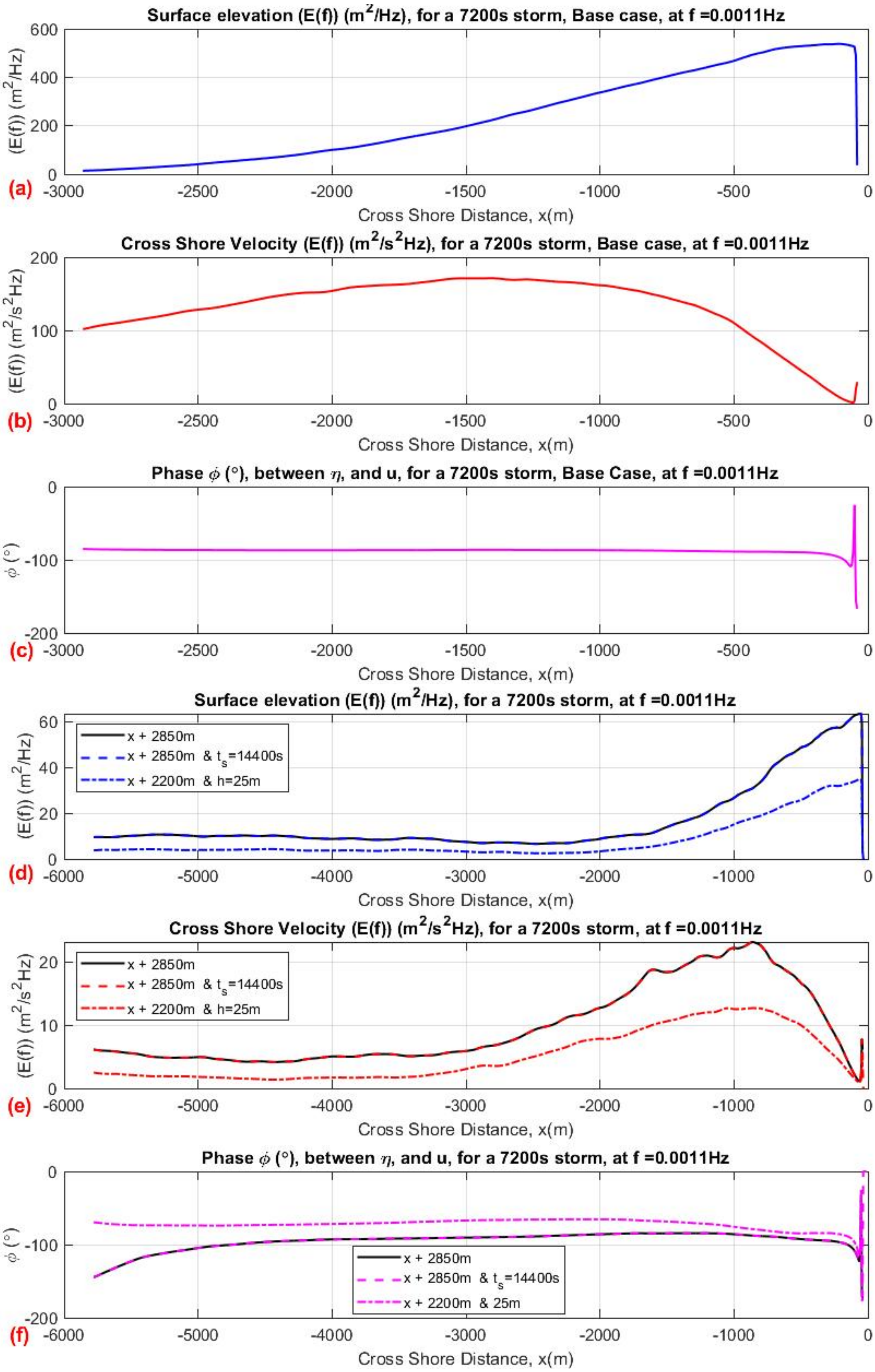

Figure 4.7: Plot of the surface elevation $E(f)$ (a), (d), cross shore velocity $E(f)$ (b), (e), phase between the surface elevation and cross shore velocity (c), (f) against cross shore distance at a frequency f = 0.0011 Hz for the very mild slope (1:130). Where (a),(b) and (c) are for the base case (depth of 20 m, 2 hour storm duration). And (d),(e),(f) are for the cross shore domain was extended by an additional 2850 m (solid line), extended storm duration of 14400 s with the extended cross shore distance (dashed line), and water depth of 25 m with the extended cross shore distance extension (dashed-dotted line). For a more clear representation of the separated Figures refer to Appendix A.

To identify if what is being observed is resonance or near resonance different boundary conditions are needed to be changed whilst keeping the same frequency. Resonance is sensitive to the boundary conditions as seen from equation 3.41 in chapter 3.3.4. The boundary conditions that the resonance is sensitive to includes (1) cross shore distance x, (2) storm duration (surface elevation magnitude related), and (3) the water depth h. These variables identified are all illustrated at Figure 4.7[(d)-(f)]. At Figure 4.7[(d)-(f)] the cross shore distance is extended with an additional x of 2850 m (marked with a solid line). In addition,the storm duration increased from 7200 s to 14400 s (marked with dashed line) which is the two hour signal repeated twice with the same extended distance of 2850 m. Lastly the water depth is extended from 20m to 25 m, where the cross shore distance is kept consistent with the other boundary changed which as a result extended x by 2200 m (marked with dashed-dotted line). To observe the individual varied variables surface elevation and velocity variance density spectra with their respective phase at f = 0.0011 Hz refer to Appendix A.

The cross shore distance extended is first addressed (solid line), where the cross shore distance is extended by an additional 2850 m as a horizontal distance at a depth of 20 m, and the surface elevation $E(f)$, velocity $E(f)$, and phase are shown at Figure 4.7[(d)-(f)] with a solid line. The same pattern of nodes and antinodes are observed for the surface elevation and velocity as the base case with a quarter of standing wave pattern. However, the surface elevation $E(f)$ at Figure 4.7(d) has magnitude of 63.5 m^2/Hz at it's antinode (nearshore) which is a decreased by a factor of 8.4 from the base case. In addition the maximum cross shore velocity $E(f)$ at Figure 4.7(b) is 171.3 m^2/s^2Hz whilst for Figure 4.7(e) its 23.1 m^2/s^2Hz which is a decreased of a factor of 7.4.

The rapid decrease of the magnitude therefore confirms that the base case was indeed at a resonance peak, which explains why there was such a drastic change in the inclusion and exclusion of the VLF results. The added cross shore distance does not necessarily mean that we have no resonance present in the domain. The effect of the resonance however if it's indeed present is severely reduced. Figure 4.7(f) show that instead of one predominant harmonic there is a bigger phase change at the offshore location showcasing that the dominant effect of the VLF wave band is not as dominant as before due to the reduction of the VLF resonance, however, the effect of VLF is still noticeable which can be still considered as partial resonance.

For the same figure, Figure 4.7[(d)-(f)]. The storm duration simulated at the start of 2 hours, is now increased to 4 hours (2 hour signal repeated twice) with the additional 2850m horizontal cross shore distance. With the increase storm duration, it can be seen that the overall magnitude of the surface elevation $E(f)$ at Figure 4.7(a), and velocity $E(f)$ at Figure 4.7(b) is consistent with the increase of the cross shore distance on its own (marked with a dashed line). It can be concluded,that the storm duration effect does not significantly affect our results from just the cross shore distance extension.

Lastly, the water depth h is increased to 25 m from 20 m in addition to the cross shore distance extension of 2200 m to be consistent with the last two consideration shown at Figure 4.7[(d)-(f)] with a dashed-dotted line. The overall magnitude of the surface elevation and velocity spectra $E(f)$ have been even further reduced when compared to the base case. With the depth increase the maximum surface elevation $E(f)$, is now at 34.7 m^2/Hz which is a factor of 15.5 less than the base case. The standing wave pattern is now illustrating a heavily reduce overall and maximum magnitude. Concluding that for the depth increase there is little to no resonance present or being enhanced.

To conclude the overall effects of resonance and its sensitivity in our results, a resonance mismatch is illustrated at Figure 4.8 against the maximum surface elevation $E(f)$. For Figure 4.8 in addition to the previous boundary conditions considered, the cross shore distance and water depth are both further varied to identify the effect of the resonance on the surface elevation variance denstiy spectrum magnitude. The resonance mismatch ($\Delta f = f_{VLF} - f_{eigen,1}$) is defined as the difference between the observation frequency f_{VLF} of 0.0011 Hz and the first eigen mode $f_{eigen,1}$. The first eigen modes, resonance mismatch, and maximum surface elevation $E(f)$ are all shown in Table 4.3 for each different case and therefore reflected at Figure 4.8.

	f_{VLF} (Hz)	$f_{eigen,1}$ (Hz)	Δ f (Hz)	Max. η $E(f)$ (m^2/Hz)
Base Case	0.00111	0.00091	0.00020	538.00
x + 2850m	0.00111	0.00055	0.00056	63.42
x + 1850m	0.00111	0.00064	0.00048	46.68
x + 1350m	0.00111	0.00069	0.00042	51.53
x + 1000m	0.00111	0.00074	0.00037	82.83
x + 850m	0.00111	0.00076	0.00035	114.10
x + 425m	0.00111	0.00083	0.00028	356.60
x + 2850m, t = 14400s	0.00111	0.00055	0.00056	63.49
x + 2200m, h = 25m	0.00111	0.00056	0.00055	34.83
x + 1200m, h = 25m	0.00111	0.00065	0.00046	27.43

Table 4.3: The resonance mismatch Δf ($\Delta f = f_{VLF} - f_{eigen,1}$), and maximum surface elevation $E(f)$ with their corresponding eigen mode and observation frequency for each different boundary conditions.

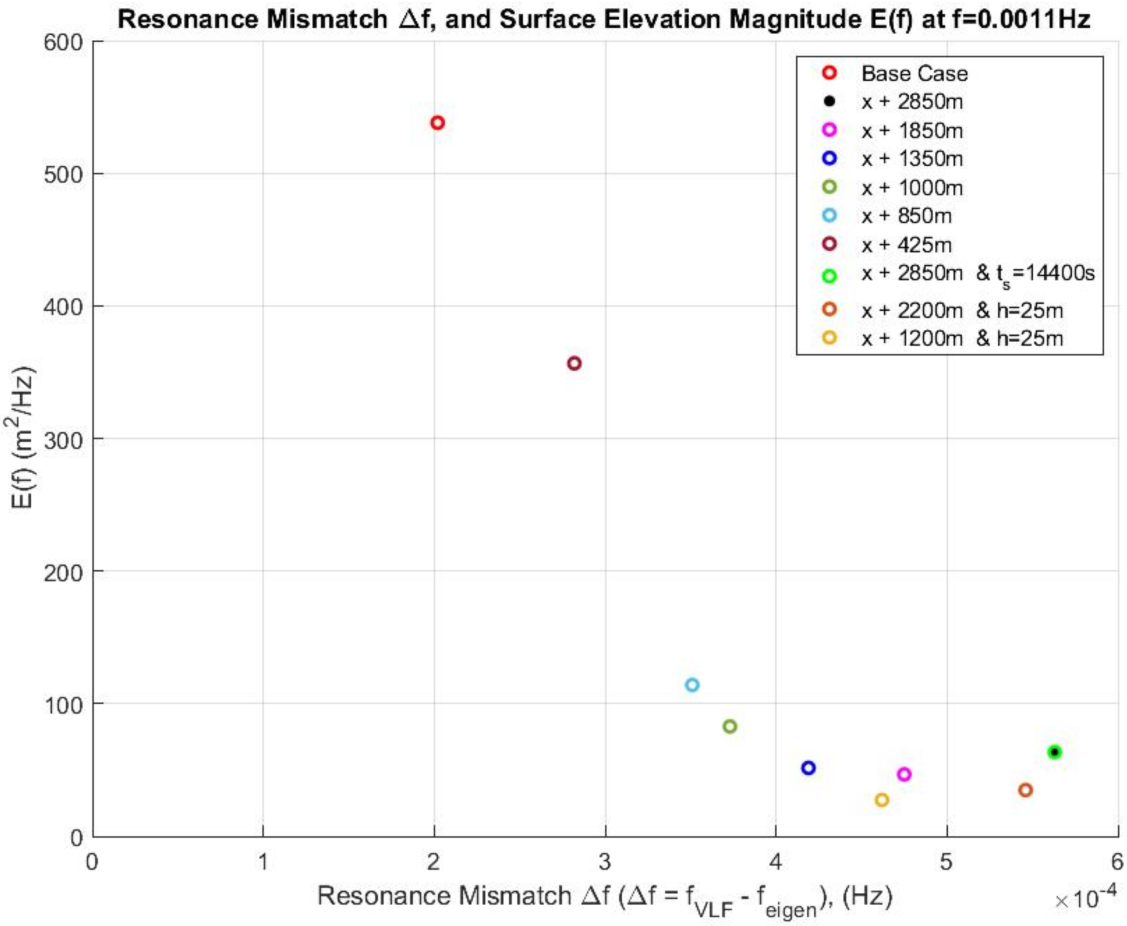

Figure 4.8: Maximum surface elevation $E(f)$ for different boundary condition changes indicating the resonance mismatch $f_{eigen,1}$ ($\Delta f = f_{VLF} - f_{eigen,1}$) for each case.

From Figure 4.8 it can be concluded that the closer the resonance mismatch Δf is to 0 (x-axis) the higher the effect the resonance has on the wave domain, as the eigen mode and observation frequency are more and more aligned. It can be seen that our base case the resonance has the most effect. Subsequently, we can see that the effect of resonance translated by the maximum magnitude of the surface elevation $E(f)$ reducing as the resonance mismatch is reduces. Since the cross shore distance variation has such a big effect and for our domain is arbitrarily chosen for a reliable computational time efficiency, it can be concluded that the resonance observed is artificially created. This artificial resonance should be removed as its a computational artefact and does not represent the wave conditions in Noordwijk where this jarkus transect is obtained from. In order to remove the artificial resonance, an frequency resolution is needed to be conducted at the post processing stage where the storm duration is simulate. Therefore, can be adjusted to eliminate this computational artefact for a reliable representation and assessment of dune coastal safety later on.

4.4.2. Frequency Resolution

The artificial resonance identified can be removed by changing the initial frequency resolution df_0 from our wave domain. The current frequency resolution df_0 used at the wave maker for our random phase model equation (3.10) thus far, is $df_0 = 0.000139$ Hz. A wider, more coarser frequency resolution can be used that removes the artificially induced VLF resonance response from our model domain as a cut off frequency. However, the resonance as we have seen in chapter 4.4 is specific to both (1) the morphological boundary conditions, and (2) the seed number (forcing). A sensitivity analysis is therefore conducted to conclude on a frequency resolution that the VLF artificial resonance is not present.

The artificial resonance was confirmed for the very mild slope (1:135) at seed number 1 as it was assessed. As a result, the very mild slope and seed number 1 is used as the basis of frequency resolution (df_0) sensitivity analysis, before concluding on the frequency resolution of the other slops. Different frequency resolutions df_0 are used when running the random phase model and their corresponding maximum surface elevation $E(f)$ is obtained closest at the first eigen mode $f_{eigen,1,vm0=0.00091Hz}$. The results of this frequency resolution's sensitivity analysis are summarised at Table 4.4, and are also visually illustrated at Figure 4.9.

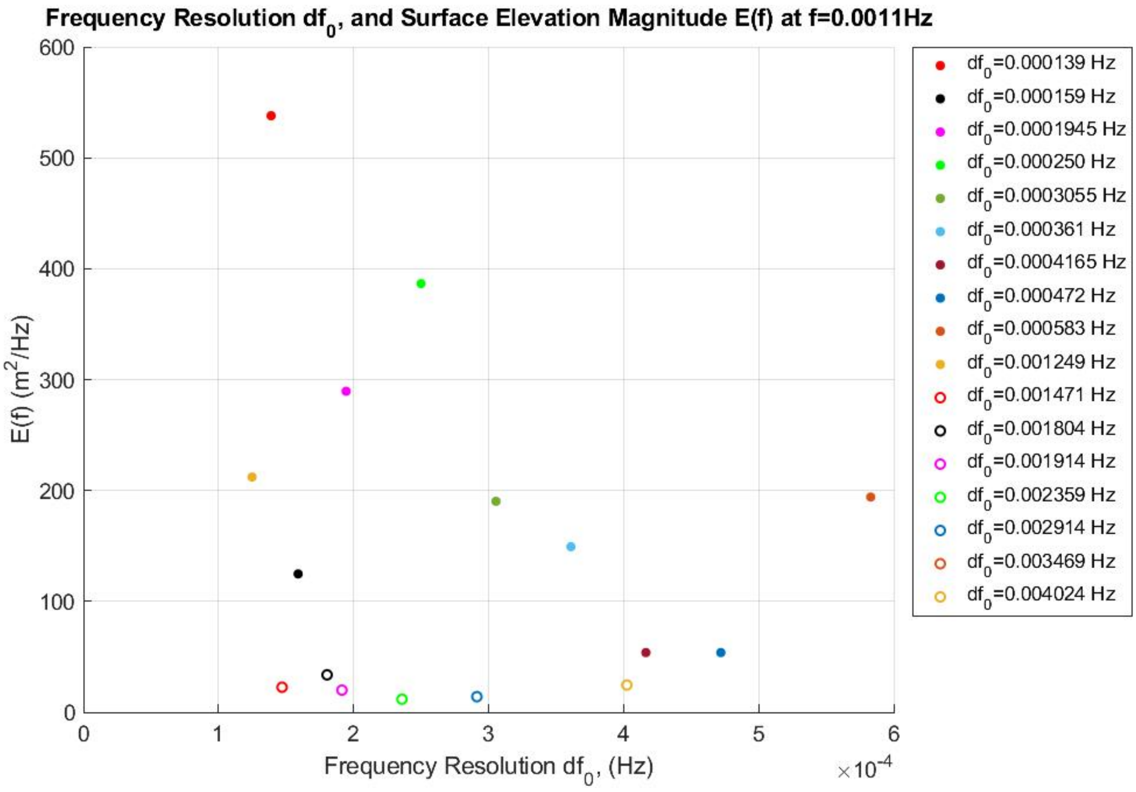

Figure 4.9: Maximum surface elevation $E(f)$ for different frequency resolutions df_0 for the same morphological boundary conditions and a frequency observation point df_{VLF}, located in the VLF wave band of $df_{VLF} = 0.0011$Hz. The initial/base frequency resolution of $df_0 = 0.000139$ Hz was used for the statistical and spectral analysis to account for the VLF waves.

df_0 (Hz)	Max.η $E(f)$ (m^2/Hz)
0.000139	538.0
0.000159	124.8
0.0001945	289.5
0.000250	386.6
0.0003055	190.3
0.000361	149.3
0.0004165	53.85
0.000472	53.85
0.000583	194.1
0.001249	212.12
0.001471	22.56
0.001804	33.79
0.001914	19.97
0.002359	11.78
0.002914	14.11
0.003469	24.09
0.004024	24.61

Table 4.4: Different frequency resolutions df_0 used and their corresponding maximum surface elevation $E(f)$.

The different frequency resolutions show a significant change in the maximum surface elevation $E(f)$ at Figure 4.9. The frequency resolution identified in the previous chapter is at $df_0 = 0.000139Hz$ at the top of Table 4.4, which is confirmed to exhibit resonance as indicated by the large $E(f)$ magnitude. From the Figure 4.9 it can be concluded that for lower frequency resolutions the potential of artificial VLF resonance is still quite prominent and starts to subside at $df_0 = 0.001471Hz$. Therefore, the first few frequencies that do not exhibit any large $E(f)$ magnitude and exhibit a fairly constant magnitude instead for the very mild slope are chosen (1) $df_0 = 0.001471Hz$, (2) $df_0 = 0.001804Hz$, and (3) $df_0 = 0.001914Hz$ to be used further in the sensitivity analysis. The sensitivity analysis to be constructed is assessing the other slopes (mild, and very mild slope). Therefore, for consistency, the frequency difference δf, where $\delta f = df_0 - f_{eigen,1}$, is used to allow for a representative frequency resolution df_0 that is constant for the different slopes as seen at Table 4.5. For each slope their maximum surface elevation $E(f)$ is obtained at the first eigen mode with their representative runup $R_{2\%}$ summarised at Table 4.5. In Table 4.5 the slopes are grouped based on their δf and the base case with $df_0 = 0.000139Hz$ used in the statistical analysis section 4.2 is also shown for comparison. By having a constant δf between the slopes it allows for the frequency resolutions of the mild (1:70), and steep slope (1:35) to be obtained from the very mild slope (1:135) and gives a comparable response in between the slopes.

As observed in Table 4.5 and Figure 4.9 the maximum surface elevation $E(f)$ for the very mild slope (1:135) seems to be fairly consistent for the frequencies higher than 0.001471 Hz showing no resonance effect. However, when compared with the mild (1:70) and steep slope (1:35), the steep slope with $df_0 = 0.003731Hz$ (Group 2 in the table) exhibits an unusually large maximum surface elevation $E(f)$ of 315.7 m^2/Hz. This unusual large magnitude for the steep slope can be potentially resonance. As a result, for our analysis, the next group of δf is used, Group 3 is in Table 4.5. The frequency resolution df_0, of $df_0 = 0.001804$ Hz, $df_0 = 0.002542$ Hz, and $df_0 = 0.004064$ Hz is used for the very mild (1:135), mild (1:70) and steep slope (1:35) respectively. For these three different frequency resolutions the spectral plots of surface elevation, cross shore velocity, and phase are shown in Appendix B at the observation point closest to their respective $f_{eigen,1}$. The 2 % exceedance of the runup $R_{2\%}$ is obtained following a F(x) as described at Appendix E, and therefore shown for each slope at Table 4.5.

To summarise, for the purpose of this report the frequency resolutions in Group 3 is used for the three different slope as shown in Table 4.5 for the rest of this report.

Group	Slope	df_0 (Hz)	$f_{eigen,1}$ (Hz)	δf (Hz)	Max.η $E(f)$ (m^2/Hz)	Runup, $R_{2\%}$ (m)
1	Very mild (1:130)	***0.000139***	0.00091	(-)	538.00	7.37
	Mild (1:70)	***0.000139***	0.00165	(-)	109.50	7.66
	Steep (1:35)	***0.000139***	0.00317	(-)	32.50	7.95
2	Very mild (1:130)	***0.001471***	0.00091	0.00056	22.56	7.38
	Mild (1:70)	***0.002209***	0.00165	0.00056	44.22	7.35
	Steep (1:35)	***0.003731***	0.00317	0.00056	315.70	7.55
3	Very mild (1:130)	***0.001804***	0.00091	0.00089	33.79	6.82
	Mild (1:70)	***0.002542***	0.00165	0.00089	11.53	7.36
	Steep (1:35)	***0.004064***	0.00317	0.00089	34.00	7.70
4	Very mild (1:130)	***0.001914***	0.00091	0.00100	19.97	7.27
	Mild (1:70)	***0.002652***	0.00165	0.00100	14.10	7.38
	Steep (1:35)	***0.004174***	0.00317	0.00100	16.31	7.96

Table 4.5: Different frequency resolutions df_0 are summarised for the three different slopes with their corresponding first eigen frequency $f_{eigen,1}$, frequency difference δf ($\delta f = df_0 - f_{eigen,1}$), maximum surface elevation $E(f)$, and Runup $R_{2\%}$. The different slopes are grouped together based on the frequency difference δf which is kept constant for each group. Group 1 is in reference to the original, base case used for the statistical analysis in 4.2. Group 2, 3, and 4 are the first three lowest frequencies identified df_0 where no VLF resonance is identified for the very mild slope (1:135).

4.5. Conclusion

Through this chapter, a statistical analysis was conducted to identify the randomness effect on our results. The effect of resonance was then considered through variance density spectra, where different boundary conditions were changed through a sensitivity analysis for a set observation frequency to conclude if the waves are indeed affected by resonance.

From the statistical analysis conducted, the random phase model's randomness can have a very large effect for our domain at different bed slopes. The milder the slope the more contribution from the VLF waves is observed. An amplification factor $\alpha_{LF/IG} = H_{XB,LF}/slashH_{XB,IG}$ of 1.98 confirms the VLF contributing for the very mild slope, indicating that there are approximately two times more VLF waves present than IG waves in the wave domain.

The standard deviation of each slope is therefore identified for different slopes at Table 4.1 and the wave height of each seed number can be seen deviating from the mean wave height considerably. VLF waves being included in the results indicated a considerable effect for the wave height. The milder the slope the bigger VLF response is seen in the wave height. As a result the very mild slope (1:135) indicated a couple of seed numbers that were deviating considerably from the mean wave height. The highest deviating seed number that exhibited the biggest wave height response at the very mild slope (1:135) due to the with the VLF inclusion is seed number 1. Seed number 1 at the very mild slope is suspected of exhibiting an unusually high wave height contribution which is why it was chosen and analysed in detail for a spectral, and resonance sensitivity analysis.

For the spectral analysis the eigen modes are identified for the very mild slope (1:135). The first eigen mode ($f_{eigen,1}$) for the very mild slope (1:135) has been identified (of $f_{eigen,1} = 0.00091$ Hz) to be the most energetic mode due to its large response in the surface elevation and cross shore velocity variance density $E(f)$ spectrum. This is conducted by observing the wave spectra for the whole cross shore distance. An observation frequency f_{VLF} is chosen closest to the first eigen mode which is at a frequency of 0.0011 Hz. Therefore, the wave spectra is conducted for the whole cross shore distance at the f_{VLF}. The surface elevation variance density spectrum at f_{VLF} of 0.0011 Hz had a maximum $E(f)$ magnitude of 583 m^2/Hz and cross shore velocity $E(f)$ of 171.3 m^2/s^2Hz located at the nearshore. The wave domain exhibit a VLF dominant standing wave pattern that shown a standing wave patter of a quarter of a wave length that further highlights the VLF contribution in the wave domain seen from the statistical analysis. The high magnitude of $E(f)$ observed is confirmed to be due to resonance which is confirmed after a resonance sensitivity analysis is conducted.

For the resonance sensitivity analysis the (1) cross shore distance, (2) storm duration, and (3) water depth boundary conditions are all varied and compared through the same observation frequency f_{VLF} of 0.0011 Hz. The maximum surface elevation $E(f)$ was obtained for each variable varied and plotted against resonance mismatch. Resonance mismatch Δf is the difference between the observation frequency f_{VLF}, and the first eigen mode $f_{eigen,1}$ of each different case. When the resonance mismatch was closer to 0, which means that the eigen mode is closest to the observation frequency, the magnitude of the variance $E(f)$ is the highest, thus further solidifying that there is an excitation of the wave domain through resonance.

However, since these boundary conditions are arbitrarily chosen for our computational domain, the resonance effect can be concluded to be a computational artefact, essentially indicating that these are not present in a real life scenario. In addition, since there is no forcing mechanism inducing a wave forcing at a set cross shore distance such as a sand bar (Liu and Cho, 1993), edge waves (Herbers et al., 1995), or coral reef (Péquignet et al., 2009; Gawehn et al., 2016; Buckley et al., 2018), which further confirms that this is indeed a computational artefact. The computational artefact identified in this case is at the VLF wave band, and needs to be removed, as that will artificially and as noted can significantly influence our wave domain when assessing dune coastal safety. The identification of this artificial resonance effect gave us an insight on the first three research questions set out to answer for this report, about the effect of computational randomness in a computational domain, and the role of resonance.

Research Question 1: What is the effect of the computational randomness of the VLF wave hydrodynamics during a storm event?

A statistical analysis shown that the different seed numbers used in our random phase model have a very large randomness observed with different wave height contributions throughout the domain. Additionally, when the VLF waves were present there was a bigger standard deviation on the seed numbers and higher wave height than only the IG wave frequency wave band counterpart. The VLF waves have been seen to be a vary major contribution of the storm on the wave height. For milder slopes the effect of this computational randomness was seen to be higher as seen as expected through the amplification factor $\alpha_{LF/IG}$ (a ratio between the LF and IG wave height) and the individual seed numbers on the milder slopes as some of the individual seed numbers deviated considerably.

The seed numbers deviating considerably are confirmed to be due to resonance. This resonance however is an artificial artefact as it changes considerably by changing the cross shore distance, which for our domain is arbitrarily chosen so that is relatively computationally efficient. The computational randomness however for regardless the boundary conditions in our random phase model in the pre-processing stage, is a real possibility in having abnormal results that can affect your results when used for wave hydrodynamic analysis as the seed number can skew the wave hydrodynamic results due to potential artificial resonance is present.

Research Question 2: What is the contribution of resonance to the VLF and Infragravity response?

The VLF waves are seen to be higher for very mild slopes rather than the steep slope. The VLF response is highest at the surf zone with a contribution of up to twice that of the IG waves for the very mild slope. The resonance confirmed is located for the VLF waves at the very mild slope at the very first eigen mode. However, the VLF resonance observed is artificial as its a product of the arbitrarily chosen cross shore distance chosen. Therefore, its not a resonance response expected in Noordwijk where our domain is located. For the IG frequency there was no resonance response observed.

Research Question 3: Can resonance be removed?

An artificial resonance response is identified at the VLF. This artificial resonance does not provide a realistic representation of our model, and as a result should be removed. The resonance observed at the very low frequencies can be removed with a frequency cut off, that in result removes the first eigen mode, that exhibits this large response. Therefore, eliminating the artificial resonance inducing frequencies in the VLF domain from our results.

5

Wave Hydrodynamics

In this chapter a frequency resolution is chosen for the wave domain so that there is no artificial resonance present in the VLF wave band. The model is then run for bound only waves $IG_{free} = 0$ where the runup is obtained for three different slopes , (1) steep $(1:35)$, (2) mild $(1:70)$, and (3) very mild $(1:130)$ slope. A spectral analysis is conducted to identify the response of the newly established frequency resolutions. The linear and non-linear wave propagation are obtained for the wave domain that are then compared with the total spectral significant wave heights obtained from XBeach, and the runup. The effect of slope is therefore assessed and compared for each different wave propagation method and linked to the runup.

5.1. Introduction

The morphology can have a significant effect on the wave hydrodynamics, runup and therefore dune coastal safety that needs to be addressed. The bed slope is identified to be a potential significant contributor that can affect the wave hydrodynamics and the runup. As a result, the model is run for the seed number 1 that was used for the sensitivity analysis in the previous chapter, Chapter 4.4 of this report. To remove the artificial resonance the frequency resolution df_0 is made coarser than the one seen so far of $df_0 = 0.000139Hz$ which subsequently sets the a cut-off frequency of the domain. The model is then run for three different slopes previously used, (1) steep (1:35), (2) mild (1:70), and (3) very mild (1:130) slope. The three different slopes have different frequency resolutions to eliminate the artificial resonance seen from the VLF frequency band. However for each different slope, the same frequency difference δf is kept constant with respect to the first eigen mode $f_{eigen,1}$ for consistent. The presence of resonance is then assessed at f_{eigen} and then the frequency resolution is chosen for each slope so that is to be used for the following hydrodynamic analysis for the rest of the report. The different slopes are then assessed through XBeach and with the addition of linear and non-linear wave propagation methods. For the linear wave propagation, the incoming and outgoing waves are modelled with (1) Guza et al. (1984 method, and (2) Sheremet et al. 2002 method. These methods are then compared with one another to assess their validity and the linear wave propagation description of the model domain that can affect the dune coastal safety. The linear wave propagation method namely Sheremet et al. (2002) method is then compared with a non-linear wave propagation method from Battjes et al. (2004) that describes the incident infragravity response with the addition of roller energy flux. The different methods are used to capture, and therefore analyse the effect of the waves during a storm and as a result give an insight on the 2 % exceedance of the runup $R_{2\%}$ obtained of each slope for the dune coastal safety.

For this chapter as concluded in chapter 4.4.2 of this report the different frequency resolutions and therefore the runup $R_{2\%}$ and maximum variance density spectra $E(f)$ is used, and therefore also summarised at Table 5.1 for ease. From Table 5.1 it can be concluded that the $R_{2\%}$ is highest for steeper slopes regardless of the potential of resonance that the slope or frequency resolution may allow.

Slope	df_0 (Hz)	$f_{eigen,1}$ (Hz)	δf (Hz)	Max.η $E(f)$ (m^2/Hz)	Runup, $R_{2\%}$ (m)
Very mild (1:130)	***0.001804***	0.00091	0.00089	33.79	6.82
Mild (1:70)	***0.002542***	0.00165	0.00089	11.53	7.36
Steep (1:35)	***0.004064***	0.00317	0.00089	34.00	7.70

Table 5.1: Different frequency resolutions df_0 are summarised for the three different slopes with their corresponding first eigen frequency $f_{eigen,1}$, frequency difference δf ($\delta f = df_0 - f_{eigen,1}$), maximum surface elevation $E(f)$, and Runup $R_{2\%}$. The different slopes are grouped together based on the frequency difference δf which is kept constant for each group. Group 1 is in reference to the original, base case used for the statistical analysis in 4.2. Group 2, 3, and 4 are the first three lowest frequencies identified df_0 where no VLF resonance is identified for the very mild slope (1:135).

5.2. Spectral Analysis

The frequency resolution df_0 is obtained for each slope, that do not amount to any potential resonance at or around the first eigen mode $f_{eigen,1}$ as concluded from the frequency resolution at section 4.9 of this report. However, in order to understand the wave hydrodynamics present in the our wave domain, and to have a better understanding of the runup values obtained the wave spectra of the whole frequency domain is conducted at an arbitrary location. If a $E(f)$ peak is identified similarly to what was observed in the previous chapter, chapter 4, a wave spectra is conducted for the whole cross shore distance at the set frequency of interest for a better insight of the results.

The spectral analysis is conducted to identify which slope can exhibit resonance. An arbitrary cross shore distance x is chosen at the breaker zone for all steep, mild, and very mild slopes at Figure 5.1. From Figure 5.1 is evident that for the steep slope there is a very defining $E(f)$ peak at the fifth eigen mode $f_{eigen,5,s0} = 0.0283 Hz$, and similarly for the mild slope at the second eigen mode $f_{eigen,2,m0} = 0.005 Hz$ for the surface elevation $E(f)$. These very defining surface elevation $E(f)$ peaks can indicate resonance, which can influence our results.

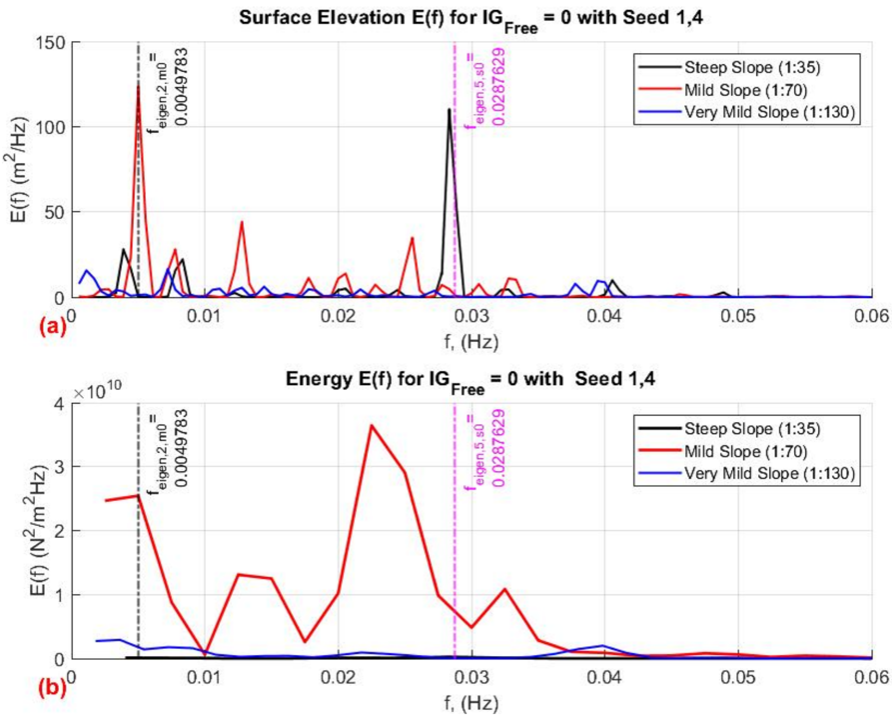

Figure 5.1: (a) Sea-swell significant wave height H_{ss}), for IG_{free} of for the steep (1:35), mild (1:70), and very mild (1:130) slope marked with a blue, red, and black solid line respectively. (b) Bottom topography $z0$ for steep, mild, and very mild slope illustrated with a blue, red, and magenta line respectively. The mean sea level MSL is marked with dashed black line, and with solid black line the water line which is a combination of the surface elevation η and surge level z_{s0}.

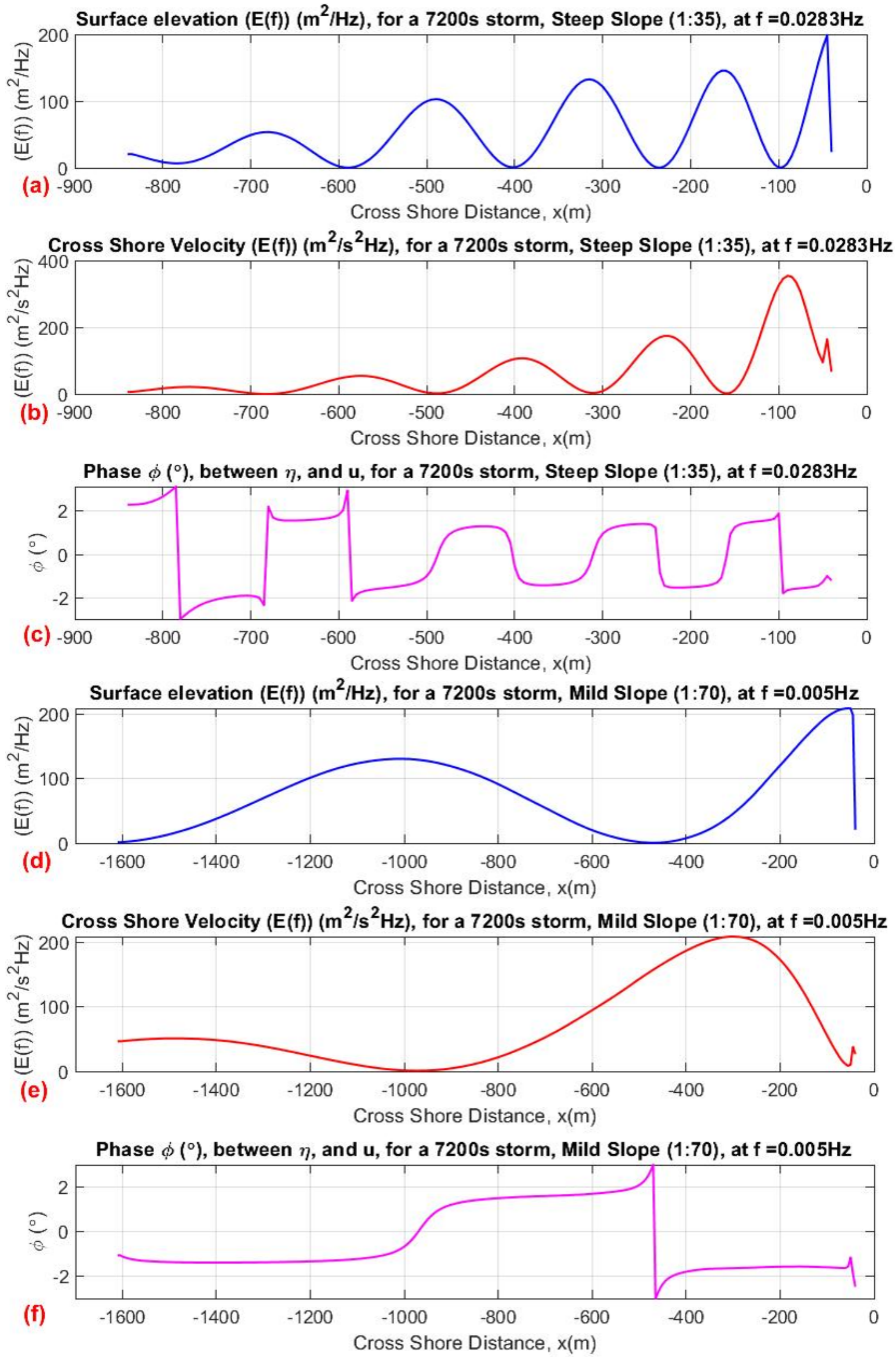

Figure 5.2: Wave domain for linear wave propagation for mild (a-c) and very mild slope (d-f) with Free infragravity wave intensity $IG_{free} = 2$. Where the significant wave height H_{m0} shown at (a) and (d), and energy flux illustrated at (b) and (e). The total significant wave height is summarised by the neon green line (H_{XB}). The dotted black line is the total wave height corresponding to the total flux of Sheremet method H_{Sher}. The blue lines show the incoming waves, and red line the outgoing waves. Sheremet et al. (2002) method is summarised with solid blue and red lines. Battjes et al. (2004) non-linear method for the incoming wave is marked with solid magenta, and cyan line for the inclusion and exclusion of the roller effect respectively. (c) and (f) are the bottom topography of the mild (1:70) and very mild slope (1:130). For the bottom topography the sea bed z_0 is marked with solid black line,s the MSL is marked with dashed black line, and the the water elevation marked with solid magenta line includes the surface elevation η, and surge level (z_{s0}).

As a result, as conducted in the previous chapter, chapter 4 the surface elevation $E(f)$, cross shore velocity $E(f)$ and phase are all examined individually at the frequency closest to the eigen mode frequency as indicated at Figure 5.2(a-f). For the steep slope the surface elevation $E(f)$ shows a maximum magnitude of 198.7 m^2/Hz as illustrated at Figure 5.2(a-c). Similarly for the mild slope the surface elevation $E(f)$ shows a maximum magnitude of 208.4 m^2/Hz as indicated at Figure 5.2(d-f). The magnitude of both steep and mild slope show a similar high magnitude which can overestimate, and therefore exaggerate the runup, and wave propagation results in the wave domain. These responses for the fifth eigen mode $feigen, 5, s0 = 0.0283Hz$ of the steep slope, and second eigen mode $f_{eigen,2,m0} = 0.005Hz$ of the mild slope can be attributed to the artificial resonance in the domain as noted in the previous chapter, since there is no realistic mechanism enforcing the eigen modes to be present at these set frequencies.

5.3. Linear Wave Propagation

To assess the coastal safety of the dunes, runup can be used and consequently identify how the significant wave height H_{m0} of the linear wave propagation defines the domain for the incoming and outgoing waves. To achieve this, different linear wave propagation methods are used to describe the wave domain. The incoming and outgoing wave heights are expressed in this chapter through (1) Guza et al. (1984 method $H^{\pm}_{Guza}$ from equation (3.21), and (2) Sheremet et al. (2002) method $H^{\pm}_{Sher}$ from equation (3.25). In addition, the total wave height in the domain is described by (3) the total significant spectral wave height H_{XB} obtained from XBeach wave energy and converted through equation (3.40) which includes the standing wave pattern of the domain. The total significant spectral wave height H_{XB} is used to compare the to the two linear wave propagation methods, and (4) the total wave height H_{Sher} that indicates the incoming and outgoing wave from Sheremet et al. (2002) method that defines the total flux in the domain. These 4 wave height components are all used for each of the three different slopes (steep (1:35), mild (1:70), and very mild (1:130) slope) to describe the linear wave propagation.

For the coastal dune safety, the linear wave propagation of incoming and outgoing waves from Guza et al. (1984) $H^{\pm}_{Guza}$, and Sheremet et al. 2002 $H^{\pm}_{Sher}$ method are both compared in this section with each other to assess the linear wave hydrodynamics in our wave domain for the three different slopes. This allows us to identify by how much these two methods differ when describing the wave domain, and providing an insight for the Runup $R_{2\%}$ value obtained from Table 5.1 for steep (1:35), mild (1:70), and very mild (1:130) slope.

The steep slope (1:35) is illustrated at Figure 5.3(a-c), mild (1:70) and very mild (1:130) slope are illustrated at Figure 5.4(a-c), and Figure 5.4(d-f). For these figures the significant spectral wave height H_{XB} is defined with a solid green line the linear wave propagation shows an incoming significant wave height H_{m0} marked with a blue line, and the outgoing wave with a red line. Guza et al. (1984 method is defined with a dashed line, and for Sheremet et al. (2002) with a solid line for the incoming and outgoing waves in the wave domain.

5.3.1. Steep Slope

For the steep slope (1:35) it can be seen that both the significant wave height of Guza et al. (1984) $H^{\pm}_{Guza}$, and he significant wave height of Sheremet et al. (2002) $H^{\pm}_{Sher}$ show a very similar description of the wave domain at Figure 5.3(a). $H^{\pm}_{Guza}$, is however on average showing higher significant wave height H_m0 when compared to $H^{\pm}_{Sher}$. The maximum deviation of $H^{\pm}_{Guza}$ and $H^{\pm}_{Sher}$ is seen at the offshore wave boundary with a difference of 0.3 m. Since these two method are describing similar information, $H^{\pm}_{Sher}$ is seen to be sufficient for defining the linear wave propagation of the steep slope due to the added variable of the linear energy flux F_L.

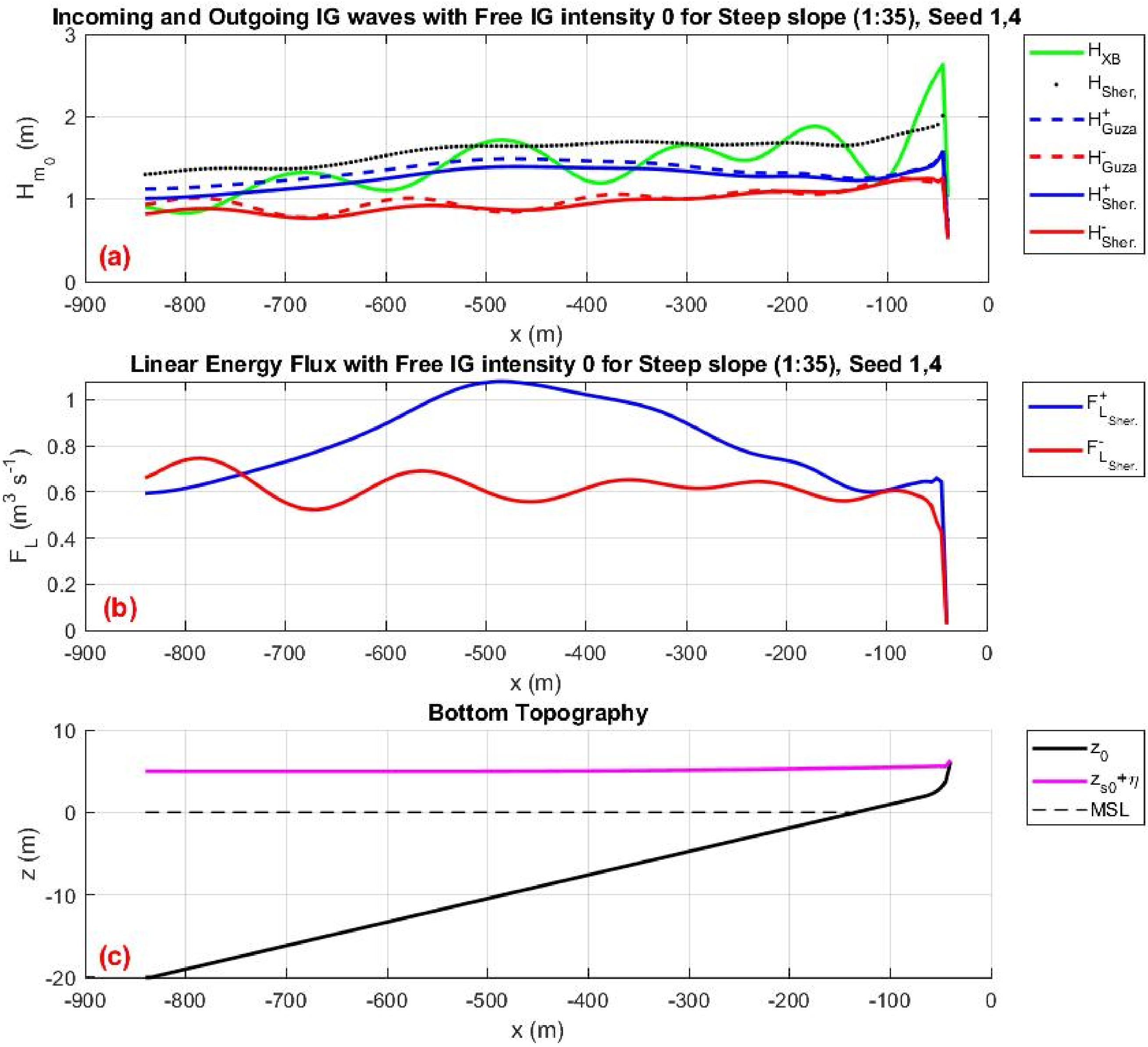

Figure 5.3: Incoming and outgoing (a) significant wave height H_{m0}), and (b) linear energy flux for the steep slope (1:35). Where the total significant wave height is summarised by the neon green line (H_{XB}. The dotted black line is the total wave height corresponding to the total flux of Sheremet method $H_{Sher.}$. The blue lines show the incoming waves, and red line the outgoing waves. Sheremet et al. (2002) method is summarised with solid blue and red lines, whilst Guza et al. (1984) is dashed blue and red lines. (c) is the bottom topography of the steep slope (1:35) where the sea bed z_0 is marked with solid black line, dashed black line indicates the MSL and the magenta line is the water elevation which includes the surface elevation η, and surge level (z_{s0}).

The significant wave height from the wave spectra H_{XB} at Figure 5.3(a) shows a standing wave pattern. The standing wave pattern is consistent with the high frequency infragravity waves that are observed dominating the wave field. This can be attributed to the significant effect from the surface elevation $E(f)$ produced at the fifth eigen mode $f_{eigen,5,s0} = 0.0283 Hz$.

The incoming significant wave height H^+_{Sher} at Figure 5.3(a) increases when moving from offshore to nearshore with a local maxima at x = -480 m, of H^+_{Sher} = 1.39 m, and at the shoreline at x = -45 m of H^+_{Sher} = 1.57 m. For a better description of this local maxima the linear energy flux F_L can be used at Figure 5.3(b) it can give a more reactive description of the model domain. The linear energy flux F_L at Figure 5.3(b) also describes the same local maxima at x = -480 m that has the highest respond in the wave field with a minor local maxima at the swash zone (x = -45 m). The biggest energy flux situated at x = -480 m indicates a large energy release that indicates an infragravity wave mechanism occurring. The standing wave pattern of H_{XB}

showing there is an antinode situated at x = -480 m (also evident in Figure 5.2(a)), which amounts to a higher than expected wave height and energy flux.

The breakpoint mechanism is more evident at steeper slopes Battjes et al. (2004) and for our case it can be concluded is present causing higher (in magnitude) waves to break further offshore. The breakpoint mechanism is also evident on the outgoing wave that exhibit a higher energy flux at the offshore wave boundary, that surpasses the incoming bound wave. The outgoing wave red solid line at Figure 5.3(a) shows the infragravity waves reflecting and propagating offshore with approximately the Green's law ($H_{Green} \sim h^{-0.25}$) with the exception at the shoreline due to the breakpoint mechanism.

As a result, after the energy flux reduction due to wave breaking is released, there are less free infragravity waves released when approaching the coast up until the coastline x = -45m. At the swash zone (x = -45m) the energy flux slightly increases as the waves break on the dune face due to the very steep slope of the dune face of $m = 0.581$. The breaking of the waves is also illustrated at Appendix F, where the sea swell wave height $H_{ss,s0}$ seem to reduce at around -500 m at the breakpoint where the wave height starts to reduce rapidly.

It can be concluded in the steep slope, that the incoming and outgoing waves are adequately described using Sheremet et al. (2002) method, with the breakpoint mechanism (Symonds et al., 1982) affecting the offshore location for the outgoing wave whilst majority of the free IG waves are released at x = -480m.

5.3.2. Mild Slope

The mild slope significant wave height, energy flux, and bottom topography are all described at Figure 5.4[(a)-(c)] respectively. Similar to the steep slope, $H^{\pm}_{Sher}$ describes the linear wave propagation quite well having a comparable wave propagation description as $H^{\pm}_{Guza}$ as illustrated at Figure 5.4(a). The standing wave pattern H_{XB} of the mild slope exhibits lower frequency waves when compared to the steep slope ones that are very pronounced. This indicates that lower frequency waves such as low infragravity or high VLF waves are becoming more dominant in the mild slope. The lower frequency dominance is evident at the surface elevation $E(f)$ at Figure 5.2(d) due to the second eigen mode $f_{eigen,2,m0=0.005Hz}$ with a magnitude of 208.4 m^2/Hz.

For the mild slope at Figure 5.4(a-b) a well defined local maxima is identified at around x = -1090 m at Figure with H^{+}_{Sher} of 1.68 m. Similarly to the steep slope the breakpoint mechanism for the mild slope is well defined. At the breakpoint the infragravity waves release from the wave groups and propagate freely. As a result the breakpoint mechanism allows for the waves to propagate offshore from the break point, allowing for a higher outgoing energy flux F^{-}_{L} between -1600 m to -1090 m as shown in Figure 5.4(b) when comparing that to the nearshore. After the majority of the free infragravity waves are released from the wave group, the waves propagate to the surf zone. Therefore, the energy flux reduces and becomes fairly constant due to no other non-linear wave effects affecting the wave propagation.

5.3.3. Very Mild Slope

The very mild slope (1:130) linear wave propagation is located at Figure 5.4(d-f). Similarly to steep and mild slope, $H^{\pm}_{Guza}$ and $H^{\pm}_{Sher}$ show a similar description of the wave domain with $H^{\pm}_{Guza}$ providing higher H_{m0} in the wave domain at Figure 5.4(d). Thus providing the same conclusion of Sheremet et al. (2002) gives a good description of the wave domain. In addition, the standing wave pattern formed by H_{XB} at Figure 5.4(d) shows that there is a combination of higher frequency wave with lower frequency waves with no real dominant standing wave pattern in the wave domain. As observed from Figure 5.1 the very mild slope does not show any real dominant frequency motion, unlike the steep or mild slope.

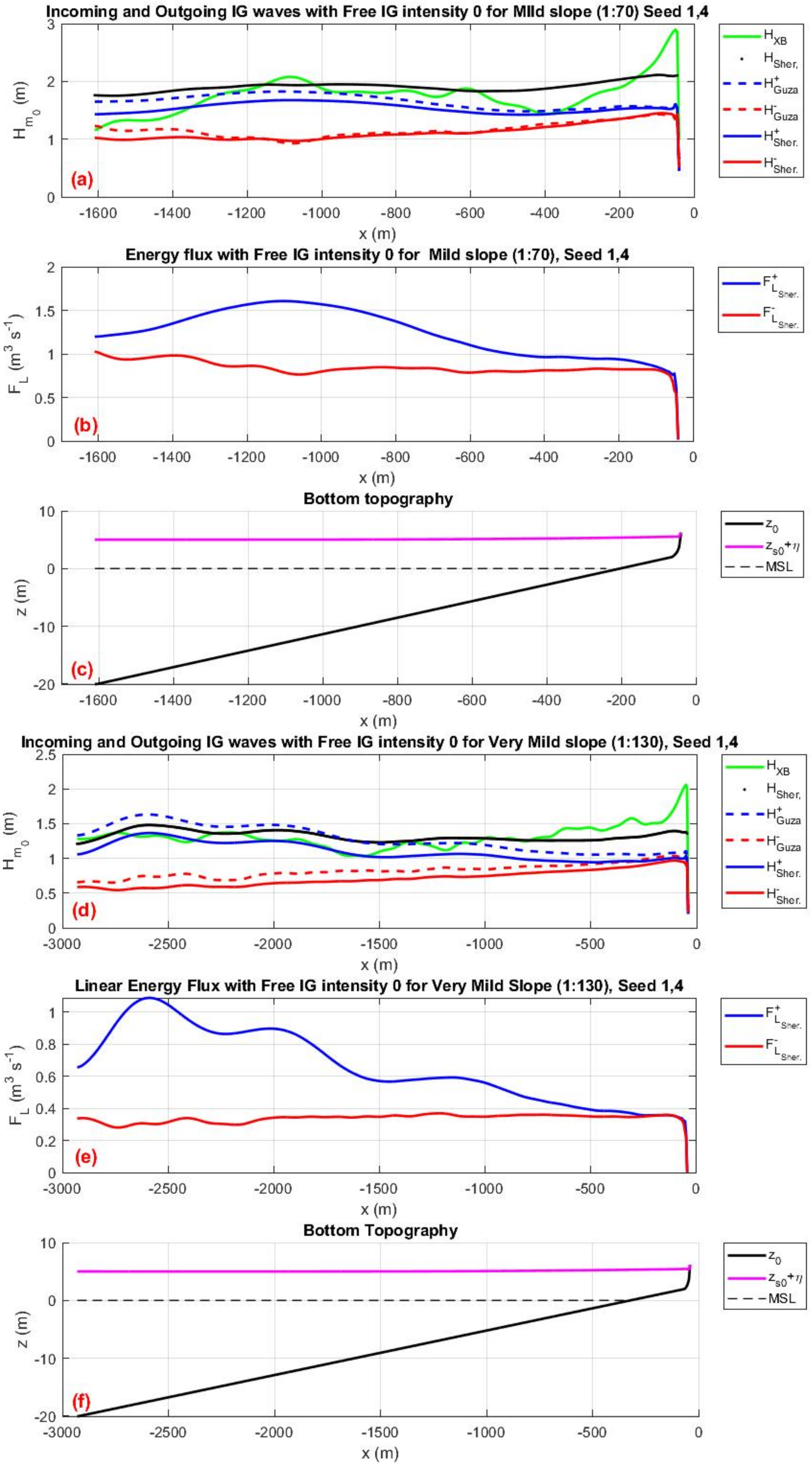

Figure 5.4: Wave domain for linear wave propagation for mild (a-c) and very mild slope (d-f). Where the significant wave height H_{m0} shown at (a) and (d), and energy flux illustrated (b) and (e). Where the total significant wave height is summarised by the neon green line (H_{XB}). The dotted black line is the total wave height corresponding to the total flux of Sheremet method $H_{Sher.}$. The blue lines show the incoming waves, and red line the outgoing waves. Sheremet et al. (2002) method is summarised with solid blue and red lines, whilst Guza et al. (1984) is dashed blue and red lines. (c) and (f) are the bottom topography of the mild (1:70) and very mild slope (1:130). For the bottom topography the sea bed z_0 is marked with solid black line is the MSL is marked with dashed black line, and the the water elevation marked with solid magenta line includes the surface elevation η, and surge level (z_{s0}).

For the very mild slope, the incoming significant wave height at Figure 5.4(d) is a lot higher at the offshore wave boundary with H^{+}_{Sher} of 1.065 m (at x = -2910 m), and gradually decreases after the initial local maxima formed at x = -2590 m. At Figure 5.4(d), the local maxima at x = -2590 m has a H^{+}_{Sher} of 1.37 m. The multiple local maxima observed however, are indicating that the magnitude of the F^{+}_{L} at Figure 5.4(e) reduces with each local maxima, resulting in the wave energy been dissipated and reduced from the wave domain. The breakpoint mechanism in the very mild slope is not as evident as it was in the steep and mild slope. Instead the triad interactions (Snl3) is what is what is potentially occurring creating these local maxima at the shoaling zone.

At the surf zone, the incoming energy flux has the same magnitude as the outgoing energy flux at Figure 5.4(e). This indicates at the nearshore we have mostly low frequency waves (infragravity and VLF waves) with little to no high frequency waves as the waves must have been mostly reduced. For Figure 5.4(d) the outgoing wave is fairly constant when propagating offshore. For the very mild slope, the breakpoint mechanism is not as defined as the mild or very mild slope, and instead its due to the triad interactions Snl3. The harder to define breakpoint mechanism is due to the multiple local maxima locations along the cross shore distance, reducing the wave energy released before reaching to the break zone, thus having considerably higher reduction in the wave height in comparison.

5.4. Non-Linear Wave Propagation

The non-linear wave propagation is assessed and compared with the linear wave propagation for steep (1:35), mild (1:70), and very mild (1:130) slope. For the non-linear wave propagation Battjes et al. (2004) method is used (equation (3.30)) which accounts for the infragravity wave response through the radiation stress S_{xx}. In addition to the radiation stress the roller momentum flux is also included as described by equation (3.34), therefore considered as a non-linear wave propagation. For the linear wave propagation, Sheremet et al. (2002) method is used when comparing it with the non-linear wave propagation.

Battjes et al. (2004) method is used for the incoming significant wave height H_{Batj} at Figure 5.5(a) for the steep slope (1:35), and at Figure 5.6(a)(d) for mild (1:70) and very mild (1:130) slope respectively indicated with a magenta line. Similarly, for the energy flux F_{Batj} Figure 5.5(b) is used for steep slope, and Figure 5.6(b)(e) for mild and very mild slope respectively. In addition, to identify the effect of the roller in our domain, the energy flux provides an insight for when there is no roller implemented $F_{Batj,nR}$ with a solid cyan line.

5.4.1. Steep Slope

For the steep slope (1:35), the non-linear wave contribution is expressed in the wave height H_{Batj} at Figure 5.5(a). The infragravity response reduces the significant wave height by 0.13 m at around the break point (at x = -480 m). As the incoming H_{Batj} wave propagates to the shore . The roller energy for the steep slope at Figure 5.6(b) showcases the inclusion F_{Batj} and exclusion $F_{Batj,nR}$ of the wave roller in the wave domain. The energy flux when waves break F_{Batj} is having a considerable contribution to the surf zone for this slope. Therefore, giving a wave height that is larger at the nearshore due to wave breaking and due to the roller energy flux contribution in the computational domain.

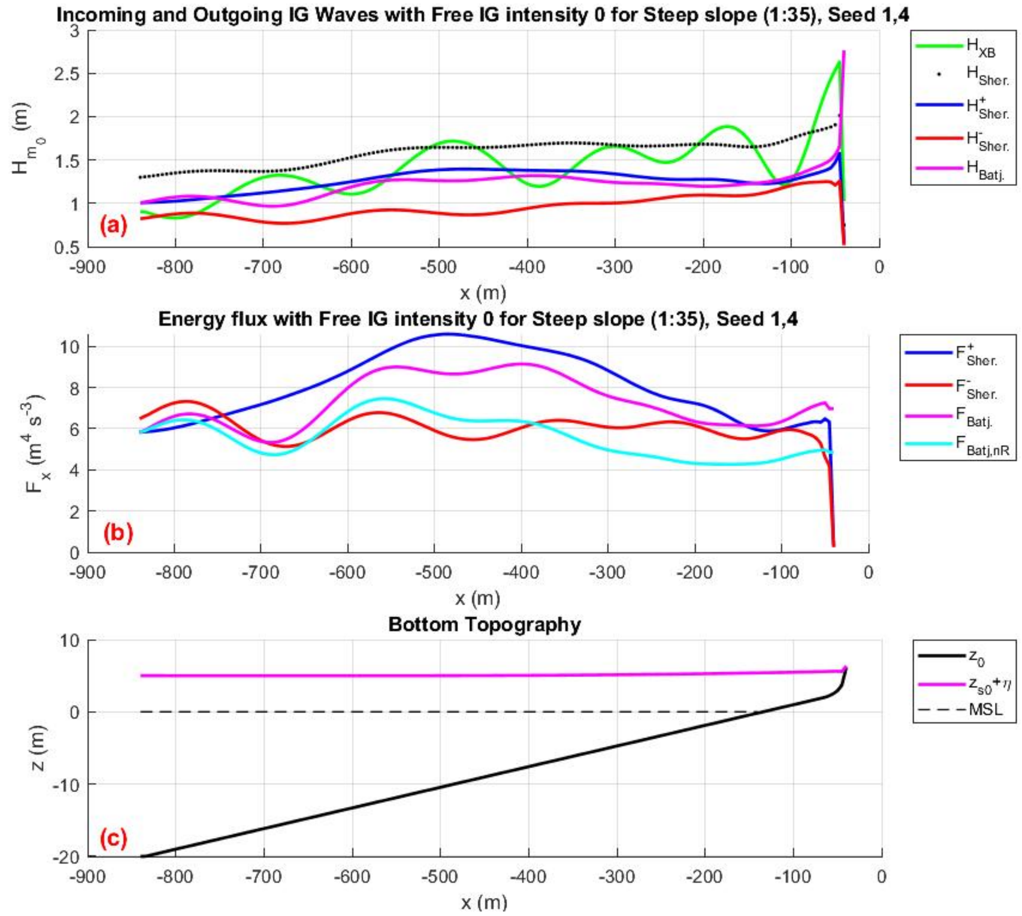

Figure 5.5: Incoming and outgoing (a) significant wave height H_{m0}), and (b) energy flux for the steep slope (1:35). Where the total significant wave height is summarised by the neon green line (H_{XB}. The dotted black line is the total wave height corresponding to the total flux of Sheremet method H_{Sher}. The blue lines show the incoming waves, and red line the outgoing waves. Sheremet et al. (2002) method is summarised with solid blue and red lines, whilst Guza et al. (1984) is dashed blue and red lines. (c) is the bottom topography of the steep slope (1:35) where the sea bed z_0 is marked with solid black line, dashed black line indicates the MSL and the magenta line is the water elevation which includes the surface elevation η, and surge level (z_{s0}).

5.4.2. Mild Slope

The non-linear wave propagation for the mild slope (1:70) is shown at Figure 5.6(a-c) through H_{Batj} (solid magenta line). As concluded in the linear wave propagation of the mild slope, the significant wave height H^+_{Sher} at Figure 5.6(a) propagates from offshore to nearshore with a big reduction in the wave height close to the breaker point (especially at $x = -900m$). In this case the wave height H_{Batj} reduces at around the breaker point up to the inner surf zone due to the radiation stress contribution. The same effect is observed in the energy flux for F_{Batj}, however there seems to be multiple local maxima before the break point located at $x = -900m$, following a pattern similar to the very mild slope F^-_{Sher} of the linear wave propagation case at Figure5.4(e).
The roller effect can be observed in Figure 5.6(b) through the difference between F_{Batj} and $F_{Batj,nR}$. The roller energy flux is seen to be present and affecting the wave domain at the break zone similarly to the mild slope situation, with a reduced magnitude, the roller is seen to be fairly constant from the breakpoint to the coastline with little effect at the swash zone.

In the surf zone, the mild slope wave height H_{Batj} reduces to magnitudes lower than the freely propagating H^-_{Sher}. The lower wave height at this region suggest that the wave height available is lower than the free infragravity wave. As a result, suggests potential dissipation of the infragravity waves at $x = -500m$ to $x = -40m$. However, since the water depth at $x = -500m$ is $h = 4.23m$ this is not realistic, as the infragravity waves breaking occurs at a few centimetres of depth.

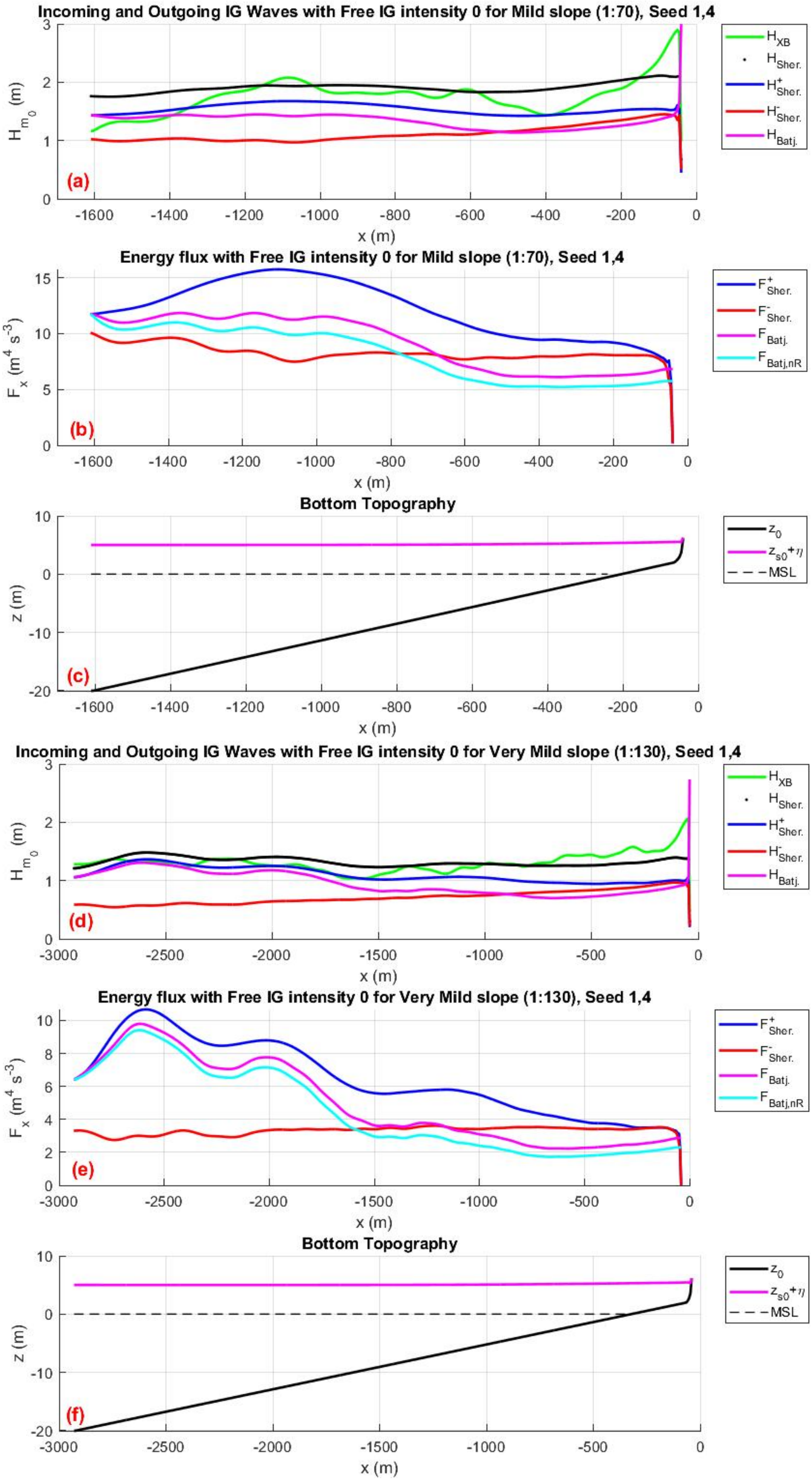

Figure 5.6: (Wave domain for linear wave propagation for mild (a-c) and very mild slope (d-f). Where the significant wave height H_{m0} shown at (a) and (d), and energy flux illustrated (b) and (e). Where the total significant wave height is summarised by the neon green line (H_{XB}). The dotted black line is the total wave height corresponding to the total flux of Sheremet method H_{Sher}. The blue lines show the incoming waves, and red line the outgoing waves. Sheremet et al. (2002) method is summarised with solid blue and red lines. Battjes et al. (2004) non-linear method for the incoming wave is marked with solid magenta line. (c) and (f) are the bottom topography of the mild (1:70) and very mild slope (1:130). For the bottom topography the sea bed z_0 is marked with solid black line,s the MSL is marked with dashed black line, and the the water elevation marked with solid magenta line includes the surface elevation η, and surge level (z_{s0}).

5.4.3. Very Mild Slope

For the very mild slope, the non-linear wave contribution H_{Batj} similarly to the linear wave contribution H^{+}_{Sher}, produce multiple local maxima at Figure 5.6(a). This effect is also captured for the energy flux contribution Figure 5.6(b), which both show (with reduced magnitude) that these maxima are still present. This phenomena is as mentioned in the linear wave propagation potentially due to the release of bound waves.

The difference between the linear energy flux F^{+}_{Sher} and non-linear energy flux F_{Batj} magnitude is not relatively large, with the exception when moving closer to the breaker point at $x = -1500m$ Figure 5.6(e). When moving closer to the break point the energy flux reduces considerably, and at x = -1500 m the energy flux reduces considerably. Similarly to the mild slope, at $x = -865m$ the significant wave height H_{Batj} reduces below the outgoing freely propagating infragravity wave H^{-}_{Sher}. This indicates that the incoming bound non-linear wave propagation at the nearshore has a wave height lower than the infragravity wave height present indicating potential infragravity wave dissipation.

Through the simulations for the non-linear wave propagation, it can be concluded that the linear wave propagate shows wave heights that are higher than their non-linear wave counterparts with the exception of the steep slope at the surf zone. The roller contribution is as expected, increasing the wave height in the domain especially at the breaker zone. The overall effect of the roller is more concentrated with a larger magnitude for steeper slopes due to higher wave energy breaking occurring. Whereas, for milder slopes the magnitude of the roller energy is lower and gradual therefore less instantaneous roller energy being released. For a better description of the roller energy contribution in the model domain refer to Appendix C of this report. The mild and very mild slope show that at the nearshore the non-linear (incoming) wave height H_{Batj} propagate at wave heights lower than the outgoing free infragravity H^{-}_{Sher}. This indicates that there is a dissipation for the incoming waves at the infragravity wave band, or that the outgoing waves are not following the same magnitude of reflection as they did when we include the non-linear wave response.

From what can be concluded however is that the wave height of the steep slope is the highest as noted by the runup ($R_{2\%}$ = 7.70 m), while the lowest is situated at the mild slope ($R_{2\%}$ = 6.82 m). The slope as a result show that there are different infragravity wave generation mechanisms, the breakpoint mechanism which is more pronounced for the steep and mild slope, whilst the release of the bound waves for the very mild slope.

5.5. Conclusion

For the computational domains to be used in a more realistic representation, a cut off frequency needs to be implemented for a computational model due to the computational artefact. However, the cut off frequency does not remove all the computational artefacts that can occur due to the arbitrary cross shore distance chosen for the model domain. This is evident through the second eigen mode being excited for the mild slope and fifth eigen mode for the steep slope as seen at Figure 5.2. The effects of these eigen modes are present in the standing wave pattern H_{XB} for the linear and non-linear wave propagation.

Sheremet et al. (2002) method shows a very good description for the linear wave propagation when compared to Guza et al.(1984). The difference between the two different linear wave propagation methods are not significant and since they both show similar information of the wave propagation, Sheremet et al. (2002) is preferred to be used due to the energy flux description it provides. From the linear wave propagation, the outgoing wave is seen to show a wave propagation similar to Green's law.

The break point is located at an approximate depth of 5.3 m for all the slopes obtained from the largest mean roller energy from Appendix F. Thus providing a fairly expected wave breaking location, however for mild and very mild slope, both have waves breaking throughout the wave domain with a more predominant wave breaker location as defined. For the steep and very mild slope the wave height is seen to be the highest close to the break point and at the coastline when interacting with the dune face. At the breaker point and the dune face, a well defined energy flux is indicated due to the wave breaking. For the very mild slope the wave breaking at the coastline is having little to no effect on the wave height or energy flux. In addition, for the very mild slope the waves are seen to experience multiple different wave height maxima prior to the breakpoint location. Through these multiple maxima reduced the wave height and the energy flux in the wave domain for the very mild slope and they can be assumed to be forced due to the triad interaction Snl3. The breakpoint mechanism is more pronounced for the steep, and mild slope due to the large defined peak at the breaker zone and the high magnitude of the outgoing wave at the offshore wave boundary.

With the inclusion of the non-linear wave propagation, the roller energy flux is seen to increase at the breaker zone. For steeper slope the roller contribution is increased at the breakpoint, whereas for milder slopes the roller energy is released gradually throughout the domain, and hence does not have as big effect as the steep slope has. Refer to Appendix C for the roller energy E_R in the wave domain for the three different slopes. The roller energy essentially provides additional energy to the wave domain through the creation of bores that propagating onshore, rather than dissipating the wave energy when the waves do break. The major effect of the non linear wave propagation from Battjes et al. (2004) is due to the radiation stress consideration. The radiation stress can be seen to show a reduce wave height and energy flux at the local maxima where the linear wave propagation showed the triad interaction oscilation effect.

For mild and very mild slope, at the nearshore the outgoing freely propagating infragravity wave H^{-}_{Sher} is having a significant wave height higher than the non-linear wave counterpart H_{Batj}. This can be potentially interpreted that the outgoing wave propagates at a wave height lower than what H^{-}_{Sher} describes, or that H_{Batj} does not fully describe the wave domain accurately for our model setup.

The runup $R_{2\%}$ values are considered at a 0.05 m depth, for all three slopes. As a result the highest runup is observed for the steep, mild and then very mild slope with $R_{2\%}$ of 7.70 m, 7.36 m, and 6.82 m respectively. The highest runup is observed at the steeper slope which is in line with the highest significant wave height observed in the linear and non-linear wave propagation thus solidifying the effect of the runup when the wave field is described by bound waves only.

Research Question 1: What is the effect of the computational randomness of the VLF wave hydrodynamics during a storm event?
The artificial resonance is not exclusively available at the VLF wave band where the first eigen mode is situated. Instead, a resonance is observed at the infragravity wave frequency wave band. As a result, can overestimate the runup, and wave heights, and therefore provide skewed results.

Research Question 4: What is the role of the infragravity and VLF waves response on the runup for different slopes?
For steep and mild slope the breakpoint mechanism is seen to be pronounced, affecting our results, whilst for very mild slope the release of bound waves at the shoaling zone. For steeper slopes high frequency infragravity waves are more pronounced whilst for milder slopes, low frequency infragravity waves are instead. Furthermore the significant wave heights and runup values both indicate that the steep slope shows the largest response, whilst the lowest for the very mild slope.

6

Free Infragravity Waves

In this chapter free infragravity waves are induced during a storm at the offshore wave boundary in addition to the bound waves as seen from the previous chapter, Chapter 5. The free infragravity waves induced at the offshore wave boundary have different intensities (which equate to magnitudes) that highlight the effect of free infragravity waves on dune coastal safety. The runup is obtained for the different free infragravity conditions and slopes, where it is considered with the wave hydrodynamics for an assessment of the additional free infragravity waves effect dune coastal safety.

6.1. Introduction

The effect of the additional free infragravity waves can have significant effects in dune coastal safety during a storm (Daouk, 2020). To assess their effect, free infragravity waves are added at the offshore wave boundary with different intensities in addition to the bound waves $IG_{free} = 0$ as was seen in previous chapter, chapter 5.3. The runup $R_{2\%}$ is then obtained for the steep (1:35), mild (1:70), and very mild (1:130) slope, where it allows us to assess the coastal safety of the dunes during a storm. For a better insight on the runup results, the wave domain is then assessed through the mean wave period T_{m01}, and the linear and non-linear wave propagation of the wave from offshore to the nearshore for a better insight on the runup values obtained.

To assess the effect of free infragravity waves on dune coastal safety different waves are induced at the offshore wave boundary of (1) bound waves condition only $IG_{free} = 0$ as seen in chapter 5, the additional free infragravity waves induced at 2 different magnitudes with the bound waves included are (2) $IG_{free} = 1$, and (3) $IG_{free} = 2$. For the situation of only infragravity waves present and with no bound waves (or any sea-swell waves) present (4) $IG_{only} = 2$, and (5) $IG_{only} = 2$ are used. As described in Table 3.2, the free infragravity wave intensity of 1 for $IG_{only} = 1$ (and $IG_{free} = 1$) translates to separate free infragravity waves with a magnitude of 1, and $IG_{only} = 2$ (and $IG_{free} = 2$) for separate free infragravity waves with a magnitude of 2. The free infragravity waves are obtained from the random phase model as seen at equation (3.18). The infragravity waves present in the bound waves during our storm simulation ($IG_{free} = 0$) are added separately at the offshore wave boundary with a factor of 1 (or 2) for a magnitude of the same (or double) of the infragravity waves present in the bound wave field during our storm simulation. The free infragravity waves are as a result induced at the offshore wave boundary and are forced, therefore constructed in the random phase model with a different seed number to the bound waves (bound waves seed number is 1 as used in Chapter 5). Therefore, the random seed number used is different from the bound waves forced in order to avoid the waves phase locking. As a result, the random seed number used for the free infragravity waves is seed number 4. As long as the seed number does not exhibit any resonance that can be cut off (VLF frequency) as observed from chapter 4.4.2, then the seed number of choice should not affect our results creating avoidable computational artefacts.

The different slopes to be considered in this section, (1) steep (1:35), (2) mild (1:70), and (3) very mild slope (1:130) are compared and analysed for each free infragravity wave intensity. The wave conditions of both the bound and additional free infragravity are both assumed to be propagating as a bound wave, therefore following equation (3.25) and equation (3.32) respectively. The reason for the waves being assumed as bounded is that the waves will theoretically act as freely propagating infragravity waves at shallow water.

For the dune coastal safety, the runup $R_{2\%}$ is first assessed following raw data cumulative distribution function $F_{data}(x)$ as further indicated at Appendix E. The runup is then observed using different free infragravity intensities to see the impact on the dunes. In order to understand the effect on the dunes the mean wave period T_{m01} is also obtained from equation (3.48). As conducted in the last chapter the runup values are compared with the linear wave propagation, and non-linear wave propagation to have a better insight on the runup values obtained. The linear wave propagation is described as concluded in the last chapter 5 through Sheremet et al. (2002) method, and non-linear wave propagation through Battjes et al. (2004). As a result, the runup and wave propagation description is obtained for the different wave conditions induced at the offshore wave boundary for 1) steep (1:35), 2) mild (1:70), and 3) very mild (1:130) slope. Lastly, the break point locations and the roller energy is described in more detail in Appendix F for all the different slopes.

6.2. Runup

The dune coastal safety can be assessed through the use of the 98^{th} percentile runup $R_{2\%}$ as describe by Stockdon et al. (2006) and in more detail in Appendix E of this report. The $R_{2\%}$ is obtained for the different slopes, and different wave conditions induced at the offshore wave boundary. The wave conditions induced at the offshore wave boundary is the (1) $IG_{free} = 0$, (2) $IG_{free} = 1$, (3) $IG_{free} = 3$, (4) $IG_{only} = 1$, and (5) $IG_{only} = 2$. The $IG_{free} = 0$, $IG_{free} = 1$, and $IG_{free} = 2$ show the wave domain with bound waves, whereas $IG_{only} = 1$, and $IG_{only} = 2$ are only infragravity waves present. The additional free infragravity waves have a multiplier of 0, 1, and 2 for the additional free infragravity waves at the offshore wave boundary. As a result, the runup $R_{2\%}$ is calculated for the different slopes and different wave combinations present. For a better insight of the results, the mean wave period T_{m01} is also obtained for each wave condition and slope to understand the nature of the waves that are dominant in the wave field.

The runup $R_{2\%}$, and mean wave period T_{m01} of the three different slopes, are described at Figure 6.1), and Figure 6.1 respectively with their values summarised at Table 6.1. For the $R_{2\%}$ at Figure 6.1(a) it is clearly evident that the $R_{2\%}$ is highest for the wave domain with more waves present, and bound waves included, therefore $IG_{free} = 2$ has the largest $R_{2\%}$. Higher $R_{2\%}$ is expected for a computational domain with more waves being present and can increase its magnitude. A certain pattern is also observed at Figure 6.1(a) for the different slopes, the mild slope exhibit on average the highest runup values for both IG_{free} and IG_{only} conditions at the offshore wave boundary, whereas the very mild slope exhibits on average the lowest. In contrast, the steep slope as observed in chapter 5 of this report, the $IG_{free} = 0$ exhibits the highest runup value. This can be potentially linked due to the different seed number used, seed number 4 when introducing the free infragravity waves at the offshore wave boundary.

Slope	**Waves Induced**	**Runup**, $R_{2\%}$ (m)	**Mean Wave period**, T_{m01} (s)
Steep (1:35)	$IG_{free} = 0$	***7.70***	28.6
	$IG_{free} = 1$	***7.96***	31.0
	$IG_{free} = 2$	***8.08***	32.0
	$IG_{only} = 1$	***6.65***	46.1
	$IG_{only} = 2$	***7.41***	44.5
Mild (1:70)	$IG_{free} = 0$	***7.36***	56.5
	$IG_{free} = 1$	***8.08***	51.1
	$IG_{free} = 2$	***8.45***	48.5
	$IG_{only} = 1$	***6.83***	47.9
	$IG_{only} = 2$	***7.58***	48.5
Very Mild (1:130)	$IG_{free} = 0$	***6.82***	75.7
	$IG_{free} = 1$	***7.37***	54.1
	$IG_{free} = 2$	***7.74***	51.2
	$IG_{only} = 1$	***6.50***	39.1
	$IG_{only} = 2$	***6.73***	42.2

Table 6.1: The wave runup $R_{2\%}$ and mean wave period T_{m01} for different slopes and waves induced at the offshore boundary boundary. The different slopes used include the steep (1:35), mild (1:70), and very mild (1:130) slope. Thd wave conditions induced, include the bound waves with free infragravity waves IG_{free}, and only free infragravity waves IG_{only}. The subscript includes a number of 0, 1, and 2, that describe the free infragravity magnitude present in the wave domain.

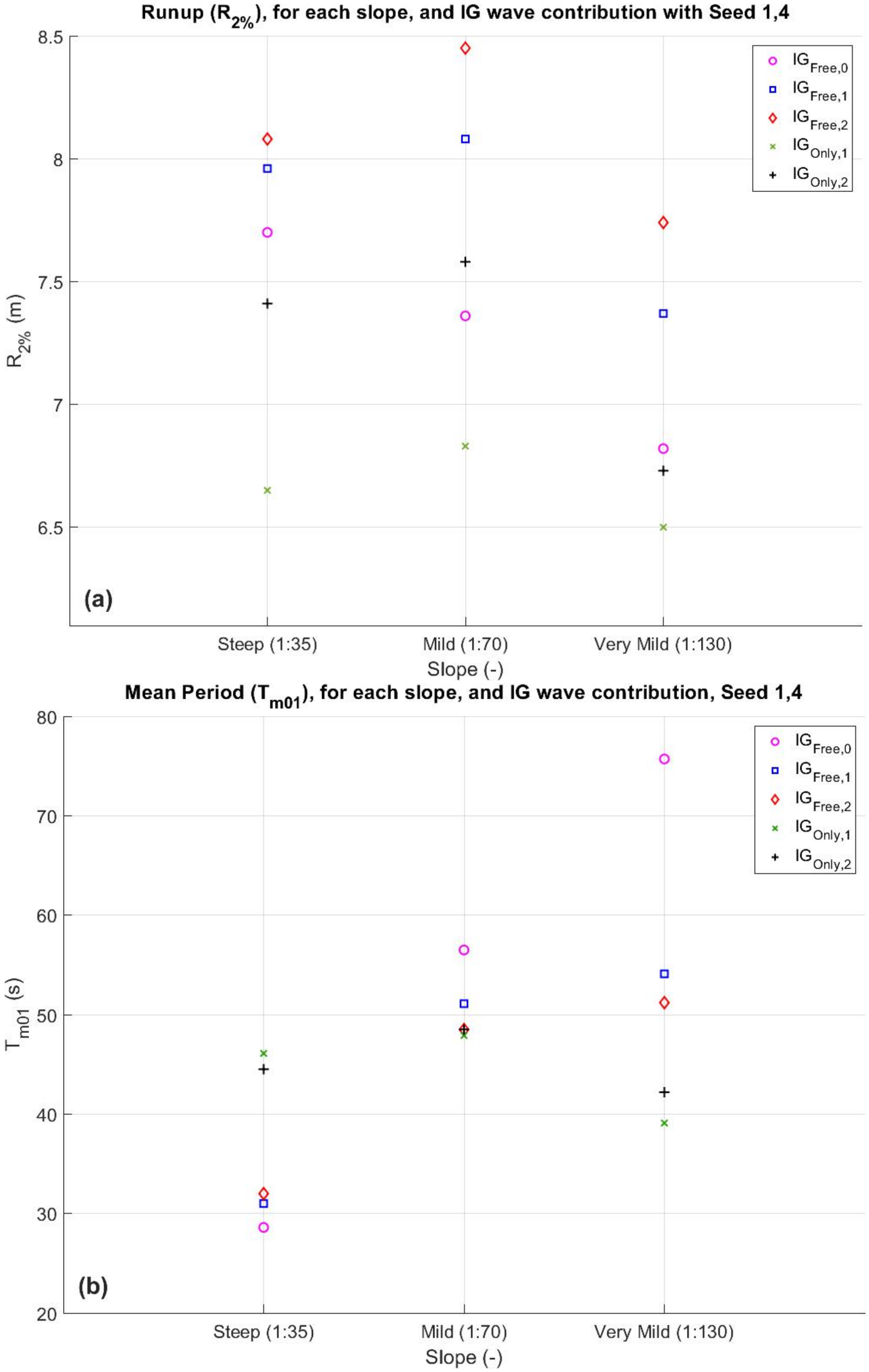

Figure 6.1: (The (a) runup $R_{2\%}$, and (b) mean wave period T_{m01} for different slops, and wave conditions induced at the offshore wave boundary. The values of this graph are summarised at Table 6.1. The different slopes used include the steep (1:35), mild (1:70), and very mild (1:130) slope. Th wave conditions induced, include the bound waves with free infragravity waves IG_{free}, and only free infragravity waves IG_{only}. The subscript includes a number of 0, 1, and 2, that describe the free infragravity magnitude present in the wave domain. These include (1) $IG_{free} = 0$ marked with circular magenta symbol, (2) $IG_{free} = 1$ with blue square symbol, (3) $IG_{free} = 2$ with red diamond symbol, (4) $IG_{only} = 1$ with green cross symbol, and (5) $IG_{only} = 2$ with a black plus symbol.

The bound waves only case $IG_{free} = 0$ suggests at Figure 6.1 that with the addition of the free infragravity waves the mild the slope, exhibits the highest runup va;ue. whereas, the for a closer $R_{2\%}$ to that of bound waves only case $IG_{free} = 0$. The effect of the runup is as can be seen, of a similar magnitude of the very mild slope for $IG_{free} = 0$ and $IG_{only} = 2$ that exhibit a very similar $R_{2\%}$ magnitude of 6.82 m and 6.50 m respectively. The runup $R_{2\%}$ from IG_{only} conditions with the addition of $IG_{free} = 0$ (bound waves only) cannot sum up to $IG_{free} = 1$ or $IG_{free} = 2$. Therefore for the effect of the additional free infragravity waves that can present as described by Daouk (2020) have to be simulated with the bound wave conditions during the storm simulation in order to effectively capture the free infragravity wave effect on coastal dune safety.

The mean wave period T_{m01} can be used for a better insight on the most prominent type of waves present. The steep slope at Figure 6.1(b) show T_{m01} of the bound waves been more closely affected by higher frequency waves, whilst the mild and very mild slope show that the contribution of free infragravity waves cause shorter wave period waves. The mild slope T_{m01} show a very similar wave period for the different wave conditions, therefore indicating that the waves present in the wave field have a relatively consistent frequency. Overall, 6.1(b) show that for all slopes the additional free infragravity waves are forcing our computational model at frequencies closer to $T_{m01} = 50s$ ($f = 0.02Hz$) which can affect our $R_{2\%}$ results.

For only the free infragravity wave conditions IG_{only} indicate that the runup $R_{2\%}$ cannot be linearly added for the same storm conditions with the bound waves only $IG_{free} = 0$ case to achieve the wave field as described by $IG_{free} = 1$ or $IG_{free} = 2$. In addition, the difference in the wave period T_{m01} can be potentially linked to the different seed numbers used in the random phase model. Therefore, inducing different mean frequency bands that are present and as a result dominating our computational domain. For a better understanding of the wave field and the dominance of the waves the waves are simulated from offshore to nearshore for the linear, and non-linear wave propagation of the wave field. In addition, wave spectra analysis is used to explain the wave harmonics and the effect of potential resonance in our domain for a better insight of the wave propagation effect, therefore on the runup $R_{2\%}$.

6.3. Spectral Analysis

In this section the spectral analysis of the wave domain will be explored to give a better insight to the runup $R_{2\%}$ values obtained. The T_{m01} values obtained indicated that potentially the seed number 4 used for the additional free infragravity waves is situated with a wave period similar to $T_{m01} = 50s$ as seen in Figure 6.1(b) for the IG_{only} variables. In addition, the steep and mild slope showed a very similar runup $R_{2\%}$ magnitude for the same IG_{free} case Figure 6.1(a). Therefore the mild slope is suspected for a resonance harmonic excitation, which as a result show a higher runup $R_{2\%}$ magnitude to the steep slope for the additional free infragravity signal as indicated in Table 6.1, and Figure 6.1(a).

The surface elevation variance density spectra $E(f)$ of steep slope Figure 6.2(a) show that with the additional IG_{free} intensities, the surface elevation $E(f)$ magnitude varies at higher frequency and lower frequencies. The $E(f)$ peak located at Figure 6.2(a) as also noted in the previous chapter 5 at the higher infragravity frequency near $f_{eigen,5}$ (of $f = 0.0283Hz$), reduces with each consecutive IG_{free} intensity added. In contrast to the $f_{eigen,5}$ the $E(f)$ magnitude at lower infragravity frequencies is observed to increase instead with each consecutive IG_{free} magnitude. As a result, there is a higher $E(f)$ magnitude, forming a peak at frequency of $f = 0.0094Hz$, and $f = 0.0283Hz$. Both $f = 0.0094Hz$, and $f = 0.0283Hz$ are illustrated at Figure 6.3(a-c), and Figure 6.3(d-f) respectively for the surface elevation, cross shore velocity, and phase for the whole cross shore distance. The IG_{LF} signal ($f = 0.0093Hz$) at Figure 6.3(a) interacts with the second eigen mode ($f_{eigen,2}$ = 0.0096 Hz), causing the surface elevation $E(f)$ to increase to a magnitude of $104m^2/Hz$ when comparing the bound waves $IG_{free} = 0$ to the $IG_{free} = 2$. For the peak observed at the fifth eigen mode ($f_{eigen,5}$ = 0.0283 Hz) Figure 6.3(d), the magnitude of the surface elevation $E(f)$ reduces by 94 m^2/Hz from the bound only wave case $IG_{free} = 0$ in comparison from the additional infragravity waves $IG_{free} = 2$.

The magnitude of the surface elevation $E(f)$ for the lower frequency infragravity waves at Figure 6.3(a) increases with each consecutive IG_{free} due to the additional IG waves are propagating at a higher infragravity frequency due to the wave forcing occurring form the seed number 4. The surface elevation $E(f)$ response at f = 0.0283 at Figure 6.3(d) is initially high for IG_{free} = 0, with a magnitude of 200 m^2/Hz

$IG_{free} = 0$, however, for $IG_{free} = 2$ the $E(f)$ magnitude is halved. This indicates that the wave field is potentially indicates that the higher infragravity waves are not as dominant as the bound only wave case, and therefore have a reduced effect. It can be concluded that the more dominant wave infragravity response from the additional free infragravity waves are seen is located at the second eigen mode with a $E(f)$ magnitude of 104 m^2/Hz.

The response observed here is as indicated in the T_{m01} response of Figure 6.1(b). The waves at the steep slope show a response closer to a T_{m01} of 30s. Therefore, confirming that the waves in the steep slope are more dominant on the lower infragravity frequencies rather than due to the higher infragravity frequencies that the bound waves only case ($IG_{free} = 0$) initially had. A potential source of the additional forcing and enhancement at the lower infragravity frequencies can be potentially linked due to the forcing of the additional free infragravity waves produced from the different seed number used, seed number 4.

For the mild slope, the same spectral analysis is conducted as located at Figure 6.4(a-e). The second eigen mode $f_{eigen,2} = 0.005Hz$ is affecting the wave domain considerably Figure 6.4(a) where with additional IG_{free} intensities the $E(f)$ response is more reactive. The magnitude of the surface elevation $E(f)$ at Figure 6.4(c) is of a maximum magnitude of 342 m^2/Hz. In this case the $IG_{free} = 2$ shows an increase by a factor of 1.61 (increased by 130 m^2/Hz) when compared to the bound waves only case $IG_{free} = 0$. This large response of $E(f)$ at the $f_{eigen,2} = 0.005Hz$ is assumed to be due to resonance as it also experience an episodic event as seen at Appendix G. The same can effect linking resonance can also be concluded due to the larger $R_{2\%}$ observed from the additional free infragravity waves at Figure 6.1(a) from the bound waves case.

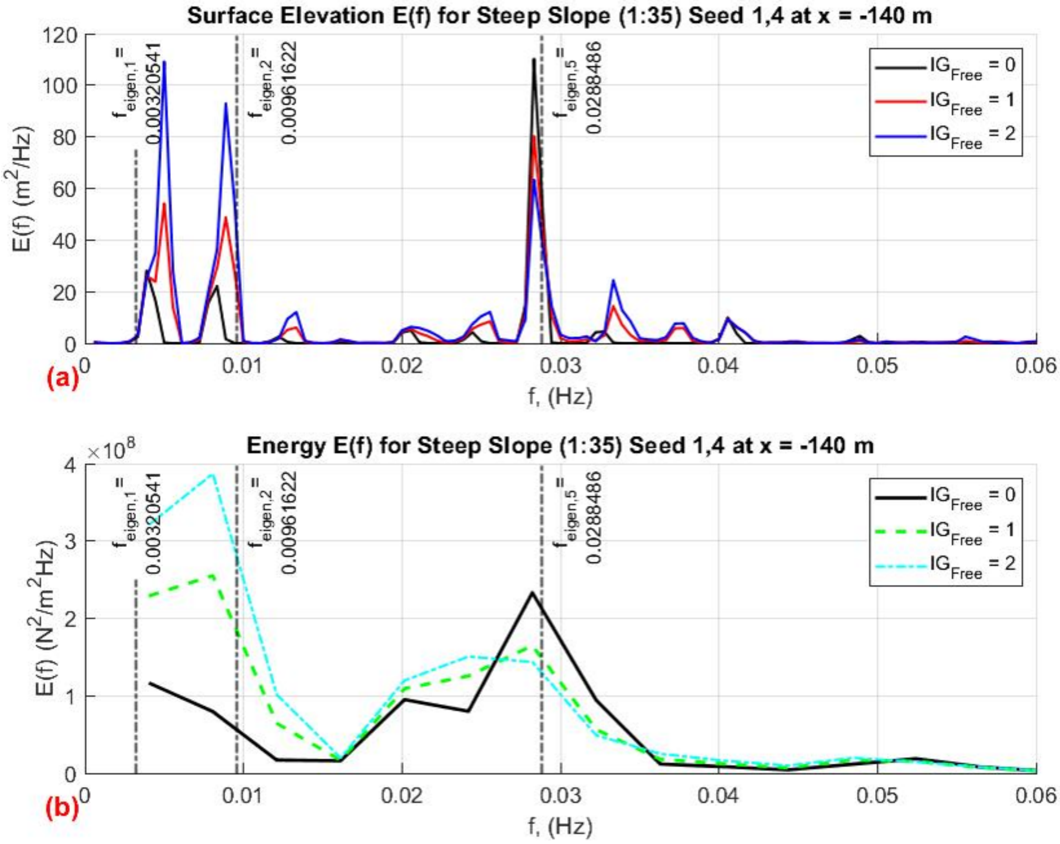

Figure 6.2: (a) surface elevation $E(f)$, and (b) Wave energy $E(f)$ at an arbitrary location of x = -140 m for the steep slope (1:35). The black solid line defines the free infragravity intensity of 0 $IG_{free} = 0$, the red and green line the $IG_{free} = 1$ with the blue and cyan line for $IG_{free} = 2$. The first second and fifth eigen modes are all shown in the wave domain with a dash-dotted black line.

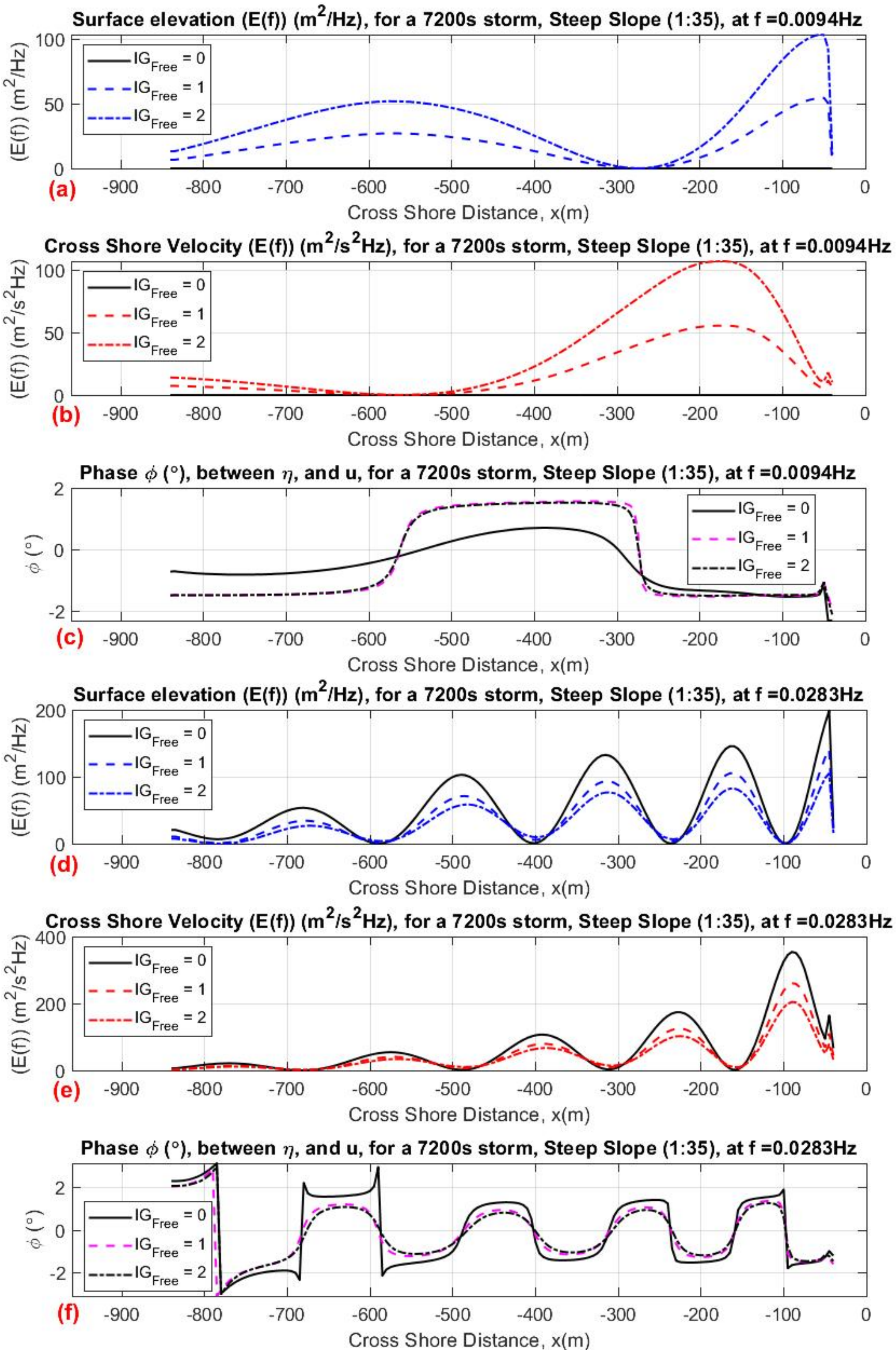

Figure 6.3: Wave spectra response of the steep slope [(a)-(c)] at the second eigen mode $f_{eigne,2} = 0.0283$, and [(d)-(f)] at the fifth eigen mode $f_{eigne,2} = 0.0094$ for three different free infragravity intensities IG_{free}. Where the (a)(d) the surface elevation $E(f)$, (b)(e) cross shore velocity $E(f)$, and (c)(f) the phase between the surface elevation and cross shore velocity is obtained. Where the solid line is for the free infragravity intensity of 0, $IG_{free} = 0$, the dashed line is for the $IG_{free} = 1$, and for the dash-dotted line for the $IG_{free} = 2$.

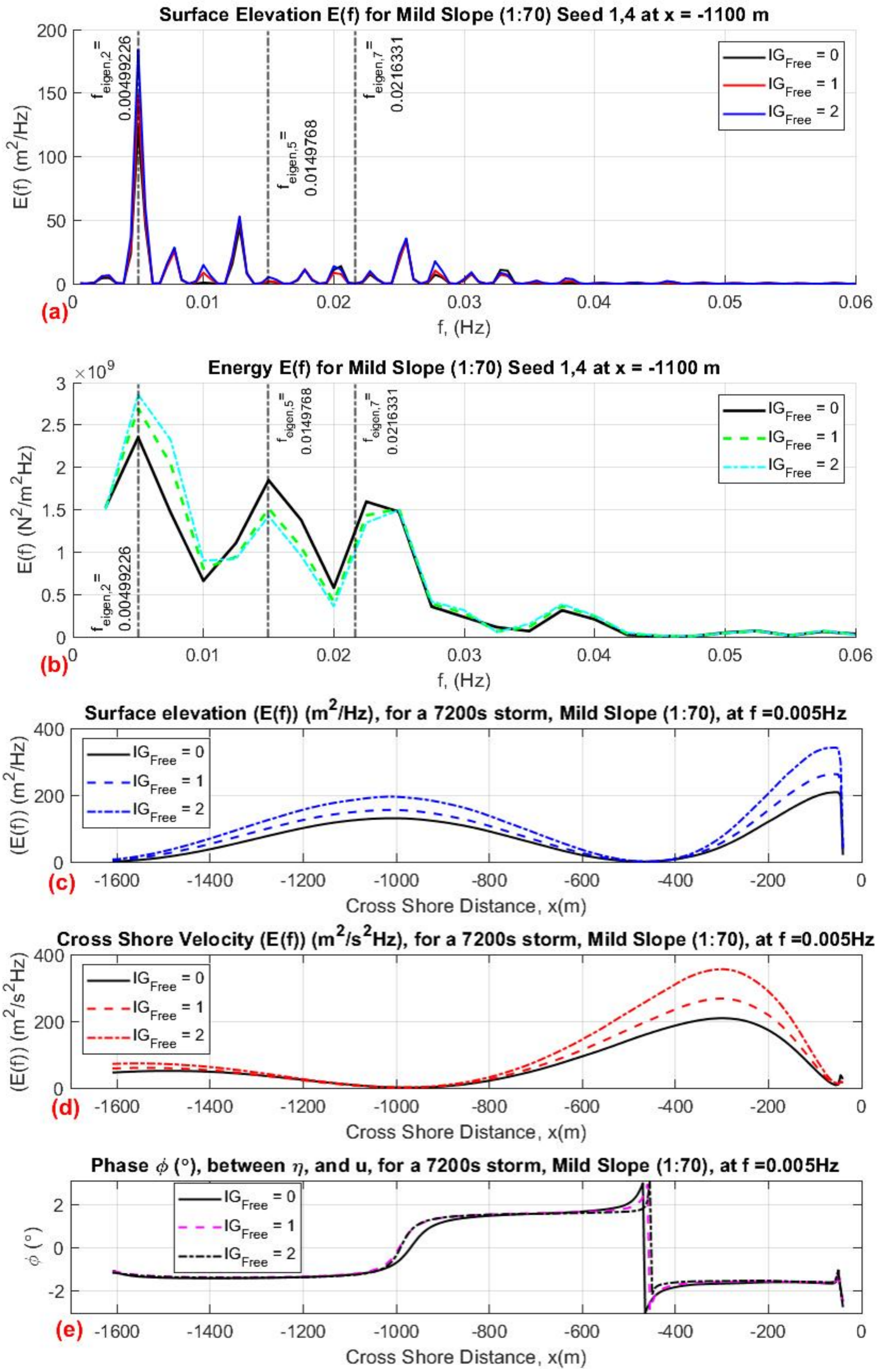

Figure 6.4: Different variance density spectra for the mild slope (1:70). (a) Surface elevation $E(f)$ at x = -1100, (b) Wave energy $E(f)$ at x = -1100, (c) Surface elevation $E(f)$ at f = 0.005Hz, (d) Cross shore velocity $E(f)$ at f = 0.005Hz, and (e) the phase between the surface elevation and cross shore velocity at f = 0.005Hz for IG_{free} = 0, IG_{free} = 1, and IG_{free} = 2. The second, fifth, and seventh eigen modes are all shown in the wave domain with a dash-dotted black line.

For the very mild slope, the wave spectra is conducted at the surf zone, at x = -1100 as shown at Figure 6.5. From the very mild slope, there is no pronounced response from the surface elevation $E(f)$ with a large magnitude or any considerable eigen mode interaction. This however is expected, given that the runup $R_{2\%}$ response at Figure 6.1(a) when compared to the steep and mild slope show a considerably lower runup effect for each different runup response.

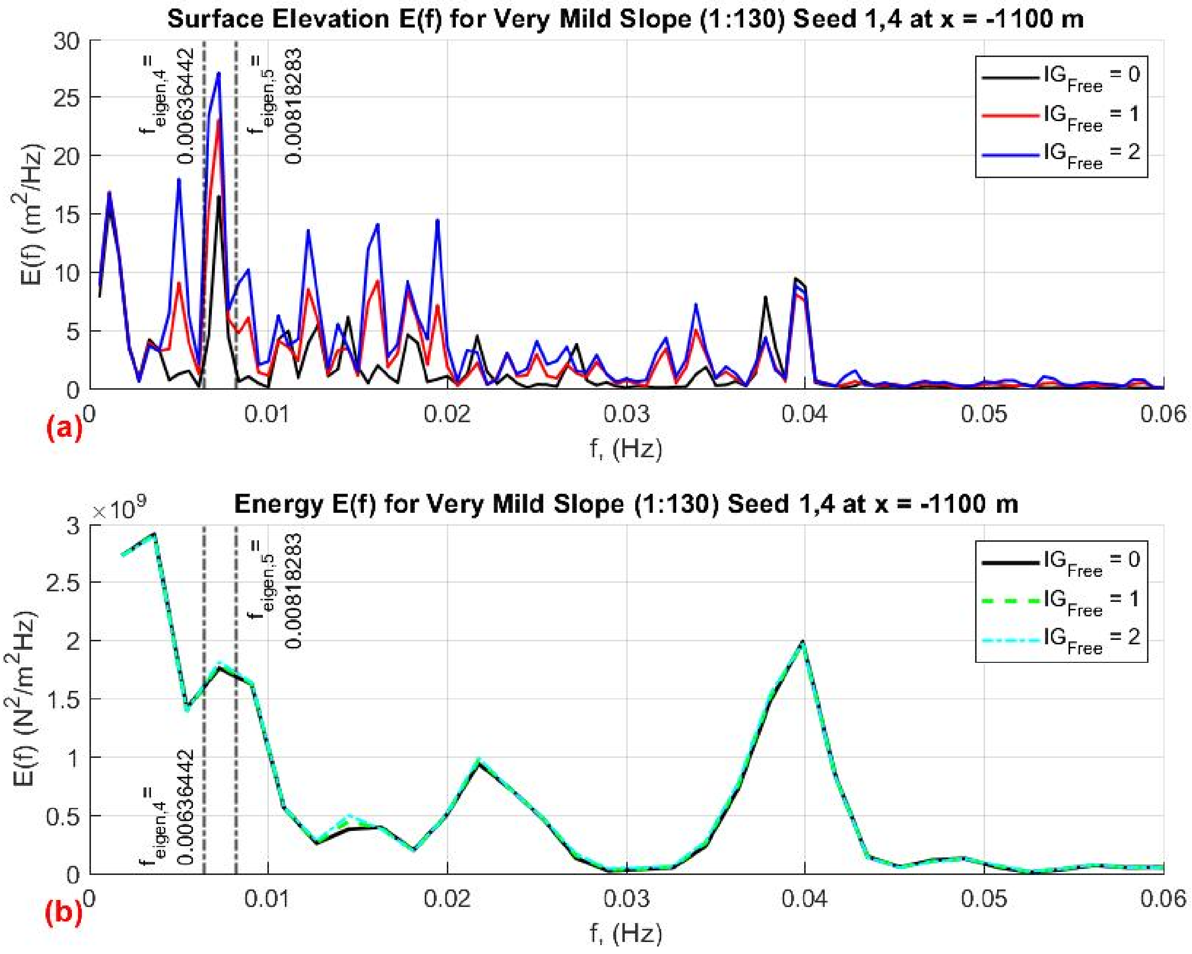

Figure 6.5: (a) Surface elevation $E(f)$, and (b) Wave energy $E(f)$ at an arbitrary location of x = -1100 m for the very mild slope (1:130). The black solid line defines the free infragravity intensity of 0 $IG_{free} = 0$, the red and green line the $IG_{free} = 1$ with the blue and cyan line for $IG_{free} = 2$. The first second and fifth eigen modes are all shown in the wave domain with a dash-dotted black line.

The wave spectra response are seen to favour the lower infragravity frequencies with each consecutive additional free infragravity intensity. As a result, the mild slope $E(f)$ magnitude is becoming more and more pronounced at the $f_{eigen,2} = 0.005Hz$. A similar pattern can be observed from the runup values $R_{2\%}$ that confirmed this observed response as illustrated at Figure 6.1(a). The higher pronounced response at the mild, can be attributed to resonance effect, given that it causes such a large magnitude from the $E(f)$. The resonance effect is more pronounced for the mild slope therefore showing a considerably larger response for the runup at Figure 6.1(a). In contrast, steep, and very mild slope exhibit no resonance response in the $E(f)$ which is consistent from what is observed in the runup values at Figure 6.1(a).

6.4. Infragravity Wave Dynamics

For this section the offshore wave boundary is induced with free infragravity waves of intensity of 1 $IG_{Free} = 1$ and free infragravity intensity of 2 $IG_{free=2}$ and compared to the bound waves only case $IG_{free} = 0$. For consistency the bound waves for all different slopes are induced with a seed number of 1 as we concluded and used in chapter 5, while the additional free infragravity waves $IG_{free} = 1, IG_{free} = 2$ are induced with a seed number of 4. The different IG_{free} cases are analysed and compared with one another for the steep, mild, and very mild slope through the linear and non-linear wave propagation of the waves for a better insight for the runup $R_{2\%}$, and therefore the dune coastal safety.

The steep slope Figure 6.8(a-c), mild slope Figure 6.10(a-c), and very mild slope Figure 6.12(a-c) are indicating the $IG_{free} = 0$, $IG_{free} = 1$, and $IG_{free} = 2$ scenarios with red, blue, and black coloured lines respectively. In addition, for the respective colour lines mentioned the line type defines different wave propagation. The dot-dashed line indicates the incoming linear wave propagation H^{+}_{Sher} (or F^{+}_{Sher}), and the dashed line the outgoing linear wave propagation H^{-}_{Sher} (or F^{-}_{Sher}). Whereas, the solid line describe the non-linear wave propagation H_{Batj}. Lastly, the standing wave pattern is illustrated through the significant wave height obtained from the spectral analysis H_{XB} with a dotted line. To identify each variable correctly without any confusion a subscript is also added. The subscript defines the slope and the free infragravity intensity, for instance, $H_{XB,s1}$ defines the total spectral significant wave height for a steep slope with $IGfree = 1$. For the individual slope and corresponding IG_{free} intensity for the linear wave propagation refer at Appendix D, and for the non-linear wave contribution at Appendix C.

6.4.1. Steep Slope (1:35)

For the steep slope (1:35) the spectral significant wave height H_{XB} at Figure 6.6(a) showcase that there is a large influence of the higher infragravity waves present for $IG_{free} = 0$ due to the more oscillations present in the model domain (red dotted line). However, at Figure 6.6 when adding additional free IG waves ($IG_{free} = 1$ blue dotted line, and $IG_{free} = 2$ black dotted line) H_{XB} increases, and the standing wave pattern has a closer resemblance to lower IG wave frequencies, which is in line with what is seen for the spectral analysis at Figure 6.2(a), and the wave period T_{m01} at Figure 6.1(b).

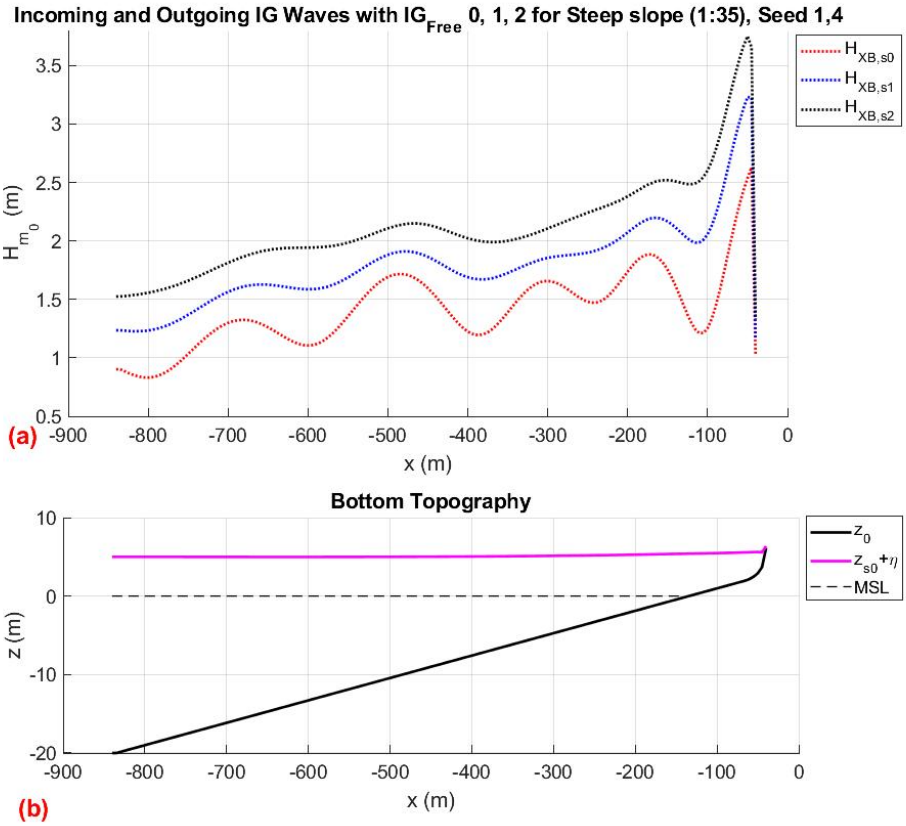

Figure 6.6: The linear and non liner wave contribution for (a) the significant wave height for the steep slope (1:35). The free infragravity intensities are coloured, red for $IG_{free} = 0$, blue for $IG_{free} = 1$, and black for $IG_{free} = 2$. The total spectral wave height H_{XB} is denoted with a dashed line. (b) The bottom topography for the steep slope (1:35), where the sea bed z_0 is marked with solid black lines, the MSL is marked with dashed black line, and the the water elevation marked with solid magenta line includes the surface elevation η, and surge level (z_{s0}).

As concluded previously both $H_{XB,s1}$ and $H_{XB,s2}$ standing wave pattern are influenced more by lower free infragravity waves as these are forced with different intensities at the offshore wave boundary. At Figure 6.6(a) $H_{XB,s2}$ has an overall higher significant wave height with a maximum of $H_{XB,s2} = 3.75m$), followed by $H_{XB,s1} = 3.23m$, and then $H_{XB,s0} = 2.63m$ located at he coastline $x = -50m$. As a result, the added free infragravity significant waves height increase the total significant wave height H_{XB} by $\approx 0.55m$ with each additional consecutive IG_{free} intensity.

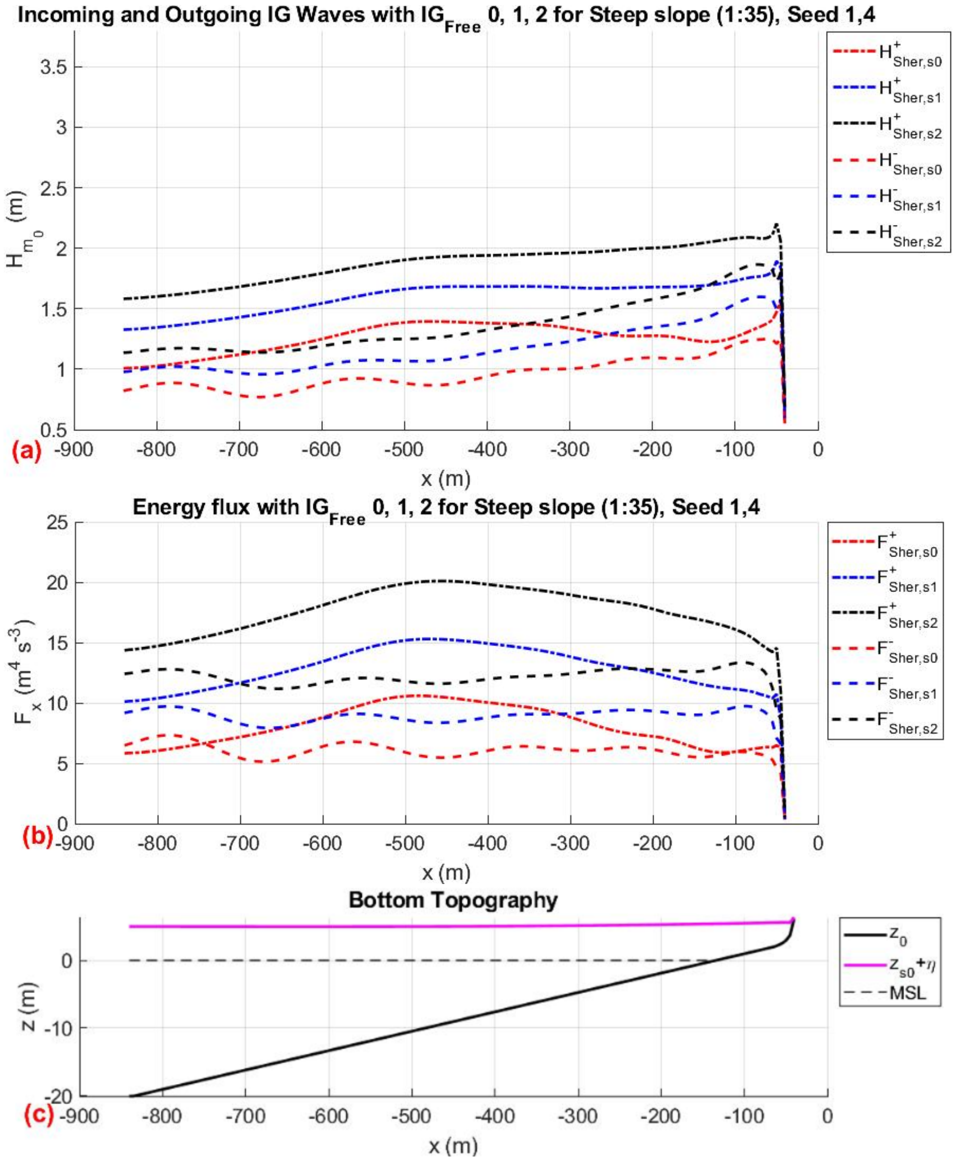

Figure 6.7: The linear and non liner wave contribution for (a) the significant wave height, (b) the energy flux for the steep slope (1:35). The free infragravity intensities are coloured, red for $IG_{free} = 0$, blue for $IG_{free} = 1$, and black for $IG_{free} = 2$. The total spectral wave height H_{XB} is denoted with a dashed line, the significant wave height $H_{m}0$ and energy flux F_x, from Sheremet et al. (2002) (subscript Sher) for incoming, and outgoing wave denoted with dashed-dot, and dashed line respectively. (c) The bottom topography for the steep slope (1:35), where the sea bed z_0 is marked with solid black lines, the MSL is marked with dashed black line, and the the water elevation marked with solid magenta line includes the surface elevation η, and surge level (z_{s0}).

The incoming (dotted-dashed), and outgoing (dashed) waves for the linear wave propagation are all summarised at Figure 6.7 for the significant wave height H_{m0}, and the energy flux F_x response. The incoming H^{+}_{Sher} and outgoing H^{-}_{Sher} are both increasing with each added free IG wave. The incoming wave height magnitude $H^{+}_{Sher,s2}$ at Figure 6.7(a) shows a larger H_{m0} response in the surf zone, than the bound wave only case $H^{+}_{Sher,s0}$. This increase can be attributed to the increase of IG waves present in the domain and the wave frequency are more dominant at the low IG waves. Therefore, it can be concluded that the wave domain is saturated with (lower) IG waves that even after the break point located at x = 500 m Figure 6.7(b) the wave height is still increasing Figure 6.7(a). The breakpoint mechanism observed due to the increase in outgoing wave height H^{-}_{Sher} at the offshore wave boundary of Figure 6.7(a) is still present even with the additional free IG waves present.

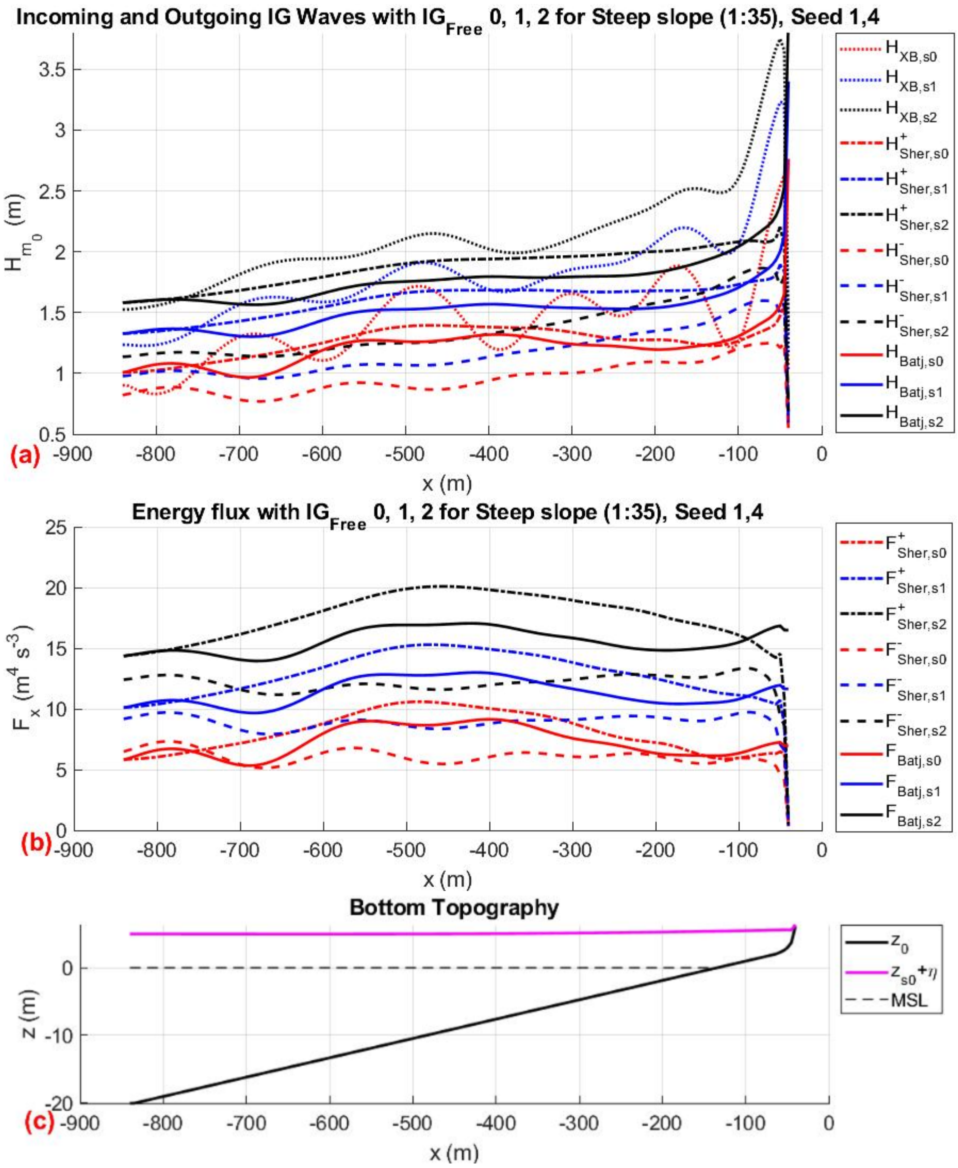

Figure 6.8: The linear and non liner wave contribution for (a) the significant wave height, (b) the energy flux for the steep slope (1:35). The free infragravity intensities are coloured, red for $IG_{free} = 0$, blue for $IG_{free} = 1$, and black for $IG_{free} = 2$. The total spectral wave height H_{XB} is denoted with a dashed line, the significant wave height H_m0 and energy flux F_x, from Battjes et al. (2004) (subscript Batj) denoted by a solid line, from Sheremet et al. (2002) (subscript Sher) for incoming, and outgoing wave denoted with dashed-dot, and dashed line respectively. (c) The bottom topography for the steep slope (1:35), where the sea bed z_0 is marked with solid black lines, the MSL is marked with dashed black line, and the the water elevation marked with solid magenta line includes the surface elevation η, and surge level (z_{s0}).

The infragravity significant wave height for the non-linear propagation, H_{Batj} at Figure 6.8 shows a constant increase of wave height from offshore to nearshore. $H_{Batj,s1}$, and $H_{Batj,s2}$ show that the infragravity wave response is more dominant at the swash zone when compared to the bound wave only wave case $H_{Batj,s0}$. The bound wave however, $H_{Batj,s0}$ shows a more closer description to the linear wave propagation $H^{+}_{Sher,s0}$ Figure 6.8(a). The energy flux response at Figure 6.8(b) shows the highest response for $F_{Batj,s1}$ and $F_{Batj,s2}$ at the swash zone. It should also be noted that the break point mechanism induced due to the break zone is still affecting the wave domain, however its effect on the outgoing significant wave height $H^{-}_{Sher,s}$ is not as significant for higher IG_{free} intensities. The increase of magnitude of the IG_{free} creates a higher magnitude difference between the H_{Batj} values when compared to the H^{-}_{Sher} at the swash zone of Figure 6.8(a). It indicates that there are more infragravity waves present at the coastline, with lower infragravity waves reflecting. .

For the steep slope the wave height increases fairly consistently with each free infragravity IG_{free} added. As a result, it is similar to what we see for the runup response of the steep slope Figure 6.1(a). The additional free infragravity waves as mentioned show a standing wave pattern closer to that of lower infragravity waves or even VLF waves. This result to a description of the wave domain for $IG_{free} = 2$ showing a closer description to a more and more dominant wave pattern that showcases the effect of the resonance as described of the spectral analysis at section 6.3 of this chapter.

Due to the discrepancy between the incoming $H_{Batj.}$ ($F_{Batj.}$), and $H^{-}_{Sher.}$ (F^{-}_{Sher}) at the coastline, for each additional IG_{free} intensity, $H_{Batj.}$ is not considered to be as reliable. Therefore, $H^{\pm}_{Sher}$ is used for a more reliable description of the incoming, and outgoing wave description for $IG_{free} = 1$, amd $IG_{free} = 2$ for the rest of the report. For a better insight on the $H_{Batj.}$ and $F_{Batj.}$ effects for the steep, mild and very mild slope refer to Appendix C.4 of this report.

6.4.2. Mild Slope (1:70)

Similar to the steep slope, the standing wave pattern at Figure 6.9 is initially exhibiting more higher frequency waves and is eventually following a lower infragravity wave standing wave pattern that is more pronounced.

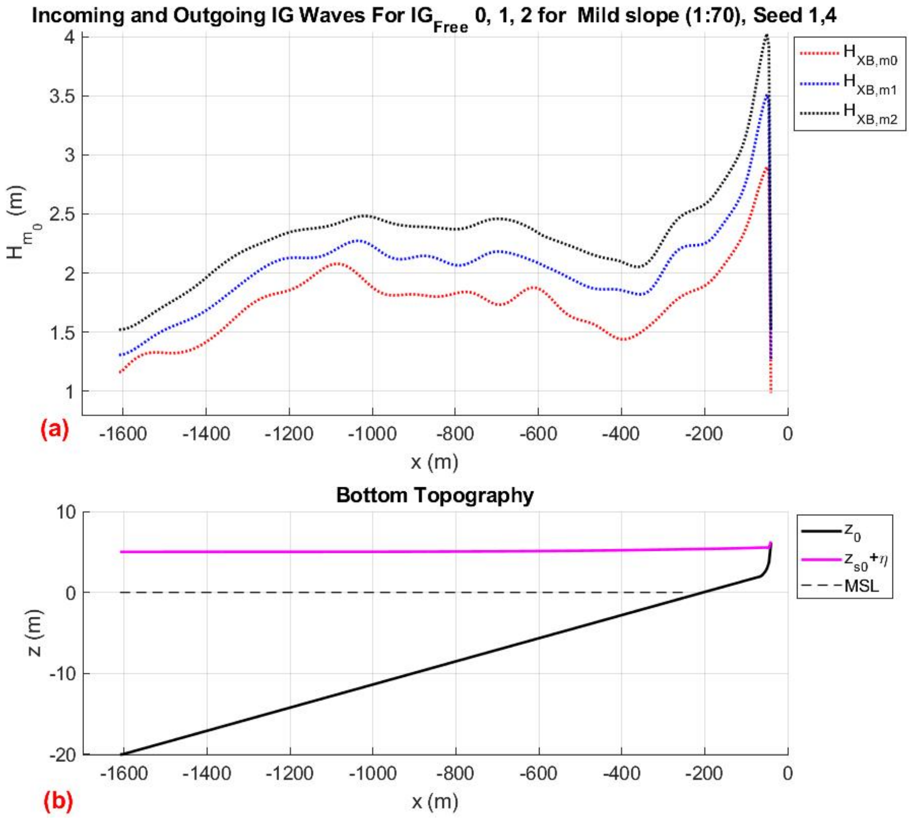

Figure 6.9: The linear and non liner wave contribution for (a) the significant wave height for the mild slope (1:70). The free infragravity intensities are coloured, red for $IG_{free} = 0$, blue for $IG_{free} = 1$, and black for $IG_{free} = 2$. The total spectral wave height H_{XB} is denoted with a dashed line. (b) The bottom topography for the mild slope (1:70), where the sea bed z_0 is marked with solid black lines, the MSL is marked with dashed black line, and the the water elevation marked with solid magenta line includes the surface elevation η, and surge level (z_{s0}).

The mild slope (1:35) at Figure 6.9(a) shows all the IG_{free} intensities wave propagation of the H_{XB}. The spectral significant wave height H_{XB} at Figure 6.10(a), the overall significant wave height $H_{XB,m2} = 4.02m$, $H_{XB,m1} = 3.51m$ and for the bound waves $H_{XB,m0} = 2.90m$ at the coastline ($x = -50m$). As a result, with the inclusion of the free infragravity waves there is a spectral wave height $H_{XB,m}$ increases with a magnitude of $\approx 0.53m$ (approximately by a factor of 1.78) which is similar increase to that of the steep slope. In comparison to the steep slope for $IG_{free} = 0$, and $IG_{free} = 2$ there is a factor of 1.10, and a factor of 1.07 increase in the H_{XB} magnitude. The H_{XB} of the IG_{free} of 1 and 2 show a larger wave height for the mild slope with a H_{XB} difference of $0.3m$ when compared to the steep slope at the swash zone. The standing wave pattern, in contrast of the steep slope exhibit a lot less higher infragravity wave frequency influence in its wave propagation. Instead, the standing wave pattern seems to be fairly consistent with a similar lower infragravity wave response. The same response is described at the T_{m01} response for the mild slop at Figure 6.1(b).

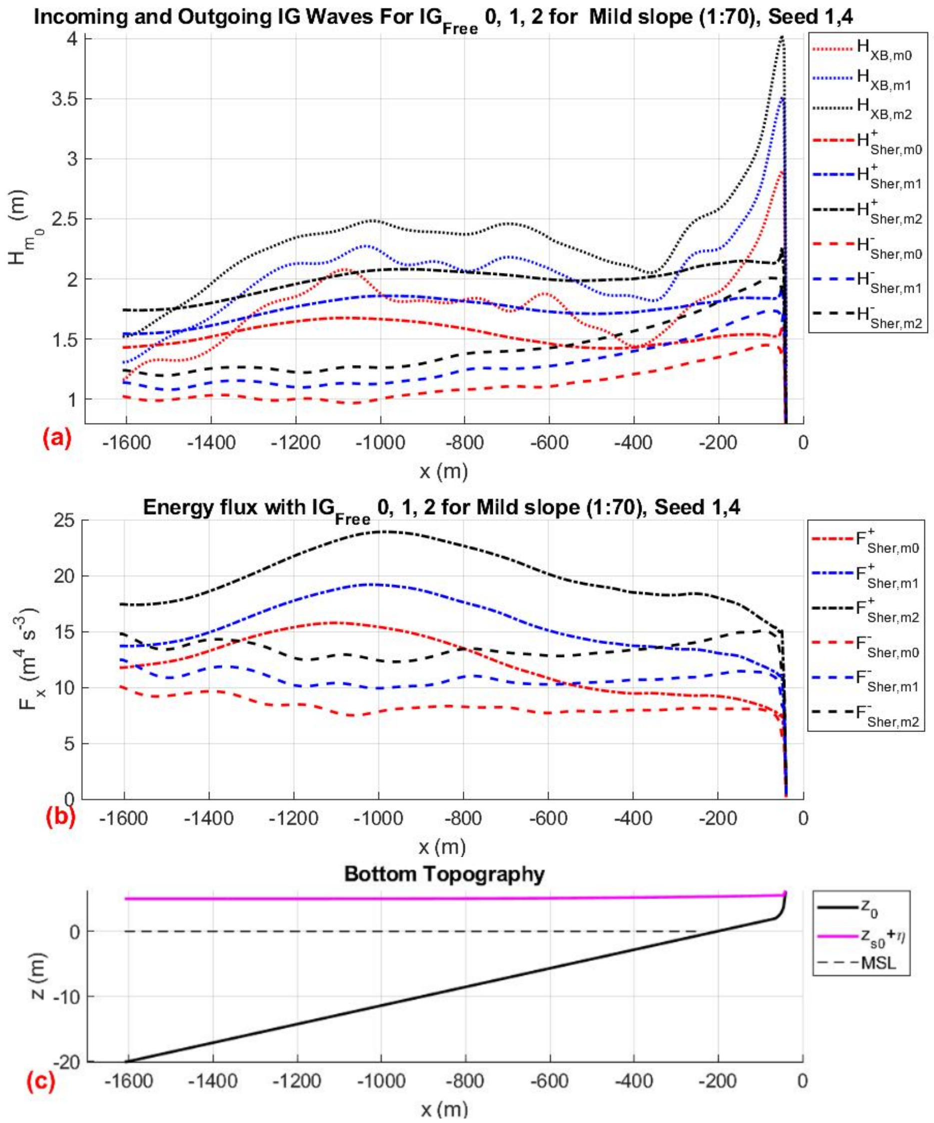

Figure 6.10: The linear and non liner wave contribution for (a) the significant wave height, (b) the energy flux for the mild slope (1:70). The free infragravity intensities are coloured, red for $IG_{free} = 0$, blue for $IG_{free} = 1$, and black for $IG_{free} = 2$. The total spectral wave height H_{XB} is denoted with a dashed line, the significant wave height H_m0 and energy flux F_x, from Sheremet et al. (2002) (subscript Sher) for incoming, and outgoing wave denoted with dashed-dot, and dashed line respectively. (c) The bottom topography for the mild slope (1:70), where the sea bed z_0 is marked with solid black lines, the MSL is marked with dashed black line, and the the water elevation marked with solid magenta line includes the surface elevation η, and surge level (z_{s0}).

The linear wave propagation H^+_{Sher} shows a better description of the wave domain close to the break point (x = -590m), and surf zone when compared to the H_{XB} for when the IG_{free} intensities are non-zero 6.10(a). For the mild slope the wave height increases fairly consistently with each free infragravity IG_{free} added. The consistent wave height increase in magnitude can be attributed to the fairly consistent standing wave pattern regardless of the IG_{free} intensity. The waves are seen to start breaking at the start of the domain, as there is a large roller contribution as observed in Appendix F. The waves however are increasing in magnitude to a maximum at around -1000 m, thus signifying where the majority of the wave energy is reduced in our model. The outgoing significant wave H^{-}_{Sher} indicates the breakpoint mechanism previously observed in the steep slope. The non-linear wave contribution is indicative graphically in Appendix C.

As concluded, from section 6.3 of this chapter there is a clear resonance forcing at $f_{eigen,2} = 0.005Hz$, therefore showing a fairly consistent standing wave pattern. This is consistent with what we observed from the runup response of the mild slope Figure 6.1(a) and from the spectral analysis 6.4. Furthermore, the additional free infragravity waves present in the wave field show fairly consistent standing wave pattern as also observed for the T_m01 response Figure 6.1(b).

6.4.3. Very Mild Slope (1:130)

Similar to the mild and steep slope, the very mild slope (1:130) is illustrated at Figure 6.11(a-c) show all the IG_{free} intensities wave propagation. The spectral significant wave height H_{XB} at Figure 6.11(a) for $IG_{Free} = 2$ ($H_{XB,m2}$) has on average higher significant wave height $H_{XB,vm2} = 2.81mm$, $H_{XB,vm1} = 2.52m$ and for the bound waves $H_{XB,vm0} = 2.06m$ located at the coastline ($x = -50m$).

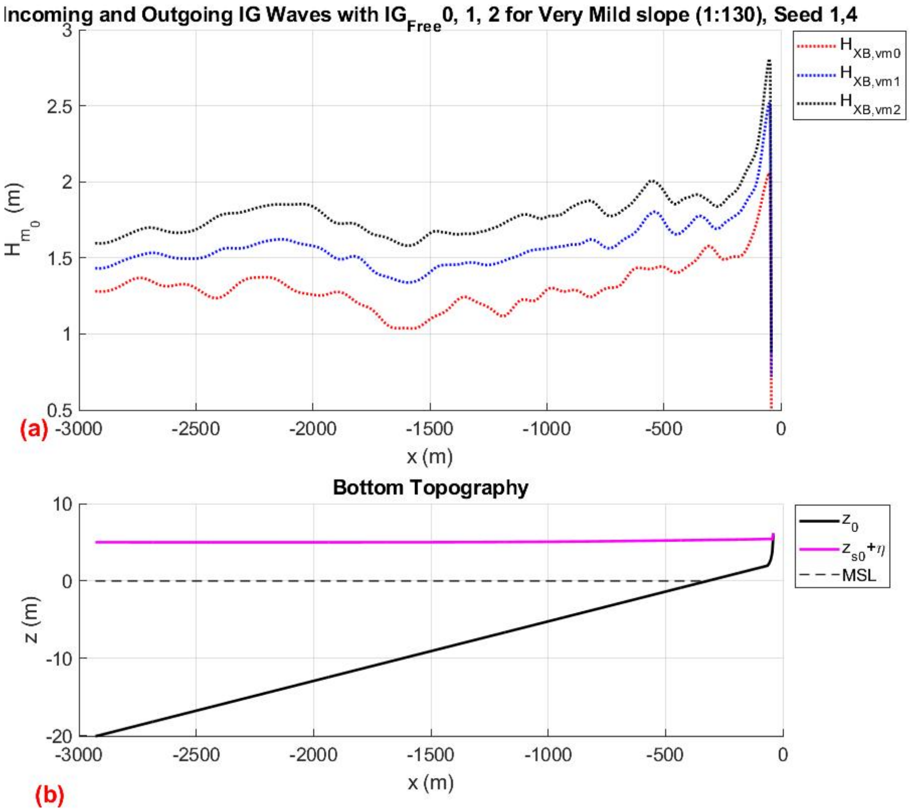

Figure 6.11: The linear and non liner wave contribution for (a) the significant wave height for the very mild slope (1:130). The free infragravity intensities are coloured, red for $IG_{free} = 0$, blue for $IG_{free} = 1$, and black for $IG_{free} = 2$. The total spectral wave height H_{XB} is denoted with a dashed line. (b) The bottom topography for the very mild slope (1:130), where the sea bed z_0 is marked with solid black lines, the MSL is marked with dashed black line, and the the water elevation marked with solid magenta line includes the surface elevation η, and surge level (z_{s0}).

As a result, with the inclusion of the free infragravity waves the spectral wave height $H_{XB,m1}$ increase to $\approx 0.44m$ (by factor of 1.2), with additional $F_{free} = 2$ the wave height increased by $\approx 0.3m$ (by a factor of 1.12). The standing wave pattern, of $H_{XB,vm0}$ exhibit a higher infragravity frequency wave pattern initially present that reduce and follow a slightly more lower infragravity wave frequencies for each consecutive IG_{free} intensity. However, the standing wave pattern seems to be fairly consistent with no real dominant wave patterns, therefore there is no real predominant wave frequency present, which is in line to the spectral analysis figure, Figure 6.5(a). In comparison for the $IG_{free} = 2$ the very mild slope is at a factor of 0.75, and 0.70 lower for the H_{XB} when compared to the steep and mild slope. Thus indicating the larger difference of magnitude of very mild slope when compared to the steep and mild slope.

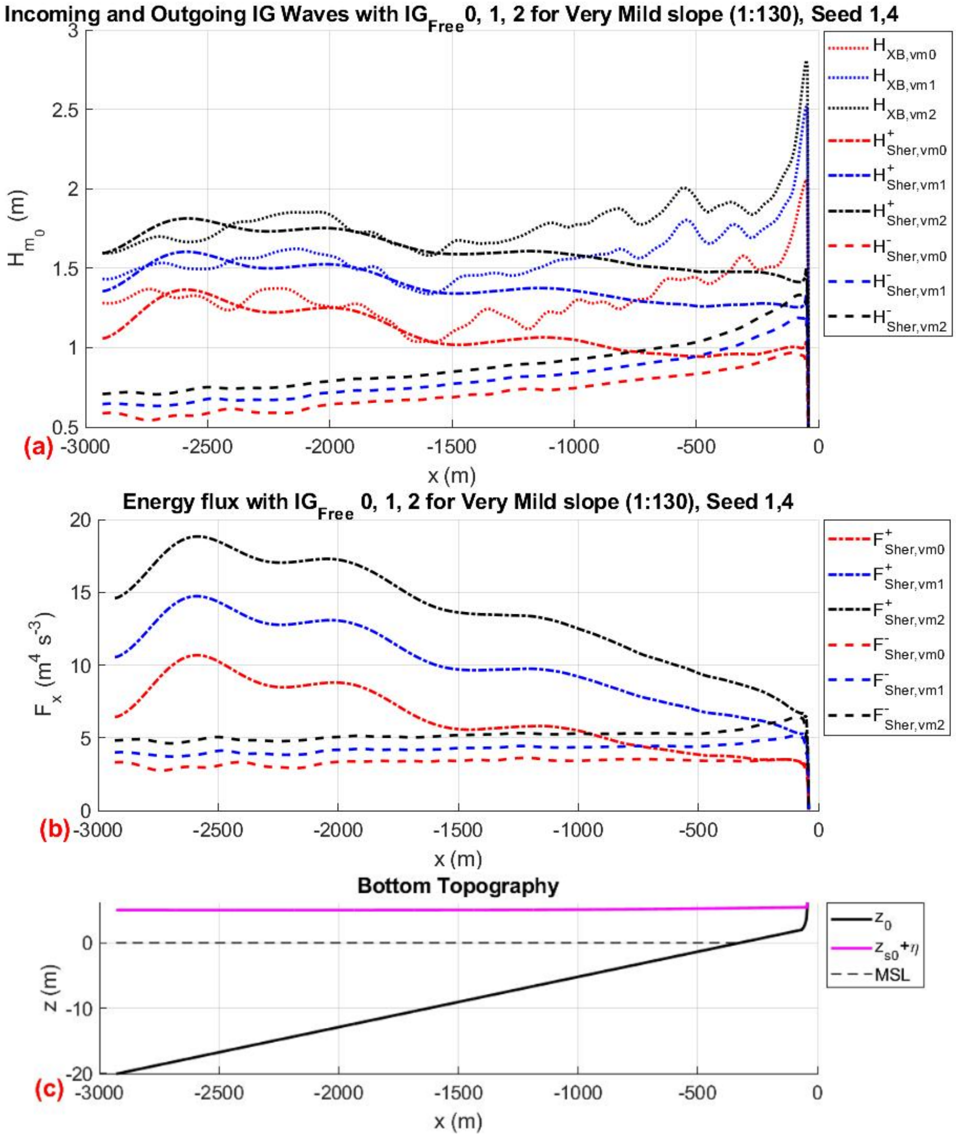

Figure 6.12: The linear and non liner wave contribution for (a) the significant wave height, (b) the energy flux for the very mild slope (1:130). The free infragravity intensities are coloured, red for $IG_{free} = 0$, blue for $IG_{free} = 1$, and black for $IG_{free} = 2$. The total spectral wave height H_{XB} is denoted with a dashed line, the significant wave height $H_m 0$ and energy flux F_x, from Sheremet et al. (2002) (subscript Sher) for incoming, and outgoing wave denoted with dashed-dot, and dashed line respectively. (c) The bottom topography for the very mild slope (1:130), where the sea bed z_0 is marked with solid black lines, the MSL is marked with dashed black line, and the the water elevation marked with solid magenta line includes the surface elevation η, and surge level (z_{s0}).

The incoming wave height H^+_{Sher} and energy flux F^+_{Sher} for all the different IG_{free} are consistently indicating that there is a periodic increase occurring at the offshore wave boundary due to the triad interactions (Snl3) Figure 6.12. This creates the variation of the increase and decrease in both H^+_{Sher} and energy flux F^+_{Sher} magnitude. The incoming waves on average dissipate when travelling from offshore to the coastline, as indicated by the roller energy from Appendix F of the very mild slope. In addition, at the surf zone the energy flux is constantly reducing as it approaches the coastline Figure 6.12(b) for all the different IG_{free} is occurring due to the shorter waves having a lot more time to dissipate. Therefore, it creates a more uniform wave domain in the surf zone, consisting of more low frequency waves (VLF and IG) waves.

The same effect can also be indicated from the runup ad time period response at Table 6.1. The very mild slope in general dissipates a lot of the free sea-swell waves throughout the wave domain with its less pronounced dominant wave frequency does not allow for a predominant waves presence in the domain. As a result, the standing wave pattern from the $H_{XB,vm}$ show a standing wave pattern that is a mixture of low IG and VLF frequencies with higher IG frequencies that are still present even after the additional free IG waves present in the wave domain.

Overall, the different slopes exhibit fairly consistent response with each additional free infragravity intensity IG_{free} added. This includes changing the standing wave pattern to lower frequency infragravity wave regime. With each consecutive free infragravity intensity, the incoming waves H_{Sher} shows a better description of the swash zone when compared to the discrepancy occurring from H_{Batj} response at the coastline. Therefore, the infragravity wave response from Sheremet et al. (2002) H_{Sher} showed a better description of the wave domain, which is considered. From the response the spectral wave height the mild slope $H_{XB,m}$ with the inclusion of added free infragravity showed that it had a higher wave height response from the steep slope $H_{XB,s}$ which is consistent with the runup response as seen in Figure 6.1(a) and the spectral analysis. This response concludes that for mild slope there is a resonance effect that has a more dominant effect on the magnitude than that of the steep and very mild slope.

6.5. Conclusion

Through the introduction of additional free infragravity waves IG_{free} at the offshore wave boundary, higher runup $R_{2\%}$ response is observed. The runup $R_{2\%}$ magnitude is considerably higher for mild slope ($R_{2\%,m2} = 8.45m$) with a factor of and 1.05 ($R_{2\%,s2} = 8.08m$), and 1.09 ($R_{2\%,vm2} = 7.74m$) when compared to the steep, and very mild slope respectively. Which in contrast for the steep slope, the runup response is higher for when $IG_{free} = 0$. The runup response as a result for the mild slope when additional IG waves are introduced show a larger than expected result in comparison with the steep and very mild slope, which can be linked to the presence of the resonance. For the steep slope, when the free IG waves were first introduced (from $IG_{free} = 0$ to $IG_{free} = 1$) the runup increases by 26 cm, the mild slope increased by 72 cm, and very mild slope by 55cm. However, for when the magnitude of the free IG waves was increased (from $IG_{free} = 1$ to $IG_{free} = 2$) the runup magnitude is 12 cm, 37cm, and 37cm for the steep, mild, and very mild slope respectively. As a result, the milder slopes show a larger response on the runup than the steep slope when the free infragravity waves are first introduced in the domain with the same effect but lower magnitude for when the free IG waves magnitude is increased. This is in line with Guza and Feddersen (2012) conclusion that for milder slopes there is a larger runup contribution from the infragravity waves. The large magnitude increase of $R_{2\%}$ when the additional free infragravity waves are added in the wave domain, signifies the need for assessing the additional free infragravity waves for the dune coastal safety.

From the T_{m01} response the mild slope shows a constant magnitude of ≈ 49 for the different free infragravity waves forced. The constant T_{m01} value show a clear dominant wave frequency pattern dominating the mild slope, with and without the free infragravity waves. Similarly for steep slope, T_{m01} show that the most dominant frequencies are located at higher frequency wave band. The effect seen of the dominant mean wave period shows approximately which type of waves are present and can have the most effect. However, with the large response from especially the mild slope for the runup $R_{2\%}$ an additional mechanism enhancing the runup can be concluded next to the additional IG_{free} intensity forced.

From the spectral analysis the resonance effect is evident for the mild slope as it has a magnitude for the surface elevation $E(f)$ of 342 m^2/Hz for $IG_{free} = 2$. This high response occurs at the second eigen mode of 0.005 Hz. As a result, from the spectral wave heights the resonance response is further confirmed due to the large wave height $H_{XB,m2} = 4.02m$ that is higher than the steep slope $H_{XB,s2} = 3.75m$. The spectral analysis for the steep slope, shows that when we increase the free infragravity intensity from the bound waves only case $IG_{free} = 0$ the higher frequency $E(f)$ magnitude at $f_{eigen,5} = 0.0283Hz$ reduces whilst at a lower infragravity frequency $f_{eigen,5} = 0.0093Hz$ it increases to a magnitude of approximately of 100 m^2/Hz. The very mild slope however does not exhibit any harmonic enhancement that can affect the hydrodynamic and runup response.

The response of the mild slope confirms that resonance is present in the wave field and is giving a significant response in the wave field and runup response. For the steep slope and very mild slope, this resonance response is not present. However, for all 3 slopes the standing wave pattern does exhibit a standing wave pattern indicating a response closer to the lower infragravity frequencies. This very evident standing wave pattern towards lower infragravity frequencies, can be potentially linked to the wave forcing (wave maker) that has a different seed number than the bound wave case. However, the resonance response for the mild slope is similar to the VLF resonance as concluded in Chapter 4, a computational artefact.

The artificial resonance noted due to the arbitrary cross shore distance of the wave domain chosen is linked to the seed number of the additional free infragravity waves induced at the offshore wave boundary (Seed number 4). As a result, the computational randomness can still have a considerable effect in our wave domain which can showcase an overestimation of the wave hydrodynamic values and the Runup $R_{2\%}$ values.

However, with and without the resonance effects, Battjes et al. (2004) method that describes the infragravity waves response is showing a less reliable surf zone description for the additional free infragravity intensities of intensity of 1 or 2 due to the incoming and outgoing wave description present at the coastline. Therefore, as stated by Battjes et al. (2004) that the infragravity response described at equation (3.30) is limited to the shoaling zone, the surf zone is indeed not adequately described in this model setup. As a result, Sheremet et al. (2002) is used to give a better description of the wave domain which is reflecting with the addition of the H_{XB} the $R_{2\%}$ response for the dune coastal safety.

The introduction of the IG_{only} wave can not be linearly added to the existing bound wave $IG_{free} = 0$ to amount the effect of $IG_{free} = 1$ or $IG_{free} = 2$ in the preexisting models of companies such as Rijkswaterstaat for dune coastal safety after the initial simulations. Therefore, the $R_{2\%}$ response from the additional free infragravity waves are required to be modelled and considered during the dune coastal safety assessment due to the tens of centimetres of runup not being considered.
Therefore with this chapter, additional information can be added for our research questions set out to answer.

Research Question 2: What is the contribution of resonance to the VLF and Infragravity response?
The seed number chosen for the simulation of the additional free infragravity waves formed an artificial resonance in the low IG frequency of the mild slope. Therefore, artificial resonance produced by the wave domain can be present not only for VLF wave bands, but for different frequency wave bands that can still dominate our wave field. As a result, affecting the runup values obtained for the artificially harmonics present in the wave domain. Therefore, can overestimate the runup or wave hydrodynamics that would be used for the dune coastal safety.

Research Question 3: Can resonance be removed?
The resonance is previously identified at the VLF. With the additional free infragravity waves at the offshore wave boundary resonance is still present, however for lower IG frequencies. Resonance can still be removed with a higher frequency cut off, however this can reduce the reliability of the wave simulations as potentially fundamental frequencies are being removed. As a result, this can impose a very conservative simulation and therefore dune coastal safety assessment.

Research Question 4: What is the role of the infragravity and VLF waves response on the runup for different slopes?
The runup response is higher for the steeper slopes as concluded in chapter 5 of this report. However, due to the resonance response from the seed number for the additional free IG waves, the mild slope exhibits the higher runup, and hence H_{XB}. The (lower) infragravity waves as observed in the report, are seen to be more dominant and affecting the runup considerably. The steeper slopes have a larger contribution on higher infragravity frequencies that, mild, or very mild slope did not exhibit as much. It is safe to assume however that the milder the slope, the lower frequencies are present, therefore, contributing in our wave results, which can be partly linked due to the frequency cut off. The runup growth between the additional free infragravity waves is higher for the milder slopes than the steep slope, as the VLF waves are present in the

wave domain for mild and even more so for the very mild slope.

Research Question 5: What is the effect of the wave run up with different additional free infragravity waves? The runup $R_{2\%}$ increases consistently with each additional free infragravity wave intensity. The runup observed is highest for the steeper slopes for the bound waves only case, and higher for the mild slope for each consecutive additional free infragravity intensity. The additional free infragravity waves $IG_{free} = 1$ show a larger response when first introduced to the domain than when the magnitude of the additional free infragravity wave is increased. For consideration of the additional free infragravity waves in our wave domain, next to the bound waves, the wave runup cannot be added for IG_{only} and $IG_{free} = 0$ to amount the combined effect of $IG_{free} = 1$ (or $IG_{free} = 2$).

7

Conclusions

In this chapter the conclusions of our findings from all previous chapters are summarised. In addition, in this chapter we address all the research questions set out to answer at the start of this report.

7.1. Conclusions

As it is evident through the results, defining the storm conditions in a computational model can cause artificial resonance. The resonance in the response can be considerable, and as a result cause an overestimation of the results. This effect can be present at VLF and infragravity frequencies alike. For the coastal safety assessment of the dunes this should be avoided as it gives unrealistic results for dune safety. The artificial resonance can occur as a result in any computational model as it is based on the arbitrary chosen length of the domain. Since there is no forcing mechanism that can induce a set cross shore distance where the wave started to break and reflect which includes (1) sandbars through Bragg reflection (Liu and Cho, 1993), (2) edge waves (Herbers et al., 1995), and (3) at the coral reefs due to the high bottom friction (Péquignet et al., 2009; Gawehn et al., 2016; Buckley et al., 2018) it can be considered a computational artefact instead.

With the VLF resonance removed the highest runup $R_{2\%}$ for the bound waves only case is located at the steep slope, and the lowest runup at the very mild slope. However, with the addition of the free infragravity waves at the offshore wave boundary the mild slope is seen to have the highest runup response instead $R_{2\%}$. The storm conditions imposed are considerably high with the storm wave height of $H_{s0} = 9m$, as a result when the waves interact with very steep dune face ($m = 0.581$) a large runup response is observed. This is especially true since there is no morphological change present with each wave interaction at the dune. Therefore, the current model setup can be potentially overestimate the runup when compared to what you would expect in the field as the dunes morphology would be constantly changing.

The runup $R_{2\%}$ for the free infragravity wave case only IG_{only} cannot be linearly added with the case when there are only bound waves present $IG_{free} = 0$ to amount for $IG_{free} = 1$ (or $IG_{free} = 2$), as these do not yield the same $R_{2\%}$ results. In contrast by linearly adding $IG_{free} = 0$ and IG_{only} you get a higher $R_{2\%}$ than $IG_{free} = 1$ (or $IG_{free} = 2$). Therefore, the effect of the free infragravity waves should be therefore added during the modelling setup for more representative results.

It should be noted that a similar study for additional free infragravity waves added at the offshore wave boundary has been conducted by Daouk (2020). Daouk (2020) uses the same slopes; steep (1:35), and mild (1:70), with the same free infragravity intensities, and storm conditions. The maximum runup $R_{2\%}$ obtained by Daouk (2020) for the steep slope (1:35) for $IG_{free} = 2$ is 9.4 m, and $R_{2\%}$ for mild slope (1:70) with $IG_{free} = 2$ is 9.0m. For the analysis conducted in this report the maximum equivalent $R_{2\%}$ for the steep slope (1:35) is 8.08 m whilst for the mild slope (1:70) is 8.45 m. Therefore, even with resonance excitation noted for the mild slope, the runup $R_{2\%}$ obtained in this report is lower by 1.32 m (for the steep slope), and 0.55 m (for the mild slope). The difference between the $R_{2\%}$ results can be linked to the boundary conditions used, (1) the morphology not allowed to change, (2) the storm duration run for two 2 hours, and (3) the frequency cut off that varies for each slope. Therefore, it can be concluded that either the current report results are more conservative, or that Daouk (2020) results are overestimating the runup results due to the above mentioned changes.

Lastly, the steep and mild slope is seen to have an effect on the incoming and outgoing wave by the break point mechanism (Symonds et al., 1982) at the offshore wave boundary while the mild and very mild slope exhibiting triad interactions Snl3 at the offshore wave boundary. The different slopes shown that the $R_{2\%}$ is higher for steeper slopes whilst is lower for milder slopes with the exception of the mild slope when under the resonance excitation when the additional free infragravity waves are present.

The current study was conducted to address the effect of the additional free infragravity waves on the dune coastal safety. The methods concluded that the model setup can be a major constituent of uncertainty, that can cause artificial resonance, therefore overestimating the effect on the dune coastal safety. It can be concluded from this report that the steeper the slope the higher the runup $R_{2\%}$ is observed. Furthermore, the additional free infragravity waves can be considered to have tens of centimetres of $R_{2\%}$ increase when they are included for the dune coastal safety. Coastal engineering companies and governmental bodies such as Rijkswaterstaat that do assess the dune coastal safety of the Dutch coast, are underestimating the effect that storms can have if these additional free infragravity waves are included in their simulations. Therefore, for a better representation of the dune coastal safety where incoming leaky waves could be present in the wave domain, the additional free infragravity waves should be included for the dune coastal safety assessment.

7.2. Research Questions

Research Question 1: What is the effect of the computational randomness of the VLF wave hydrodynamics during a storm event?
The storm conditions are conducted through a random phase model that includes different randomly generated seed numbers for both bound and free infragravity waves situations. The computational randomness effect is apparent through a resonance response observed in the wave field. The resonance varies for the different slopes, which therefore means cross shore distance. As a result, the VLF response exhibit a resonance response due to their interaction with the different eigen modes that are produced due to the randomly generated seed number and arbitrary cross shore distance. For the very mild slope, the VLF significant wave height is ≈ 2 times that of the IG waves. The resonance response is a computational artefact, rendering its effect unrealistic which should be excluded from modelling. As a result, the computational randomness is originating from the random phase model (the forcing) and the model's domain length, which both enhances and creates artificial resonance in the model. With this enhancement the runup and wave heights obtained from the model are unrealistic, and consequently overestimating the dune coastal safety during a storm.

Research Question 2: What is the contribution of resonance to the VLF and Infragravity response?
The VLF waves are seen to be higher for very mild slopes rather than the steep slope. The VLF response is highest at the surf zone with a contribution of up to twice that of the IG waves for the very mild slope. The resonance confirmed is located for the VLF waves at the very mild slope at the very first eigen mode of VLF. In addition, for when free infragravity waves are introduced in the wave field, resonance is observed at the mild slope at low infragravity frequencies. As a result, overestimating the runup and significant wave height magnitudes values obtained. However, the VLF and low IG resonance observed is artificial as its a product of the arbitrarily chosen cross shore distance chosen. Therefore, its not a resonance response expected in Noordwijk where our model domain is located. In addition the seed number chosen in the random phase model produces a forcing that has a chance to create this artificial resonance effect.

Research Question 3: Can resonance be removed?
Resonance is identified at the VLF (first eigen mode) and lower infragravity frequency. The resonance observed at the VLF can be removed with a frequency cut off that in result will remove the first eigen mode, that exhibits this large response. Therefore, eliminating the resonance inducing frequencies in the VLF domain from our results. However, the resonance observed at low infragravity frequencies can be removed with a frequency cut off, however, it can reduce the reliability of the wave simulations conducted for assessing the dune coastal safety. As a result, this can impose a very conservative simulation and therefore dune coastal safety assessment.

Research Question 4: What is the role of the infragravity and VLF waves response on the runup for different slopes?
The runup response is higher for the steeper slopes for when only bound waves are present. However, due to

the resonance response from the seed number for the additional free IG waves, the mild slope exhibits the higher runup, and hence H_{XB}. The (lower) infragravity waves as observed in the report, are seen to be more dominant and affecting the runup considerably. The steeper slopes have a larger contribution on higher infragravity frequencies that, mild, or very mild slope did not exhibit as much. The runup growth between the additional free infragravity waves is higher for the milder slopes than the steep slope, as the VLF waves are present in the wave domain for mild and even more so for the very mild slope.

Research Question 5: What is the effect of the wave run up with different additional free infragravity waves? The runup $R_{2\%}$ increases consistently with each additional free infragravity wave intensity. The runup observed is highest for the steeper slopes for the bound waves only case, and higher for the mild slope for each consecutive additional free infragravity intensity. The additional free infragravity waves $IG_{free} = 1$ show a larger response when first introduced to the domain than when the magnitude of the additional free infragravity wave is increased. For consideration of the additional free infragravity waves in our wave domain, next to the bound waves, the wave runup cannot be added for IG_{only} and $IG_{free} = 0$ to amount the combined effect of $IG_{free} = 1$ (or $IG_{free} = 2$).

8

Recommendations

In this chapter, different recommended suggestions for further research are highlighted for a better insight on the coastal dune safety.

8.1. Model Setup

The artificial resonance is a very dominant feature in the computational domain. Therefore is recommended for a better model setup, a bi-spectral analysis or Fourier transform to be used for a more accurate description of the dune coastal safety. Fourier transform and bi-spectral analysis will allow to identify the the eigen frequencies exhibiting the artificial resonance and removed, hence providing a more accurate representation of the additional free infragravity wave effect produced during a storm.

In addition, a better definition on the probability and how severe the artificial resonance identified can prove to be very useful. This will allow a better insight for the computational modellers such as Rijkswaterstaat to accurate simulating the storm conditions without any overestimation of the runup or erosion rates in the results. Furthermore, even a larger sample size N, can provide confidence on how probable this artificial resonance is.

8.2. Morphological Change

Morphological changes can allow for the dunes to exhibit a more realistic and dynamic change to the storm, showing more accurate runup response closer to what you would expect in the field.
The morphology changing can allow for the model to be closer to a more realistic case of what would be expected during a storm. The additional free infragravity waves are thought to allow for a more complex description on dune erosion and dynamic morphological change with time. Thus can even a provide a morphological features such as sand bars in the model domain that can cause additional wave breaking and as a result vary the runup response.

In addition different dune processes can allow for varied morphodynamic response resulting in a higher dune erosion volume for the same wave forcing. Avalanche is one such dune process that can speed up the dune erosion rate which in response is a significant contributor to coastal safety of the dune (van Rijn, 2009). With the addition of the free infragravity waves such dune process can be more significant to be looked into, as they might occur a lot sooner, and hence prove to be a major factor for dune coastal safety

8.3. 2D Model

A better description of the model can be obtained through having additional hydrodynamic processes that occur due to the oblique incident waves, therefore using a 2D model. In the Netherlands the 1D method cannot express all the coastal locations accurately as observed in 3 Figure 3.1 (van Santen et al., 2012). As a result 2D model is even advantageous for certain locations across the Dutch coast for a more accurate description of the model domain. In addition, 2D modelling allow for different wave processes that can affect the hydrodynamics and potentially affect the coastal erosion.

The oblique incident waves is a potential feature of the 2D model. For oblique incident waves, entering the wave domain at an oblique angle wave trapping can occur in the surf zone, also known as edge waves, (Herbers et al. 1995). Edge waves can enhance the infragravity waves presence in the surf zone and due to the forcing mechanism can induce a standing wave pattern (Van Dongeren et al. 2007). As a result, the edge waves can potentially increase the runup as they are trapped in the surf zone. However, if the oblique incident waves enter at an acute angle the waves are leaky waves that can escape the wave domain. As a result, can still enhance the outgoing waves hence enhance the outgoing infragravity waves. This effect on dune coastal safety with the addition of the free infragravity waves at the offshore wave boundary is not yet researched.

Lastly, With the 2D modelling, the coastline shape can differ to a concave or convex layout that can define an irregular coastline shape. A convex coastline can have more erosion than a straight coastline (Den Heijer, 2013). Therefore, the coastline shape can introduce different wave interaction which can provide a better description of the runup values obtained.

Bibliography

[1] Baldock, T., Huntley, D., Bird, P., O'hare, T., and Bullock, G. (2000). Breakpoint generated surf beat induced by bichromatic wave groups. Coastal Engineering, 39(2-4):213–242.

[2] Battjes, J. A., Bakkenes, H. J., Janssen, T. T., and van Dongeren, A. R. (2004). Shoaling of subharmonic gravity waves. Journal of Geophysical Research, 109(C2).

[3] Bertin, X., de Bakker, A., Van Dongeren, A., Coco, G., André, G., Ardhuin, F., Bonneton, P., Bouchette, F., Castelle, B., Crawford, W. C., et al. (2018). Infragravity waves: From driving mechanisms to impacts. Earth-Science Reviews, 177:774–799.

[4] Buckley, M. L., Lowe, R. J., Hansen, J. E., van Dongeren, A. R., and Storlazzi, C. D. (2018). Mechanisms of wave-driven water level variability on reef-fringed coastlines. Journal of Geophysical Research: Oceans, 123(5):3811–3831.

[5] Chen, X., Zhang, X., Church, J. A., Watson, C. S., King, M. A., Monselesan, D., Legresy, B., and Harig, C. (2017). The increasing rate of global mean sea-level rise during 1993-2014. Nature Climate Change, 7(7):492–495.

[6] Cheriton, O. M., Storlazzi, C. D., and Rosenberger, K. J. (2016). Observations of wave transformation over a fringing coral reef and the importance of low-frequency waves and offshore water levels to runup, overwash, and coastal flooding. Journal of Geophysical Research: Oceans, 121(5):3121–3140.

[7] Daouk, H. (2020). Impact of Free Long Waves on Dune Erosion Predictions in Numerical Modelling. Delft University of Technology.

[8] De Bakker, A., Brinkkemper, J., Van der Steen, F., Tissier, M., and Ruessink, B. (2016b). Cross-shore sand transport by infragravity waves as a function of beach steepness. Journal of Geophysical Research: Earth Surface, 121(10):1786–1799.

[9] de Bakker, A., Tissier, M., and Ruessink, B. (2014). Shoreline dissipation of infragravity waves. Continental Shelf Research, 72:73–82.

[10] De Bakker, A., Tissier, M., and Ruessink, B. (2016a). Beach steepness effects on nonlinear infragravity-wave interactions: A numerical study. Journal of Geophysical Research: Oceans, 121(1):554–570.

[11] de Beer, A., McCall, R., Long, J., Tissier, M., and Reniers, A. (2021). Simulating wave runup on an intermediate–reflective beach using a wave-resolving and a wave-averaged version of xbeach. Coastal Engineering, 163:103788.

[12] de Vries, J. v. T., Van Gent, M., Walstra, D., and Reniers, A. (2008). Analysis of dune erosion processes in large-scale flume experiments. Coastal Engineering, 55(12):1028–1040.

[13] Den Heijer, C. (2013). The role of bathymetry, wave obliquity and coastal curvature in dune erosion prediction, volume 12. IOS Press.

[14] Do, K., Shin, S., Cox, D., and Yoo, J. (2018). Numerical simulation and large-scale physical modelling of coastal sand dune erosion. Journal of Coastal Research, 85:196–200.

[15] Gawehn, M., van Dongeren, A., van Rooijen, A., Storlazzi, C. D., Cheriton, O. M., and Reniers, A. (2016). Identification and classification of very low frequency waves on a coral reef flat. Journal of Geophysical Research: Oceans, 121(10):7560–7574.

[16] Guza, R. and Feddersen, F. (2012). Effect of wave frequency and directional spread on shoreline runup. Geophysical Research Letters, 39(11).

[17] Guza, R., Thornton, E., and Holman, R. (1984). Swash on steep and shallow beaches. Coastal Engineering Proceedings, 1(19):48.

[18] Hasselmann, K., Barnett, T. P., Bouws, E., Carlson, H., Cartwright, D. E., Enke, K., Ewing, J., Gienapp, A., Hasselmann, D., Kruseman, P., et al. (1973). Measurements of wind-wave growth and swell decay during the joint north sea wave project (jonswap). Ergaenzungsheft zur Deutschen Hydrographischen Zeitschrift, Reihe A.

[19] Henderson, S. M. and Bowen, A. (2002). Observations of surf beat forcing and dissipation. Journal of Geophysical Research: Oceans, 107(C11):14–1.

[20] Henderson, S. M., Guza, R. T., Elgar, S., Herbers, T. H. C., and Bowen, A. J. (2006). Nonlinear generation and loss of infragravity wave energy. Journal of Geophysical Research, 111(C12).

[21] Herbers, T., Elgar, S., and Guza, R. (1995). Generation and propagation of infragravity waves. Journal of Geophysical Research: Oceans, 100(C12):24863–24872.

[22] Holman, R. (1986). Extreme value statistics for wave run-up on a natural beach. Coastal Engineering, 9(6):527–544.

[23] Holthuijsen, L. H. (2010). Waves in oceanic and coastal waters. Cambridge University Press.

[24] Janssen, T., Battjes, J., and Van Dongeren, A. (2003). Long waves induced by short-wave groups over a sloping bottom. Journal of Geophysical Research: Oceans, 108(C8).

[25] Liu, P. L.-F. and Cho, Y.-S. (1993). Bragg reflection of infragravity waves by sandbars. Journal of Geophysical Research, 98(C12):22733–22741.

[26] Longuet-Higgins, M. S. and Stewart, R. (1962). Radiation stress and mass transport in gravity waves, with application to ‘surf beats’. Journal of Fluid Mechanics, 13(4):481–504.

[27] Moura, T. and Baldock, T. (2017). Remote sensing of the correlation between breakpoint oscillations and infragravity waves in the surf and swash zone. Journal of Geophysical Research: Oceans, 122(4):3106–3122.

[28] Munk, W. (1949). Surf beats. EOS, Transactions American Geophysical Union, 30(6):849–854.

[29] Munk, W. H. (1950). On the wind-driven ocean circulation. Journal of Atmospheric Sciences, 7(2):80–93.

[30] Oh, J.-E., Jeong, W.-M., Chang, Y. S., and Oh, S.-H. (2020). On the separation period discriminating gravity and infragravity waves off gyeongpo beach, korea. Journal of Marine Science and Engineering, 8(3):167.

[31] Péquignet, A.-C. N., Becker, J. M., and Merrifield, M. A. (2014). Energy transfer between wind waves and low-frequency oscillations on a fringing reef, ipan, guam. Journal of Geophysical Research: Oceans, 119(10):6709–6724.

[32] Péquignet, A. C. N., Becker, J. M., Merrifield, M. A., and Aucan, J. (2009). Forcing of resonant modes on a fringing reef during tropical storm man-yi. Geophysical Research Letters, 36(3).

[33] Pomeroy, A., Lowe, R., Symonds, G., Van Dongeren, A., and Moore, C. (2012a). The dynamics of infragravity wave transformation over a fringing reef. Journal of Geophysical Research: Oceans, 117(C11).

[34] Pomeroy, A. W. M., Van Dongeren, A., Lowe, R., Van Thiel de Vries, J., and Roelvink, J. (2012b). Low frequency wave resonance in fringing reef environments. Coastal Engineering Proceedings, 1(33):25.

[35] Rieneke, v. N. (2021). Infragravity wave resonance over coral reef lined coasts. Delft University of Technology.

[36] Rijkswaterstaat, D. (1989). Guidelines for the evaluation of safety of dunes as coastal defense. TAW/ENW.

[37] Rijnsdorp, D. P., Ruessink, G., and Zijlema, M. (2015). Infragravity-wave dynamics in a barred coastal region, a numerical study. Journal of Geophysical Research: Oceans, 120(6):4068–4089.

[38] Roelvink, D. and Reniers, A. (2011). A guide to modeling coastal morphology, volume 12. world scientific.

[39] Roelvink, D., Reniers, A., Van Dongeren, A., De Vries, J. V. T., McCall, R., and Lescinski, J. (2009). Modelling storm impacts on beaches, dunes and barrier islands. Coastal engineering, 56(11-12):1133–1152.

[40] Ruessink, B. G. (1998). Bound and free infragravity waves in the nearshore zone under breaking and nonbreaking conditions. Journal of Geophysical Research: Oceans, 103(C6):12795–12805.

[41] Rutten, J., Torres-Freyermuth, A., and Puleo, J. (2021). Uncertainty in runup predictions on natural beaches using xbeach nonhydrostatic. Coastal Engineering, 166:103869.

[42] Sallenger, A. H. J. (2000). Storm impact scale for barrier islands. Journal of Coastal Research, pages 890–895.

[43] Sénéchal, N., Dupuis, H., Bonneton, P., Howa, H., and Pedreros, R. (2001). Observation of irregular wave transformation in the surf zone over a gently sloping sandy beach on the french atlantic coastline. Oceanologica Acta, 24(6):545–556.

[44] Sheremet, A., Guza, R. T., Elgar, S., and Herbers, T. H. C. (2002). Observations of nearshore infragravity waves: Seaward and shoreward propagating components. Journal of Geophysical Research, 107(C8):10–1–10.

[45] Stockdon, H. F., Holman, R. A., Howd, P. A., and Sallenger, A. H. (2006). Empirical parameterization of setup, swash, and runup. Coastal Engineering, 53(7):573–588.

[46] Svendsen, I. A. (1984a). Wave heights and set-up in a surf zone. Coastal engineering, 8(4):303–329.

[47] Svendsen, I. A. (1984b). Mass flux and undertow in a surf zone. Coastal engineering, 8(4):347–365.

[48] Symonds, G., Huntley, D. A., and Bowen, A. J. (1982). Two-dimensional surf beat: Long wave generation by a time-varying breakpoint. Journal of Geophysical Research, 87(C1):492.

[49] Thomson, J., Elgar, S., Raubenheimer, B., Herbers, T. H. C., and Guza, R. T. (2006). Tidal modulation of infragravity waves via nonlinear energy losses in the surfzone. Geophysical Research Letters, 33(5).

[50] Thornton, E. B. and Guza, R. (1986). Surf zone longshore currents and random waves: Field data and models. Journal of Physical Oceanography, 16(7):1165–1178.

[51] Tissier, M., Bonneton, P., Michallet, H., and Ruessink, B. G. (2015). Infragravity-wave modulation of short-wave celerity in the surf zone. Journal of Geophysical Research: Oceans, 120(10):6799–6814.

[52] Tissier, M., Bonneton, P., Ruessink, B., et al. (2017). Infragravity waves and bore merging. Proceedings Coastal Dynamics 2017, pages 451–460.

[53] Tucker, M. (1950). Surf beats: Sea waves of 1 to 5 min. period. Proceedings of the Royal Society of London. Series A. Mathematical and Physical Sciences, 202(1071):565–573.

[54] Van Dongeren, A., Battjes, J., Janssen, T., Van Noorloos, J., Steenhauer, K., Steenbergen, G., and Reniers, A. (2007). Shoaling and shoreline dissipation of low-frequency waves. Journal of Geophysical Research: Oceans, 112(C2).

[55] Van Geer, P., Den Bieman, J., Hoonhout, B., and Boers, M. (2015). Xbeach 1d–probabilistic model: Adis, settings, model uncertainty and graphical user interface. Tec. Rep, 1209436.

[56] van Rijn, L. C. (2009). Prediction of dune erosion due to storms. Coastal Engineering, 56(4):441–457.

[57] van Santen, R., Steetzel, H., de Vries, J. v. T., and van Dongeren, A. (2012). Modeling storm impact on complex coastlines. westkapelle, the netherlands. Coastal Engineering Proceedings, 1(33):52–52.

[58] Winde, H. (2012). Wave height from pressure measurements. Delft University of Technology.

A

Sensitivity Analysis

For the sensitivity analysis in Chapter 4.4 the surface elevation, cross shore velocity $E(f)$, and phase are all used at an observation frequency of $f = 0.0011 Hz$. The different boundary conditions used in Figure 4.7 are the (1) base case (the original Jarkus transect with a constant slope), (2) the extended cross shore distance of 2850 m, (3) the storm duration of 4 hours with the addition of the cross shore distance, and (4) water depth increase of 25m with a cross shore distance extension of 2200 m. These are all are all reflected in (1) Figure 4.6(a-c) (located in chapter 4), (2) Figure A.1(d-f), (3) Figure B.2(a-c), (4) Figure B.2(d-f).

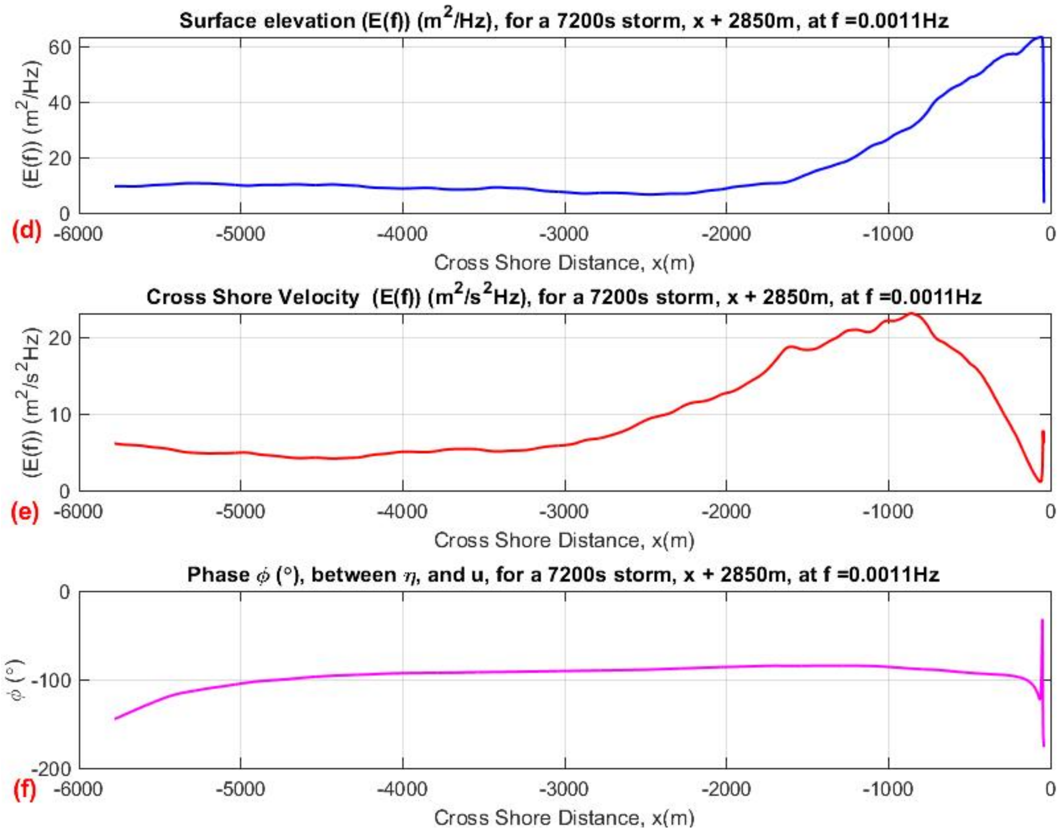

Figure A.1: Plot for the for the cross shore domain was extended by an additional 2850 m for (a) the surface elevation $E(f)$, (b)cross shore velocity $E(f)$, (c) phase between the surface elevation and cross shore velocity, against cross shore distance at a frequency f = 0.0011 Hz for the very mild slope (1:130).

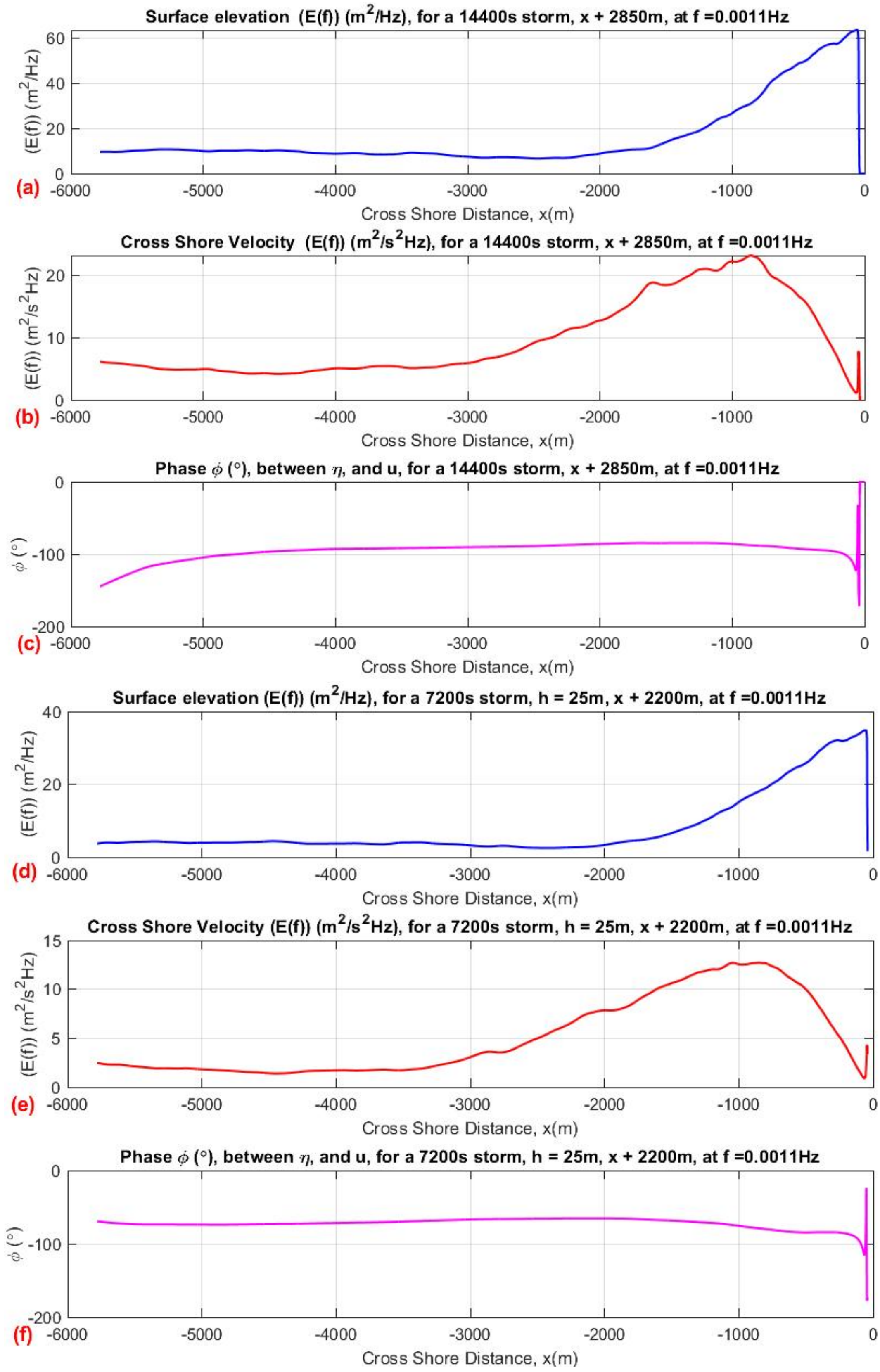

Figure A.2: Plot of the surface elevation $E(f)$ (a), (d), cross shore velocity $E(f)$ (b), (e), phase between the surface elevation and cross shore velocity (c), (f) against cross shore distance at a frequency f = 0.0011 Hz for the very mild slope (1:130). Where (a),(b) and (c) the extended storm duration of 14400 s with the extended cross shore distance. And (d),(e),(f) water depth of 25 m with the extended cross shore distance extension.

B

Spectral Analysis for the cut off Frequency

Spectral analysis is conducted for the steep mild and very mild slope at the location closest to the first eigen mode. As a result, as a check for near resonance effect from the VLF frequency. where For steep $f_{eigen,s} = 0.004064Hz$, mild $f_{eigen,m} = 0.002542Hz$, and very mild slope $f_{eigen,vm} = 0.00091Hz$ located at Figure B.1, Figure B.2[(a)-(c)], Figure B.2[(d)-(f)].

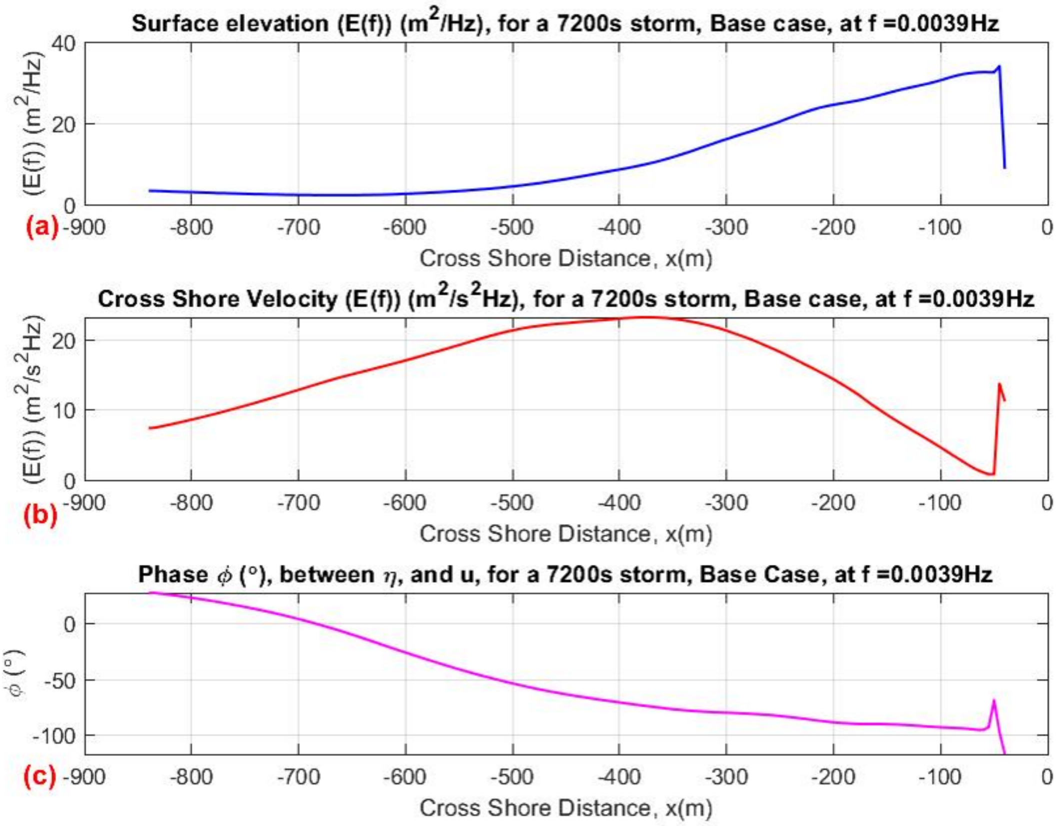

Figure B.1: Plot for the for the cross shore domain of the steep slope (1:35) at the observation frequency of 0.0039Hz (a) the surface elevation $E(f)$, (b)cross shore velocity $E(f)$, (c) phase between the surface elevation and cross shore velocity, against cross shore distance at a frequency f = 0.0011 Hz for the steep slope (1:35).

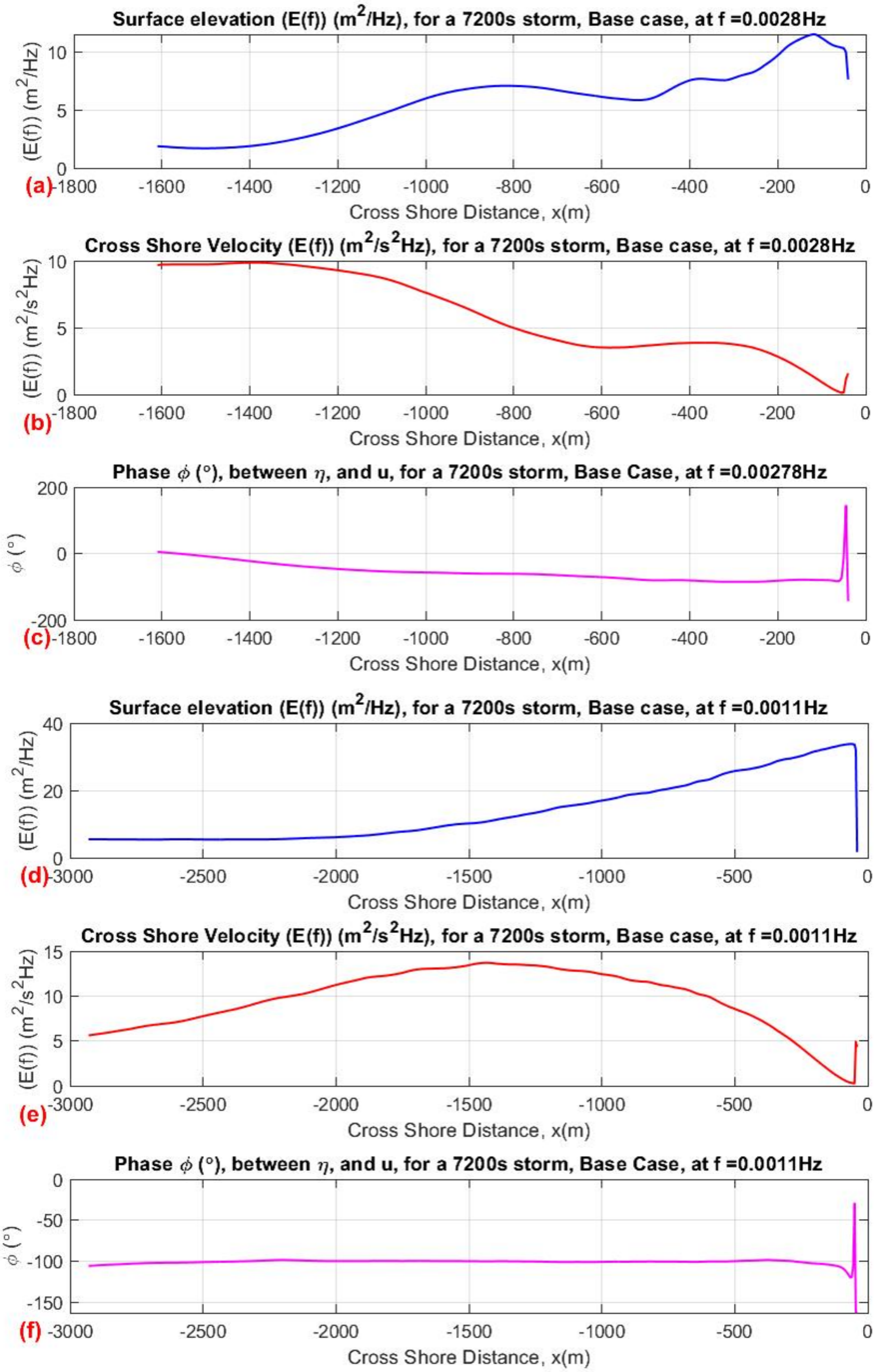

Figure B.2: Plot of the surface elevation $E(f)$ (a), (d), cross shore velocity $E(f)$ (b), (e), phase between the surface elevation and cross shore velocity (c), (f) against cross shore distance. Where (a),(b) and (c) is for the mild slope (1:70) at an observation frequency of 0.0028 Hz. And (d),(e),(f) is for the very mild slope (1:135) at an observation frequency of 0.00091 Hz.

C

Non-linear Wave Propagation

The roller energy is included with each different free infragravity intensity IG_{free} for all the different slopes in addition to the linear and non-linear wave propagation for the significant wave height H_{m0} and the energy Flux F_x. The roller energy E_R is also presented for high frequency HF and low frequency LF contributions. The energy flux when you do include the roller energy and without the roller energy is also included to show the effect of this roller energy in the energy flux F_x contribution in our model domain. In addition the contribution of all the IG_{free} intensities at each slope are also summarized for a more complete picture of the results

C.1. Non-linear wave propagation for Bound waves only $IG_{free} = 0$

C.1.1. Steep Slope (1:35) with $IG_{free} = 0$

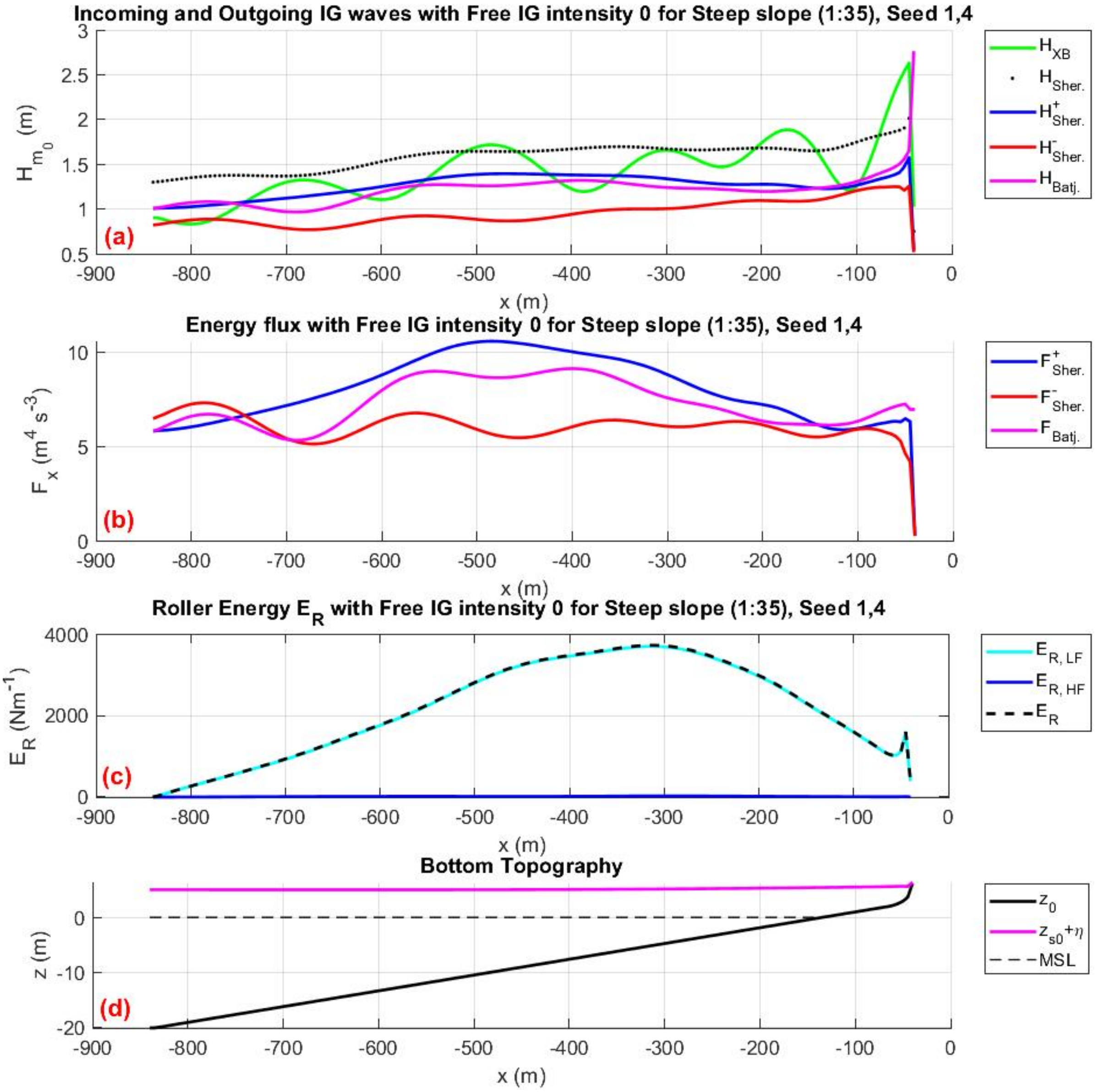

Figure C.1: Incoming and outgoing (a) significant wave height H_{m0}), and (b) energy flux for the steep slope (1:35) with $IG_{free} = 0$. Where the total significant wave height through specral analysis is summarised by the neon green line (H_{XB}. The dotted black line is the total wave height corresponding to the total flux of Sheremet et al. (2002) method H_{Sher}. The blue lines show the incoming waves, and red line the outgoing waves. Sheremet et al. (2002) method is summarised with solid blue and red lines respectively respectively. The solid magenta, and cyan line is the non-linear wave propagation of the incoming wave through Battjes et al. (2004) method by including, and excluding the roller effect respectively. (c) Roller energy E_R marked with dashed blue line for steep slope (1:35), where the blue and cyan solid lines are for the low frequency $E_{R,LF}$, and high frequency $E_{R,HF}$ contribution respectively. (d) is the bottom topography of the steep slope (1:35) where the sea bed z_0 is marked with solid black line, dashed black line indicates the MSL and the magenta line is the water elevation which includes the surface elevation η, and surge level (z_{s0}).

C.1.2. Mild Slope (1:70) with $IG_{free} = 0$

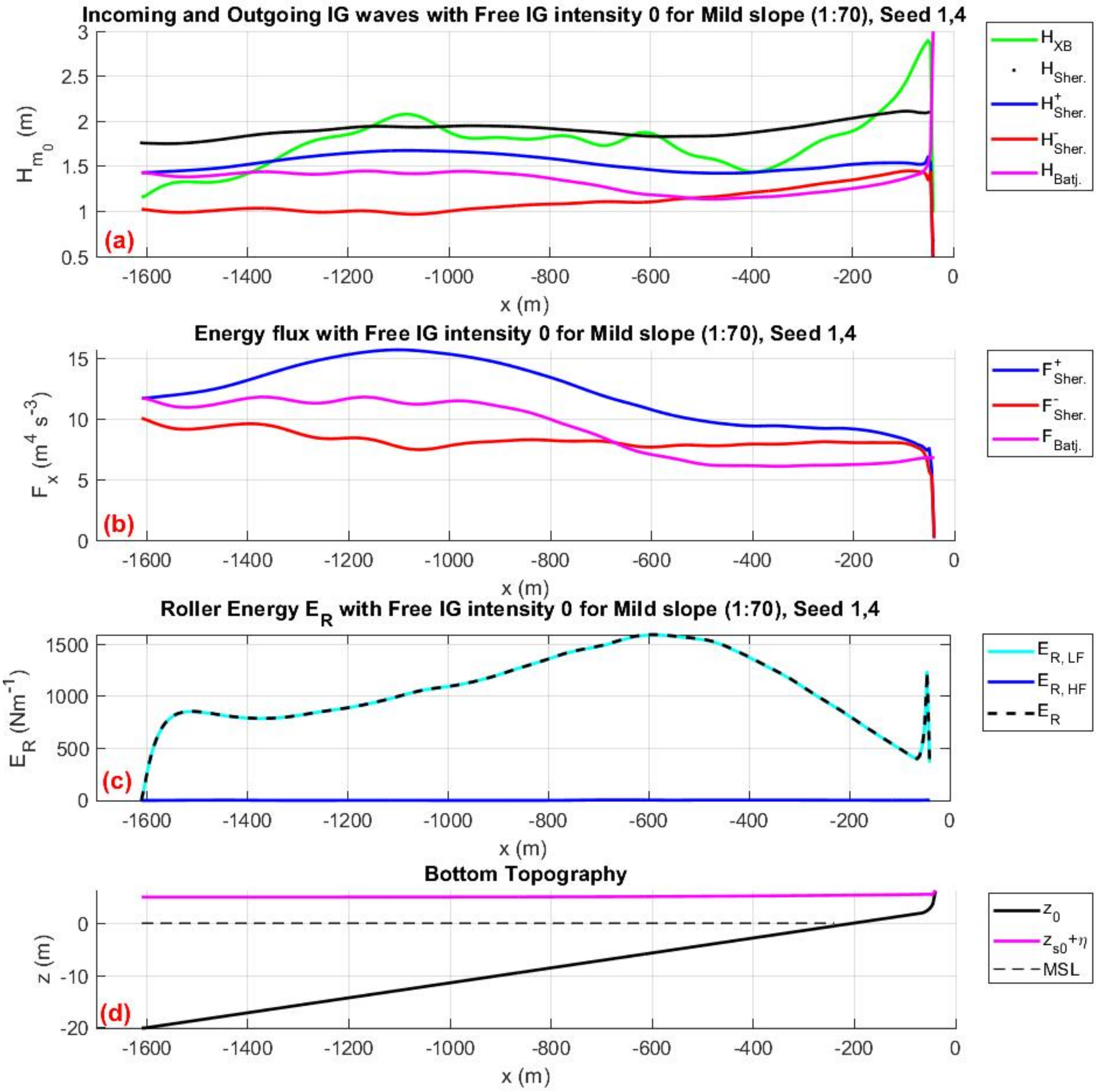

Figure C.2: Incoming and outgoing (a) significant wave height H_{m0}), and (b) energy flux for the mild slope (1:70) with $IG_{free} = 0$. Where the total significant wave height through specral analysis is summarised by the neon green line (H_{XB}. The dotted black line is the total wave height corresponding to the total flux of Sheremet et al. (2002) method H_{Sher}. The blue lines show the incoming waves, and red line the outgoing waves. Sheremet et al. (2002) method is summarised with solid blue and red lines respectively respectively. The solid magenta, and cyan line is the non-linear wave propagation of the incoming wave through Battjes et al. (2004) method by including, and excluding the roller effect respectively. (c) Roller energy E_R marked with dashed blue line for mild slope (1:70), where the blue and cyan solid lines are for the low frequency $E_{R,LF}$, and high frequency $E_{R,HF}$ contribution respectively. (d) is the bottom topography of the mild slope (1:70) where the sea bed z_0 is marked with solid black line, dashed black line indicates the MSL and the magenta line is the water elevation which includes the surface elevation η, and surge level (z_{s0}).

C.1.3. Very Mild Slope (1:130) with $IG_{free} = 0$

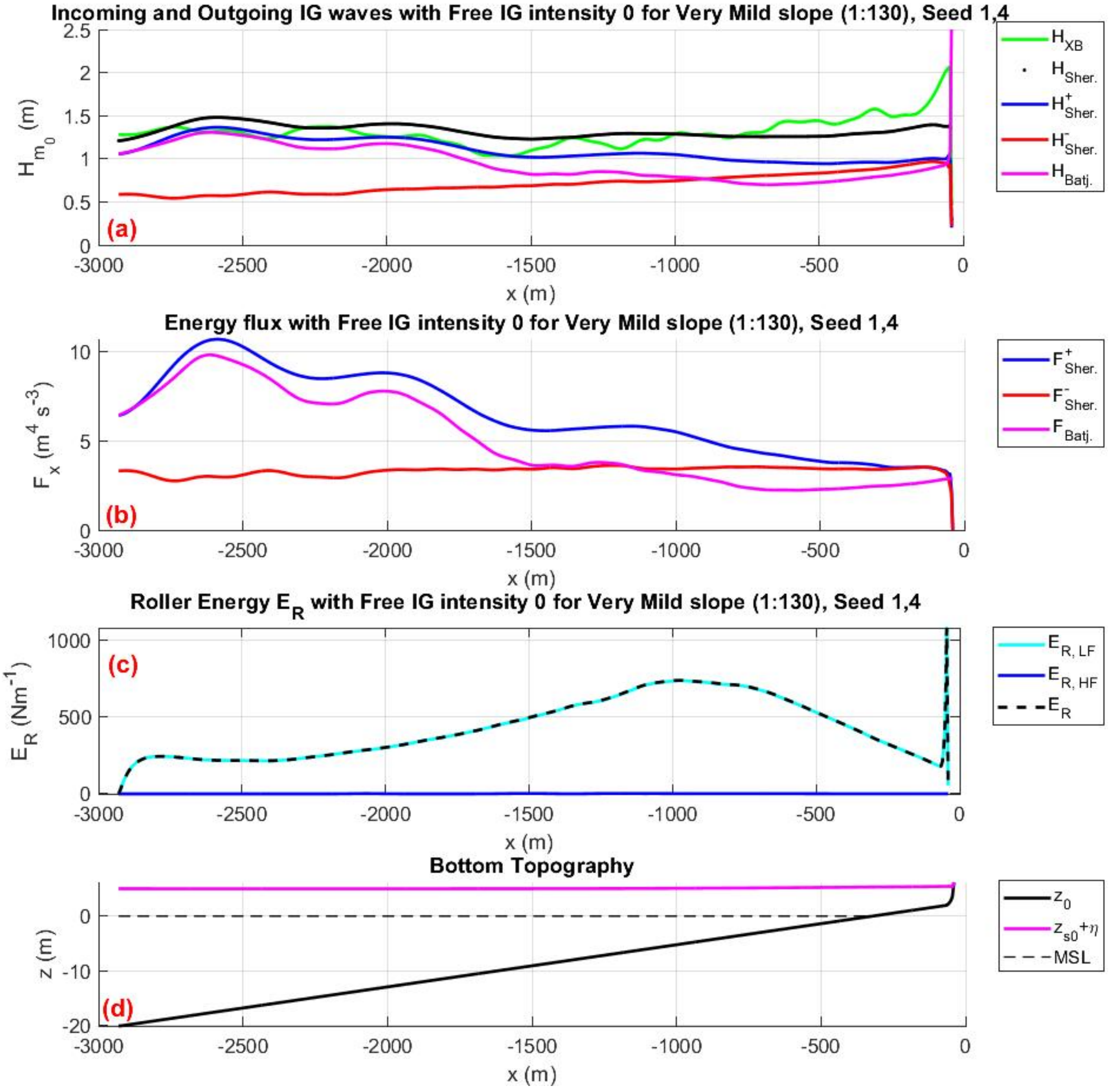

Figure C.3: Incoming and outgoing (a) significant wave height H_{m0}), and (b) energy flux for the very mild slope (1:130) with $IG_{free} = 0$. Where the total significant wave height through specral analysis is summarised by the neon green line (H_{XB}. The dotted black line is the total wave height corresponding to the total flux of Sheremet et al. (2002) method H_{Sher}. The blue lines show the incoming waves, and red line the outgoing waves. Sheremet et al. (2002) method is summarised with solid blue and red lines respectively respectively. The solid magenta, and cyan line is the non-linear wave propagation of the incoming wave through Battjes et al. (2004) method by including, and excluding the roller effect respectively.(c) Roller energy E_R marked with dashed blue line for very mild slope (1:130), where the blue and cyan solid lines are for the low frequency $E_{R,LF}$, and high frequency $E_{R,HF}$ contribution respectively. (d) is the bottom topography of the very mild slope (1:130) where the sea bed z_0 is marked with solid black line, dashed black line indicates the MSL and the magenta line is the water elevation which includes the surface elevation η, and surge level (z_{s0}).

C.2. Non-linear wave propagation for $IG_{free} = 1$

C.2.1. Steep Slope (1:35) with $IG_{free} = 1$

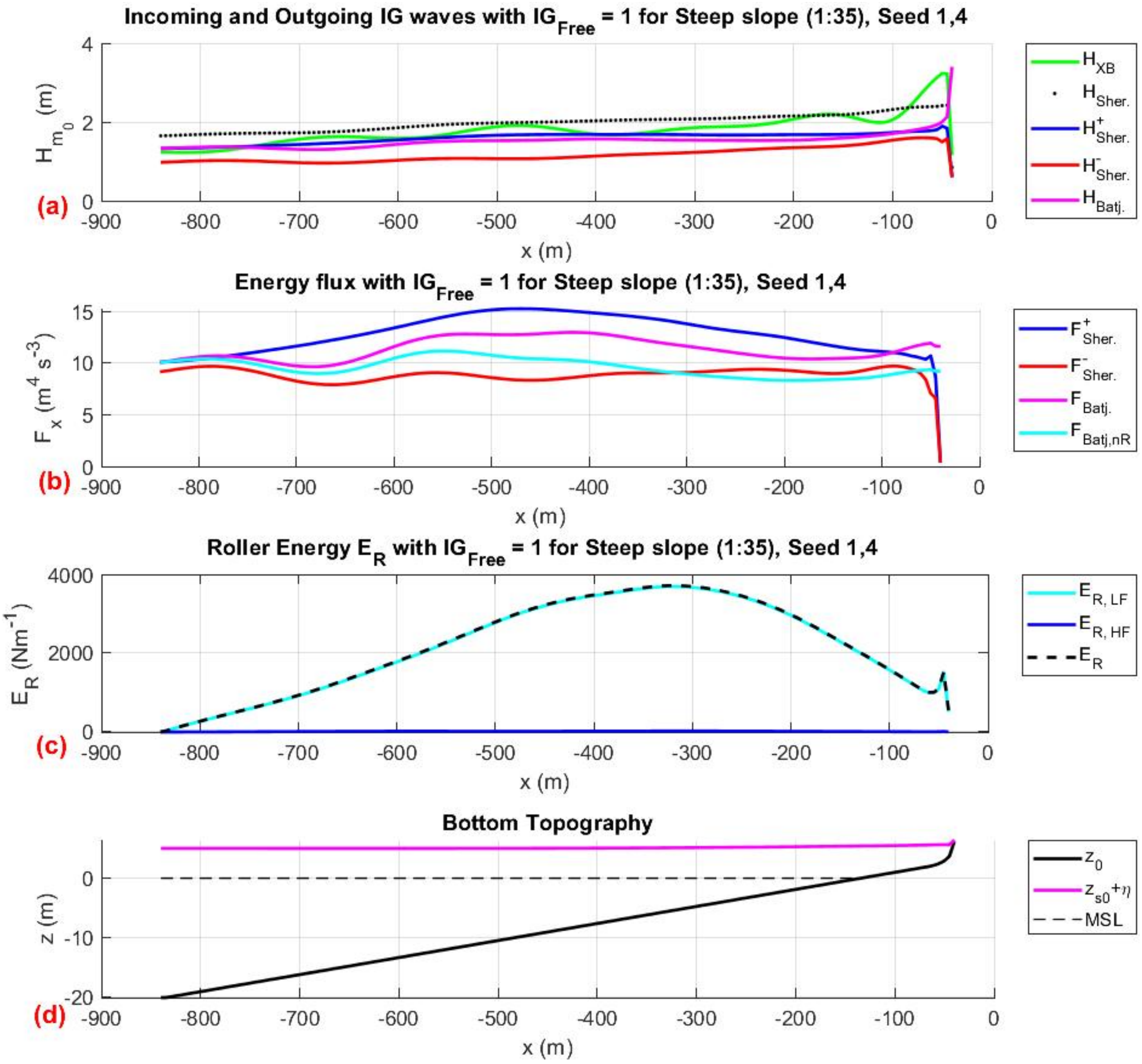

Figure C.4: Incoming and outgoing (a) significant wave height H_{m0}), and (b) energy flux for the steep slope (1:35) with $IG_{free} = 1$. Where the total significant wave height through specral analysis is summarised by the neon green line (H_{XB}. The dotted black line is the total wave height corresponding to the total flux of Sheremet et al. (2002) method H_{Sher}. The blue lines show the incoming waves, and red line the outgoing waves. Sheremet et al. (2002) method is summarised with solid blue and red lines respectively respectively. The solid magenta, and cyan line is the non-linear wave propagation of the incoming wave through Battjes et al. (2004) method by including, and excluding the roller effect respectively. (c) Roller energy E_R marked with dashed blue line for steep slope (1:35), where the blue and cyan solid lines are for the low frequency $E_{R,LF}$, and high frequency $E_{R,HF}$ contribution respectively. (d) is the bottom topography of the steep slope (1:35) where the sea bed z_0 is marked with solid black line, dashed black line indicates the MSL and the magenta line is the water elevation which includes the surface elevation η, and surge level (z_{s0}).

C.2.2. Mild Slope (1:70) with $IG_{free} = 1$

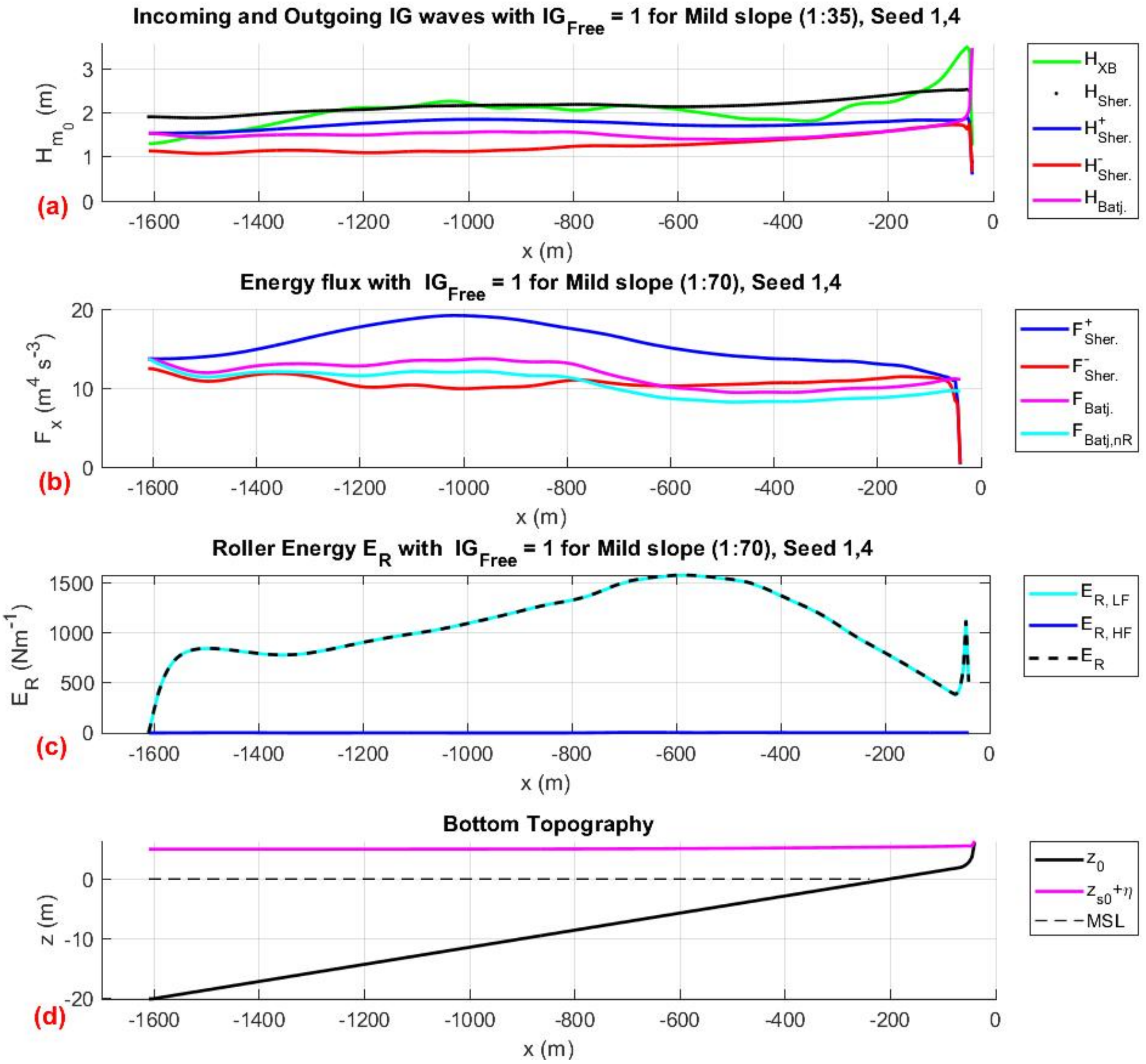

Figure C.5: Incoming and outgoing (a) significant wave height H_{m0}), and (b) energy flux for the mild slope (1:70) with $IG_{free} = 1$. Where the total significant wave height through specral analysis is summarised by the neon green line (H_{XB}. The dotted black line is the total wave height corresponding to the total flux of Sheremet et al. (2002) method H_{Sher}. The blue lines show the incoming waves, and red line the outgoing waves. Sheremet et al. (2002) method is summarised with solid blue and red lines respectively respectively. The solid magenta, and cyan line is the non-linear wave propagation of the incoming wave through Battjes et al. (2004) method by including, and excluding the roller effect respectively. (c) Roller energy E_R marked with dashed blue line for mild slope (1:70), where the blue and cyan solid lines are for the low frequency $E_{R,LF}$, and high frequency $E_{R,HF}$ contribution respectively. (d) is the bottom topography of the mild slope (1:70) where the sea bed z_0 is marked with solid black line, dashed black line indicates the MSL and the magenta line is the water elevation which includes the surface elevation η, and surge level (z_{s0}).

C.2.3. Very Mild Slope (1:130) with $IG_{free} = 1$

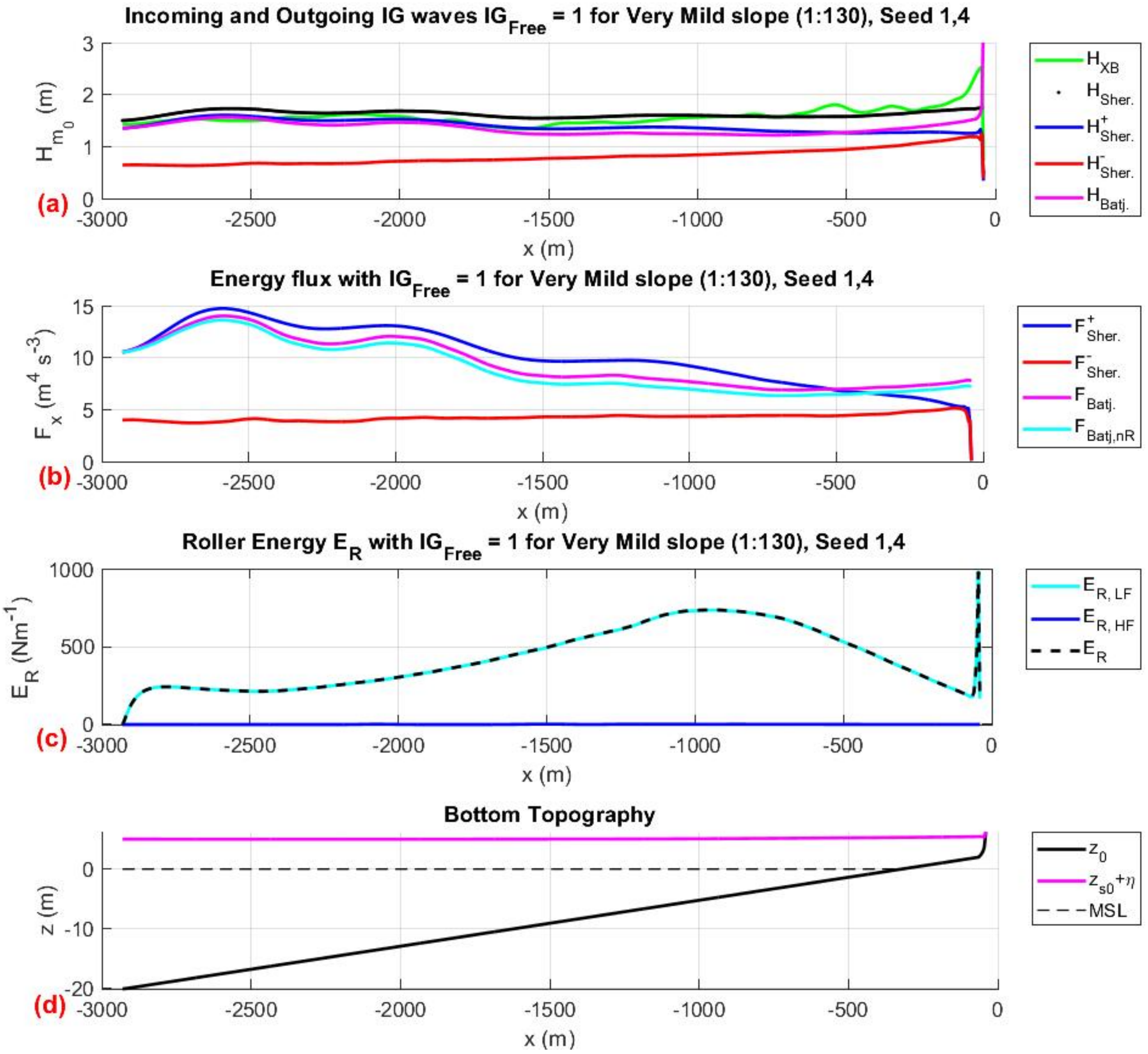

Figure C.6: Incoming and outgoing (a) significant wave height H_{m0}), and (b) energy flux for the very mild slope (1:130) with $IG_{free} = 1$. Where the total significant wave height through specral analysis is summarised by the neon green line (H_{XB}. The dotted black line is the total wave height corresponding to the total flux of Sheremet et al. (2002) method H_{Sher}. The blue lines show the incoming waves, and red line the outgoing waves. Sheremet et al. (2002) method is summarised with solid blue and red lines respectively respectively. The solid magenta, and cyan line is the non-linear wave propagation of the incoming wave through Battjes et al. (2004) method by including, and excluding the roller effect respectively. (c) Roller energy E_R marked with dashed blue line for very mild slope (1:130), where the blue and cyan solid lines are for the low frequency $E_{R,LF}$, and high frequency $E_{R,HF}$ contribution respectively. (d) is the bottom topography of the very mild slope (1:130) where the sea bed z_0 is marked with solid black line, dashed black line indicates the MSL and the magenta line is the water elevation which includes the surface elevation η, and surge level (z_{s0}).

C.3. Non-linear wave propagation for $IG_{free} = 2$

C.3.1. Steep Slope (1:35) with $IG_{free} = 2$

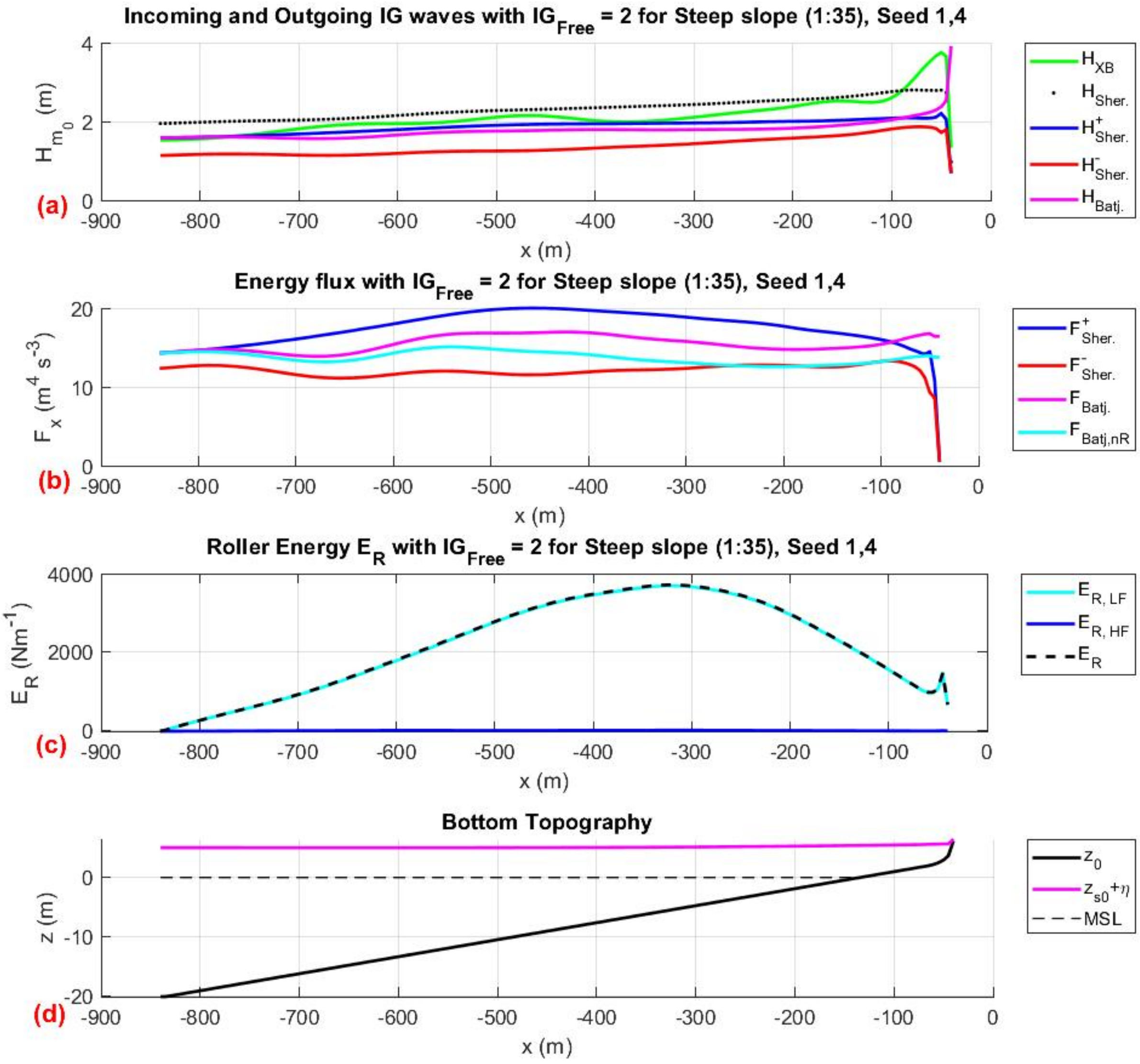

Figure C.7: Incoming and outgoing (a) significant wave height H_{m0}), and (b) energy flux for the steep slope (1:35) with $IG_{free} = 2$. Where the total significant wave height through specral analysis is summarised by the neon green line (H_{XB}. The dotted black line is the total wave height corresponding to the total flux of Sheremet et al. (2002) method H_{Sher}. The blue lines show the incoming waves, and red line the outgoing waves. Sheremet et al. (2002) method is summarised with solid blue and red lines respectively respectively. The solid magenta, and cyan line is the non-linear wave propagation of the incoming wave through Battjes et al. (2004) method by including, and excluding the roller effect respectively. (c) Roller energy E_R marked with dashed blue line for steep slope (1:35), where the blue and cyan solid lines are for the low frequency $E_{R,LF}$, and high frequency $E_{R,HF}$ contribution respectively. (d) is the bottom topography of the steep slope (1:35) where the sea bed z_0 is marked with solid black line, dashed black line indicates the MSL and the magenta line is the water elevation which includes the surface elevation η, and surge level (z_{s0}).

C.3.2. Mild Slope (1:70) with $IG_{free} = 2$

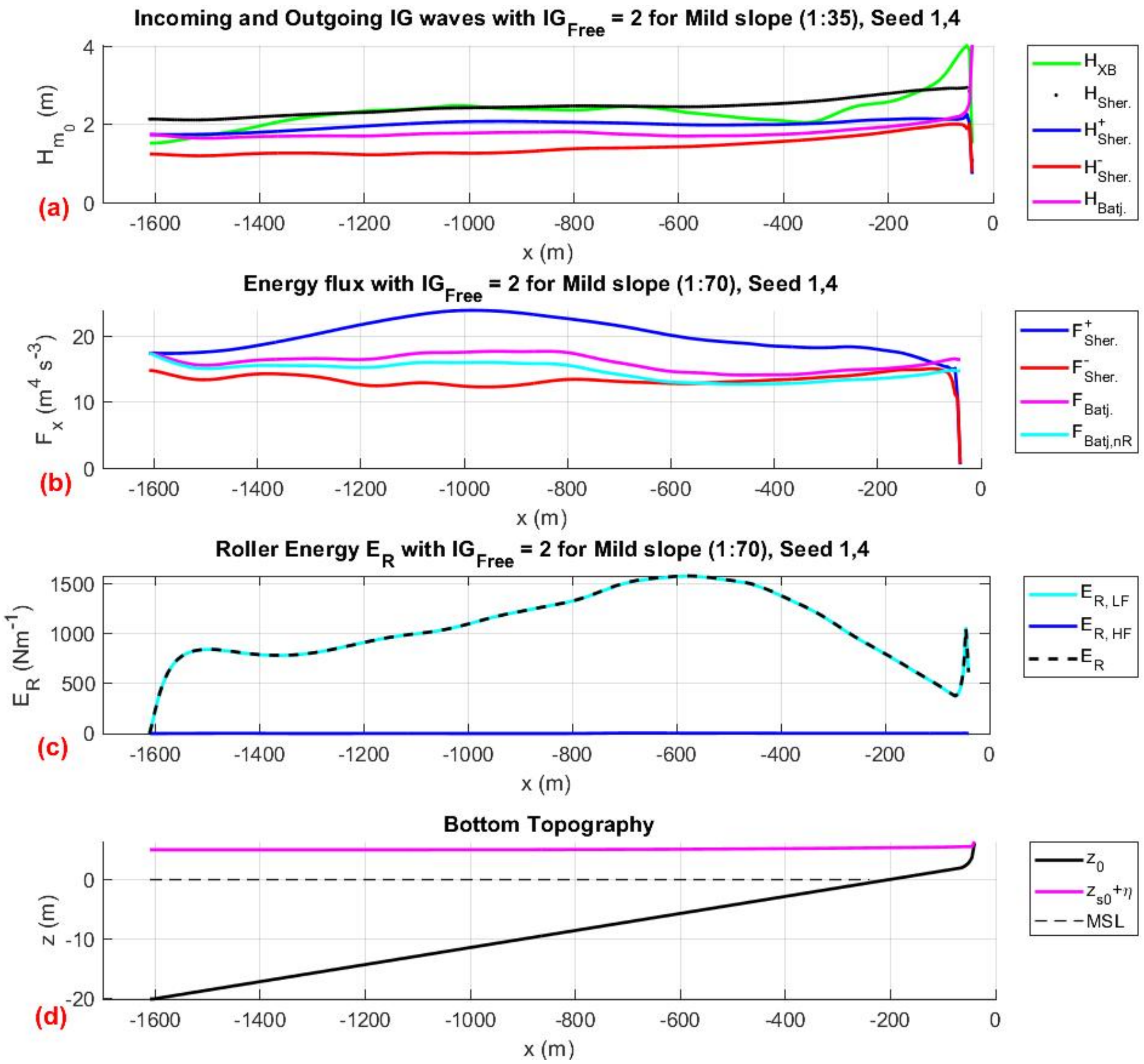

Figure C.8: Incoming and outgoing (a) significant wave height H_{m0}), and (b) energy flux for the mild slope (1:70) with $IG_{free} = 2$. Where the total significant wave height through specral analysis is summarised by the neon green line (H_{XB}. The dotted black line is the total wave height corresponding to the total flux of Sheremet et al. (2002) method H_{Sher}. The blue lines show the incoming waves, and red line the outgoing waves. Sheremet et al. (2002) method is summarised with solid blue and red lines respectively respectively. The solid magenta, and cyan line is the non-linear wave propagation of the incoming wave through Battjes et al. (2004) method by including, and excluding the roller effect respectively. (c) Roller energy E_R marked with dashed blue line for mild slope (1:70), where the blue and cyan solid lines are for the low frequency $E_{R,LF}$, and high frequency $E_{R,HF}$ contribution respectively. (d) is the bottom topography of the mild slope (1:70) where the sea bed z_0 is marked with solid black line, dashed black line indicates the MSL and the magenta line is the water elevation which includes the surface elevation η, and surge level (z_{s0}).

C.3.3. Very Mild Slope (1:130) with $IG_{free} = 2$

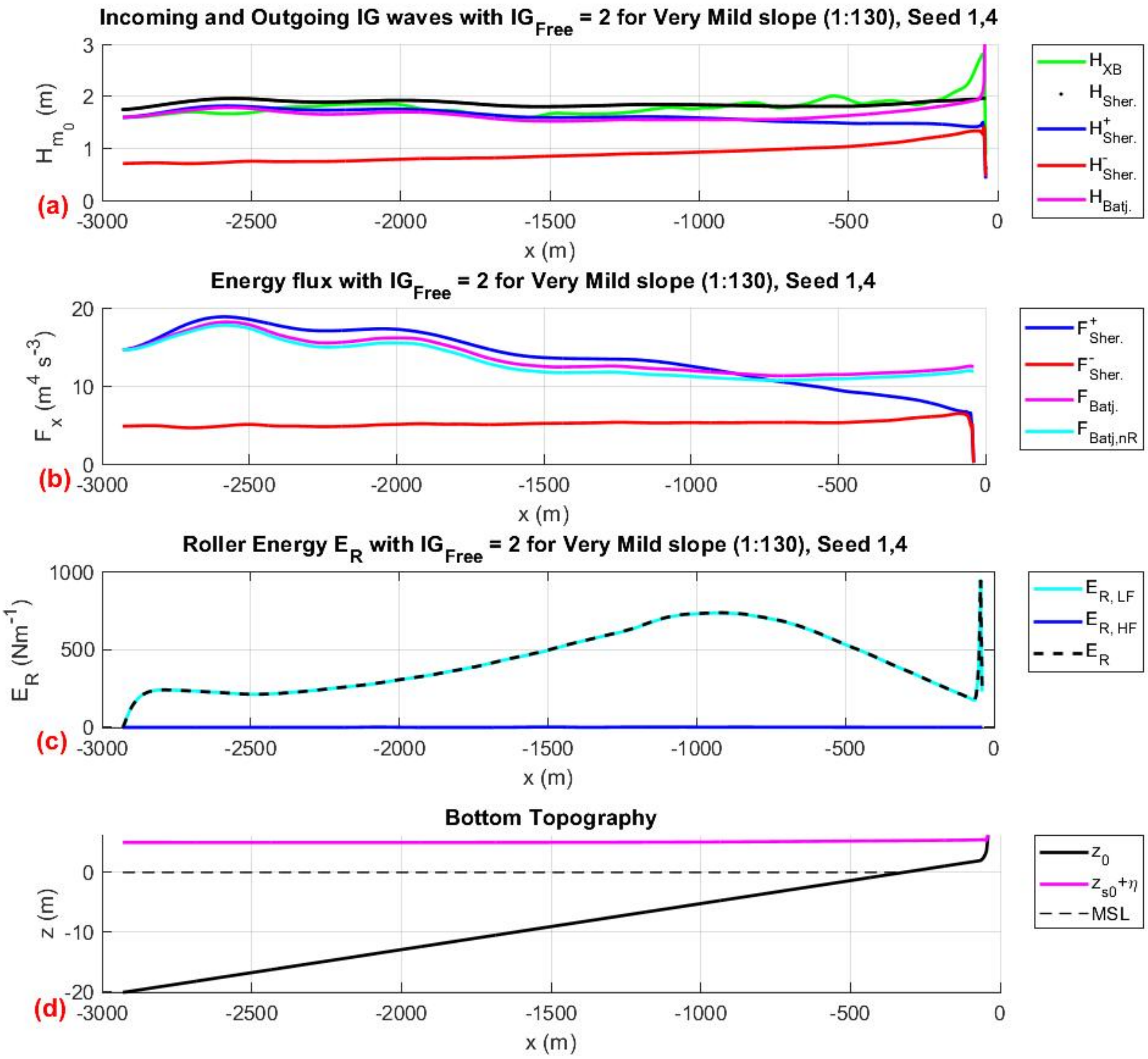

Figure C.9: Incoming and outgoing (a) significant wave height H_{m0}), and (b) energy flux for the very mild slope (1:130) with $IG_{free} = 2$. Where the total significant wave height through specral analysis is summarised by the neon green line (H_{XB}. The dotted black line is the total wave height corresponding to the total flux of Sheremet et al. (2002) method H_{Sher}. The blue lines show the incoming waves, and red line the outgoing waves. Sheremet et al. (2002) method is summarised with solid blue and red lines respectively respectively. The solid magenta, and cyan line is the non-linear wave propagation of the incoming wave through Battjes et al. (2004) method by including, and excluding the roller effect respectively. (c) Roller energy E_R marked with dashed blue line for very mild slope (1:130), where the blue and cyan solid lines are for the low frequency $E_{R,LF}$, and high frequency $E_{R,HF}$ contribution respectively. (d) is the bottom topography of the very mild slope (1:130) where the sea bed z_0 is marked with solid black line, dashed black line indicates the MSL and the magenta line is the water elevation which includes the surface elevation η, and surge level (z_{s0}).

C.4. Contribution of all IG_{free} intensities at each individual slope

C.4.1. Steep Slope (1:35) with $IG_{free} = 0$, $IG_{free} = 1$, and $IG_{free} = 2$

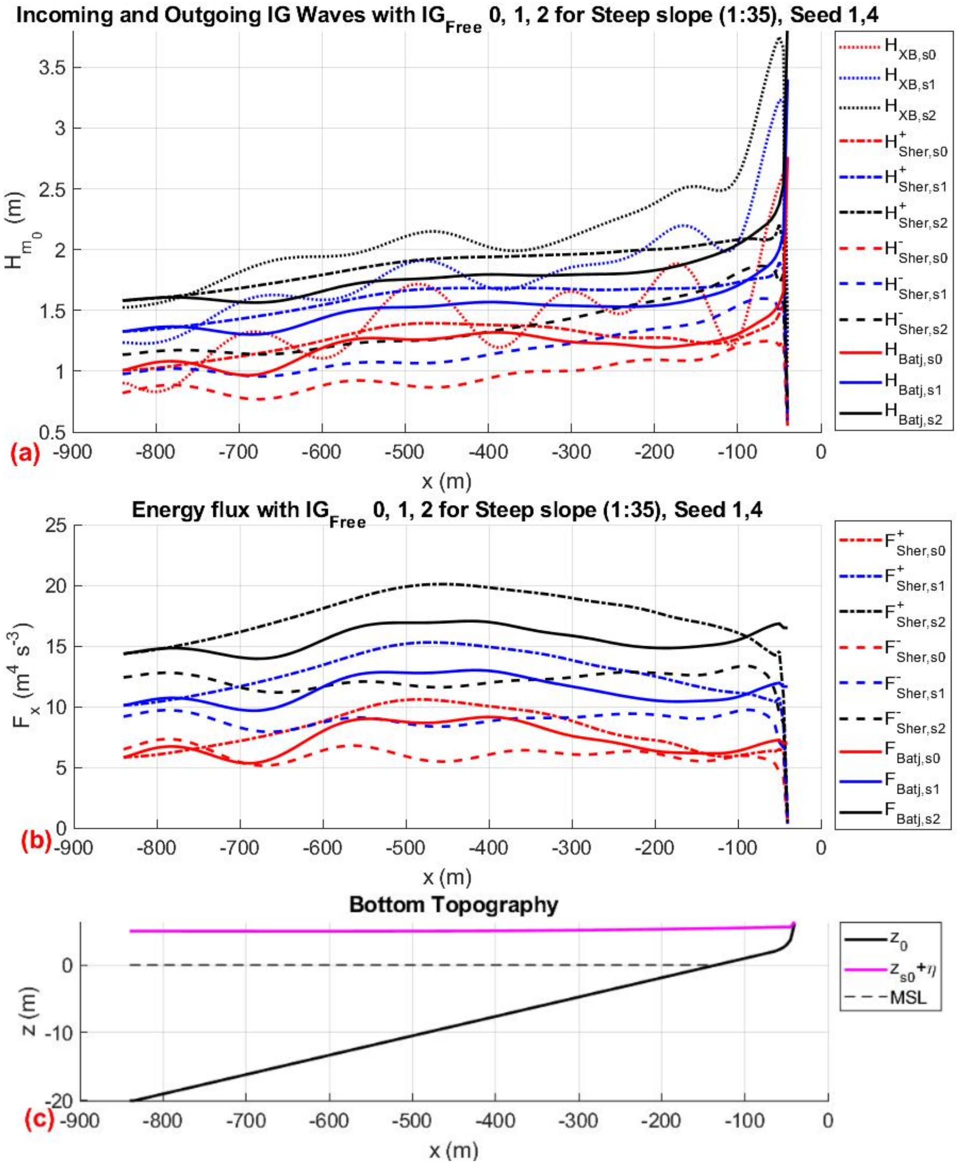
Incoming and Outgoing IG Waves with IG_{Free} 0, 1, 2 for Steep slope (1:35), Seed 1,4

Energy flux with IG_{Free} 0, 1, 2 for Steep slope (1:35), Seed 1,4

Bottom Topography

Figure C.10: The linear and non liner wave contribution for (a) the significant wave height, (b) the energy flux for the steep slope (1:35). The free infragravity intensities are coloured, red for $IG_{free} = 0$, blue for $IG_{free} = 1$, and black for $IG_{free} = 2$. The total spectral wave height H_{XB} is denoted with a dashed line, the significant wave height H_m0 and energy flux F_x, from Battjes et al. (2004) (subscript Batj) denoted by a solid line, from Sheremet et al. (2002) (subscript Sher) for incoming, and outgoing wave denoted with dashed-dot, and dashed line respectively. (c) The bottom topography for the steep slope (1:35), where the sea bed z_0 is marked with solid black lines, the MSL is marked with dashed black line, and the the water elevation marked with solid magenta line includes the surface elevation η, and surge level (z_{s0}).

C.4.2. Mild Slope (1:70) with $IG_{free} = 0$, $IG_{free} = 1$, and $IG_{free} = 2$

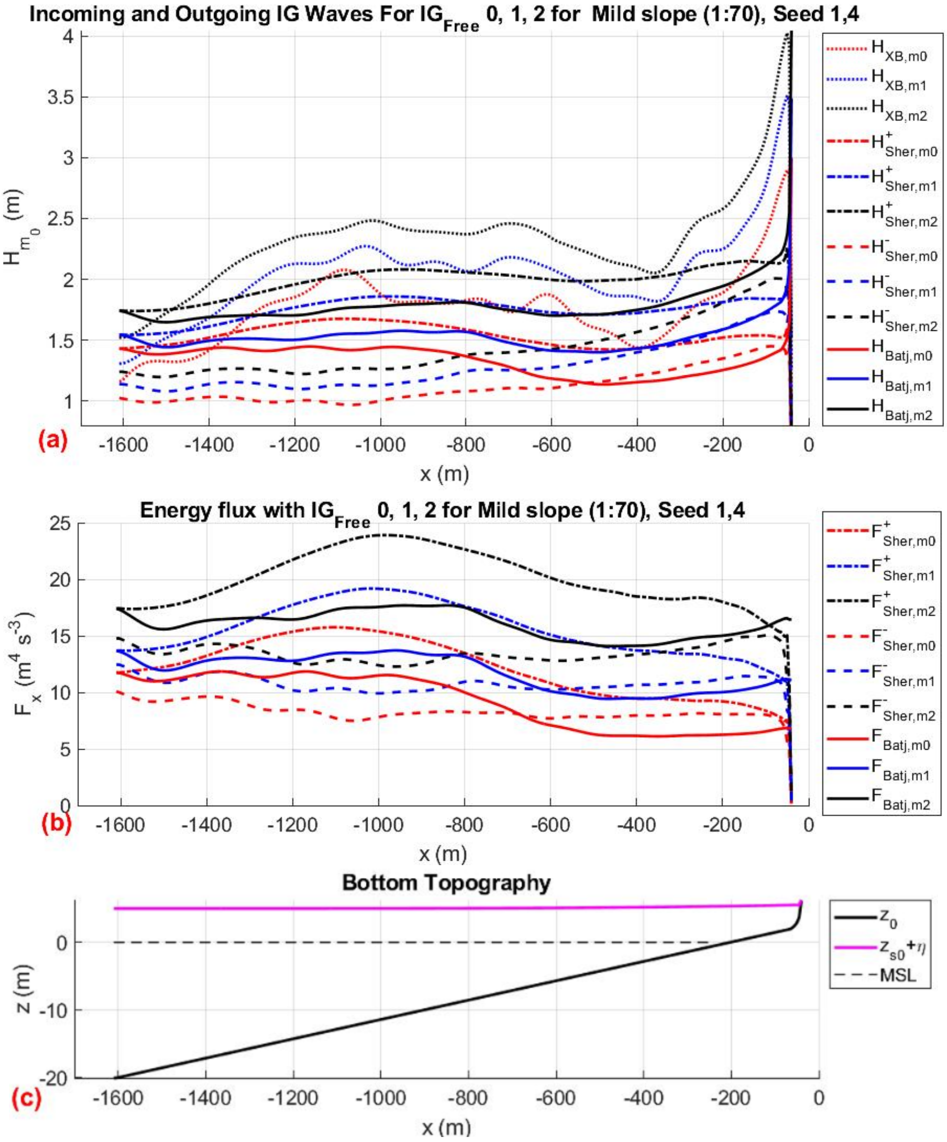

Figure C.11: The linear and non liner wave contribution for (a) the significant wave height, (b) the energy flux for the mild slope (1:70). The free infragravity intensities are coloured, red for $IG_{free} = 0$, blue for $IG_{free} = 1$, and black for $IG_{free} = 2$. The total spectral wave height H_{XB} is denoted with a dashed line, the significant wave height H_m0 and energy flux F_x, from Battjes et al. (2004) (subscript Batj) denoted by a solid line, from Sheremet et al. (2002) (subscript Sher) for incoming, and outgoing wave denoted with dashed-dot, and dashed line respectively. (c) The bottom topography for the mild slope (1:70), where the sea bed z_0 is marked with solid black lines, the MSL is marked with dashed black line, and the the water elevation marked with solid magenta line includes the surface elevation η, and surge level (z_{m0}).

C.4.3. Very Mild Slope (1:130) with $IG_{free} = 0$, $IG_{free} = 1$, and $IG_{free} = 2$

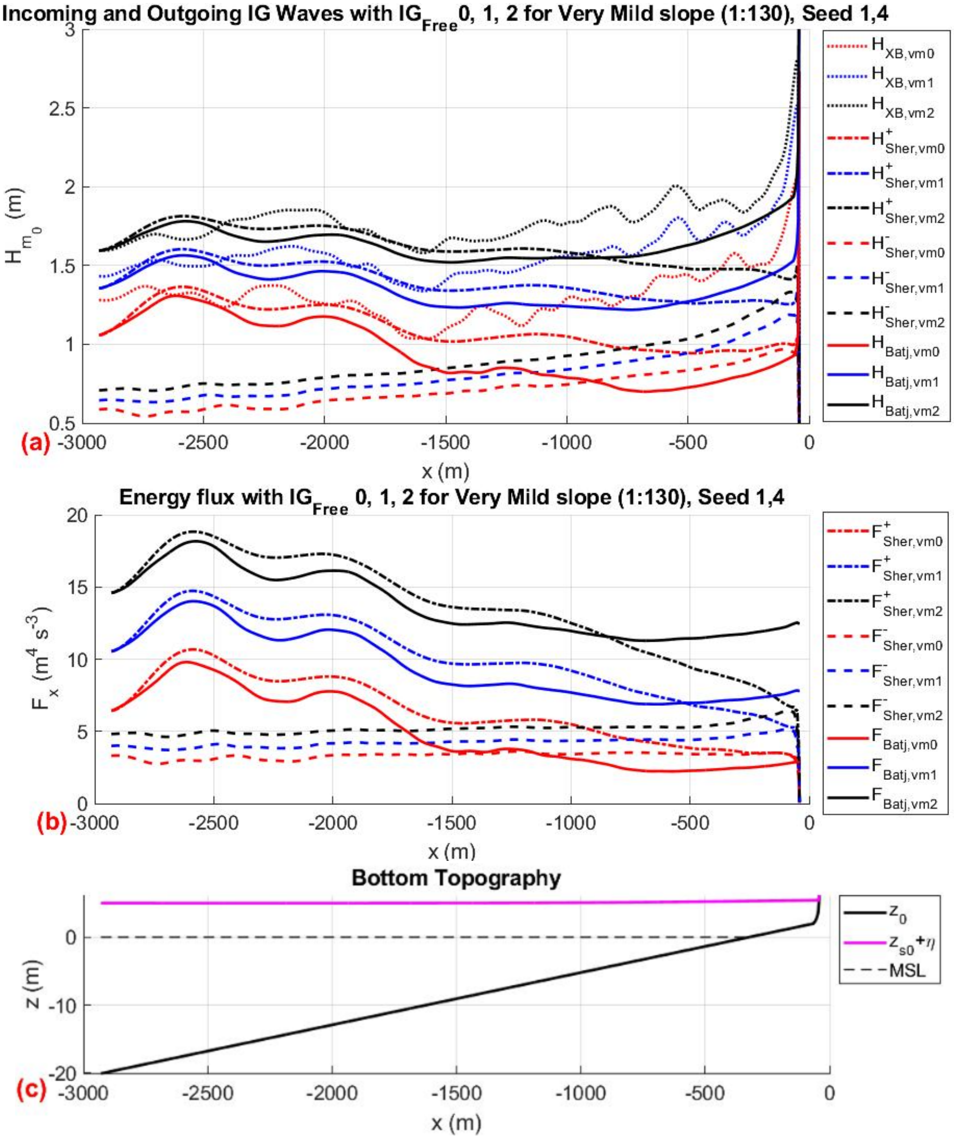

Figure C.12: The linear and non liner wave contribution for (a) the significant wave height, (b) the energy flux for the very mild slope (1:130). The free infragravity intensities are coloured, red for $IG_{free} = 0$, blue for $IG_{free} = 1$, and black for $IG_{free} = 2$. The total spectral wave height H_{XB} is denoted with a dashed line, the significant wave height H_m0 and energy flux F_x, from Battjes et al. (2004) (subscript Batj) denoted by a solid line, from Sheremet et al. (2002) (subscript Sher) for incoming, and outgoing wave denoted with dashed-dot, and dashed line respectively. (c) The bottom topography for the very slope (1:130), where the sea bed z_0 is marked with solid black lines, the MSL is marked with dashed black line, and the the water elevation marked with solid magenta line includes the surface elevation η, and surge level (z_{vm0}).

D

Linear Wave Propagation

D.1. Linear Wave propagation of $IG_{free} = 1$

D.1.1. Steep slope (1:35) with $IG_{free} = 1$

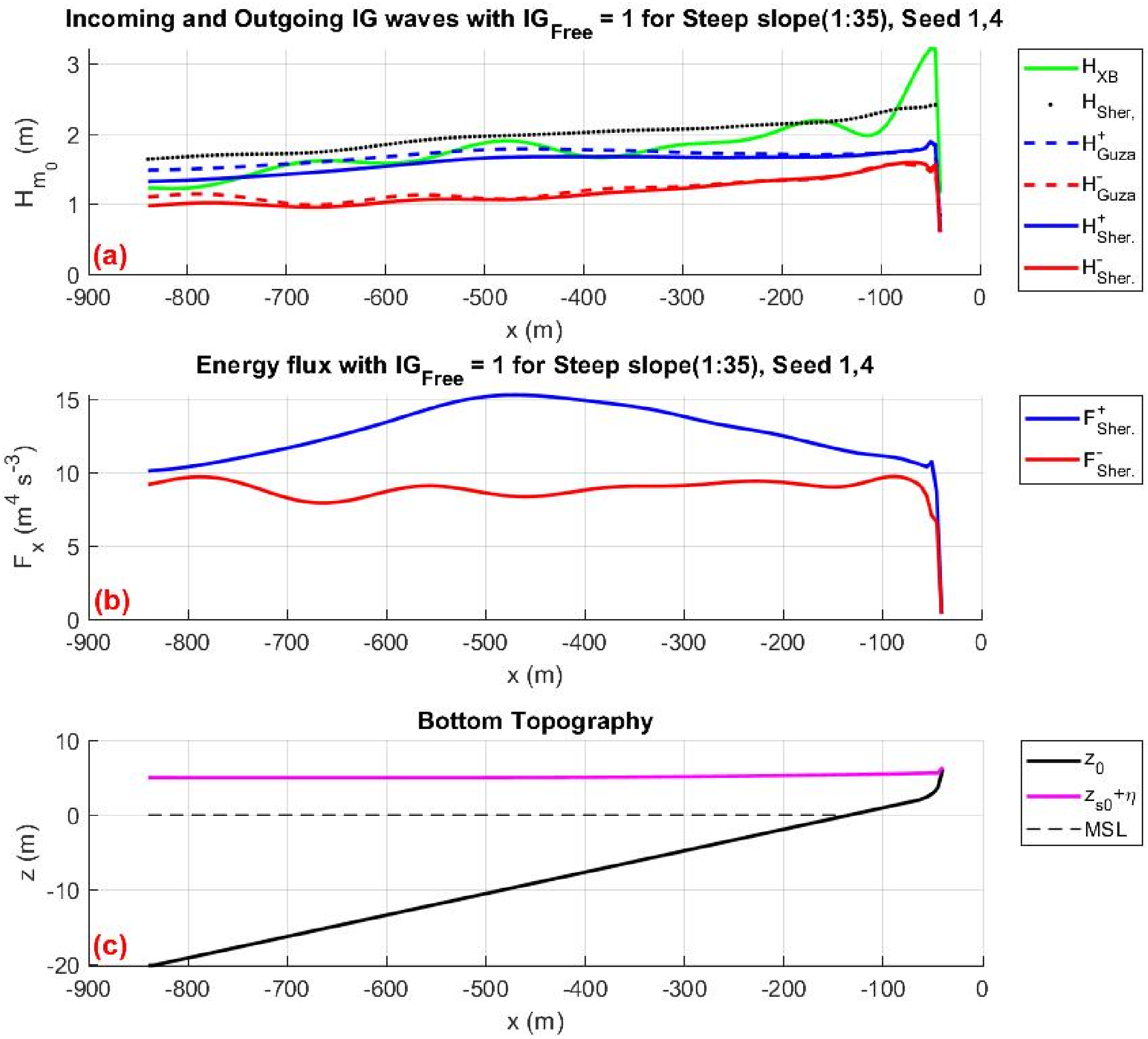

Figure D.1: Incoming and outgoing (a) significant wave height H_{m0}), and (b) linear energy flux for the steep slope (1:35) with $IG_{free=1}$. Where the total significant wave height is summarised by the neon green line (H_{XB}. The dotted black line is the total wave height corresponding to the total flux of Sheremet method $H_{Sher.}$. The blue lines show the incoming waves, and red line the outgoing waves. Sheremet et al. (2002) method is summarised with solid blue and red lines, whilst Guza et al. (1984) is dashed blue and red lines. (c) is the bottom topography of the steep slope (1:35) where the sea bed z_0 is marked with solid black line, dashed black line indicates the MSL and the magenta line is the water elevation which includes the surface elevation η, and surge level (z_{s0}).

D.1.2. Mild slope (1:70) with $IG_{free} = 1$

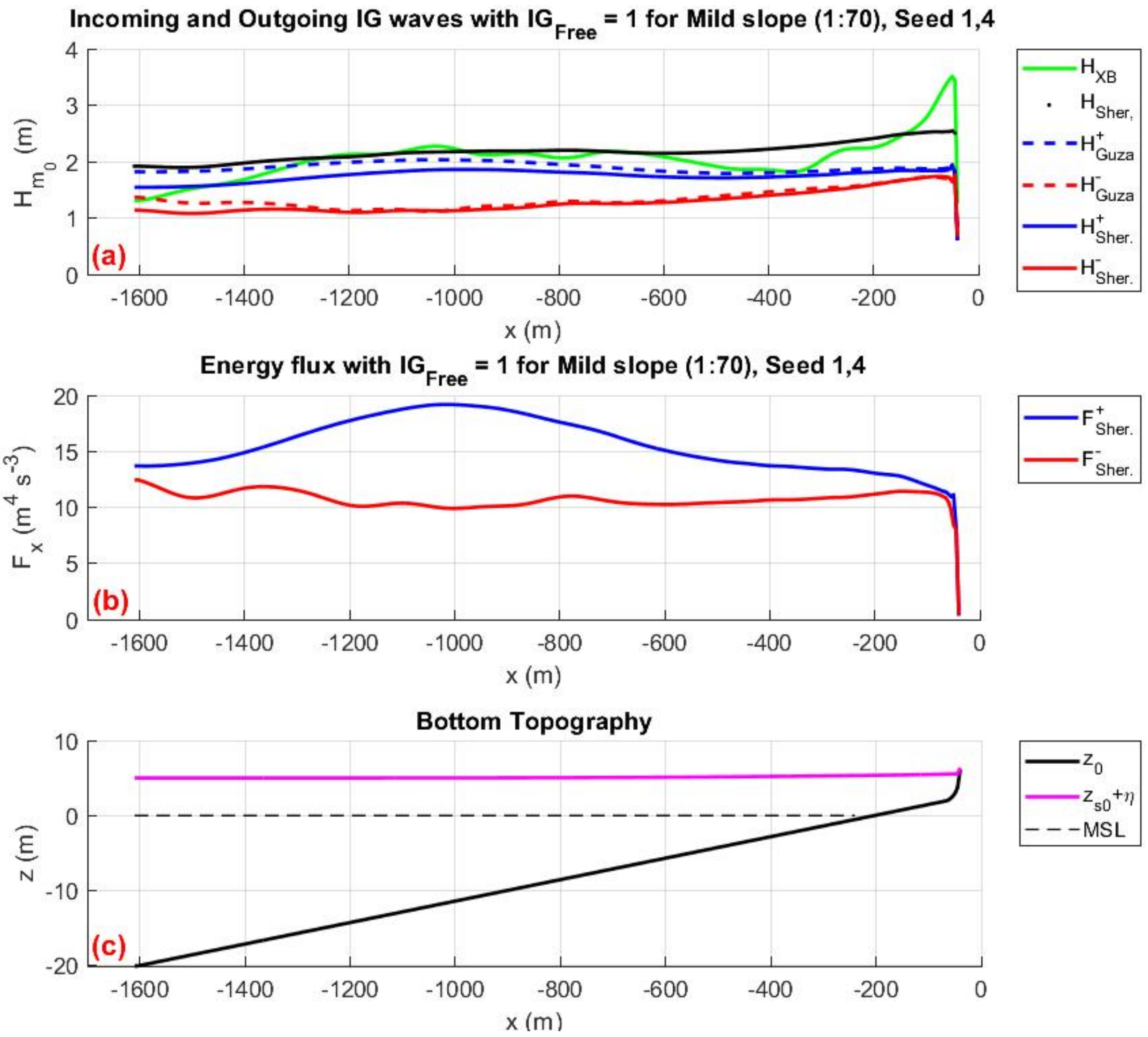

Figure D.2: Incoming and outgoing (a) significant wave height H_{m0}), and (b) linear energy flux for the mild slope (1:70) with $IG_{free=1}$. Where the total significant wave height is summarised by the neon green line (H_{XB}. The dotted black line is the total wave height corresponding to the total flux of Sheremet method $H_{Sher.}$. The blue lines show the incoming waves, and red line the outgoing waves. Sheremet et al. (2002) method is summarised with solid blue and red lines, whilst Guza et al. (1984) is dashed blue and red lines. (c) is the bottom topography of the mild slope (1:70) where the sea bed z_0 is marked with solid black line, dashed black line indicates the MSL and the magenta line is the water elevation which includes the surface elevation η, and surge level (z_{s0}).

D.1.3. Very Mild slope (1:130) with $IG_{free} = 1$

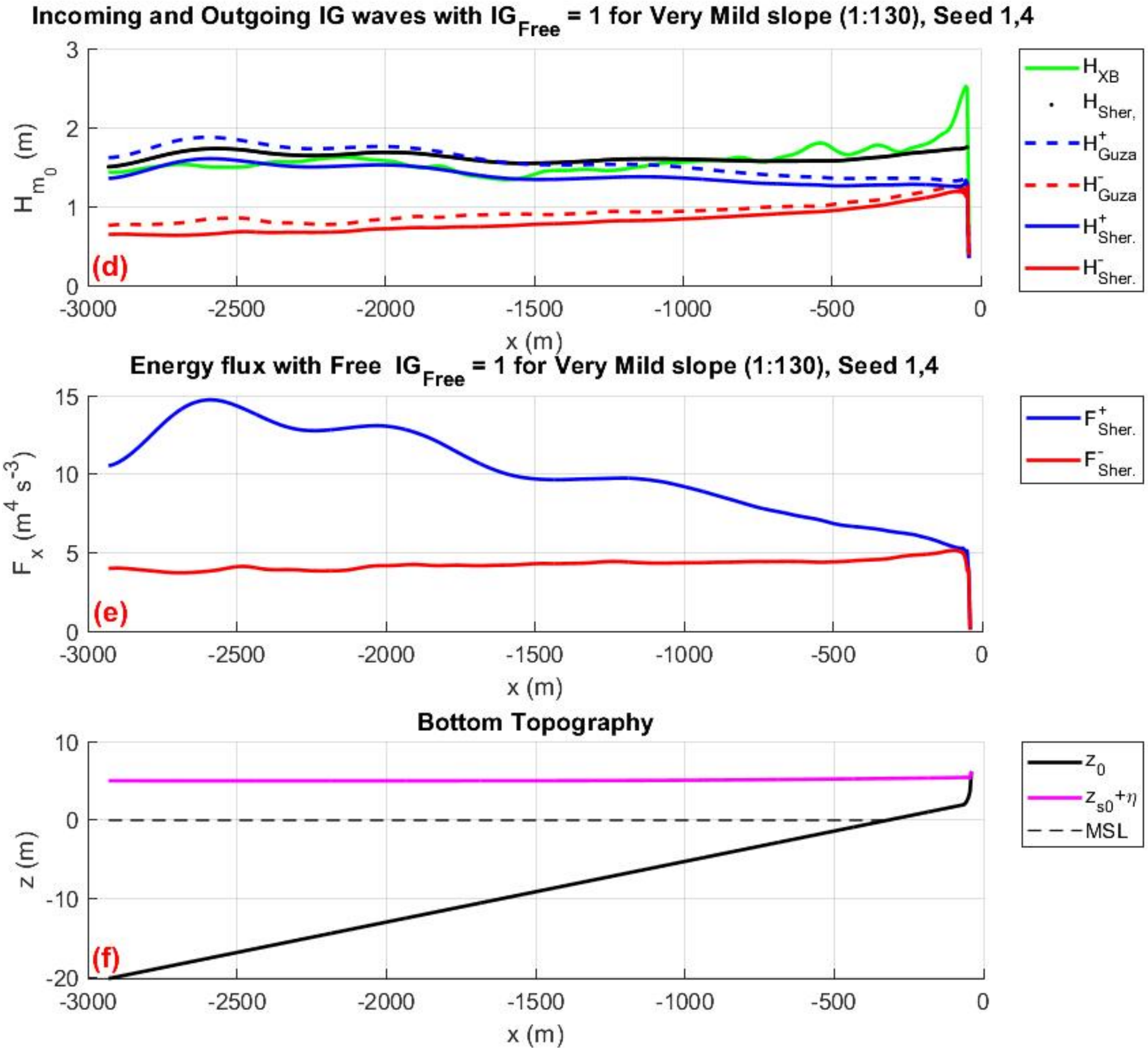

Figure D.3: Incoming and outgoing (a) significant wave height H_{m0}), and (b) linear energy flux for the very mild slope (1:130) with $IG_{free=1}$. Where the total significant wave height is summarised by the neon green line (H_{XB}. The dotted black line is the total wave height corresponding to the total flux of Sheremet method $H_{Sher.}$. The blue lines show the incoming waves, and red line the outgoing waves. Sheremet et al. (2002) method is summarised with solid blue and red lines, whilst Guza et al. (1984) is dashed blue and red lines. (c) is the bottom topography of the very mild slope (1:130) where the sea bed z_0 is marked with solid black line, dashed black line indicates the MSL and the magenta line is the water elevation which includes the surface elevation η, and surge level (z_{s0}).

D.2. Linear Wave propagation of $IG_{free} = 2$

D.2.1. Steep slope (1:35) with $IG_{free} = 2$

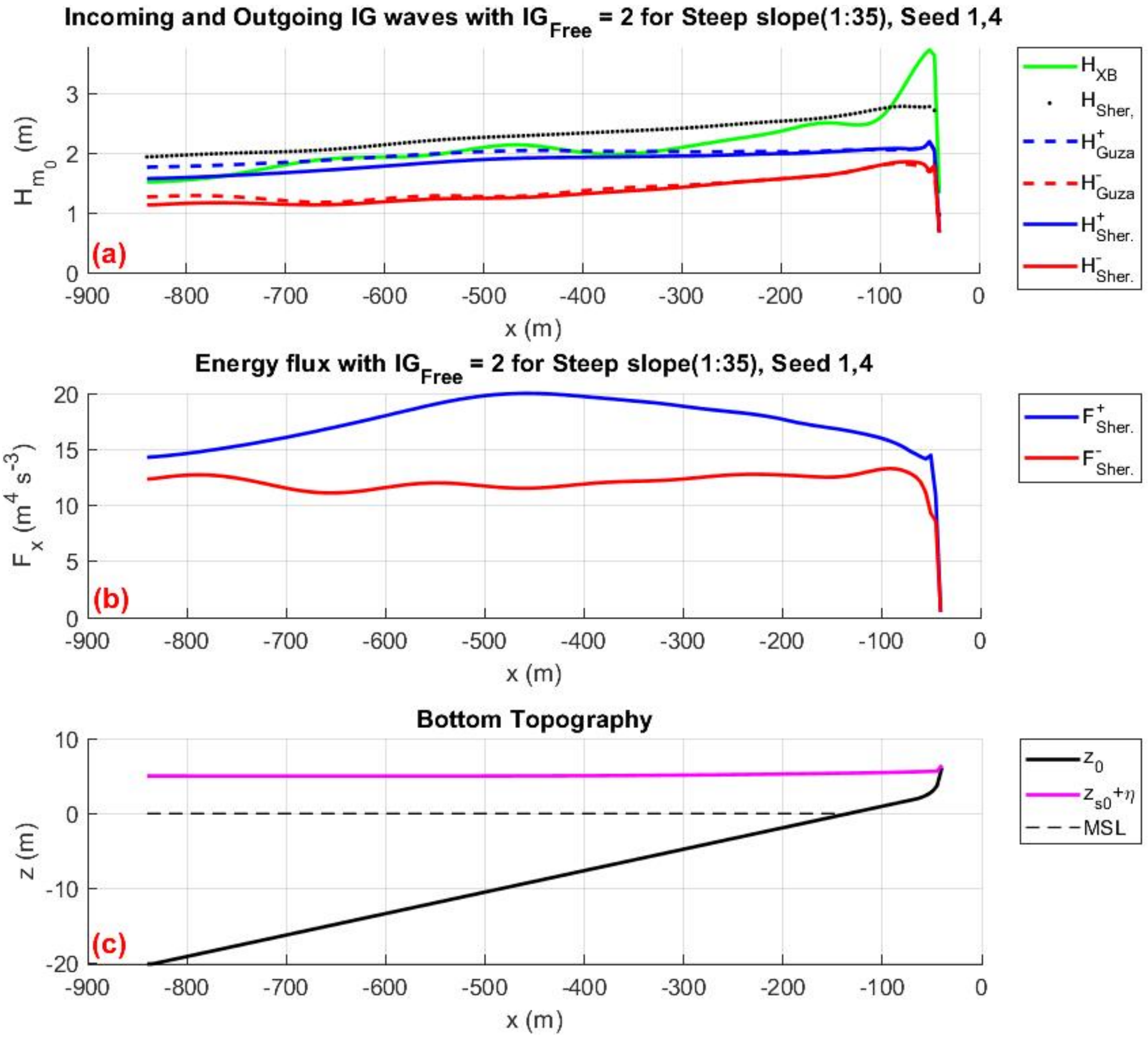

Figure D.4: Incoming and outgoing (a) significant wave height H_{m0}), and (b) linear energy flux for the steep slope (1:35) with $IG_{free=2}$. Where the total significant wave height is summarised by the neon green line (H_{XB}. The dotted black line is the total wave height corresponding to the total flux of Sheremet method $H_{Sher.}$. The blue lines show the incoming waves, and red line the outgoing waves. Sheremet et al. (2002) method is summarised with solid blue and red lines, whilst Guza et al. (1984) is dashed blue and red lines. (c) is the bottom topography of the steep slope (1:35) where the sea bed z_0 is marked with solid black line, dashed black line indicates the MSL and the magenta line is the water elevation which includes the surface elevation η, and surge level (z_{s0}).

D.2.2. Mild slope (1:70) with $IG_{free} = 2$

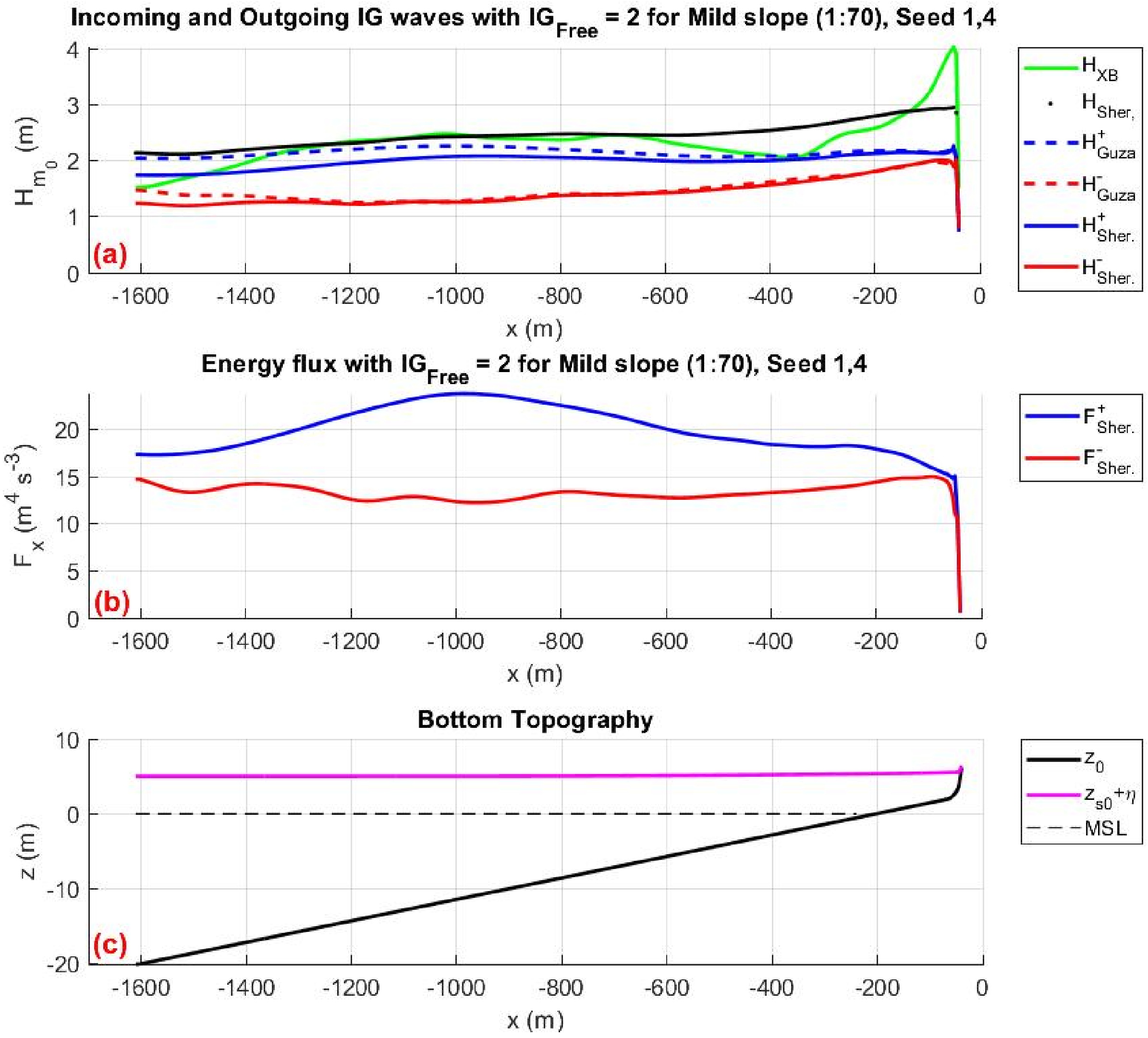

Figure D.5: Incoming and outgoing (a) significant wave height H_{m0}), and (b) linear energy flux for the mild slope (1:70) with $IG_{free=2}$. Where the total significant wave height is summarised by the neon green line (H_{XB}. The dotted black line is the total wave height corresponding to the total flux of Sheremet method $H_{Sher.}$. The blue lines show the incoming waves, and red line the outgoing waves. Sheremet et al. (2002) method is summarised with solid blue and red lines, whilst Guza et al. (1984) is dashed blue and red lines. (c) is the bottom topography of the mild slope (1:70) where the sea bed z_0 is marked with solid black line, dashed black line indicates the MSL and the magenta line is the water elevation which includes the surface elevation η, and surge level (z_{s0}).

D.2.3. Very Mild slope (1:130) with $IG_{free} = 2$

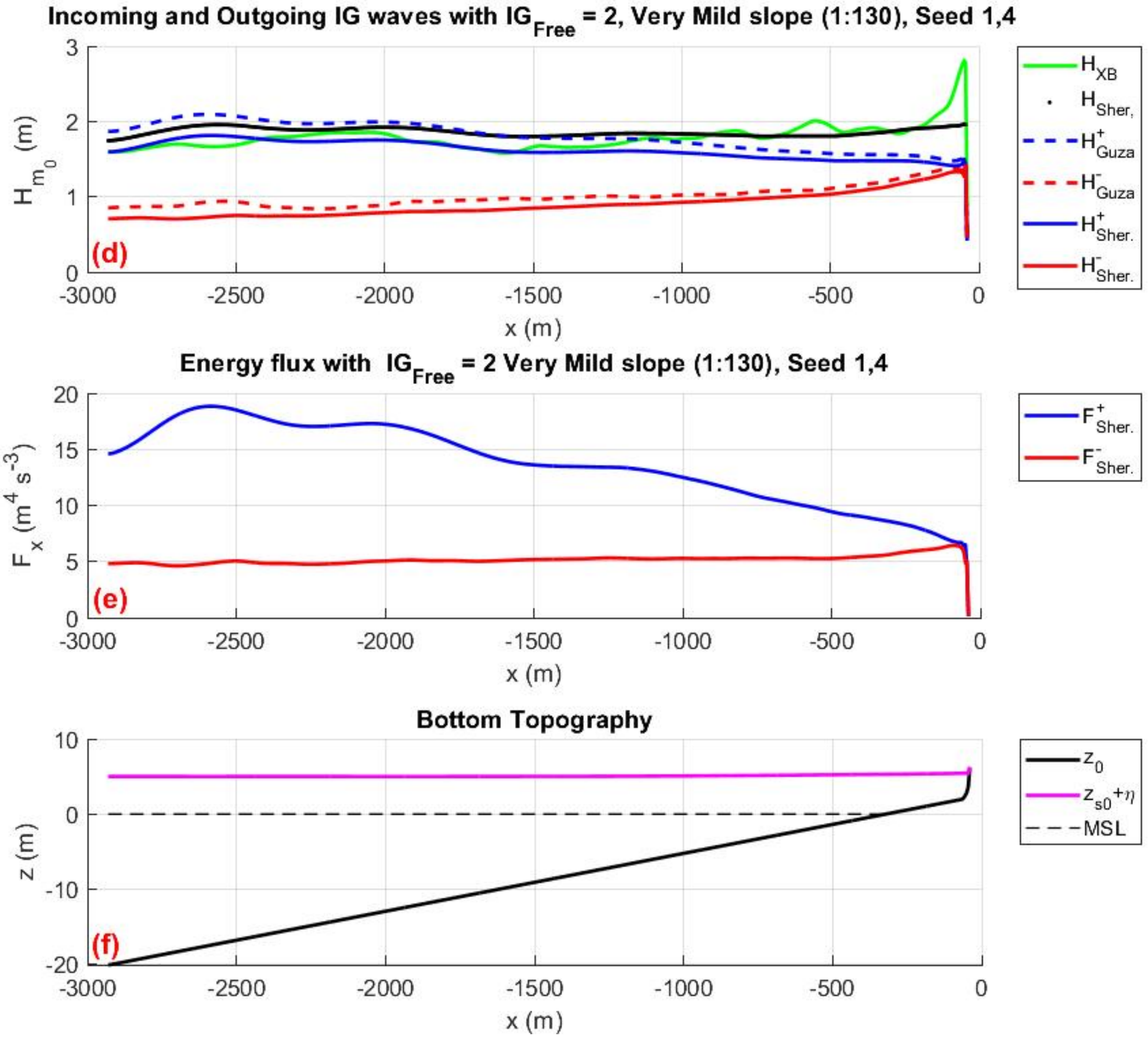
Incoming and Outgoing IG waves with IG_{Free} = 2, Very Mild slope (1:130), Seed 1,4

Energy flux with IG_{Free} = 2 Very Mild slope (1:130), Seed 1,4

Bottom Topography

Figure D.6: Incoming and outgoing (a) significant wave height H_{m0}), and (b) linear energy flux for the very mild slope (1:130) with $IG_{free=2}$. Where the total significant wave height is summarised by the neon green line (H_{XB}. The dotted black line is the total wave height corresponding to the total flux of Sheremet method $H_{Sher.}$. The blue lines show the incoming waves, and red line the outgoing waves. Sheremet et al. (2002) method is summarised with solid blue and red lines, whilst Guza et al. (1984) is dashed blue and red lines. (c) is the bottom topography of the very mild slope (1:130) where the sea bed z_0 is marked with solid black line, dashed black line indicates the MSL and the magenta line is the water elevation which includes the surface elevation η, and surge level (z_{s0}).

E

Runup

The runup is conducted using the empirical $R_{2\%}$ from Stockdon et al. (2006) method equation (3.45), and the cumulative distribution F(x) of the data $F_{data}(x)$ that is specific to our case. The cumulative distribution obtained from our data $F_{data}(x)$ is then fitted with empirical cumulative distributions $F_{emp.}(x)$ as described in Figure E.1 with the method as described in section 3.3.5 of this report.

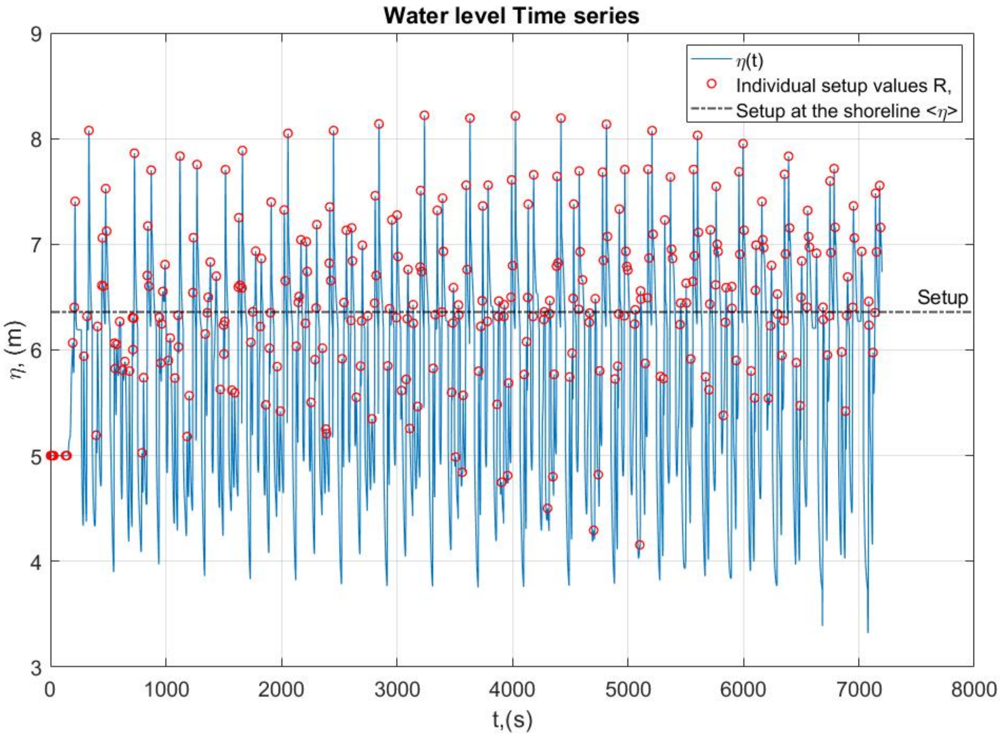

Figure E.1: Water level time series $\eta(t)$ (blue line), with the maximum setup $<\eta>$ (black dash-dotetd line), and the individual runup maxima R (red circles) are indicated for the Mild slope with $IG_{free} = 1$.

The distributions considered for the $F_{emp.}(x)$ are (1) Generalized Extreme Value GEV, (2) Extreme value EV, (3) Normal N, (4) Weibull WB, and (5) tLocationScale tLS. The F(x) distribution can be observed between the data and GEV distribution at Figure E.2 for the mild slope with $IG_{free} = 1$. These 5 distributions are then compared and define with the $F_{data}(x)$ through a 'goodness of fit' test through the sum of square differences SSD, and Kolmogorov Smirnov ks test as defined in equation (3.46), and equation (3.47) respectively. The closer the value obtained by both SSD and ks the better the $F_{emp.}(x)$ fit is to the $F_{data}(x)$.

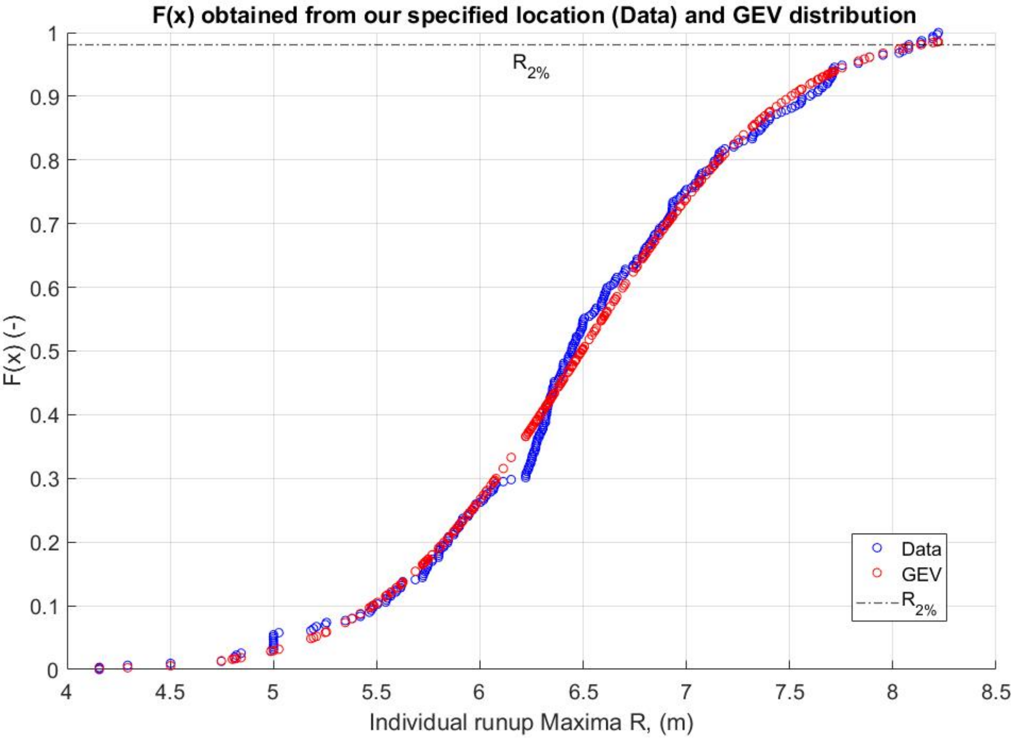

Figure E.2: Water level time series $\eta(t)$ (blue line), with the maximum setup $< \eta >$ (black dash-dotted line), and the individual runup maxima R (red circles) are indicated for the Mild slope with $IG_{free} = 1$.

The comparison between the two different obtained $R_{2\%}$ methods from Stockdon et al. (2006), and with the F(x) method are both summarised at Table E.1. Since the F(x) distributions are varying in the same slope and between each different slope, F_{data}(x) is chosen to define the $R_{2\%}$ values, and not the $F_{emp.}$(x) $R_{2\%}$ values. The best fitted distribution $R_{2\%}$ values are not indicated in the table below, due to this above conclusion, therefore, not considered.

Slope	**Waves Induced**	$R_{2\%,data}$ (m)	**F(x)** (-)	**ks** (-)	**SSD** (-)	$R_{2\%,Stock}$ (m)
Steep (1:35)	$IG_{free} = 0$	***7.70***	WB	0.1647	1.802	7.46
	$IG_{free} = 1$	***7.96***	WB	0.079	0.168	7.59
	$IG_{free} = 2$	***8.08***	WB	0.056	0.182	7.69
	$IG_{only} = 1$	***6.65***	WB	0.047	0.131	7.13
	$IG_{only} = 2$	***7.41***	EV	0.060	0.193	7.31
Mild (1:70)	$IG_{free} = 0$	***7.36***	N	0.083	0.608	7.39
	$IG_{free} = 1$	***8.08***	GEV	0.064	0.174	7.54
	$IG_{free} = 2$	***8.45***	GEV	0.072	0.256	7.65
	$IG_{only} = 1$	***6.83***	EV	0.070	0.191	7.14
	$IG_{only} = 2$	***7.58***	EV	0.080	0.524	7.30
Very Mild (1:130)	$IG_{free} = 0$	***6.82***	EV	0.081	0.360	7.13
	$IG_{free} = 1$	***7.37***	EV	0.086	0.411	7.31
	$IG_{free} = 2$	***7.74***	EV	0.086	0.403	7.38
	$IG_{only} = 1$	***6.50***	GEV	0.073	0.111	7.04
	$IG_{only} = 2$	***6.73***	GEV	0.086	0.320	7.13

Table E.1: The wave runup $R_{2\%}$ obtained from the raw data of our simulations $R_{2\%,data}$, and from the empirical method of Stockdon et al. (2006 $R_{2\%,Stock}$ both obtained for different slopes and waves induced at the offshore boundary boundary. The different slopes used include the steep (1:35), mild (1:70), and very mild (1:130) slope. Kormokorov Smirnov ks and Sum of Square Differences SSD are both used to describe the 'goodness of fit' of the raw data between the empirical cumulative distribution function F(x). The wave conditions induced, include the bound waves with free infragravity waves IG_{free}, and only free infragravity waves IG_{only}. The subscript includes a number of 0, 1, and 2, that describe the free infragravity magnitude present in the wave domain.

F

Break Point

The breakpoint is obtained through both the roller energy highest point, and the sea-swell significant wave height change when observed through the cross shore distance.

F.1. Roller Energy

Roller energy of steep (1:35), mild (1:70), and very mild slope (1:135) illustrated at Figure F.1 for IG_{free} = 0, IG_{free} = 1, and IG_{free} = 2 conditions. The highest mean roller energy E_R s located at depth of 5.3 m approximately.

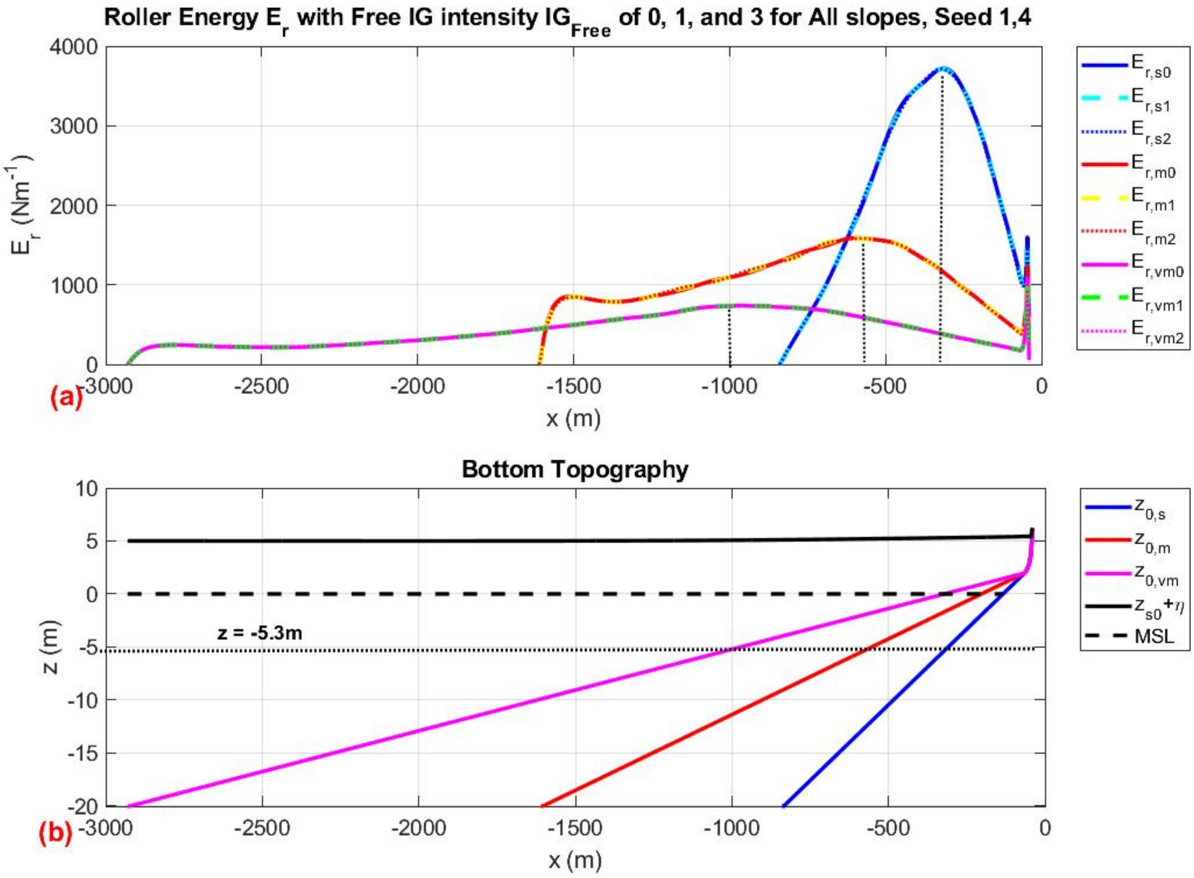

Figure F.1: (a) Mean Roller Energy E_r), for IG_{free} of 0, 1 and 2 for steep (1:35), mild (1:70), and very mild (1:130) slope. Where the solid line is the $IG_{Free} = 0$ therefore bound waves, dashed line is the $IG_{Free} = 1$, and dotted line is $IG_{Free} = 2$. The blue and cyan line are referring to the steep slope, red and yellow line to the mild slope, lastly magenta and green line to the very mild slope.(b) Bottom topography $z0$ for steep, mild, and very mild slope illustrated with a blue, red, and magenta line respectively. The mean sea level MSL is marked with dashed black line, and with solid black line the water line which is a combination of the surface elevation η and surge level z_{s0}.

F.2. Sea-swell Significant Wave Height

To have a better understanding of our domain, the breaker point is first defined for the different slopes, and wave conditions induced Figure F.2. The breaker point is constant for the same slope regardless of the different IG_{free} intensities Figure F.2. The waves are therefore breaking at a similar water depth h of 3.5 m as noted in Figure F.2 and Table F.1. The reason of the wave breaker point being the relatively the same for the same slope is due to the sea-swell wave forcing of the bound waves is constant induced with the same seed number (number 4). However due to the different forcing mechanisms the breaker point effect is observed throughout the wave domain especially more so for the milder slopes. The same conclusion can be obtained from the roller energy E_R present in the cross shore shown in Appendix F.1. As a result, with Figure F.2 the waves are assumed to break at the same depth and corresponding to approximate cross shore distance as summarised at Table F.1.

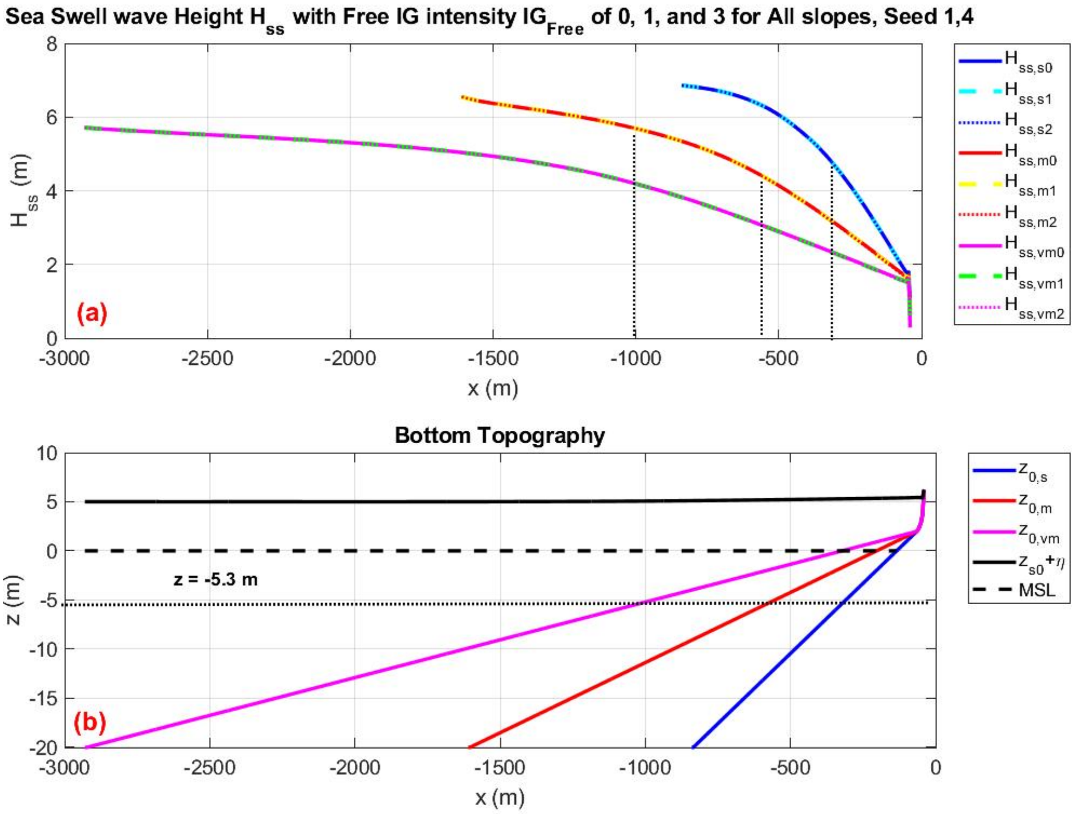

Figure F.2: (a) Sea-swell significant wave height H_{ss}), for IG_{free} of 0, 1 and 2 for steep (1:35), mild (1:70), and very mild (1:130) slope. Where the solid line is the $IG_{Free} = 0$ therefore bound waves, dashed line is the $IG_{Free} = 1$, and dotted line is $IG_{Free} = 2$. The blue and cyan line are referring to the steep slope, red and yellow line to the mild slope, lastly magenta and green line to the very mild slope.(b) Bottom topography $z0$ for steep, mild, and very mild slope illustrated with a blue, red, and magenta line respectively. The mean sea level MSL is marked with dashed black line, and with solid black line the water line which is a combination of the surface elevation η and surge level z_{s0}.

Slope (-)	Water Depth, h (m)	Cross shore Distance x (m)
Steep (1:35)	5.3	-320
Mild (1:70)	5.3	-575
Very Mild (1:70)	5.3	-1000

Table F.1: Approximate breaker zone, for the different slopes with their respective approximate water depth and cross shore distance.

G

Surface Elevation time series

Surface elevation for the steep and mild slope for (1) $IG_{free} = 0$, (2) $IG_{free} = 1$, (3) $IG_{free} = 2$.

G.1. Steep Slope (1:35)

G.1.1. $IG_{free} = 0$

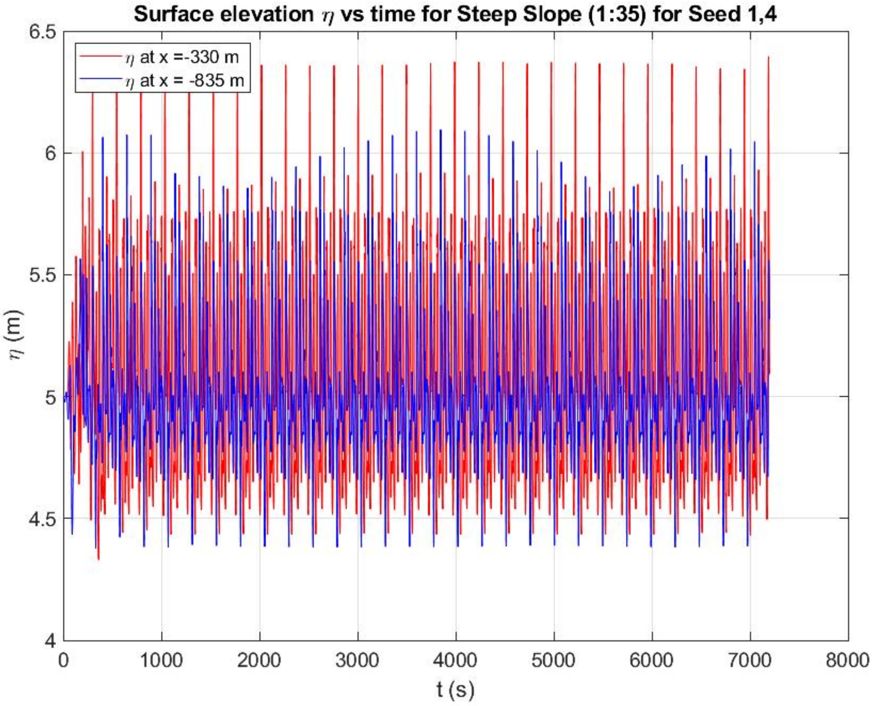

Figure G.1: Surface elevation for the steep slope (1:35) for $IG_{free} = 0$.

G.1.2. $IG_{free} = 1$

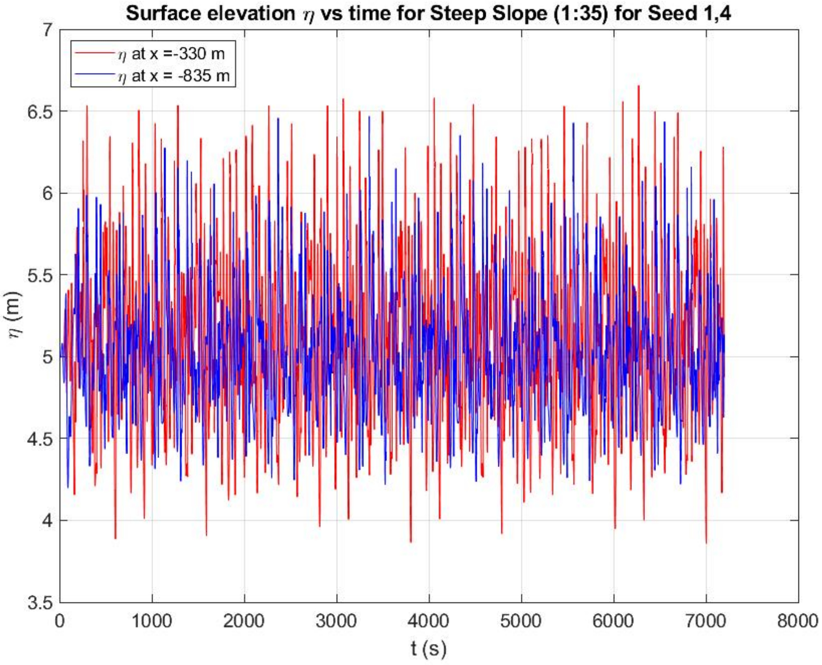

Figure G.2: Surface elevation for the steep slope (1:35) for $IG_{free} = 1$.

G.1.3. $IG_{free} = 2$

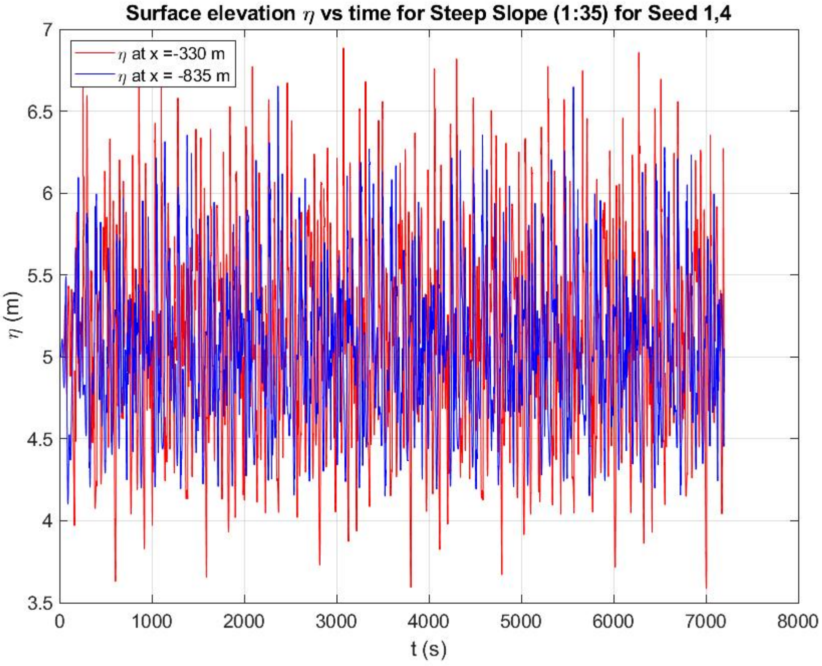

Figure G.3: Surface elevation for the steep slope (1:35) for $IG_{free} = 2$.

G.2. Mild Slope (1:35)

G.2.1. $IG_{free} = 0$

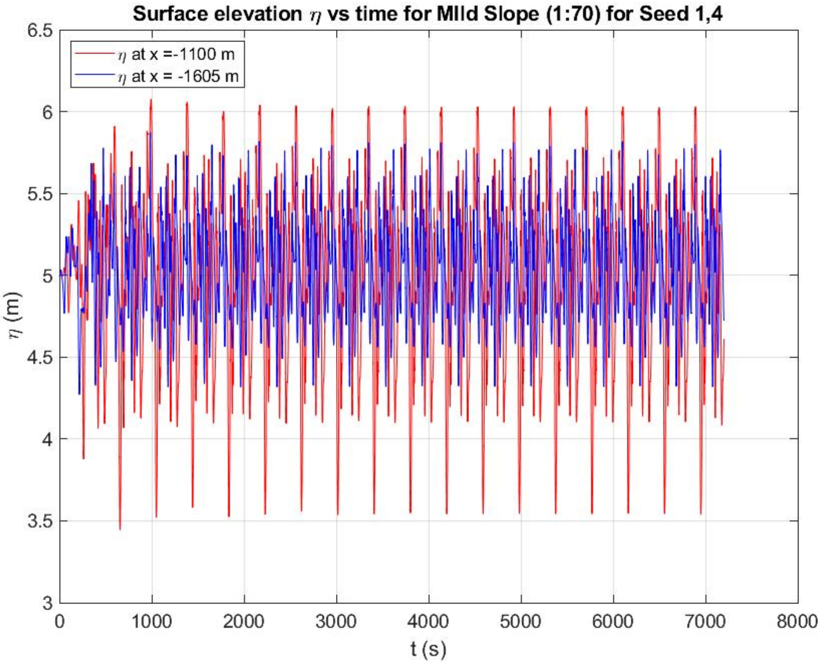

Figure G.4: Surface elevation for the Mild slope (1:70) for $IG_{free} = 0$.

G.2.2. $IG_{free} = 1$

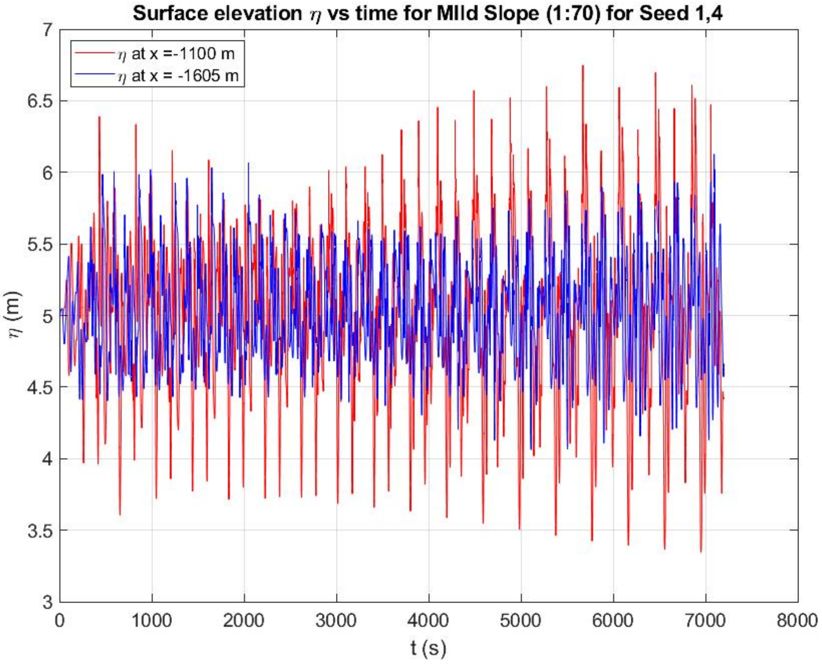

Figure G.5: Surface elevation for the Mild slope (1:70) for $IG_{free} = 1$.

G.2.3. $IG_{free} = 2$

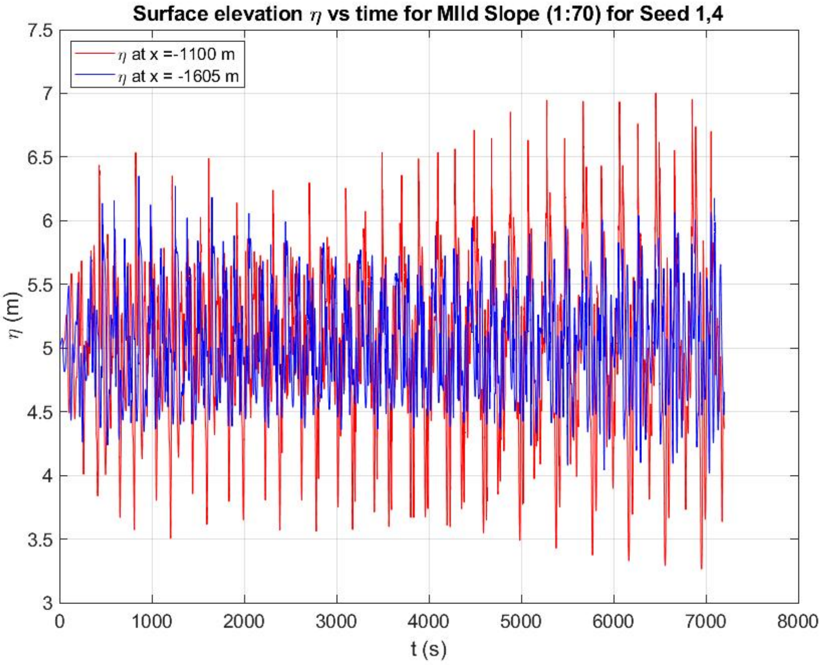

Figure G.6: Surface elevation for the Mild slope (1:70) for $IG_{free} = 2$.

List of Figures

List of Tables